U. S. Department of Energy
1000 Independence Avenue, S.W.
Washington, D.C. 20585

Fiscal Year 2021: Fourth Quarter

Progress Reports:
Advanced Battery Materials Research (BMR) Program
&
Battery500 Consortium

Released December 2021
for the period of July – September 2021

Approved by

Tien Q. Duong
Manager, Advanced Battery Materials Research Program & Battery500 Consortium
Batteries & Electrification R&D
Office of Energy Efficiency and Renewable Energy – Vehicle Technologies Office
U.S. Department of Energy

ACKNOWLEDGMENTS

This report has been edited by the following team members:

- **T. A. Zachry,** Energy & Environmental Resources Group
- **Simon Thompson,** U. S. Department of Energy – Vehicle Technologies Office
- **Patricia H. Smith,** Naval Surface Warfare Center – Carderock

TABLE OF CONTENTS

Advanced Battery Materials Research Program

Battery500 Consortium Program

TABLE OF FIGURES

TABLE OF TABLES

A MESSAGE FROM THE MANAGER: ADVANCED BATTERY MATERIALS RESEARCH AND BATTERY500 CONSORTIUM

As we close Fiscal Year 2021, I would like to take the opportunity to congratulate our Team members on a job well done. The BMR and Battery500 Principal Investigators made significant progress in developing next-generation battery materials and novel cell/electrode design concepts that will help steer our nation from a dependency on fossil fuel to more sustainable and cleaner alternatives. The Team had an impressive record of accomplishments in FY 2021. They published 154 journal articles, received 9 patents, and filed 5 invention disclosures as part of the patent application process. Throughout these endeavors, many Principal Investigators took an active role in developing a pipeline of talent for future development efforts by providing training to the next generation of battery scientists and engineers. Finally, I would like to acknowledge the efforts of the Team Leads and our Editorial group who continued to improve the quality of the quarterly reports. Each quarter they worked with the Principal Investigators to deliver a highly informative 200+ page document that continues to be a beneficial resource for the battery community.

A few notable achievements from the BMR investigators this quarter are summarized below:

- University of Houston (Y. Yao's group) developed an *operando* scanning electron microscopy observation platform suitable for investigation of morphological evolution and failure mechanisms at the electrolyte–electrode interface in solid-state micro-cells.
- Lawrence Berkeley National Laboratory (G. Chen's group) demonstrated stable cycling of all-solid-state Li-metal battery cells employing an NMC-811 cathode and a Li_3YCl_6 solid-state electrolyte for well over 100 cycles.
- Lawrence Livermore National Laboratory (J. Ye's Group) developed low-binder LLZTO and LLZTO / NMC-622 ink formulations for three-dimensional printing that aid densification during the sintering process.
- Argonne National Laboratory (K. Amine's Group) discovered a new metal-free catalytic platform of high efficacy for $Li\text{-}O_2$ cathodes. The charge potential can be consistently maintained below 3.5 V versus Li^+/Li, far outperforming systems that employ metal-based catalysts.
- Pacific Northwest National Laboratory (J. Zhang's group) developed a non-flammable, highly stable electrolyte that also exhibits excellent wettability with the polyethylene or polypropylene separators, solving the problem of non-wettability of current Na-ion battery electrolytes.

Highlights from the Battery500 consortium team include the following:

Keystone Project 1: Materials and Interfaces

- The stability of an undoped $LiNiO_2$ cathode with advanced electrolytes was demonstrated by a comparison between localized high concentration electrolytes (LHCE) and a typical carbonate electrolyte (92% capacity retention after 200 cycles with LHCE versus 56% for carbonate).

Keystone Project 2: Electrode Architecture

- A combination of X-ray fluorescence and sulfur K-edge X-ray absorption spectroscopy techniques showed that the distribution of sulfur-based species is inhomogeneous on the pristine sulfurized polyacrylonitrile (SPAN) cathode, but the chemical status (valence state of sulfur) is uniform.

Keystone Project 3: Cell Fabrication, Testing, and Diagnosis

- The effect of lithium thickness on cell performance was investigated, leading to new insights into designing a high-cycle life cell. The results of this work were published in *Nature Energy*.

Our next report is expected to be available in April 2022.

Sincerely,

Tien Q. Duong

Tien Q. Duong
Manager, Advanced Battery Materials Research Program & Battery500 Consortium
Batteries & Electrification R&D
Energy Efficiency and Renewable Energy
U.S. Department of Energy

TASK 1 – Liquid/Polymer Solid-State Electrolytes

Team Lead: Jihui Yang, University of Washington

Summary and Highlights

The U. S. Department of Energy (DOE) Advanced Battery Material Research (BMR) Program goal is to develop long-life batteries superior to commercial Li-ion systems in terms of cost, vehicle range, and safety. The BMR Program addresses the fundamental problems of electrode chemical and mechanical instabilities that have slowed development of affordable and high-performance automotive batteries. The aim is to identify electrode/electrolyte materials that yield enhanced battery performance and lead to greater acceptance of electric vehicles (EVs). Currently, the Vehicle Technologies Office (VTO) supports 14 projects in the BMR Program under this Task. These projects can be categorized into four general topics:

- **Liquid.** The projects for liquid electrolyte (LE) aim to develop electrolyte formulations, based on fluoro-chemistries, to achieve significantly improved operating voltage, increased durability, and increased energy density of Li-ion batteries at a reasonable cost. Nonaqueous polyelectrolyte (PE) solutions with high Li^+ transference numbers will be developed to achieve high rate capabilities at room temperature. In addition, electrolytes with new polymer binders bearing a pentafluorophenyl group on the backbone will be designed, synthesized, and tested.
- **Polymer.** The targets of PE projects include inorganic/polymer and polymer/gel hybrid electrolytes that have flexibility, mechanical strength, thermal stability, high ionic conductivity, stable interfaces against lithium metal, and polysulfide-trapping capability enabling high-energy-density Li-S batteries, with comparable cycle life.
- **Self-Forming & Self-Healing.** The self-forming, self-healing electrolyte projects are focused on developing and implementing Li-metal-based metal-fluorite and metal-iodide batteries, capable of energy densities > 400-500 Wh/kg and 1000 Wh/L.
- **Solid-State.** The solid-state projects are to develop high conductivity solid electrolytes (SEs) / composite SEs that are scalable, are chemically and electrochemically stable, and will enable low-cost, high-energy-density solid-state lithium batteries (SSLBs).

Highlights. The highlights for this quarter are as follows:

- The Lawrence Berkeley National Laboratory group (LBNL, N. Balsara) conducted X-ray tomography (XRT) experiments on Li-polymer-Li symmetric cells to quantify dendrite growth in block copolymer electrolytes. The team compared the nature of electrodepositions between two organic-inorganic hybrid copolymer electrolytes, namely poly(ethylene oxide)-b-poly(acryloisobutyl polyhedral oligomeric silsesquioxane) (PEO-POSS) diblock copolymer and POSS-PEO-POSS triblock copolymer containing lithium bis(trifluoromethanesulfonyl)imide (LiTFSI) salt. Both the copolymers have similar conducting phase volume fraction, molecular weight, and storage moduli; however, the yield stress of POSS-PEO-POSS is three times higher than PEO-POSS. They found that the cycle life of Li/POSS-PEO-POSS/Li cells are 50 times higher than that of cells with diblock copolymer. XRT images of the cycled symmetric cells reveal that dendrites are formed in the cells having diblock copolymer, while globular protrusions are formed cells with triblock copolymer electrolytes.
- The Wildcat Discovery Technologies group (D. Strand and G. Cheng) successfully fabricated a stand-alone solid composite electrolyte membrane with a thickness of 50 µm and > 75 wt% $Li_7La_3Zr_2O_{12}$ (LLZO). As the Li^+ diffusion pathway in the composite electrolyte is achieved due to surface reaction between PE and Li-La-Zr-Ta-O (LLZTO) particles, the high ionic conductivity can be realized. When LiTFSI / polyvinylidene (di)fluoride (PVDF) mass ratio increases from 0.5 to 3, the highest ionic

conductivity of 8×10^{-4} mS/cm is obtained at room temperature. In addition, Wildcat successfully assembled various components and demonstrated an all-solid-state full cell that exhibited a capacity retention of 91% at the end of 50 cycles.

- At Solid Power Inc. (P. Zhang), the team has developed multifunctional SE materials with high conductivity and stability. The high voltage stability of the new electrolyte was evaluated in a Li-NMC full cell. They also tested LPS electrolyte as a baseline. When tested at 2.5-4.5 V, C/10-C/10, and 45°C, the new electrolyte cell is stable after 10 cycles, while the baseline electrolyte (BE) cell shows 20% resistance growth. The new electrolyte cell also shows 60% lower cell resistance than the baseline cell. The cycle life of the electrolyte was evaluated in a Li-NMC pouch cell. When tested at 2.8-4.2 V, C/5-C/5, and ambient temperature (~ 25°C), the pouch cell showed 90% capacity retention after 500 cycles. The cycle life of 500 has passed the *Go/No-Go Decision* point.

Task 1.1 – Characterization and Modeling of Li-Metal Batteries: Characterization of Li^+ Transport in Polyelectrolytes
(Bryan D. McCloskey, University of California, Berkeley)

Project Objective. This task aims to understand lithium plating and stripping in non-traditional electrolyte systems, specifically PE solutions and concentrated binary salt electrolytes that have been proposed to reduce dendrite formation during lithium stripping and plating due to their high Li^+ transference numbers (t_+). The team will develop capabilities that allow them to understand how ion dynamics in these electrolytes impact macroscale transport properties and Li-metal plating and stripping.

Impact. Ultimately, this task will develop an understanding of how electrolyte composition and molecular interactions can be manipulated to positively impact ion transport of potential electrolytes for Li-metal batteries. This will provide a set of general design rules for novel electrolytes enabling stable, efficient high capacity Li-metal stripping and plating.

Approach. To understand various aspects of lithium plating and ion transport in these systems, the team will develop novel diagnostic and computational modeling techniques. Model PEs, with pendant triflimide anions, will be used as polyanions, as their properties can be easily tuned via changes in the polymerization chemistry. Solution parameters that can be varied for both PE solutions and concentrated electrolytes include solvent and salt composition, additive inclusion, and the aforementioned polymer properties, all of which can have a profound impact on electrostatic interactions between charged species in solution, as well as interfacial stability and reaction kinetics of the lithium electrode. The team will develop capabilities that allow them to understand the impact of molecular-level ion dynamics in these electrolytes on macroscale transport properties and Li-metal plating and stripping. These computational simulations will be validated and refined by comparing results to experimentally measured transport properties of these electrolytes. The team will optimize electrochemical methods for these electrolytes to evaluate relevant transport properties under the Newman concentrated solution theory framework, which has never been performed on these non-traditional electrolytes. ^1H and ^{19}F nuclear magnetic resonance (NMR) diffusometry will also be used to measure single-ion self-diffusion coefficients without an applied electric field; solution viscosity measurements using a state-of-the-art rotating sphere viscometer can be performed under entirely air-free and water-free conditions. The team will develop capabilities to quantitatively understand degradation mechanisms of various electrolytes during Li-metal stripping and plating. Specifically, differential electrochemical mass spectrometry (DEMS) will be used to study outgassing that occurs from electrolyte degradation processes.

Out-Year Goals. The ultimate goal of this project is to understand the influence of electrolytes with novel transport characteristics on the performance of Li-metal electrodes. Work will continue to build toward a complete understanding of Li-ion and counterion transport in PE solutions and concentrated electrolytes, as well as the impact of electrolyte transport properties on Li-metal uniformity during electrochemical stripping and plating. Outgassing measurements using DEMS will be developed to further probe the interfacial reactivity of lithium metal with electrolytes created in this project.

Collaborations. Collaborators on this project include K. Persson (atomistic and coarse-grained modeling) and N. Balsara (electrochemical characterization of PEs), both at LBNL.

Milestones

1. Establish a simple method to measure activity coefficients and thermodynamic factors for a model electrolyte. (Q1, FY 2021; Completed)
2. Synthesize very low molecular weight oligomer triflimide-based polyions (pTFSI). (Q2, FY 2021; Completed).

3. Measure conductivity, self-diffusion, and concentration cells for model pTFSI solutions. (Q3, FY 2021; Completed)

4. Establish electrophoretic NMR (eNMR) techniques for measuring the true Li^+ transference number of pTFSI solutions. (Q4, FY 2021; Completed)

Progress Report

This quarter, the team scaled up synthesis of their PEs, synthesizing a 10-repeat unit, 20-repeat unit, and 40-repeat unit lithium triflimide appended polystyrene in 5 g batches. They are characterizing transport of these polyions in carbonate solutions. They continued last quarter's progress measuring the transference number of the lithium triflimide appended polystyrene in 3:7 ethylene carbonate : ethyl methyl carbonate (EC:EMC) PE solutions. They successfully measured the electrophoretic mobilities (via eNMR) and conductivity (using a conductivity probe) of a lithium-triflimide styrene monomer, as well as 10-repeat and 20-repeat unit lithium triflimide appended polystyrene (see Figure 1). They measured mobilities of 1.2×10^{-9} m^2/Vs for the Li^+ ion and 2.63×10^{-9} m^2/Vs for the anionic monomer, yielding a true transference number of 0.32 and a conductivity of 2.01 mS/cm. The transference number of the monomeric system is notably higher than that of the 10-repeat unit oligomeric system the team measured last quarter, which has a true transference number of 0.16. This aligns well with the team's developed theory predicting that increasing anion-anion correlation with polymer chain length will decrease the true transference number. This theory predicts that at long chain lengths and low concentrations, eventually the transference number will become negative with respect to the center of mass, meaning that lithium is dragged in multi-ion clusters in the "wrong-direction" in the applied electric field. The team has recently completed initial measurements on a 0.5 molal 20-repeat unit PSTFSI [poly(4-styrenesulfonyl (trifluoromethane-sulfonyl) imide)] in EC:EMC system, which indicate a negative transference number of -0.15 with respect to the center of mass. Follow-up measurements and rigorous analysis need to be performed to confirm this phenomenon, as it would be the first known observation of a negative true transference number in nonaqueous PE systems using electrophoretic methods. The team continues to measure longer chain oligomers in the coming quarter to see if their predicted trends of decreasing transference number with increasing polyanion molecular weight hold true in this system. They will also expand this study to examine the effect of concentration on correlated ion motion

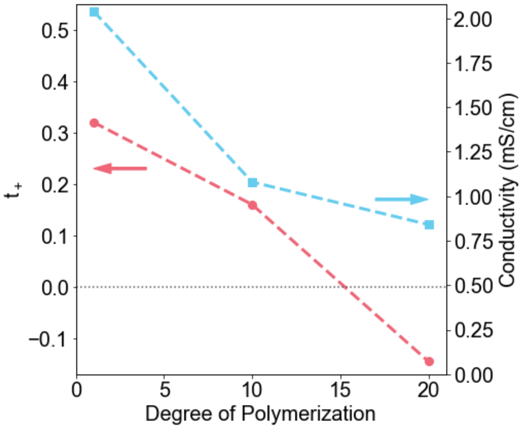

Figure 1. Transference number (pink) and conductivity (blue) versus degree of polymerization for 0.5 m solutions of lithium-triflimide polystyrene in 3:7 EC:EMC. Note that for the highest degree of polymerization, the team observes a negative transference number.

In addition to the eNMR progress, the team continues to modify and adapt their ultra-low volume Hittorf Cell method developed last quarter. Initial studies using lithium electrodes and a model system of $LiPF_6$ in EC:EMC were promising; however, they noticed significant instability in the measurements due to the highly reactive nature of lithium metal. In many solutions, they observed lithium particles and debris floating in the cathodic chamber. This quarter, the team has addressed this by experimenting with eliminating all lithium metal from their Hittorf design; instead, they are using intercalation electrodes [graphite, lithium titanate, nickel-manganese-cobalt (NMC), and lithium-iron-phosphate (LFP)] to polarize the cell. They observe significantly more stable and repeatable electrochemistry. They have started to apply this method to the PE system and in the coming quarter hope to be able to validate the eNMR transference number methods using the Hittorf method.

Patents/Publications/Presentations

The project has no patents, publications, or presentations to report this quarter.

Task 1.2 – Advanced Polymer Materials for Batteries
(Zhenan Bao and Yi Cui, Stanford University)

Project Objective. This project will develop new polymer materials for batteries. The team will develop polymer coatings with specific mechanical properties that can accommodate the volume expansion and contraction of the Li-metal anode associated with deposition and stripping (charging and discharging).

Project Impact. The cycling stability and Coulombic efficiency (CE) of Li-metal electrodes will be increased by implementation of a polymer-based protective layer that functions as an artificial solid electrolyte interphase (SEI) with desired properties. The improved performance will enable further development toward practical utilization of Li-metal anodes with higher cycling efficiency and less susceptibility to dendrite-based failure.

Approach. The project uses soft polymer coatings with dynamic crosslinking to give the resulting polymers liquid-like rheological properties and stretchable and self-healing properties. In previous work, the project has shown that such coatings resulted in uniform deposition/stripping of lithium metal and improved cycling stability of Li-metal electrodes. To understand the design rules for effective polymer coatings, the team chose a few representative polymers to systematically understand structure property relationships. Here, the team investigates the correlation between surface energy of the polymer and exchange current for lithium deposition.

Out-Year Goals. Work will progress toward the correlation between dielectric constant and exchange current. These findings will enable further understanding and development of various polymer coatings for protecting Li-metal anodes.

Collaborations. This quarter, the team is collaborating with J. Qin at Stanford.

Milestones

1. New lithium anode coating design. Analyze the polymer chemistry and mechanical property using NMR, differential scanning calorimetry (DSC), and rheology. (Q1, FY 2021; Completed)
2. Analyze stability of the polymer in electrolyte and its ability to reduce the reaction in the Li-metal surface with electrochemical impedance spectroscopy (EIS). (Q2, FY 2021; Completed)
3. Characterize the impact of the polymeric coating on lithium deposition morphology using scanning electron microscopy (SEM). (Q3, FY 2021; Completed)
4. Coat Li-metal electrodes with the polymeric coating and achieve stable lithium cycling for 150 cycles at 1 mA/cm^2 and 2 mA/cm^2 current density. (Q4, FY 2021; Completed)

Progress Report

Introduction

The team hypothesizes that an effective method to address the lithium anodic interfacial instability is to fundamentally alter the Li-ion deposition pathways by electrostatically blocking the heterogenous surface regions that concentrate lithium ions due to high electric field. This can be experimentally implemented using electro-inactive cations at the interface that can 'shield' the inhomogeneous protrusion on the electrode surface to neutralize the electric field landscape. However, this strategy can be successful only when it is ensured that these electro-inactive cations do not undergo reduction during lithium deposition process. In other words, their reduction potential needs to be even lower than that of Li^+ ions that already have the lowest intrinsic reduction potentials among metallic cations. Previously, Ding et al. pointed out that Cs^+ can achieve lower reduction potential than Li^+ by tuning its concentration based on Nernst Equation. Furthermore, it was shown that addition of Cs^+ ions in electrolyte resulted in improved lithium deposition morphology and battery operation. However, the concentration-dependent electrochemical stability of Cs^+ ions can be undermined by their localized aggregation at the electrode surface, resulting in the reduction of Cs^+.

Instead of using free cations, the team proposes here to tether the electroactive cations (pyrrolidinium, Py^+) onto a flexible and stable polymer backbone (polydimethylsiloxane, PDMS) to form a PDMS-based poly (ionic liquid) (PDMS-Py) coating that would homogenize the electric field distribution on the electrode surface and promote uniform lithium deposition. Based on previous study, Py^+ was selected based on its lower reduction potential compared to Li^+ and its chemical stability with the Li-metal anode. Incorporation of Py^+ in a polymer coating on the lithium anode is a facile method that does not alter existing manufacturing capabilities and also limits their interaction with other battery components. Building on previous studies of anodic coating using polymers (PEO, Nafion, PVDF), and drawing on their knowledge of designing cation-tethered polymeric coating on anode surface, the team work on the interfacial material is designed on economically viable chemistry, chemically and electrochemically inertness with lithium metal, possession of conducting pathway for lithium conduction, and mechanical robustness for adapting to rapid volume changes.

Polymer Coating Design

The schematic of Figure 2a illustrates lithium anode coated with PDMS-Py-trifluoromethanesulfonylimide (PDMS-PyTFSI) containing electro-inactive cations and its counter anion TFSI. In the absence of any coating, the concentrated electric field at surface protrusion triggers a self-amplified surface roughening process of lithium deposition (Figure 2b). The presence of cations is hypothesized to neutralize the radiating electric field and helps to homogenize lithium deposition pathways. Figure 2c showcases the "cationic shielding" phenomenon where the presence of the PDMS-PyTFSI coating results in redistribution of Li^+ ions away from the surface protrusions, leading to a more uniform topology. The physicochemical prerequisites of the PDMS-Py polymer coating for the cationic shielding mechanism are the following: (1) the cations in PDMS-PyTFSI backbone should have a lower reduction potential than that of Li^+, and (2) sufficient mobility of the polymer chains is essential for electric-field-based response of the cations.

In previous work, the team utilized a system of random copolymer on poly(acrylic) backbone: one copolymer side chain contains the Py^+ cation units, and the other side chain is perfluoroalkyl as an inert component that can also lower the glass transition of the final copolymer and introduce mobility to the polymer chains.

Instead of using a relative rigid poly(acrylic) backbone, the new design (Figure 2d) utilizes the flexible PDMS backbone, which efficiently brings down the polymer's glass transition temperature (T_g) so that they no longer need to introduce another fluorinated component, and all of the polymer side chains can be functionalized with the Py^+ cation units. Beyond the benefit of mechanical flexibility, PDMS-based polymer is more economically viable compared to any fluorinated polymer, its mechanical property can be regulated via controlled crosslinking, and it is inert and electrochemically stable with lithium metal.

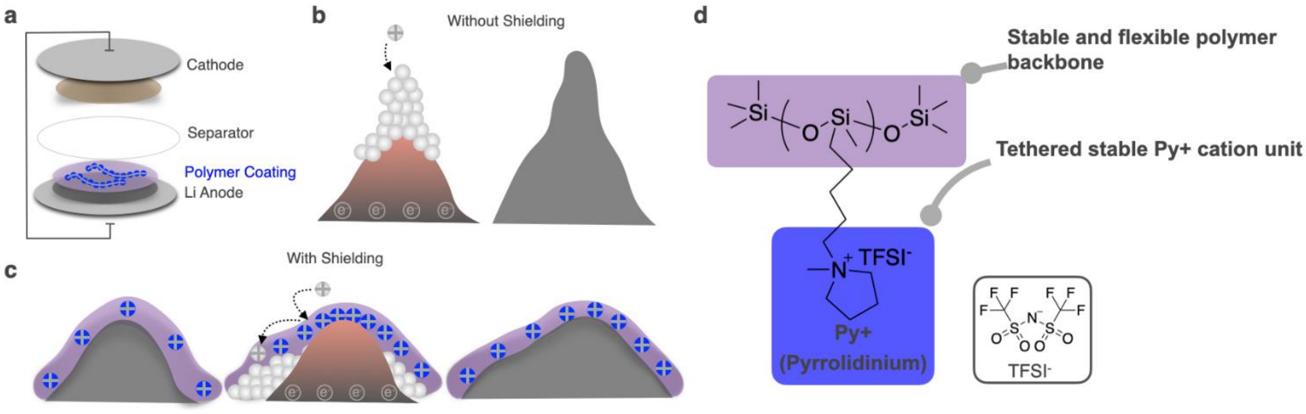

Figure 2. PDMS-Py as the anodic coating for Li-metal batteries. (a) Li-metal battery with polymer-coated anode. (b) The concentrated electric field at vicinity of surface protrusions causes the self-amplifying dendritic deposition of lithium ions. (c) Coating on Li-metal anode. During Li⁺ deposition, cations in polymeric ionic liquid coating remain electrochemically stable and can effectively shield the Li⁺ ions, resulting in more flat and homogeneous deposition. (d) Chemical structure of the PDMS-PyTFSI coating.

Long-Term Cycling with Lithium Electrodes

To examine the stability of the PDMS-PyTFSI coating with Li-metal electrodes during long-term cycling, a layer of polymer coating was applied to the lithium electrodes, and a Li||Li symmetric cell was assembled with 40 µl of three types of electrolytes, as shown in Figure 3. The team stripped-and-plated 1 mAh/cm^2 lithium at 1 mA/cm^2 current density for three electrolytes, and they increased current density to 2 mA/cm^2 for the fluorinated 1,4-dimethoxylbutane (FDMB) electrolyte.

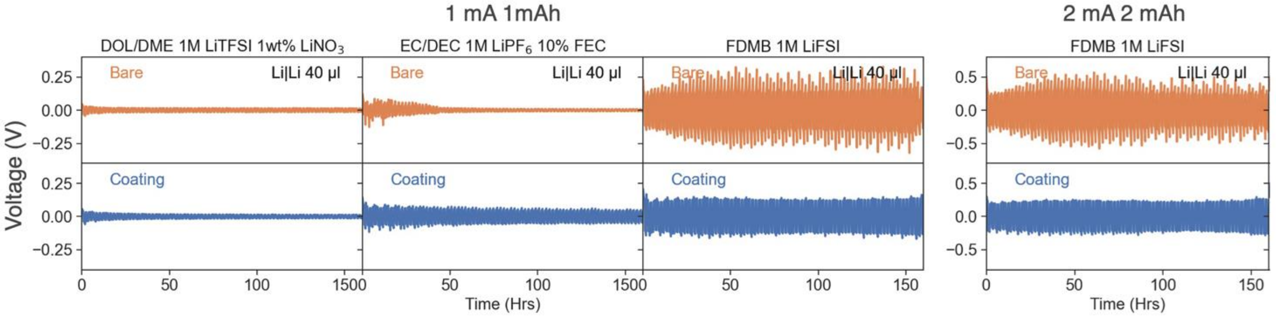

Figure 3. Li||Li cycling with polymer coating on the electrodes. The electrolyte composition and cell configurations are marked in the graph.

At 1 mA/cm^2 current density, the Li-metal-coated electrodes showed stable cycling performance over 150 cycles in all three electrolytes (that is, ether, carbonate, and FDMB). In 1,3-dioxolane (DOL) / 1,2-dimethoxyethane (DME) electrolyte, the application of the coating slightly increased the overpotential. In EC / diethyl carbonate (DEC) electrolyte, the lithium electrodes without polymer coating demonstrated a soft shorting at ~ 50 hours of cycling, indicating non-stable cycling and lithium deposition behavior. For the lithium electrodes with the polymer coating in EC/DEC electrolyte, the team observed stable voltage profile over cycles. In FDMB electrolyte, the uncoated lithium metal showcased increase in overpotential ~ 30 cycles. This is consistent with literature-reported behavior, attributed to formation of a resistive SEI layer on the Li-metal surface. With the layer of coating applied, the voltage profile was stabilized without increasing over cycles, demonstrating that a more conductive SEI layer was formed. Similar behavior was observed on the FDMB electrolyte at both 1 mA/cm^2 and 2 mA/cm^2 current density.

This series of cycling performance shows that the PyPDMS coating promotes the stable cycling behavior of Li-metal anodes in three types of electrolytes.

Patents/Publications/Presentations

Publication

- Tsao, Y., H. Gong, S. Chen, G. Chen, Y. Liu, T. Z. Gao, Y. Cui, and Z. Bao. “A Nickel-Decorated Carbon Flower/Sulfur Cathode for Lean-Electrolyte Lithium–Sulfur Batteries.” *Advanced Energy Materials* 11, No. 36 (2021): 2101449.

Awards

- American Chemical Society (ACS) Chemistry of Materials Award; Z. Bao.
- Chinese American Chemical Society Achievement Award; Z. Bao.
- Materials Research Society (MRS) Mid-Career Award; Z. Bao.
- Global Energy Prize; Y. Cui.

Task 1.3 – Improving the Stability of Lithium-Metal Anodes and Inorganic-Organic Solid Electrolytes (Nitash Balsara, Lawrence Berkeley National Laboratory)

Project Objective. The project objective is to establish a new hybrid electrolyte that will be stable against cells with a Li-metal anode.

Project Impact. PEs offer increased stability in lithium batteries in comparison to more widely used LEs. Nanostructured electrolytes containing both soft, ion-conducting domains and rigid, nonconducting domains offer the opportunity to tune both mechanical and electrical properties separately. Such electrolytes are conveniently made by block copolymer self-assembly. Most of the block copolymer electrolytes studied thus far comprise organic polymer chains for both the conducting and rigid domains. The team hopes to synthesize new electrolytes that simulataneously have high transport properties and have greater stability against lithium in comparison to organic diblock copolymers.

Approach. First, the team synthesizes hybrid diblock copolymers by incorporating monomers that contain an inorganic component. Then, electrolytes are prepared by mixing these diblock copolymers with salt. Electrochemical and mechanical characterization of these materials is performed before carrying out cycling XRT experiments and *in situ* small angle X-ray scattering (SAXS) experiments. The combination of these approaches enables rational design of materials that exhibit improved stability against lithium metal.

Out-Year Goals. The project will synthesize a new hybrid electrolyte that is designed to be stable against lithium metal. The material is a block copolymer in which one block contains acryloisobutyl POSS. The second block is a conventional PE (PEO). Electrochemical characterization of this polymer will include measurement of all transport properties including conductivity, diffusion coefficient, and transference number. The stability against lithium metal will be evaluated by cyclic voltammetry (CV), while its applications as an electrolyte will be evaluated and visualized using cycling XRT experiments on symmetric Li-hybrid-Li cells.

Collaborations. There are no active collaborations this quarter.

Milestones

1. Synthesize at least 2 POSS-containing single ion conductors (SICs). (Q1, FY 2021; Completed)
2. Develop the relationship between non-linear mechanical properties and ion transport in solid block copolymer electrolytes. (Q2, FY 2021; Completed)
3. Conduct *in situ* X-ray scattering experiments on Li-polymer-Li symmetric cells to quantify polymer morphology in the presence of an applied field. (Q3, FY 2021; Completed)
4. Conduct XRT experiments on Li-polymer-Li symmetric cells to quantify dendrite growth in block copolymer electrolytes. (Q4, FY 2021; Completed)

Progress Report

Formation of non-planar electrodeposition during charging is one of the main disadvantages in implementing Li-metal anode batteries. XRT is used to directly image plating and stripping of lithium protrusions during electrodeposition of symmetric lithium/polymer/lithium cells.

The electrolyte used in this study is a poly(styrene-b-ethylene oxide) (SEO) copolymer mixed with LiTFSI salt. The symmetric cells were preconditioned at a current density of 0.02 mA cm^{-2} for 14 cycles. After preconditioning, the cells were polarized at a current density of 0.175 mA cm^{-2} till they short-circuited due to growth of globular lithium protrusions. The cells are imaged at different time intervals before failure.

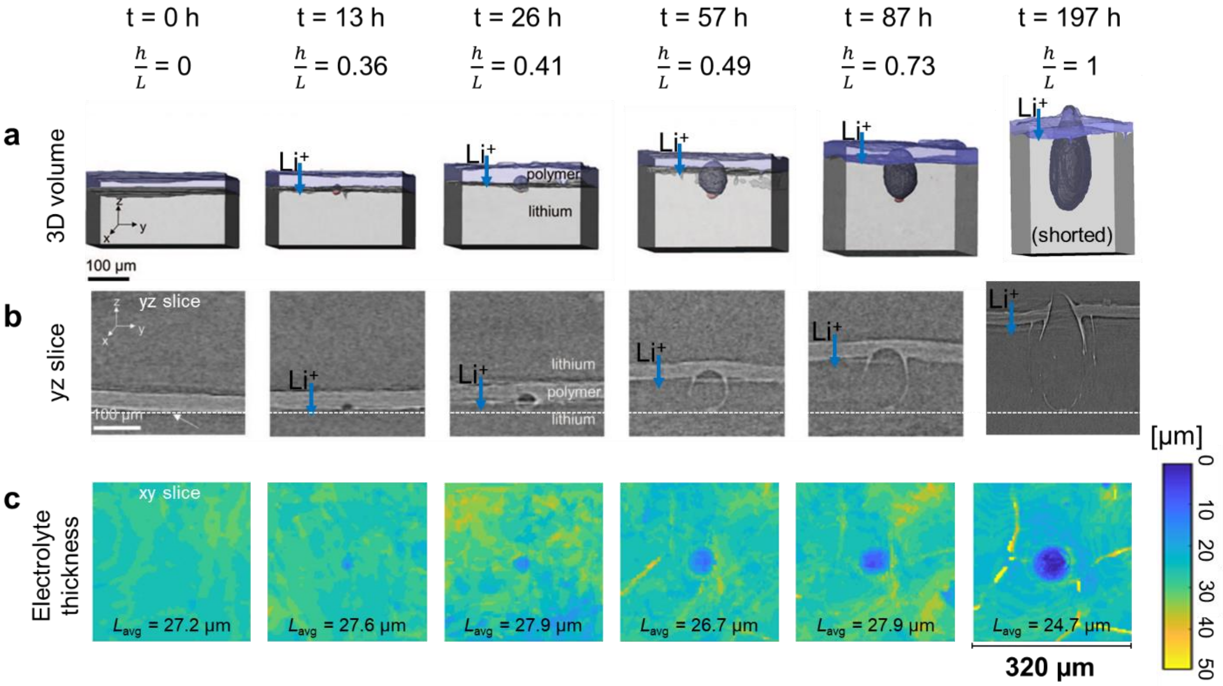

Figure 4. (a) Volume rendering of a lithium globule at different time intervals. The lithium globule is rendered in dark gray, while the electrolyte is rendered in purple, the bottom lithium in light gray, and the impurity particle in dark red. The top lithium electrode is transparent. Lithium is plated from the top to the bottom electrode. (b) yz slice through the 3D reconstruction. The darker gray lithium sandwiches the lighter gray electrolyte. The approximate location of the original electrode-electrolyte interface is marked with the dashed white line. (c) Maps of electrolyte thickness, or interelectrode distance, in the xy plane. The first five sections of panels (a) and (b) were previously published [Harry, K. J., K. Higa, V. Srinivasan, and N. P. Balsara. *Journal of the Electrochemical Society* 163 (2016): 2216–2224].

The local current density maps for both electrodes of a lithium symmetric cell during the growth of a lithium globule on the bottom electrode are presented in Figure 5.

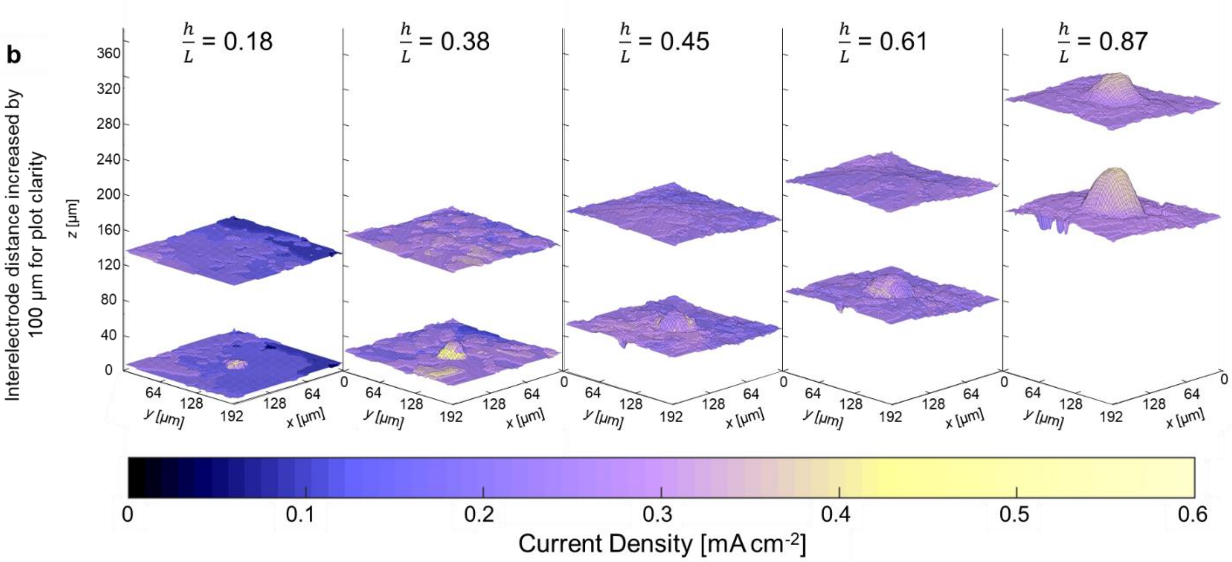

Figure 5. Local current density maps for the top and bottom electrode during increasing time of growth for lithium globule on the bottom electrode. Each set of maps is labeled with the time point and normalized globule height corresponding to midway between the start and end points, where the start and end points are the two 3D renderings that were compared to calculate the plotted current density. The colormap indicates the calculated local current density at each *x, y* position. The plot represents an averaged 3D surface, representing the interface between the electrode and electrolyte between the two time points used in the current density calculation. The *z* dimension represents the location of the interface, if *z = 0* represents the initial position of the bottom electrode-electrolyte interface at *t = 0*. The plotted surfaces of the two electrodes were separated by an additional 100 µm for clarity.

Correlation functions were calculated to show that current density between the two parallel electrodes was not highly correlated until the interelectrode distance decreased to less than six µm at the protrusion, despite the initial interelectrode distance of 25 µm.

The nature of electrodepositions was compared between two organic-inorganic hybrid copolymer electrolytes: PEO-POSS diblock copolymer, and POSS-PEO-POSS triblock copolymer containing LiTFSI salt. Both the copolymers have similar conducting phase volume fractions, molecular weights, and storage moduli, but the yield stress of POSS-PEO-POSS is three times higher than PEO-POSS.

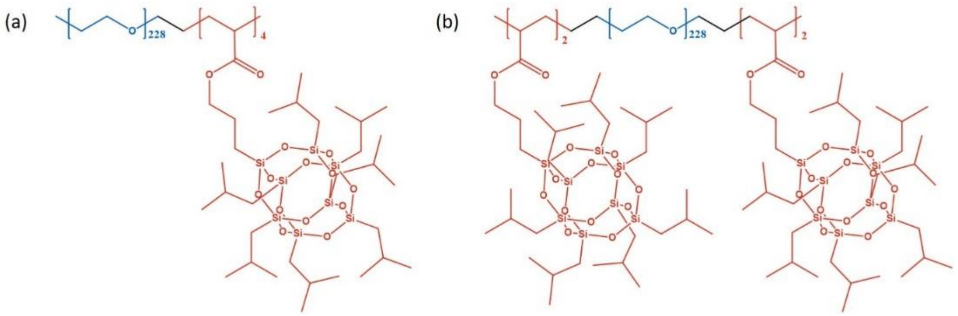

Figure 6. Chemical structure of (a) PEO-POSS (b) POSS-PEO-POSS.

The cycle life of lithium/POSS-PEO-POSS/lithium cells is 50 times higher than that of cells with diblock copolymer. XRT images of the cycled symmetric cells reveal that dendrites are formed in the cells having diblock copolymer, while globular protrusions are formed in case of cells with triblock copolymer electrolytes.

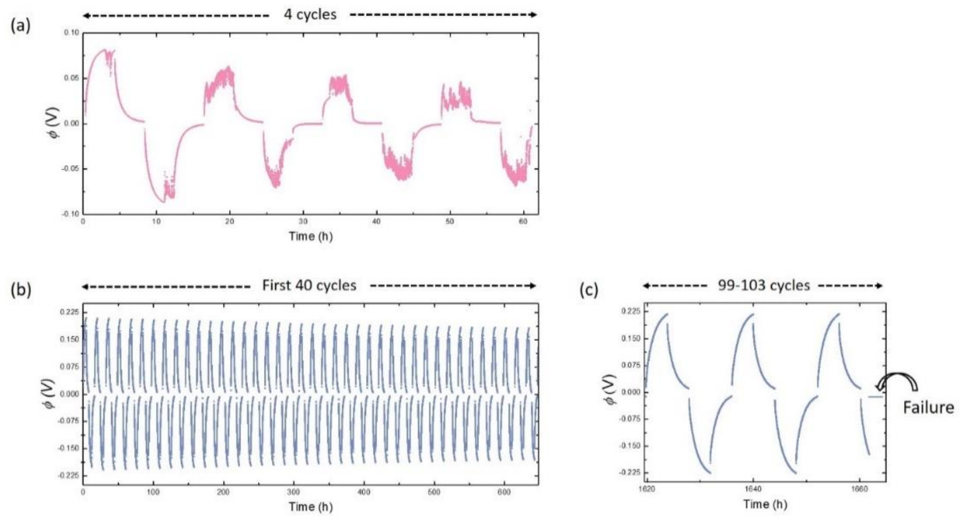

Figure 7. (a) The voltage (Φ) versus time plot during cycling of the cell for PEO-POSS copolymer electrolyte. (b) Φ versus time plot for POSS-PEO-POSS electrolyte shown up to first 40 cycles. (c) Φ versus time plot for last 3 cycles before failure. The cells were cycled at 0.15 mA cm^{-2} current density for 4 hours in both positive and negative directions, followed by 4 hours of rest. Cell failure was determined by the abrupt drop in the potential.

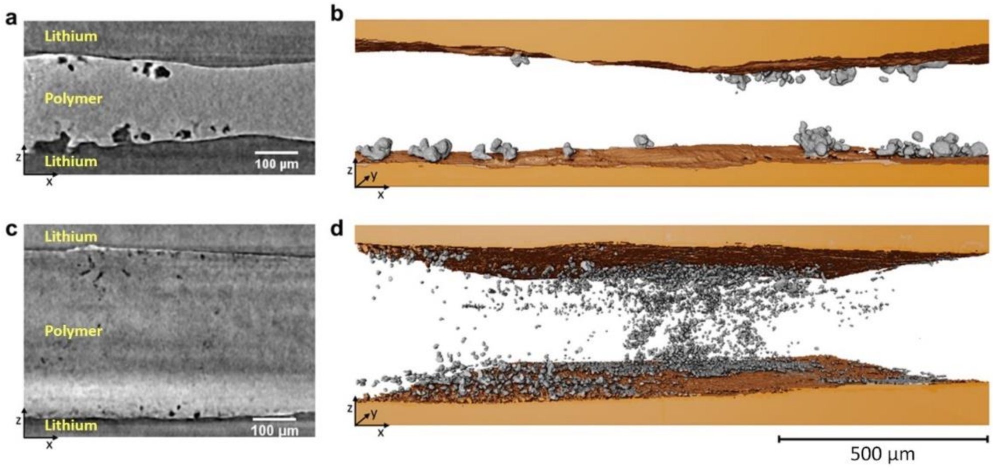

Figure 8. Cross-sections through the cell are represented in the left side panels for (a) POSS-PEO-POSS after 40 cycles and (c) PEO-POSS after failure. 3D visualizations of the dendrites are represented in the right-side panels, (b) POSS-PEO-POSS and (d) PEO-POSS. The protrusions are represented in gray, and the lithium electrodes are represented in orange.

Patents/Publications/Presentations

Publication

- Galluzzo, M. D., L. S. Grundy, C. J. Takacs, C. Cao, H. G. Steinrück, S. Fu, M. A. R. Valadez, M. F. Toney, and N. P. Balsara. “Orientation-Dependent Distortion of Lamellae in a Block Copolymer Electrolyte under DC Polarization.” *Macromolecules* 54, No. 17 (2021): 7808–7821.

Task 1.4 – Development of Thin, Robust, Lithium-Impenetrable, High-Conductivity, Electrochemically Stable, Scalable, and Low-Cost Glassy Solid Electrolytes for Solid-State Lithium Batteries
(Steve Martin, Iowa State University of Science and Technology)

Project Objective. The project objective is to develop new Li^+-conducting mixed oxy-sulfide nitride (MOSN) glassy solid electrolytes (GSEs) that are impermeable to lithium dendrites, have high conductivities, are scalable through low-cost glass manufacturing, are chemically and electrochemically stable, and will enable low-cost, high-energy-density SSLBs. The SSLBs constructed from these new GSEs will meet and exceed all program objectives: usable specific energy @ C/3 $\geq$ 350 Wh/kg, calendar life 15 years, cycle life (C/3 deep discharge with < 20% energy fade) 1000, and cost $\leq$ \$100/kWh.

Project Impact. This project will enable the team to demonstrate the following: (1) thin MOSN GSE films yield superior performance in a much safer, lower-cost, and Li-dendrite impenetrable form, and (2) high rate and long cycle life can be achieved in SSLBs using thin-film MOSN GSEs. The new GSEs in SSLBs are anticipated to increase energy density (anode basis) from ~ 300 mAh/g to ~ 4,000 mAh/g, enabling replacement of internal combustion engines in both light-duty and heavy-duty vehicles. Each 20% reduction in the ~ 1.6 billion liters of gasoline used per day in the United States would reduce CO_2 emissions by ~ 4 billion kg or 2×10^{12} l of CO_2 per day. The team will also increase scientific and engineering knowledge of thin-film GSEs in SSLBs.

Approach. The MOSN mixed glass former (MGF) glasses used for the GSEs in this project were developed in previous work to have the necessary thermal stability and high ionic conductivity for successful use as a drawn-film electrolyte. In this project, the glass chemistry will be tuned for even more desirable properties, by investigating structure-property relationships and testing variations in glass chemistry.

Out-Year Goals. Work will progress toward developing a glass capable of being drawn to 100-µm thickness, while having high conductivity and electrochemical stability and good cycling ability.

Collaborations. There are no active collaborations this quarter.

Milestones

1. Accomplish: 100 cycles against lithium metal with no cell shorting and < 20% degradation of other properties. (Q4, FY 2021; Completed)
2. Accomplish: Optimize draw conditions for MOSN GSE to achieve 5 m × 5 cm × < 100-µm thin films. (Q4, FY 2021; Completed)
3. Accomplish: Fabricate MOSN MGF Li|GSE|Li cells in small area format, ~ 1 cm^2. (Q4, FY 2021; Completed)
4. *Go/No-Go Decision*: Micro-sheet glass ribbon processing facility optimized / design capable of meeting the following performance requirements: glove box enclosing preform redraw facility reaches 10 ppm O_2 and H_2O, and 3 samples of MOSN MGF GSE ribbons have been drawn at 5 m × 5 cm × 100 µm. Analysis indicates technical approach capable of achieving performance targets. (Q4, FY 2021; Completed)

Progress Report

Develop Optimized High Li^+ Ion Conductivity MOSN MGF GSEs

Develop MOSN MGF GSEs with Target Properties Capable of Cycling Lithium against Lithium Metal

This quarter, the team focused efforts on continued development of MOSN MGF GSEs with advantageous properties for use as GSE films. This includes development of GSEs with elevated Li^+ conductivity at room temperature, improved voltage stability windows toward both cathodic and anodic decomposition, and increased chemical toughness toward lithium metal. They also worked on developing glass compositions that are resistant to crystallization to enable preparation of high-quality glass films.

Table 1. Chemical composition and naming scheme of various mixed oxy-sulfide nitride glasses.

Sample ID	Compositional Formula
ISU-5	$0.60Li_2S + 0.40SiS_2 + 0.1LiPO_3$
ISU-6	$0.58Li_2S + 0.315SiS_2 + 0.105LiPO_3$
ISU-7(x)	$0.58Li_2S + 0.315\ SiS_2 + 0.105\ [(1\text{-}x)\ Li_{0.67}PO_{2.87} + xLiPO_{2.83}N_{0.314}]$
ISU-8(x,y)	$yLi_2S + 0.75(1\text{-}y)SiS_2 + 0.25(1\text{-}y)LiP_{1\text{-}x}Al_xO_{3\text{-}x}$
GSE-1	$yLi_2S + (1\text{-}y)[(1\text{-}x)SiS_2 + xLiPO_3]$
ISU-9(z)	$0.58Li_2S + 0.315SiS_2 + 0.105[(1\text{-}z)LiPO_3 + zLi_2SiO_3]$

Previous reports have detailed the strategy of nitrogen-doping through the use of LiPON during glass synthesis. This quarter, the team addressed the need to further characterize and understand nitrogen's impact on the structure of ISU-7(x) GSEs. They used Fourier transform infrared (FTIR) spectroscopy to identify key bonding motifs impacted by incorporation of LiPON. The FTIR spectra were identified for ISU-7 ($x = 0.0\text{-}0.5$), as shown in Figure 9. Two bands can be seen in the spectra from 500-800 cm^{-1} and 800-1200 cm^{-1}. In the first band, three absorbance modes are identified for the peaks at 565 cm^{-1}, 583 cm^{-1}, and 615 cm^{-1}, which have been assigned to the δ(Si-O-Si) of SiO_2^-, the $\nu_{as}(PS_3^{2-})$ of $P_2S_6^{4-}$, and the non-bridging sulfur (NBS) of PS_4^{3-}, respectively. For the second band, three more absorbance modes are identified at 671 cm^{-1}, 683 cm^{-1}, and 710 cm^{-1}, which correspond to NBS Si-S^- of SiS_3^{2-}, the NBS P-S^- of $PS_xO_{3\text{-}x}^-$, and P = S bond of $PS_xO_{3-x}^-$. Also for the second band, from 800-1200 cm^{-1}, there are four main absorbance modes at 913 cm^{-1}, 960 cm^{-1}, 1050 cm^{-1}, and 1100 cm^{-1}, which correlate to the $\nu_{as}(P\text{-}O\text{-}P)^-$, the PO_3^{2-} structure, the non-bridging oxygen (NBO) P-O^- of PO_4^{3-}, and the NBO of $PS_xO_{3\text{-}x}^-$. With the addition of LiPON, there are shifts in intensity that affect all spectra with PS_4^{3-} and ν_s(P-S-P) remaining unchanged. Specifically, there is a decrease of the δ(Si-S-Si), $\nu_{as}(PS_3^{2-})$, and ν_{as}(P-O-P) modes and an increase in the Si-S^-, P-S^-, P = S, P-O^-, and $PS_xO_{3\text{-}x}^-$ modes. As LiPON is added to the material, there is an increase in the number of non-bridging species (sulfur and oxygen), which creates more sites for lithium ions to occupy. In addition, there is a subtle decrease of the ν_{as}(P-O-P) mode and increase in the P-O^- mode, implying that nitrogen is incorporating into the material by replacing the oxygen in the P-O-P bonds and facilitating the creation of non-bridging species. Importantly, the spectra of $x = 0.2$ (red trace) has the lowest ν_{as}(P-O-P) and highest P-O^- modes, suggesting that there are more lithium sites, which results in a higher conductivity value of 0.64 mS/cm. This analysis has given greater insight into the GSE atomic-level structure and the impact LiPON has on that structure.

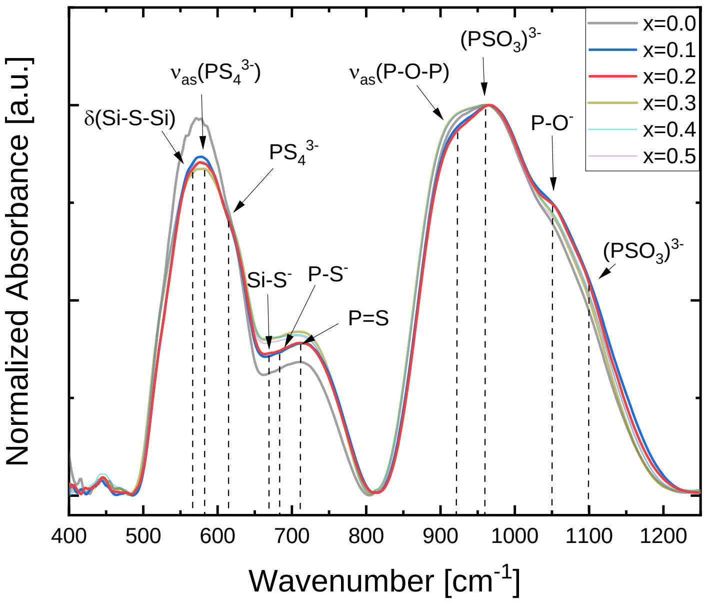

Figure 9. Fourier transform infrared spectra of $0.58Li_2S + 0.32SiS_2 + 0.1[(1\text{-}x)Li_{0.67}PO_{2.87} + xLiPO_{2.83}N_{0.314}]$, y = 0.314 series ranging from $0.0 \le x \le 0.5$, with modes identified to respective bonds.

A common feature in the MOSN compositional series is the use of multiple glass formers, in this case silicon and phosphorus, to take advantage of the MGF effect. By using multiple glass formers, various properties such as ionic conductivity and glass network strength can be enhanced. A systematic study was conducted to identify changing short-range order (SRO) structural units in the GSE-1 series going from a pure silicate glass ($x = 0$) to a pure phosphate glass ($x = 1$).

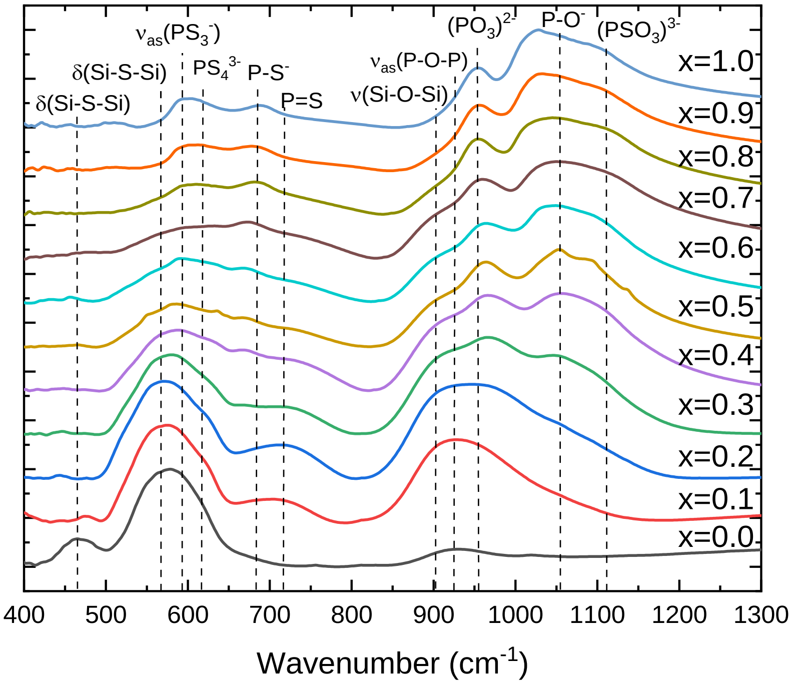

Figure 10. Fourier transform infrared spectra of $0.58Li_2S + 0.42[xSiS_2 + (1\text{-}x)LiPO_3]$ series ranging from $0.0 \le x \le 1.0$, with modes identified to respective bonds.

As shown in Figure 10, FTIR measurements were used to identify various polyhedral SRO units and linkages in the compositional series. As $LiPO_3$ is added and SiS_2 is removed, there is a decrease in the intensity of vibrational modes associated with SiS_2 in the 500-800 cm^{-1} band, and an increase in the intensity of modes associated with $LiPO_3$ in the 800-1200 cm^{-1} band. In particular, the δ(Si-S-Si) peak at 571 cm^{-1} loses intensity as more $LiPO_3$ is added and replaces SiS_2. Simultaneously, the $\nu(PS_4^-)$ and $NBS(P-S^-)$ peaks at 617 cm^{-1} and 683 cm^{-1} grow stronger in intensity in the phosphate rich glasses, x increasing above 0.5, indicating a greater number of non-bridging units that leads to a lower network connectivity and a weaker glass when compared to silicate-rich glasses. This indicates that changing the glass former can be used to tune the strength of the glass.

Due to the need to improve crystallization resistance and the desire to increase ionic conductivity of the GSE, work this quarter continued on the alumina-doped ISU-8(x) glass series. Multiple compositions were prepared with varying levels of modifier and dopant for DSC experiments to determine the thermal behavior and the effect of alumina on the viscosity and effective working range of the GSE. As can be seen in Figure 11, the glass transition temperatures (T_g) and crystallization temperatures (T_c) increase slightly with addition of alumina, while the largest changes occur due to the amount of modifier present in the glass (*y*). As the modifier amount increases, the T_g decreases and the T_c decreases more significantly. From the Mauro-Yue-Ellison-Gupta-Allan (MYEGA) model for viscosity, the team observes that the addition of alumina tends to stiffen the glass network, creating a glass that does not see significant improvement in drawability. Following work described in earlier reports, different DSC experiments were conducted with varying heating rates to determine the crystallization onset temperature at the heating rate utilized during thin-film preparation. This value is shown for a selection of the ISU-8(x) series as the end point of the viscosity curve in Figure 14.

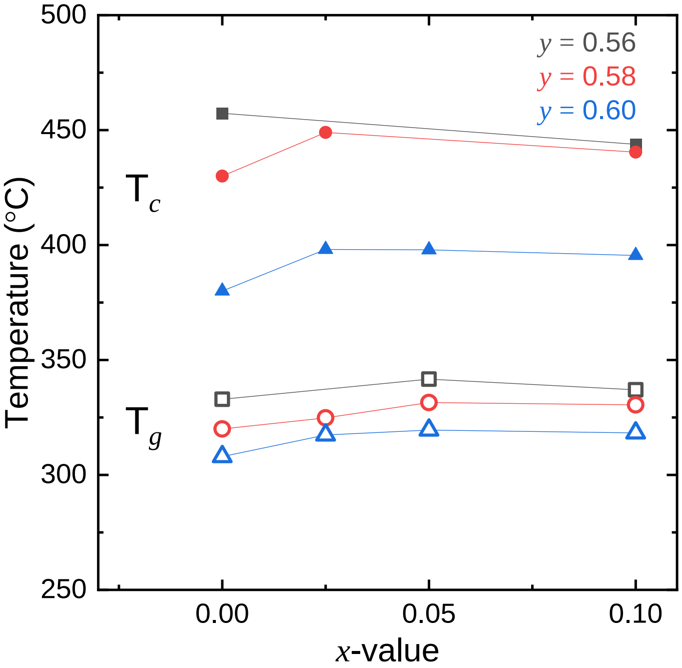

Figure 11. Glass transition temperatures (T_g) and crystallization temperatures (T_c) of the ISU-8(x) glass series as a function of x-value. The largest changes in T_c and T_g occur due to the modifier amount rather than the alumina incorporation.

Develop Optimized High Li^+ Ion Conductivity MOSN MGF GSEs

Initiate Development of Preforms of MOSN MGF GSEs that Do Not Crystallize

A new series was developed with the hopes of increasing the crystallization resistance of the mixed oxy-sulfide (MOS) GSEs. This series started with the ISU-6 composition, and a direct substitution of Li_2SiO_3 for $LiPO_3$ was made. As silicon forms stronger bonds with oxygen than phosphorous does, an increase in network strength, and therefore crystallization resistance, is expected. An additional benefit is the increased concentration of lithium ions in the glass without affecting the networking species, as both Li_2SiO_3 and $LiPO_3$ contain the same number of terminal oxygens and both form chain-like structures. As can be seen from Figure 12, the T_g increases linearly with substitution of Li_2SiO_3, while the T_c does not systematically change; however, the ISU-9, $z = 1.0$ composition does show a high T_c, leading to one of the highest working ranges seen in a lithium MOS GSE of 137°C. Following this promising result, the team conducted more DSC experiments to determine viscosity behavior using the MYEGA model and to determine the T_c at slow heating rates similar to the expected drawing conditions. The expected viscosity and crystallization behavior can be seen in the viscosity plot of Figure 14. It can also be seen that introduction of Li_2SiO_3 leads to a decrease in the fragility index of the glass due to the stronger networking of the added Li_2SiO_3 compared to that of the $LiPO_3$-doped GSEs, with the fragility index, m, decreasing from 49 to 41 from the ISU-6 composition to ISU-9, $z = 1.0$. The team is conducting further work to continue characterizing this series, including conductivity testing, electrochemical testing, and DSC studies.

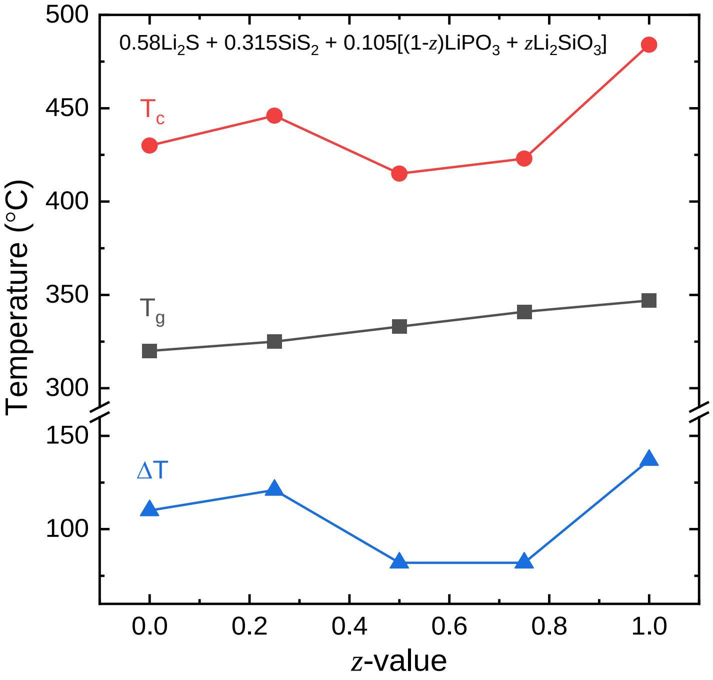

Figure 12. Glass transition temperatures (T_g) and crystallization temperatures along with computed working ranges for the Li_2SiO_3 substituted ISU-9 series showing high working ranges and linearly increasing T_g.

Develop Micro-Sheet Glass Ribbon Processing Facility for GSEs

Develop and Optimize GSE Micro-Sheet Glass Ribbon Processing Facility

Over the last quarter, progress has been made to optimize the micro-sheet glass ribbon processing facility. This includes careful profiling of the temperature gradient within the furnace, control methods for film forming, and exploration of various glass compositions to identify behavior trends. As shown last quarter, variations between set point and actual temperature in the draw tower furnace can cause GSE film to experience local heating above crystallization temperature. By adjusting furnace baffles and airflow, a much more consistent temperature profile is realized. These measurements have allowed for development of more accurate heating profiles this quarter, which improves GSE consistency. Use of these heating profiles has produced successful results as part of a companion project on sodium MOSN ion-conducting glasses.

In addition to optimizing of the draw tower conditions, extensive efforts have succeeded in relating glass viscosity to film-drawing conditions. This allows for the selection of glass compositions that meet predetermined criteria without preparation of large, expensive preforms. As will be detailed here, the MYEGA model for glass viscosity was used, along with crystallization studies that mimic the conditions found in the draw tower. Through continued development of analytical tools that can be applied to small batches of material, it is possible to optimize composition for film drawability.

While outside the scope of this project, use of analytical models for film drawing has been demonstrated in a separate effort by this group. Thin films of a Na-ion-conducting MOSN glass have been prepared across multiple compositions, and film lengths in excess of 1 meter have been successfully produced.

Develop Processing Conditions Micro-Sheet Ribbons of MOSN MGF GSEs

Complete Optimization of Draw Conditions for Optimized Oxide GSEs < 500 µm, and for Optimized MOS MGF GSEs < 200 µm and < 100 µm

The team continued work started last quarter on using the MYEGA model of glass viscosity to describe the necessary conditions for preparing micro-sheet ribbons of GSEs. This model uses several analytically determined parameters to describe the viscosity of a glass as a function of temperature. It was successfully applied to $LiPO_3$, which was used as a model system by the team throughout FY 2020. By modeling the glass viscosity under film drawing conditions, it was possible to identify target parameters for MOSN GSEs.

The MYEGA model was proposed by Mauro et al. using data on hundreds of glass compositions produced at Corning Inc.[1] The name is taken from the five authors of the 2009 paper and gives the following equation for the viscosity of a glass as a function of temperature:

$$\log_{10}\eta(T)=\log_{10}\eta_\infty+(12-\log_{10}\eta_\infty)\frac{T_g}{T}\exp[(\frac{m}{12-\log_{10}\eta_\infty}-1)(\frac{T_g}{T}-1)]$$

with η_∞ as infinite temperature viscosity, T_g as glass transition temperature, and m as calorimetric fragility. η_∞ is consistent for a family of glasses, and is usually approximated at -0.5 from literature; T_g and m can both be measured by a simple DSC experiment. Combining these values results in an estimate of $\log_{10}$(viscosity) (Pascal · seconds) versus Temperature (°C) for a given composition, as show in Figure 14. This gives an estimate for the minimum temperature necessary for successful film drawing.

Another crucial parameter for film drawing is the T_c of the GSE. Previously, the team has shown that ISU-6 can crystallize through homogenous nucleation processes during film preparation. These nucleation points serve as fracture points in the film and also lead to poor electrochemical stability of the GSE. The T_c is determined through DSC experiments and is strongly dependent on heating rate. It is especially important to consider the T_c at low heating rates, as thin film preparation uses heating rates of < 1°C/min. As shown in Figure 13a, the T_c varies with heating rate and is determined by fitting the onset of the exothermic crystallization event. The onset T_c, which is defined as the temperature at which the exothermic glass crystallization event begins, is used as this represents the range in which minimal crystallization has occurred. By extracting the T_c value at various heating rates, as shown in Figure 13b, an Arrhenius type plot is used to determine T_c values at low (< 1 C/min) heating rates used during film drawing.

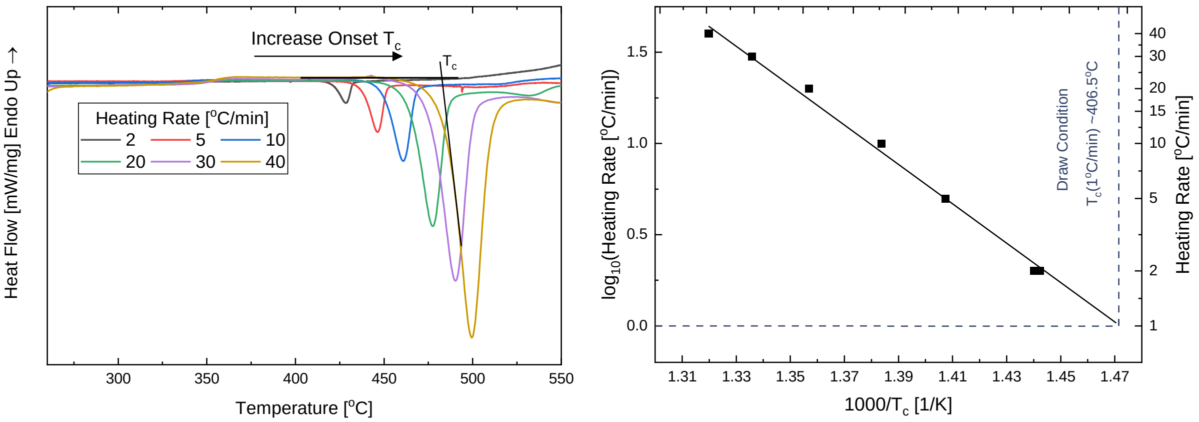

Figure 13. (a) Differential scanning calorimetry thermograms showing crystallization of the ISU-6 GSE at various heating rates. (b) Arrhenius plots can be used to extract crystallization temperatures at various heating rates.

As previously described, the MYEGA model of glass viscosity is used to determine the temperature required for glass softening to enable film drawing. By adding a crystallization temperature, T_c, as a cut-off in the MYEGA model, a description of the range of film-forming temperatures for a given glass composition can be determined. This process has been applied to various glass compositions to assess their viability for film-drawing. As shown in Figure 14, the glass viscosity is dependent on temperature, while an ideal film-forming range has been identified through past experiments. The previously determined T_c provides a maximum temperature that a given glass composition can experience. This allows for small batches of samples to be assessed for film-drawing prior to large-scale preform preparation.

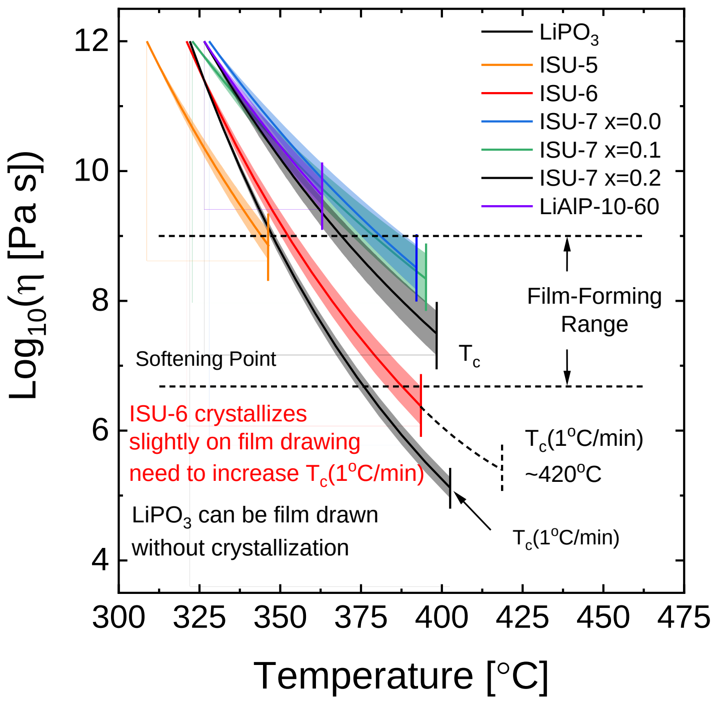

Figure 14. This graph shows the compositional viscosity curves as calculated from the MYEGA model with their respective crystallization cut-offs. This graphic comparison can be used to evaluate candidate glassy solid electrolytes with an ideal chemistry viscosity curve extending below the softening point, which ISU-6 does.

Based on Figure 14, the ISU-6 chemistry appears to still be the most favorable for film drawing. Unfortunately, while Li_2SiO_3 and Al_2O_3 additions increase crystallization temperatures, they also increase minimum draw temperatures, resulting in no overall gain. Further work is planned to potentially combine multiple dopants, with the goal of seeing gains on both crystallization and viscosity.

Fabricate and Test All-Solid-State Lithium Battery (ASSLB) GSEs in Large Area Planar Formats

Complete Testing of Optimized MOSN MGF GSE in Small-Cell-Format ASSLBs; Initiate Testing of Optimized MOSN MGF GSE in Intermediate-Cell-Format and in Large-Cell-Format ASSLBs

A series of procedures has been implemented to prepare and test ASSLBs to determine optimal designs and cycling conditions. This includes preparation and testing of hybrid cell designs, with a ‘wet’ cathode and a ‘dry’ anode using various electrode and electrolyte configurations. Simultaneously, progress has been made on composite all-solid-state cathode film preparations, which show low interfacial impedance and good reversibility. Multiple cell configurations have been explored to understand the role of electrode loading, anode choice, stack pressure, temperature, and other parameters.

Hybrid cell designs, in which SE is paired with minimal LE additives, have been shown to greatly improve full-cell performance by improving cathode-electrolyte interfaces (CEIs), accommodating electrode volume change, and bridging interparticle gaps. As reported in the second quarter, the team has demonstrated the addition of small amounts of $LiPF_6$ in a carbonate solvent blend to a conventional $LiFePO_4$ cathode to improve electrochemical capacity. However, the carbonate solvent used with the cathode eventually degraded the MOS GSE, leading to large increases in interfacial impedance and increasing polarization during cycling. Therefore, recent efforts have explored a less corrosive LE additive in the ionic liquid (IL) family. Equimolar complexes of triglyme solvent and LiTFSI salt were used to create a viscous solvate IL that does not corrode MOS glass and can be used in a hybrid cell with a dry anode and a wetted cathode. As shown in Figure 15, good cycling behavior is seen over multiple cycles.

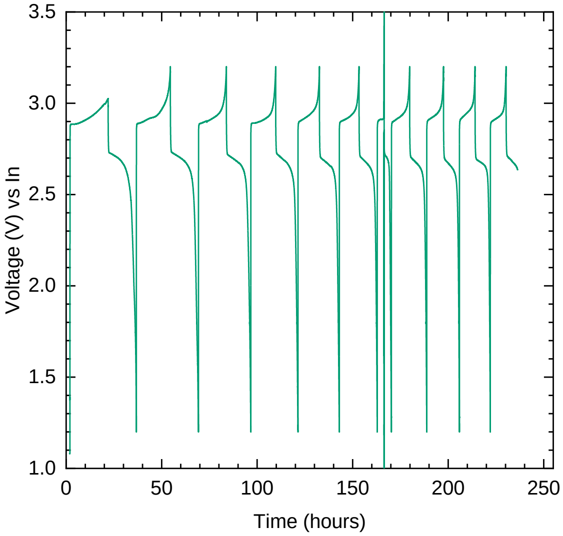

Figure 15. Hybrid cell cycling demonstrates good reversibility in cell using a mixed-oxy-sulfide glassy solid electrolyte with an $LiFePO_4$ cathode and indium anode. A pressure cell design was used to ensure good layer contact.

Figure 15 depicts cycling of a hybrid cell composed of a $LiFePO_4$ cathode film impregnated with a small volume of LiTFSI-triglyme (Li(G3)TFSI) IL complex. The addition of the Li(G3)TFSI electrolyte to the cathode aids in formation of a low-impedance CEI. Indium foil was used as a high-capacity alloying anode to test the viability of Li-free anode cells. A custom-built pressure cell was used to ensure adequate pressure was maintained throughout cycling. During the cycling process, smooth charge-discharge voltage curves are observed.

In addition to hybrid cells, composite cathodes were prepared by blending MOS glass, conductive carbon, cathode active material, and binders to create all-solid-state cell designs. This quarter, the team made progress on optimizing a deposition process for slurry coating composite cathodes directly onto MOS GSE film. This coating process improves interfacial contact and provides a highly scalable electrode preparation method. A composite cathode was prepared with $LiFePO_4$, ISU-6, super phosphorus carbon, and styrene butadiene binder. Xylene solvent was used to create a slurry dispersion, which was then coated directly onto MOS glass film. The slurry-coated electrode was then dried by heating and was seen to have good adhesion to the SE film. Cells were prepared by attaching a lithium or indium foil anode to the SE film and were sealed using coin-cell casings. Galvanostatic cycling was conducted at 60°C to improve conductivity of the electrolyte, leading to a relatively low polarization during the cycling process. As shown in Figure 16, preliminary cycling results indicate good capacity during the charge-discharge process and decent reversibility. Next quarter, the team will focus on improving performance of this design. Efforts will explore changes to the composite electrode formulation, large area depositions, and increased cycling.

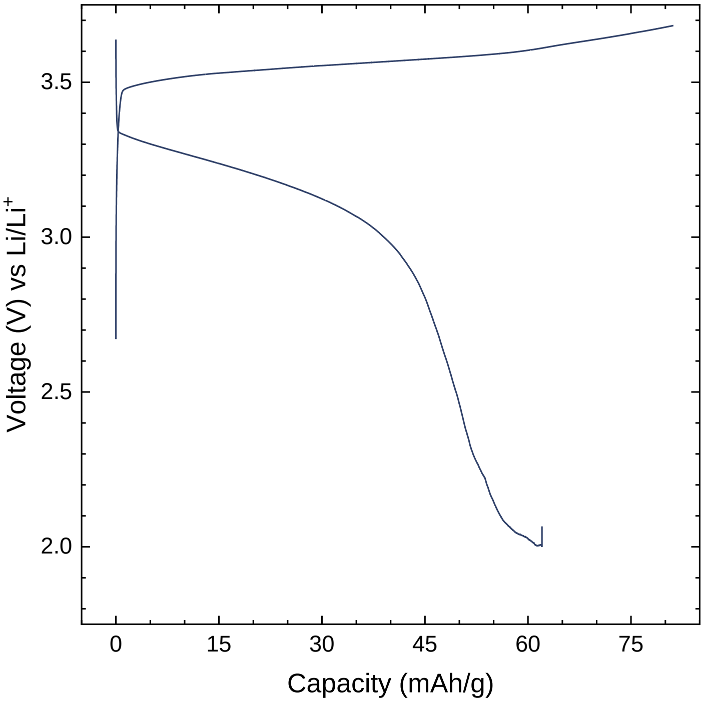

Figure 16. Galvanostatic cycling of $LiFePO_4$ solid-state electrodes deposited on ISU-6 glass film. Preliminary results show a relatively low polarization can be achieved, leading to smooth cycling. By depositing electrode material directly onto electrolyte film, all-solid-state full cells can be produced more easily.

Reference

[1] Mauro, J. C., Y. Yue, A. J. Ellison, P. K. Gupta, and D. C. Allan. "Viscosity of Glass-Forming Liquids." *Proceedings of the National Academy of Sciences of the United States of America* 106, No. 47 (2009): 19780–19784.

Patents/Publications/Presentations

Publication

- Wheaton, J., S. Kmiec, D. Schuler, C. Sorensen, and S. W. Martin. "Electrochemical Behavior of Drawn Thin-Film Vitreous Lithium Metaphosphate." *ACS Applied Energy Materials* 4, No. 10 (2021): 10835–10842.

Presentations

- All Iowa Glass Conference (2021): "Thin Film Processing of Ion Conducting Glasses by the Glass Redraw Method"; D. Schuler, C. Sorensen, J. Lovi, S. Kmiec, and S. W. Martin.
- All Iowa Glass Conference (2021): "Electrochemical Characterization of $y\text{Li}_2\text{S}+0.75(1-y)\text{SiS}_2-0.25(1-y)\text{LiP}_{1-x}\text{Al}_x\text{O}_{3-x}$"; J. Wheaton, S. Leland, S. Kmiec, and S. W. Martin.

Task 1.5 – Composite Solid Ion Conductor with Engineered Lithium Interface
(Dee Strand and Gang Cheng, Wildcat Discovery Technologies)

Project Objective. In this project, Wildcat Discovery Technologies seeks to perform focused, fundamental research and development on composite polymer/ceramic electrolytes and for the protection of Li-metal anodes to develop a Li-metal all-solid-state battery (ASSB) that achieves DOE requirements for performance. Wildcat will leverage its high-throughput (HT) battery platform to explore a broad composite electrolyte compositional space. Additionally, the HT platform will allow the team to screen hundreds of inorganic and organic coatings for Li-metal protection and translate the best results to all solid cells.

Project Impact. Successful widespread commercialization of EVs is contingent on developing safe high-energy-density batteries capable of long cycle life. Lithium metal affords the highest theoretical capacity (3,860 mAh/g) and lowest electrochemical potential (-3.04 V versus self-healing electrolyte), which offers the highest specific energy density of anode materials today. However, significant progress toward the passivation of lithium metal must occur before the energy density benefit can be realized. The intrinsic high reactivity between lithium metal with conventional Li-ion electrolytes (organic carbonate-based solvents) makes it extremely difficult to overcome these problems. The proposed composite polymer/ceramic electrolyte and a protected Li-metal anode will enable a Li-metal ASSB. Performance targets for a safe all-solid-state Li-metal pouch cell are over 350 Wh/kg and over 1,000 cycles (C/3) with the cost estimate below $100/kWh.

Approach. The project approach involves (1) identifying a suitable combination of solid ion conductor, polymer, and additive that minimizes overall interfacial impedance between the PE and solid ion conductor, and (2) identifying stable Li-metal protection agent or combination of agents that shows enhanced cycling performance (relative to a non-protected system) using the down-selected cell architectures.

Out-Year Goals. The out-year goals involve screening of cathode composites to minimize interfacial resistance, down selection of the best solid-state electrolyte (SSE), and down selection of the best passivation approach for lithium metal. Following these developments, the final tasks will be to integrate these three components into a full ASSB with improved cycle life.

Collaborations. All project tasks will be performed at Wildcat Discovery Technologies.

Milestones

1. Down select passivation approaches. (Q1, FY 2021; Completed)
2. Optimize SE. (Q2, FY 2021; Completed)
3. Integrate SE with cathode. (Q3, FY 2021; Completed)
4. Final testing. (Q4, FY 2021; Completed)

Progress Report

This quarter, the team started fabricating composite polymer/ceramic electrolyte with high weight loading (> 75%) of LLZTO powders, which is a so-called "polymer-in-ceramics" composite electrolyte. The LLZTO ceramic particles serve as the primary phase to provide the bulk ionic conductivity and mechanical strength. The small portion of PE provides flexibility of the resulting composite electrolyte. Because the intrinsic properties and surface modification of LLZTO play a crucial role in the final conductivity of the composite electrolyte, the Wildcat team revisited the LLZTO synthesis and developed an improved synthesis method to better control the particle size of LLZTO. In combination with previous PE studies, the ionic conductivity of composite electrolytes with high content of ceramics was improved.

Large-Scale Manufacture of Ultrafine (< 2 µm) LLZTO Powder

As the team's previous LLZTO synthesis produced a large particle size with low yield, they wanted to develop a more efficient synthetic procedure to obtain uniform small particle size with high yield. After systematic evaluation of the amount of lithium source material (Figure 17a) and sintering conditions, they developed a one-step annealing process to produce much smaller LLZTO particles with good batch-to-batch reproducibility. The X-ray diffraction (XRD) pattern in Figure 17b shows that all the identified peaks can be perfectly indexed to the standard pattern of cubic garnet structure, indicating high purity of the LLZTO powder. SEM images in Figure 17c reveal that most of the particles of the LLZTO powder are smaller than 2 µm, with most at the nanoscale. Compared to the previous LLZTO powder (~ 20 µm), the smaller particle size significantly increases the active surface area that is needed to create interactions between polymer and ceramic powders. With the simplified annealing and mixing procedure, the new process can provide over 1 kg of LLZTO powder per day based on current setup and can be easily scaled in the future.

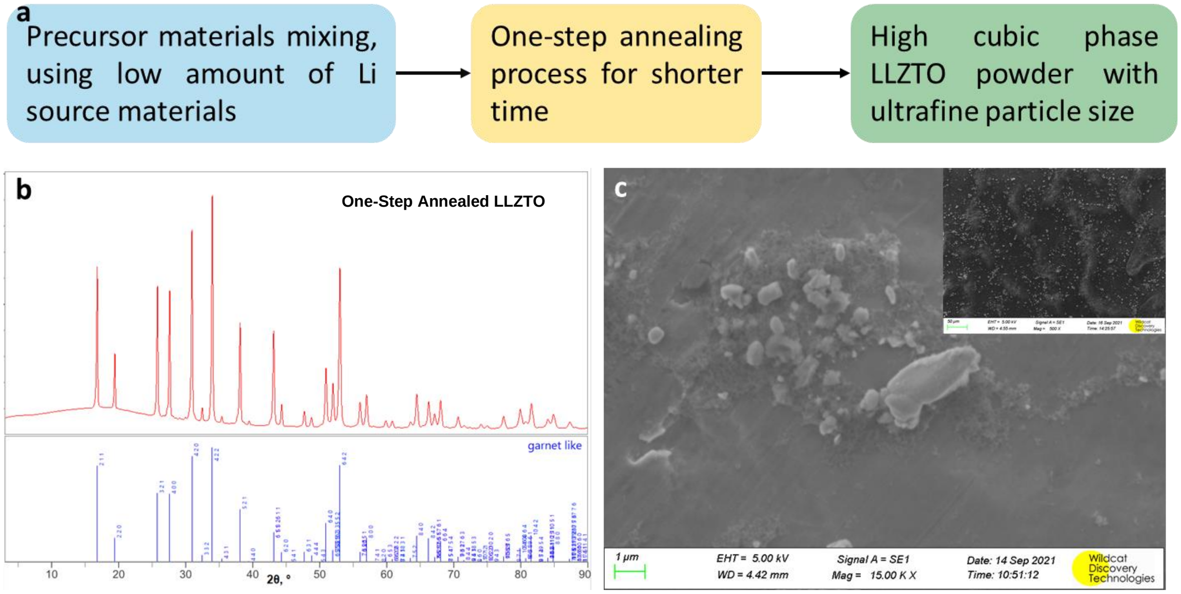

Figure 17. Synthesis of ultrafine LLZTO powder. (a) Flow chart of LLZTO synthesis process. (b) X-ray diffraction pattern of one-step sintered LLZTO, consistent with standard cubic garnet structure. (c) Scanning electron microscopy image LLZTO powder, revealing the particle size lower than 2 µm.

High Lithium Salts Concentration of PE Film

The PE is another critical component in the composite SE. Even though the main ionic conductivity is contributed by the solid ion conductor, the ionic conductivity of PE still affects the overall conductivity. More importantly, the composition of PE determines interface interactions with the ceramic phase. Last quarter, the team started systematically investigating polymer type, lithium salt type, and their ratio for effect on ionic conductivity, as well as processability. Based on that, they focused on PVDF-type polymer with LiTFSI salt and used it to fabricate high ceramic-loading solid composite electrolytes.

After studying various mixing methods as well as composition of mixing solvents, they found that PE films can be easily made by mixing specific PVDF powders and LiTFSI powder in specific solvents. The resulting slurry can be directly casted on glass plates to yield the white-colored semi-transparent film after the solvent is evaporated (Figure 18a). To optimize the formulation, Wildcat studied different concentrations of LiTFSI in the polymer. As shown in Figure 18b, the optimal LiTFSI/polymer ratio in this case is 3, which offers ionic conductivity around 2 × 10^{-4} S/cm. As they further increase the ratio of LiTFSI/polymer, gel formation occurs. Higher ratios can possibly be achieved without gel formation if different types of mixing solvents are used. To exclude the possible effect of solvent contribution to the Li^+ conductivity, the PE was further dried in an aggressive drying process (72 hours at 70°C under vacuum); however, conductivity remains at 10^{-4} S/cm. The slightly decreasing conductivity is likely due to the polymer structure damage caused by aggressive drying conditions.

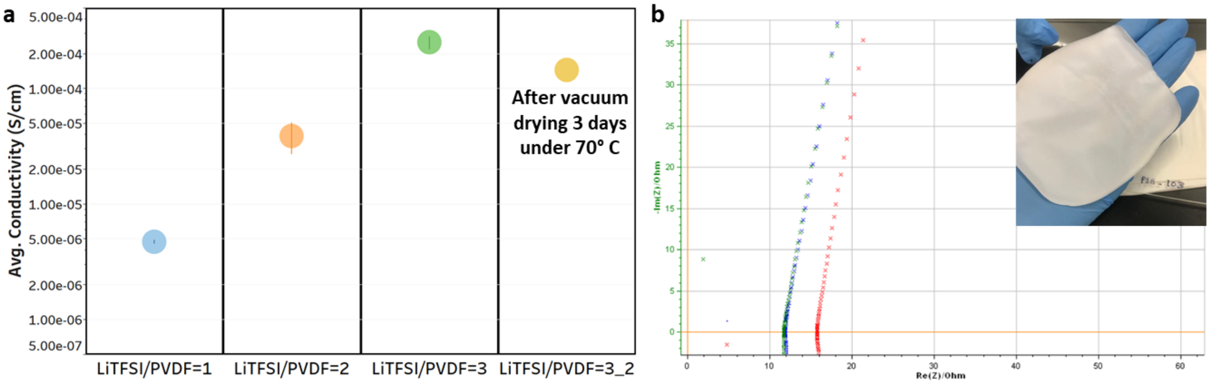

Figure 18. High lithium salts concentration for polymer electrolyte (PE). (a) Impedance spectra and digital image of prepared free-standing PE with optimized condition. (b) Conductivity comparison between polymers with different formulas and drying times.

Flexible, Ultrathin, and Highly Conductive Composite Electrolyte Film

The motivation for designing "polymer in ceramics" composite electrolytes is to increase the mechanical strength to suppress lithium dendrite growth. However, as the amount of LLZTO ceramics in the composite electrolyte increases (> 75wt%), the composite electrolyte often turns into powder. To overcome this challenge, Wildcat developed a dry-mixing method to produce a thin film by introducing a small amount of film-forming additive (Figure 19a). The low concentration of film-forming additive does not seem to negatively affect ionic conductivity, but does significantly improve the flexibility of the solid composite electrolyte membrane. Following this strategy, Wildcat successfully fabricated a stand-alone solid composite electrolyte membrane with a thickness of 50 µm (Figure 19b). As the Li^+ diffusion pathway in the composite electrolyte was achieved due to surface reaction between PE and LLZTO particles, high ionic conductivity can be realized. The composition of the LLZO – LiTFSI – PVDF was then investigated to approach optimal room-temperature conductivity. It turns out that when LiTFSI/PVDF mass ratio increases from 0.5 to 3, the highest ionic conductivity of 8 × 10^{-4} mS/cm was obtained (Figure 19c) at room temperature.

Furthermore, the team studied its temperature dependence by measuring ionic conductivity at various temperatures. A major factor influencing ionic conductivity at different temperatures is the activation energy for faster ion mobility because it corresponds to the energy barrier for ionic conduction. The activation energies E_a for the conduction were evaluated using the equation:

$$\sigma_T = \sigma_0 \exp\left(-\frac{E_a}{k_\beta T}\right)$$

where σ_T is the total conductivity, σ_0 is the pre-exponential parameter, T is absolute temperature, E_a is the activation energy, and k_β is the Boltzmann constant. The E_a for conduction (Figure 19e), is then calculated from the slope of an Arrhenius plot. It turns out that E_a of the composite electrolyte is only 0.11 eV, which is much lower than most SSEs (0.2 ev ~ 0.3 ev), which means that the ionic conductivity of the composite electrolyte is much less temperature dependent. Shown in Figure 19d, the ionic conductivity of the solid composite electrolyte could still reach up to 4 × 10^{-4} mS/cm even at 0°C.

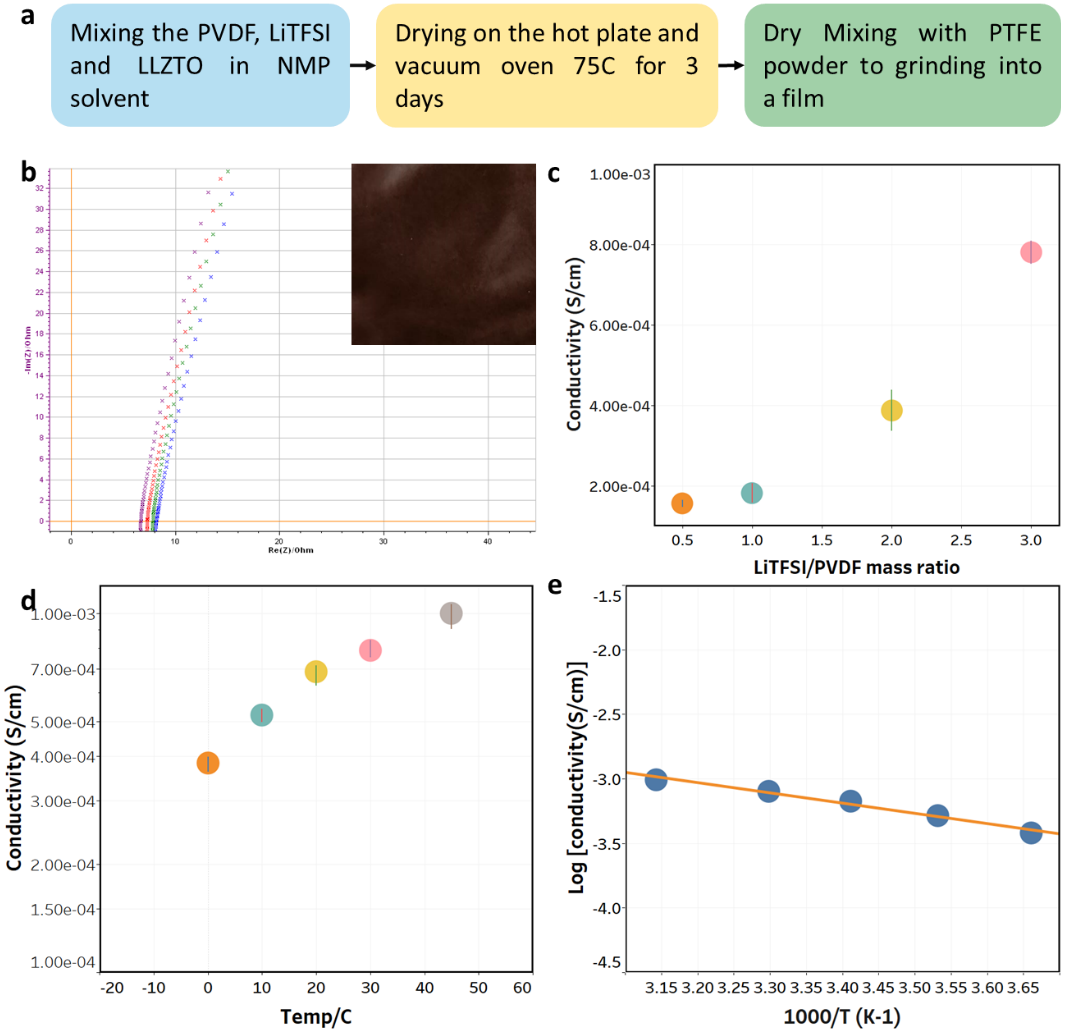

Figure 19. Composite electrolyte conductivity. (a) Flow chart of composite electrolyte film preparation. (b) Impedance spectra and digital photo of prepared composite electrolyte film with optimized formulation. (c) Effect of LiTFSI/PVDF mass ratio on room-temperature conductivity. (d) Composite electrolyte conductivity under different temperatures. (e) Arrhenius plot of composites electrolyte, revealing the low activation energy of ~ 0.11 eV.

Solid-State Full-Cell Development

Over the last few quarters, Wildcat independently evaluated several PVDF polymer types in the composite SSE and catholyte compositions using its HT platform and shortlisted candidates based on their conductivities and full-cell performance, respectively. This systematic evaluation led to the selection of a PVDF polymer type and a catholyte/cathode configuration optimized toward assembly in an all-solid-state cell format with Li-metal anode and the Li-metal protection layer developed in Thrust 2. This quarter, Wildcat focused its effort on further optimizing full-cell cycling performing using the SSE composite (SSE B) down-selected last quarter with 45 wt% of LLZTO with 1×10^{-5} s/cm ionic conductivity. Two versions of the SSE composite SSE B were made and labeled ‘SSE B – Gen 1’ and ‘SSE B – Gen 2’ to indicate that they differ only in the synthesis approach. To be more specific, SSE B – Gen 1 was using LLZTO made by the old synthesis method, and SSE B – Gen 2 was using the LLZTO with reduced particle size made by the newly developed method. All-solid-state full cells were built with these two composite SSEs, the optimized catholyte, and the protected lithium metal from Thrust 2. These full cells were cycled in the voltage range 3.0 V to 4.3 V at a temperature of 60°C. Figure 20a-b shows the cycle life plots of the all-solid-state full cells. After a series of rate capability test steps carried out at 0.1C and 0.2C, the cycle life test step was started at 7th cycle at the rate of 0.1C. At the end of 50 cycles, the discharge capacities were 148 mAh/g and 163 mAh/g, corresponding to capacity retention values of 83.7 % and 90.6 %. The optimized SSE candidate, SSE B – Gen 2 shows an improvement in the capacity retention by 7% over SSE B – Gen 1. Figure 20c shows the voltage traces of the full cells built with the two different SSE composites at 1st and 50th cycles. The voltage traces at all cycles showed smooth and full-charge profiles up to 4.3 V, demonstrating the good high-voltage stability and good cyclability of the all-solid-state full cells.

In summary, over the course of the project, Wildcat has developed and optimized each component of an all-solid-state cell, namely, the SSE composite, catholyte/cathode, and Li-metal anode coupled with a custom-built protection layer. On optimization, Wildcat successfully assembled these components and demonstrated an all-solid-state full cell that exhibited a capacity retention of 91% at the end of 50 cycles. As Wildcat continues improving ionic conductivity of solid composite electrolyte as well as its film quality, it is reasonable to expect that better cycle life can be achieved not only at elevated temperature but also at lower temperatures.

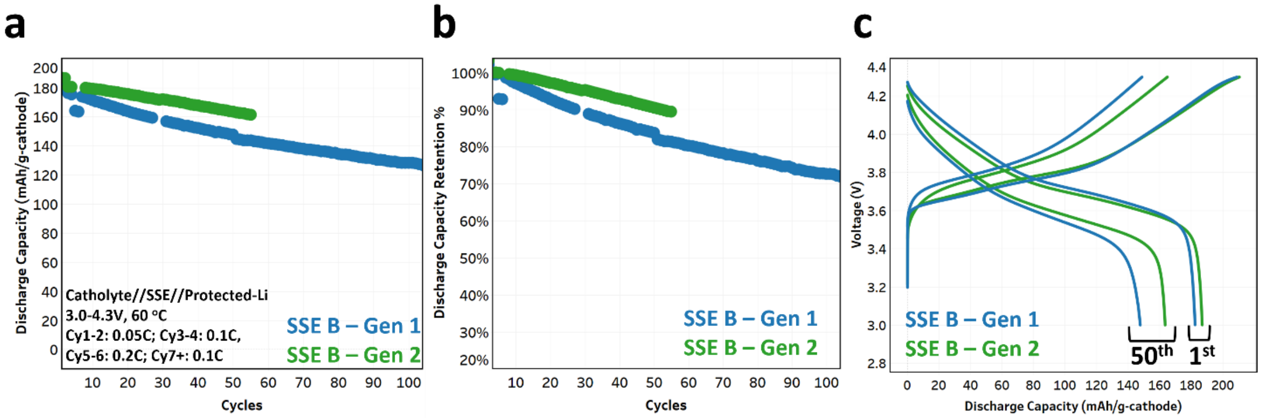

Figure 20. Performance of all-solid-state full cells. (a) Cycle life plot of all-solid-state Li//NMC full cells with two different SSE types; cycling conditions are provided in the inset. (b) Capacity retention plot. (c) Voltage traces of Cycles 1 and 50 of all-solid-state Li//NMC full cells with two different SSE types.

Patents/Publications/Presentations

Presentation

- VTO Annual Merit Review Meeting, Washington, D. C. (June 24, 2021): Bat479 "Composite Solid Ion Conductor with Engineered Lithium Interface Meeting"; G. Cheng.

Task 1.6 – Physical and Mechano-Electrochemical Phenomena of Thin-Film Lithium-Ceramic Electrolyte Constructs
(Jeff Sakamoto, University of Michigan)

Project Objective. While a small number of SEs exhibit high ionic conductivity (~ 1 mS cm at 298 K), few are stable against lithium metal. The garnet-type SE, based on the nominal formula LLZO, is unique in that it is a fast ion conductor and—as demonstrated in the team's recent project (DE-EE-00006821)—is stable against lithium. Moreover, the team's former project successfully demonstrated a decrease in Li-LLZO interface resistance from 12,000 Ω cm^2 to 2 Ω cm^2 and stable cycling at 1 mA cm^2 for 100 cycles (± 15 µm of lithium per cycle). Although the past project demonstrated that LLZO is a viable SE for enabling batteries using metallic lithium, the studies used thick pellets (1 mm) and thick anodes (~ 500 µm). The goal of this project is to acquire a deep fundamental understanding of the physical and mechano-electrochemical phenomena that control the performance of cells consisting of thin LLZO (~ 10 µm), thin lithium anodes (~ 20 µm), and thin solid-state composite cathodes.

Project Impact. If successful, the project will gain knowledge to guide closely related commercialization efforts to scale the production of LLZO-based solid-state batteries (SSBs).

Approach. The team believes that to achieve a step increase in technology readiness level (TRL), the same performance characteristics previously shown should be demonstrated in technologically relevant cells, for example, thin LLZO and thin lithium.

Out-Year Goals. Out-year goals involve the following: custom thin-film composite (TFC) development, preliminary cycling studies, Vis cell development, lithium cycling, and polymer gel electrolyte (PGE) screening.

Collaborations. This project collaborates with N. Dasgupta and D. Siegel of University of Michigan (UM), Mechanical Engineering.

Milestones

1. Initial design, fabrication, testing, and optimization of custom *operando* optical visualization cell. (Q1, FY 2021; Completed)
2. Initial integration of precision micro reference electrodes with thin lithium and TFC for 100 cycle tests. (Q2, FY 2021; Completed)
3. In thin lithium and thin LLZO TFC, determine max cycling rates versus lithium thickness ranging between 2 µm and 17 µm. (Q2, FY 2021; Completed)
4. Refinement of custom *operando* optical visualization cell to quantify topographic lithium plating homogeneity versus cycle number. (Q4, FY 2021; Completed)

Progress Report

Interfaces play a crucial role in the stability and life of a battery. In a Li-LLZO-S battery, the Li-metal – LLZO interface has shown a significantly low resistance of < 2 Ωcm^2, whereas the LLZO-cathode interface remains unoptimized and resistive. A small quantity of LE can improve the kinetics between the LLZO and sulfur cathode. However, interactions between the LLZO and LEs have not been extensively studied. This quarter, a platform was established (Figure 21a) to investigate LLZO-LE interactions. The interface between LLZO and DME was investigated using this platform (Figure 21b).

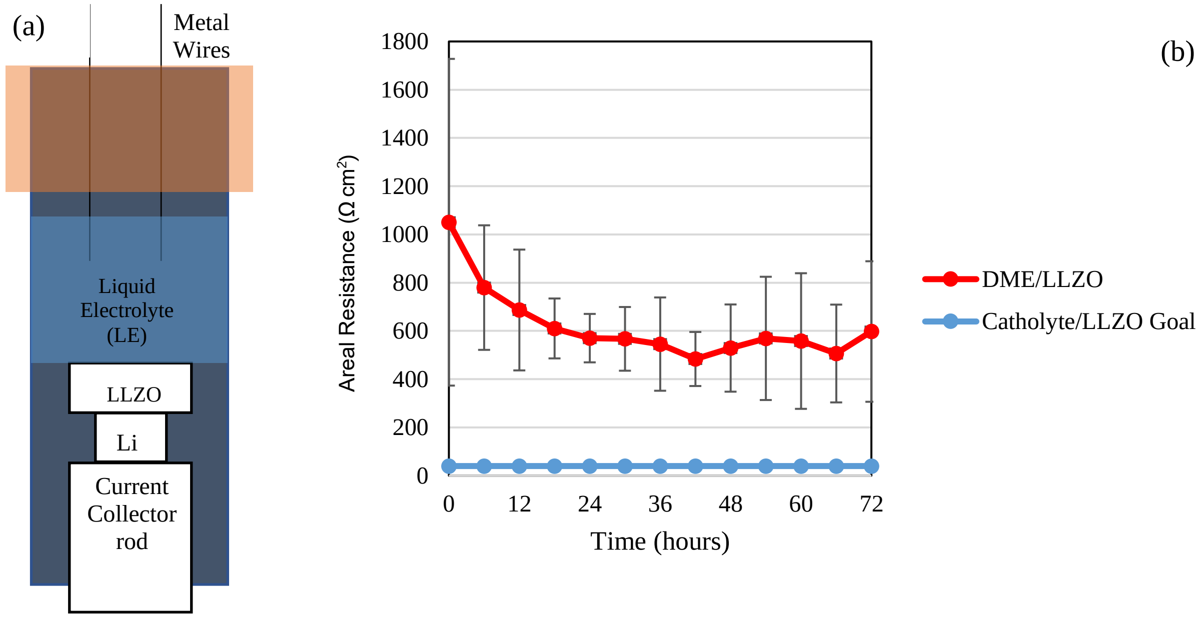

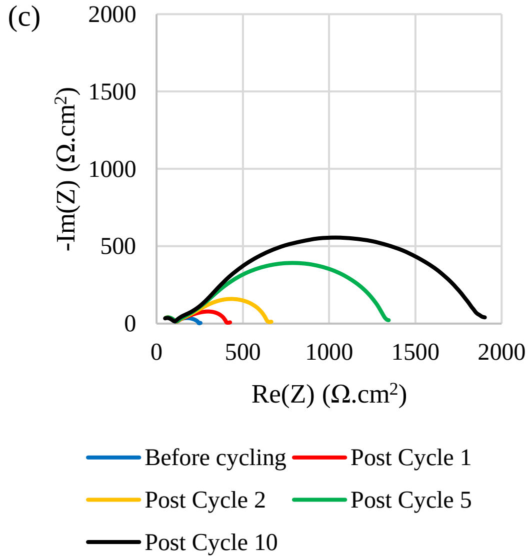

Figure 21. (a) Modified Swagelok cell that was designed to study the interface between LLZO and various liquid electrolytes. (b) Interfacial impedance between LLZO and 1 M LiTFSI in DME over 72 hours using the modified Swagelok. (c) The impedance of a Li-S hybrid full cell with 1 M LiTFSI in DME as the catholyte. Electrochemical impedance spectroscopy was performed after each cycle.

A Novel Platform to Study the Interfaces in a Hybrid Battery. A modified Swagelok cell in a three-electrode system was developed to resolve the LLZO-LE interface without the presence of the sulfur cathode (Figure 21a). The modified cell is leak-free and evaporation-free, and it allows simultaneous tracking of the anode-LLZO and catholyte-LLZO interface over time. Utilizing this cell, a 1 M LiTFSI in DME electrolyte against LLZO shows an interfacial impedance stabilizing ~ 600 Ωcm^2 after 3 days (Figure 21b). In a Li-S full cell, the DME electrolyte can show a lower initial impedance with LLZO; however, during cycling, the DME-LLZO interface increases on each cycle (Figure 21c). After 10 cycles, the interfacial impedance is ~ 2000 Ωcm^2. These results have implications for the design of LEs for Li-S hybrid batteries.

Patents/Publications/Presentations

Publication

- Liu, X., R. Garcia-Mendez, A. R. Lupini, Y. Cheng, Z. D. Hood, F. Han, A. Sharafi, J. C. Idrobo, N. J. Dudney, C. Wang, and C. Ma. “Local Electronic Structure Variation Resulting in Li ‘Filament’ Formation within Solid Electrolytes.” *Nature Materials* (2021): 1–6.

Presentation

- Testimony to The House Committee on Transportation regarding Vehicle Electrification in the State of Michigan; J. Sakamoto.

Task 1.7 – Lithium Dendrite-Free Li_7N_2I-LiOH Solid Electrolytes for High-Energy Lithium Batteries (Chunsheng Wang, University of Maryland)

Project Objective. The objective of this project is to research, develop, and test Li-metal-based batteries that implement solid Li-ion conductors (LICs) equipped with Li_7N_2I-LiOH SE capable of achieving cell performance of 350 Wh/Kg energy density for 1000 cycle life with a cost of ≤ \$100/kWh.

Project Impact. Lithium dendrite growth during charge/discharge cycles limits the use of ASSBs. A criterion for lithium dendrite suppression that is developed through systematical investigation on thermodynamics and kinetics of lithium dendrite growth will guide the electrolyte design. Li_7N_2I-LiOH and Li_3YCl_6 SE with high ionic conductivity and low electronic conductivity will be used to validate the criterion for lithium dendrite suppression, to achieve the project objective.

Approach. The team will establish the relationship among interface energy, lithium plating/stripping overpotential, interface resistance, SE stability with lithium, and critical current density (CCD). The dendrite suppression criterion will be developed based on the relationship. The dendrite suppression capability for the Li_7N_2I-LiOH pellet will be evaluated by testing the CCD.

Out-Year Goals. The project will study the thermodynamics and kinetics of lithium dendrite growth in SSEs and develop a lithium dendrite suppression criterion in SSEs. The Li_7N_2I-LiOH electrolytes and Li_7N_2I-LiOH/Li_3YCl_6 bi-layer electrolytes will be used to validate the developed dendrite suppression criterion and support Ni-Co-Mn (NCM) cathodes.

Collaborations. There are no reported collaborations this quarter.

Milestones

1. Determine critical overpotential (COP) of Li_7N_2I-LiOH, Li_3PS_4 (LPS), and LLZO electrolytes. (Q1, FY 2021; Completed)
2. Develop lithium dendrite suppression criterion for SSEs. (Q2, FY 2021; Completed)
3. Develop a kinetics model of SSEs. (Q3, FY 2021; Completed)
4. Achieve critical current of Li_7N_2I-LiOH electrolytes at > 4 mA/cm^2 at 3 mA/cm^2 of current. (Q4, FY 2021; Completed)

Progress Report

Critical Current Achieves Requirements by Using Mixed-Conductive Li_7N_2I – Carbon Nanotube (CNT) Interlayer with High Surface Energy against Lithium

The highlights for this quarter are as follows:

- The team demonstrated high lithium dendrite suppression capability of mixed-conductive Li_7N_2I-CNT interlayer with a high surface energy against lithium.
- The Li_7N_2I-CNT interlayer enables CCD of > 4.0 mA cm^{-2} and long cycling stability of > 600 hours under cycling condition of 4 mA cm^{-2} / 4 mAh cm^{-2}.
- The team explored activation behavior of lithiophobic Li_7N_2I-CNT interlayer.

Next-generation, high-energy batteries must utilize high-capacity anodes and high-voltage / high-capacity cathodes to maximize energy density. Among all, development of SSLBs using nonflammable inorganic or organic SSEs has been reckoned as a promising direction due to enhanced safety and high energy density. In this project, the team proposes a new type of SSE (Li_7N_2I) with excellent stability to lithium metal to enable high-performance solid-state Li-metal batteries (SSLMBs).

The utilized Li_7N_2I electrolyte was prepared by sintering a mixture of Li_3N and LiI at 550°C. Multi-walled carbon nanotube (MWCNT) was purchased from Sigma Aldrich and fully dried before use. Fine Li_7N_2I powder was carefully mixed with 5 wt% MWCNT by hand to use as the interface between Li_7N_2I electrolyte and lithium anode. The Li|Li_7N_2I-CNT|Li_7N_2I| Li_7N_2I-CNT|Li symmetric cell was first pre-cycled at low current density of 0.1 mA cm^{-2} to fully activate the interface. As can be seen in Figure 22a, the cell voltage of lithium symmetric cell gradually decreases from 0.3 V to ~ 0.07 V and then stabilizes. The stable cycling of the Li|Li_7N_2I-CNT|Li_7N_2I|Li_7N_2I-CNT|Li symmetric cell is due to introduction of ionic/electronic conducting and lithiophobic Li_7N_2I-CNT interlayer. The team further studied the CCD of the Li_7N_2I with the designed interlayer in lithium symmetric cells (Figure 22b). As can be seen, cell voltage increases with the current density. Finally, a record-breaking high CCD of > 4.0 mA/cm^2 at a capacity of 4.0 mAh cm^{-2} was obtained. On the other hand, the total resistance of the lithium symmetric cell measured using EIS decreases from 2500 Ω cm^2 (Figure 22c) to 800 Ω cm^2 (Figure 22d) during the pre-cycling at 0.1 mA cm^{-2}. This process can effectively activate the interface and is essential to fully unleash the lithium dendrite suppression capability of the interlayer. The high lithium dendrite suppression capability of the electrolytes with the designed electronic/ionic mixed-conducting interlayer was demonstrated by high CCD, as shown in Figure 22b. Although total resistance of the lithium symmetric cell is significantly reduced after cycling (Figure 22e), the EIS profile shows obvious diffusion region at a low frequency of 0.1Hz, which indicates the cell has not been shorted by lithium dendrite formation.

Figure 23 shows the cycling performance of the lithium symmetric cell with Li_7N_2I-5% MWCNT protected Li_7N_2I electrolyte at a current density of 4.0 mA cm^{-2} and a capacity of 4 mAh cm^{-2}. In general, cell voltage slightly decreases at the first 25 cycles and becomes stable due to penetration of lithium metal into the porous structure of lithiophobic MWCNT-Li_7N_2I interlayer. Since the Li_7N_2I electrolyte is thermodynamically stable and has high interface energy against lithium, lithium penetration into the electrolyte is self-limited. Figure 23b-c further shows the enlarged view of the time-voltage profile during cycling. There is no sudden voltage drop observed during the long cycling of > 600 hours. Therefore, the goal for a high CCD of 3 mA/cm^2 with capacity of 3 mAh/cm^2 for > 600 hours in this quarter's milestone has been reached.

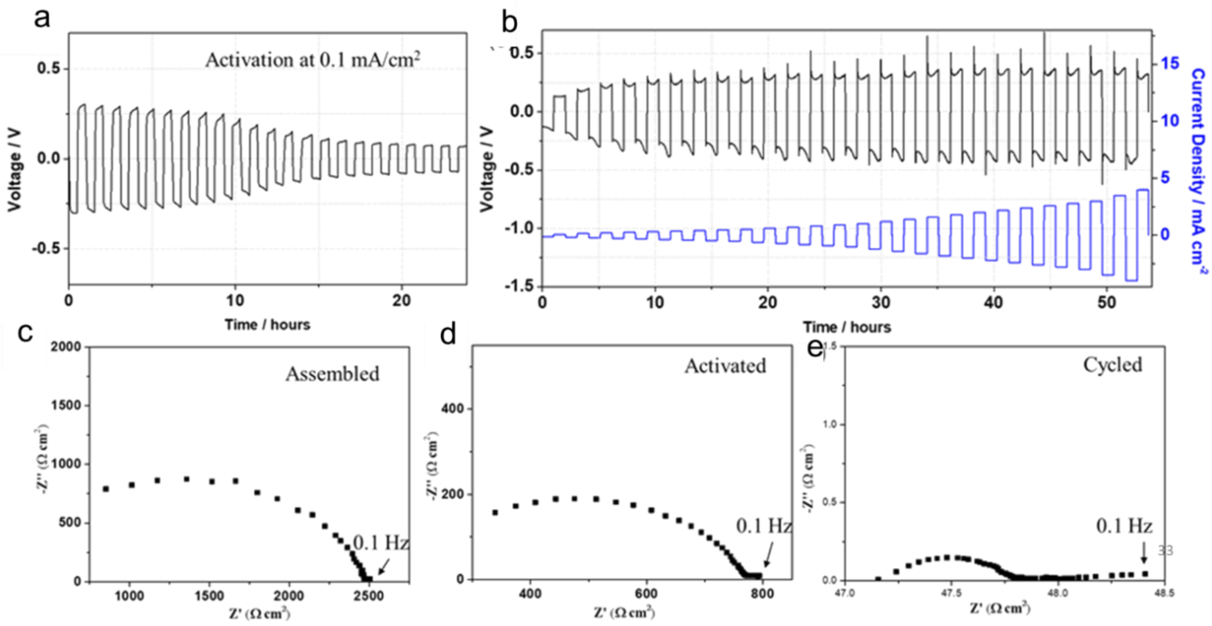

Figure 22. The lithium plating/stripping behavior of the Li_7N_2I-5% MWCNT protected Li_7N_2I electrolyte in lithium symmetric cell configuration at room temperature. (a) Galvanostatic cycling of the lithium symmetric cell at a current density of 0.1 mA cm^{-2}. (b) Voltage profiles of the cell under step-increased current densities from 0.2 to 4.0 mA cm^{-2} for lithium plating/stripping with fixed time of 1 hour. (c-e) Nyquist plots of the symmetric cell under different conditions: (c) before cycle (d) after activation, and (e) after cycling at 4 mAh cm^{-2} for 600 cycles.

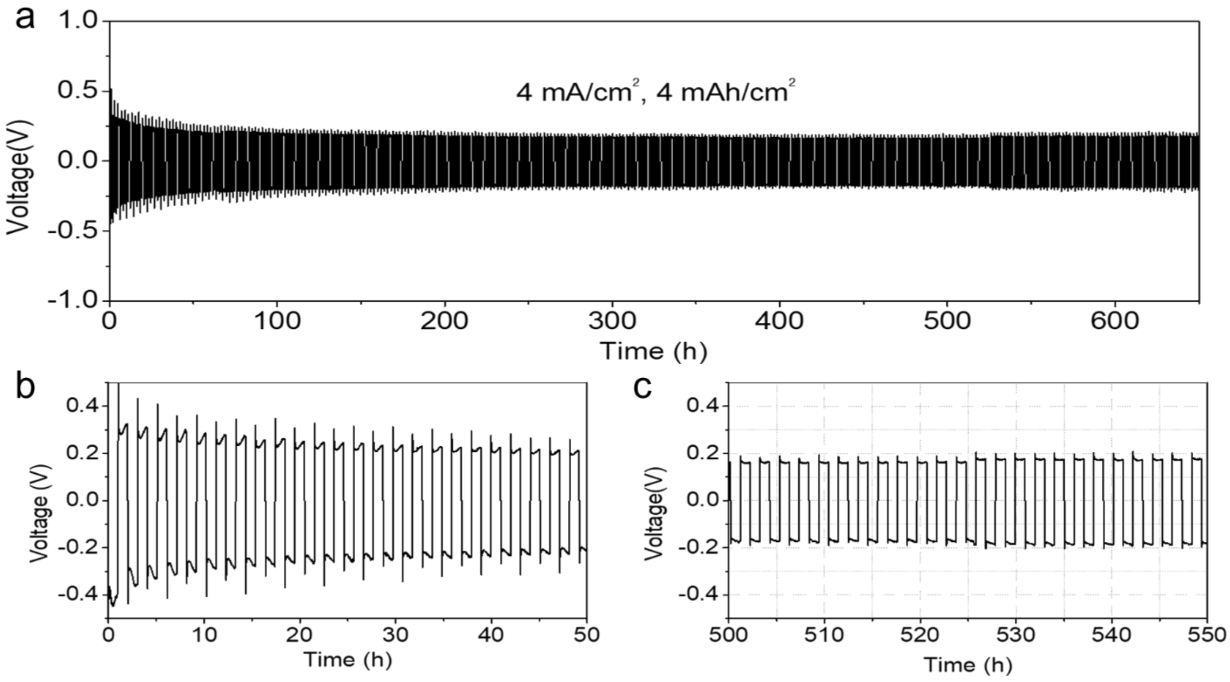

Figure 23. Electrochemical performance of the Li||Li symmetric cell using Li_7N_2I-5% MWCNT protected Li_7N_2I electrolytes. (a) Galvanostatic cycles of $Li|Li_7N_2I|Li$ cells with Li_7N_2I-5% MWCNT interlayers at current density of 4 mA cm^{-2} with constant plating/stripping time of 1 hour. (b-c) Enlarged view of voltage profiles in panel (a) during (b) 0-50 hours and (c) 500-550 hours.

The mixed ionic/electronic property of Li_7N_2I-MWCNT interlayer was optimized by changing the composition of Li_7N_2I-x% MWCNT. The electronic/ionic conductivity of Li_7N_2I-x% MWCNT was measured using Gamry Echem Analyst™ software. The ionic and electronic conductivities of pure Li_7N_2I powders were determined to be 0.1 mS/cm and 7×10^{-6} mS/cm, respectively. With the increase of MWCNT into SSE powder, the electronic conductivity of mixture gradually increased. In this work, the Li_7N_2I-5% MWCNT sample is an electronic/ionic mixed conductor, as shown in Figure 24a. Further increase of MWCNT can lead to electron-conductive dominance, which is not good for uniform lithium plating and stripping.

In addition, the activation process of the high-surface-energy interlayer with mixed ionic/electronic conductivity was investigated. When cycled at a low current density of 0.1 mA/cm^2, the cell voltage of Li|Li_7N_2I|Li symmetric cell coated with Li_7N_2I-5% MWCNT interlayer was gradually decreased from 0.3 V to 0.07 V. In contrast, the cell voltage of the Li|Li_7N_2I|Li symmetric cell with Li_7N_2I-0.5% MWCNT and Li_7N_2I-50% MWCNT remained constant. The different cycling behavior is highly related to electron and ion conduction of interlayer. When the interlayer is Li-ion conduction-dominant, the lithium can grow from lithium anode without nucleation, as demonstrated by a flat plating/stripping profile. When the interlayer becomes a pure electronic conductor, lithium could easily deposit between the interface and electrolyte. Therefore, the pure electron-conducting interface cannot protect SE from reduction and lithium dendrite growth. Only when the interface is a mixed conductor with balanced ionic and electronic conduction and highly lithiophobic property can lithium grow from lithium anode and reversibly penetrate into porous lithiophobic interlayer without contacting SE. The lithium penetration into lithiophobic porous interlayer can increase the contact area, thus reducing overpotential. Lithium does not contact SEs, which can suppress SE reduction and lithium dendrite growth. This lithiophobic interlayer can also avoid local stress concentration and lead to mechanistic failing of SE.

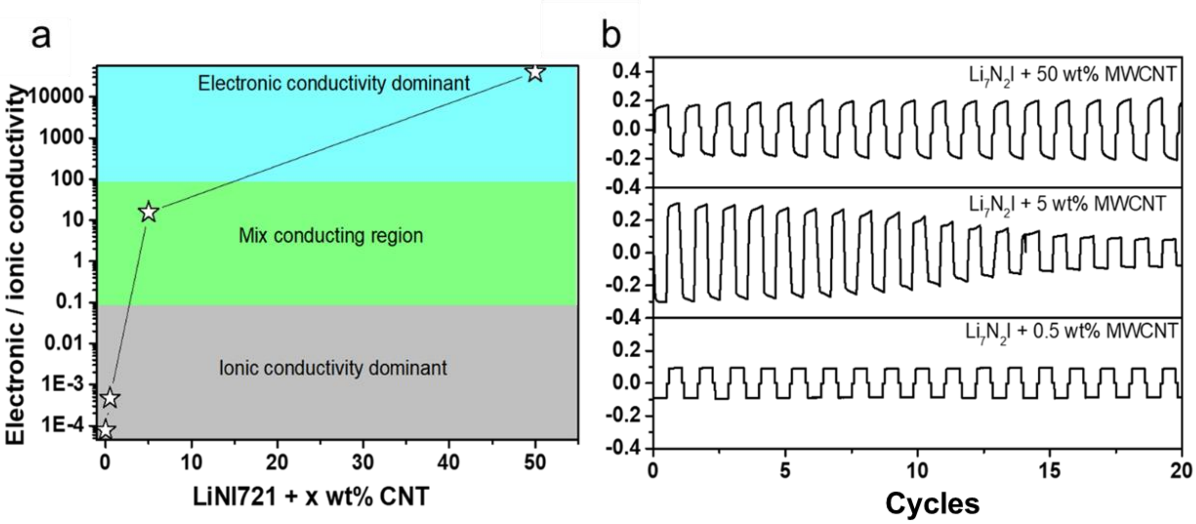

Figure 24. (a) Electronic/ionic conductivity regions of mixed-interface as a function of the composition for Li_7N_2I-x% multi-walled carbon nanotube (MWCNT) sample. (b) The lithium plating/stripping behavior of the Li_7N_2I-x% MWCNT protected Li_7N_2I electrolyte in lithium symmetric cell (x = 0.5, 5, 50) at a current density of 0.1 mA cm^{-2}.

Kinetics Model of Lithium Stripping in SE Batteries

The highlights for this quarter are as follows:

- The team analyzed kinetics for Li-metal diffusion near Li/SSE interface by phase-field model.

Lithium metal is the ultimate anode for SSBs to achieve comparable or higher energy density than Li-ion batteries. Even after decades of effort regarding fast-ionic SSEs with high mechanical strength, integration of lithium anode into SSBs is still constrained by unstable interphase formation, as well as lithium dendrite propagation due to electro-chemo-mechanical challenges of the current SSE system. Once the thickness of SSEs is reduced to 100 μm or less, dendrite penetration can even be prominent. Based on thermodynamic and kinetic analysis of the interface of Li/SSE, a lithiophobic SEI should be formed between the SSEs and lithium anode.

Recent findings demonstrate that the kinetics of lithium diffusion in Li-metal anode play a critical role in lithium dendrite growth for ASSBs. Figure 25 shows the Li-metal stripping process at an applied current density. At a stripping current of 0.1 mA cm^{-2}, a solid-solution lithium diffusion process takes place with the decreases in density of lithium metal at Li/SSE interface. After 119640 seconds, some voids can be observed. At the time of 126340 seconds, an apparent void formed on the Li/SSE interface; after 153810 seconds, the lithium anode completely detatched from the SSE. The morphological evolution of the lithium metal results in rapid increase of polarization during the stripping process. At a large current density of 1.0 mA cm^{-2} and 2.0 mA cm^{-2}, the detachment of the lithium metal and SSE is much earlier than that at 0.1 mA cm^{-2}. These results indicate that the kinetics for Li-metal diffusion are important for achieving a high COP and CCD.

Therefore, new interfacial engineering methods should be applied to stabilize the lithium anode with thin SSE film and high-loading cathode composites, aiming to maximize the energy density of SSLBs using current SSE systems. The team expects to develop a general approach to engineer the lithium anode for realizing stable cycling of SSLBs**.**

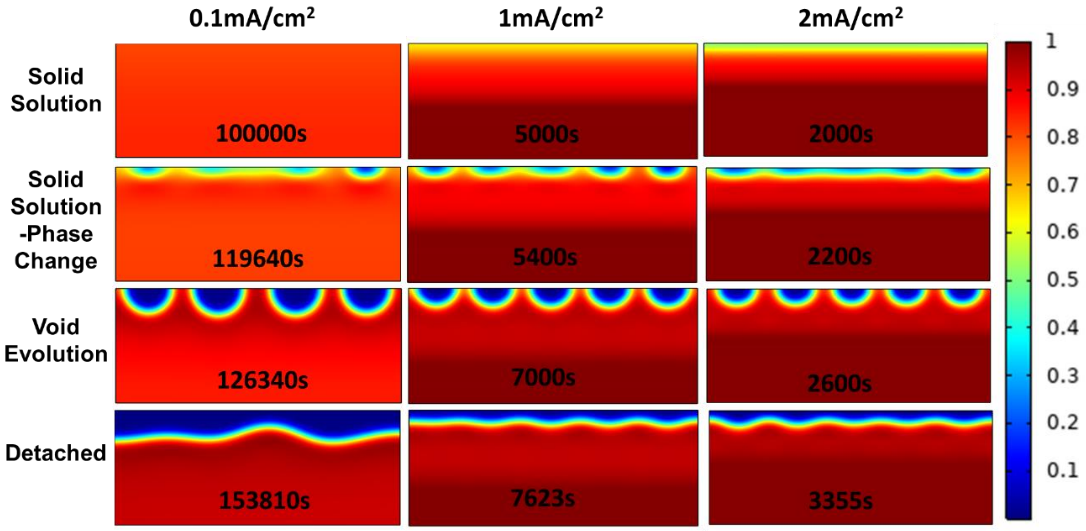

Figure 25. Li-metal stripping kinetics at different current density simulated by phase-field model.

Universal Interphase Design Capable of Meeting Performance Requirements

The highlights for this quarter are as follows:

- Demonstrated engineered thin lithium anode with excellent stability to current electrolytes.
- Thin-film electrolyte (< 100 μm) presents good cycling stability at 0.2/0.5 mA cm^{-2}.

Figure 26a shows the energy density predication of SSLBs utilizing widely used SSEs, including Li_6PS_5Cl (LPSCl), $Li_{6.5}La_3Zr_{1.5}Ta_{0.5}O_{12}$ (LLZTO), PEO-based polymer, and Li_3YCl_6 (LYC) halides-type electrolytes. The thickness of lithium anode in calculation is 20 μm (4 mAh cm^{-2}), and $LiNi_{0.8}Mn_{0.1}Co_{0.1}O_2$ (NMC-811) areal capacity is 4 mAh cm^{-2}. Compared with the volumetric energy density (Figure 26b), the calculated gravimetric energy density of SSBs is more affected by the thickness of SSEs due to mass density differences. As can be seen, the energy density of SSLBs can reach to 200-370 Wh kg^{-1} after reducing the SSE thickness to ~ 100 μm, which is comparable to current Li-ion battery technology. Meanwhile, the volumetric energy density of SSLBs is ~ 750 Wh L^{-1} when 100-μm SSEs are utilized. Thus, to meet the energy density requirements of SSLBs, it is necessary to explore new methods or strategies to engineer the thin lithium anode while testing with thin SSE film. This quarter, the team introduced a concept of engineered lithium (eLi), which is thin with known capacity (4 mAh cm^{-2}). Such a surface engineering method for lithium anode not only stabilizes the Li-SSEs interface, but also provides a cheap option for large-scale production in SSLB application.

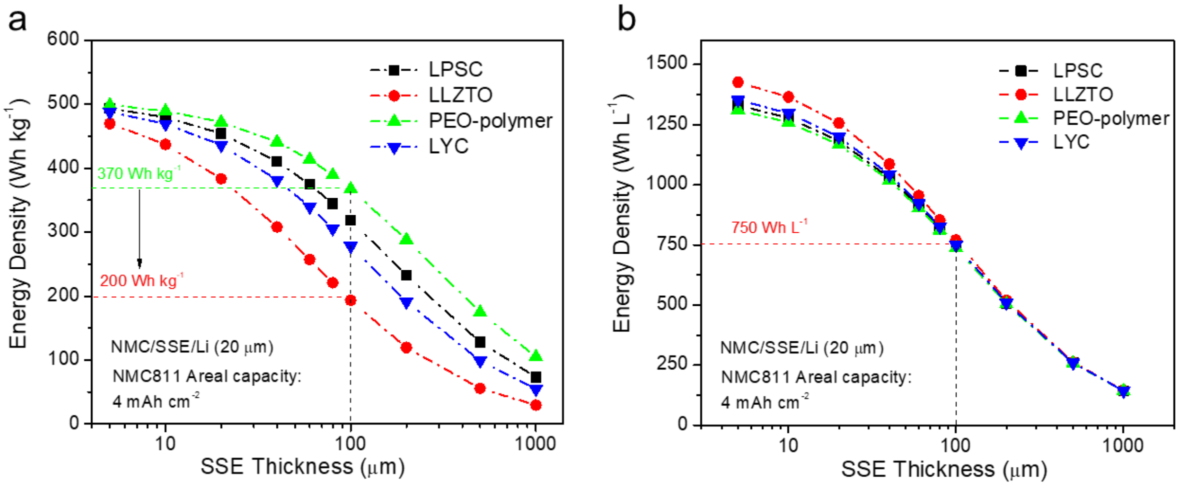

Figure 26. Energy density prediction of solid-state batteries (SSBs) using typical SSEs, including LPSC, LLZTO, PEO, and LYC. (a) The calculated gravimetric energy density of SSBs with an NMC-811|SSE|Li configuration as a function of solid-state electrolyte (SSE) membrane thickness. (b) Calculated volumetric energy density of SSBs with an NMC-811|SSE|Li configuration as a function of SSE membrane thickness. Thickness of lithium anode is 20 μm (4 mAh cm^{-2}) and NMC-811 areal capacity is 4 mAh cm^{-2}, corresponding to an anode/cathode capacity ratio of 1:1. The weight of battery accessories is ignored.

Last quarter, the team reported that the engineered anode is generally stable to thin LPSCl film electrolytes (80-100 μm) by achieving a high CCD of 1.6 mA cm^{-2} and small surface resistance. The LPSCl film was prepared by grinding the LPSCl powder with polytetrafluoroethylene (PTFE) binder, followed by mold-cutting into discs with a diameter of 10 mm. This quarter, the team further assembled the lithium symmetric cells with LLZTO electrolyte to demonstrate dendrite suppression capability and cycling stability (Figure 27a-b). The LLZTO with a thickness of ~ 700-800 μm was prepared by a conventional solid-state method with a high relative density of ≈ 93%. Tantalum doping is able to enhance the Li^{+} conductivity and improve LLZTO stability to lithium metal. All the testing of lithium symmetric cells was based on the Swagelok-type cell. As shown in Figure 27a, the Li|LLZTO|Li cell using eLi was cycled with a constant current density of 0.2 mA cm-2 under a fixed plating/stripping time of 30 minutes. Overall, cell voltage remains stable, with a slight increase from ~ 90 mV to 130 mV after 300 hours of plating/stripping. Such an increase in cell voltage might relate to the change of surface contact under small stacking pressure conditions. Figure 27b shows the impedance change of the symmetric lithium cell during CCD testing. Only one semicircle can be observed in the EIS curves: the interception at high-frequency range is attributed to bulk resistance of the LLZTO electrolyte (~ 60 Ω cm^{2}), while the semicircle in the intermediate frequency could be caused by the resistances from SEI, charge-transfer, and surface layer of lithium (350 Ω cm^{2} in total). On the other hand, the total resistance of the lithium symmetric cell remains almost stable after long cycling. In addition, the total resistance of the symmetric cell with LLZTO is larger than that of LPSCl film (410 versus 145 Ω cm^{2}), which is due to the large surface resistance between LLZTO and eLi anode.

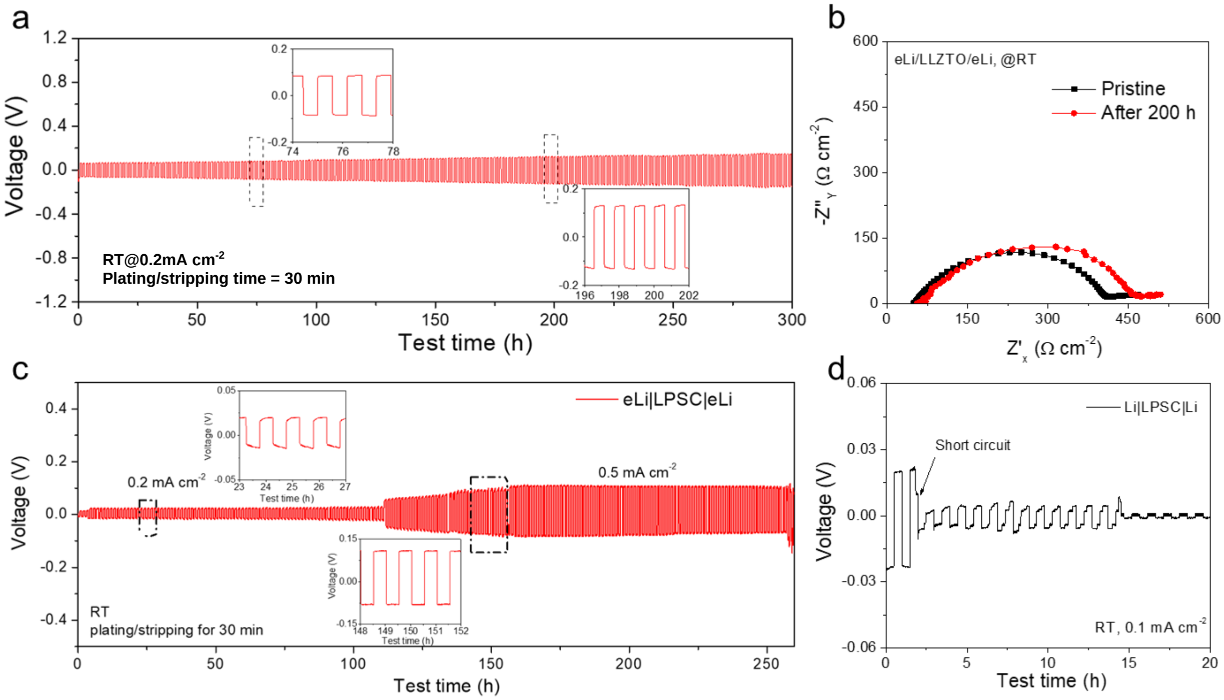

Figure 27. Electrochemical performance of eLi|LLZTO|eLi and eLi|LPSC|eLi symmetric lithium cells at room temperature. (a) Voltage profiles of the cell at constant current density of 0.2 mA cm^{-2} for lithium plating/stripping with a fixed time of 30 minutes. (b) Nyquist plots of the symmetric cell before and after cycling for 200 hours. (c-d) Galvanostatic cycling of (c) eLi|LPSC|eLi cell at current densities of 0.2-0.5 mA cm^{-2}. (d) Li|LPSC|Li cell at current density of 0.1 mA cm^{-2} with constant plating/stripping time of 30 minutes: the thickness of LPSCl film is ~ 100 μm, while for LLZTO it is 0.7-0.8 mm. Insets: enlarged view of selected voltage profiles for comparison.

Apart from the LLZTO, the team also tested the cycling stability of Li|LPSC|Li cell using eLi at constant current density of 0.2/0.5 mA cm^{-2}. As shown in Figure 27c, the cell presents pretty stable cycling with small voltage of ~ 20 mV under a small current density of 0.2 mA cm^{-2}. After increasing the current to 0.5 mA cm^{-2}, the cell voltage shows an increment and finally stabilizes to ~ 100 mV after more than 250 hours of cycling. In contrast, the cell with LPSCl film and fresh lithium anode was easily shorted within 2 hours (Figure 27d) due to lithium dendrite formation. To demonstrate the stability mechanisms, the team prepared engineered Li|LPSC|stainless steel (SS) and Li|LPSC|SS semi-blocking electrode cells for CV. As shown in Figure 28, the small peak at 0.6 V might be related to the reforming of the SEI layer due to additive reduction. After the reformation, the highly overlapping CV curves demonstrate the excellent stability of eLi to LPSCl film electrolyte. For the cell with fresh lithium, the CV curve of the symmetric lithium cell presents an irregular shape due to surface reaction. Even worse, the cell was partially shorted by lithium dendrite, thus presenting abnormal peaks in the 2nd cycle. In general, these results demonstrate that the eLi anode can effectively stop the continual reduction of electrolytes and simultaneously protect the Li-SSE [LPSCl, LLZTO, composite polymer electrolyte (CPE), etc.] interface by suppressing lithium dendrite penetration and preventing loss of surface contact due to morphology change.

Figure 29a shows the scanning electron microscope (SEM) image of layered structure of the cycled Li|LPSC|Li cell using eLi. The cross-sectional images further demonstrate that the good contact between the SSE and eLi was maintained after long cycling, thus leading to uniform lithium deposition/dissolution near the interface. Further energy-dispersive X-ray spectroscopy (EDS) mapping (Figure 29b-i) shows uniform distributions of phosphorus, sulfur, chlorine, carbon, iron, and oxygen elements, indicating good incorporation of the PTFE polymer into LPSCl particles, which helps improve the mechanical strength of film electrolyte. On a large scale, the SEM-EDS mappings for the engineered Li/LPSCl interface show a relatively high signal of carbon, iron, and oxygen element in specific spots (Figure 29g-i), which might be due to diffusion of the

N-rich, F-rich interphase. Overall, this part focuses on the novel method to engineer the thin lithium anode to realize stable, long-cycling of SSLBs, which accelerates the transformation from cell components research to real battery technologies. Further efforts should be devoted to understanding the interphase formation of eLi and preparing the full cell with high capacity based on the thin SSE films.

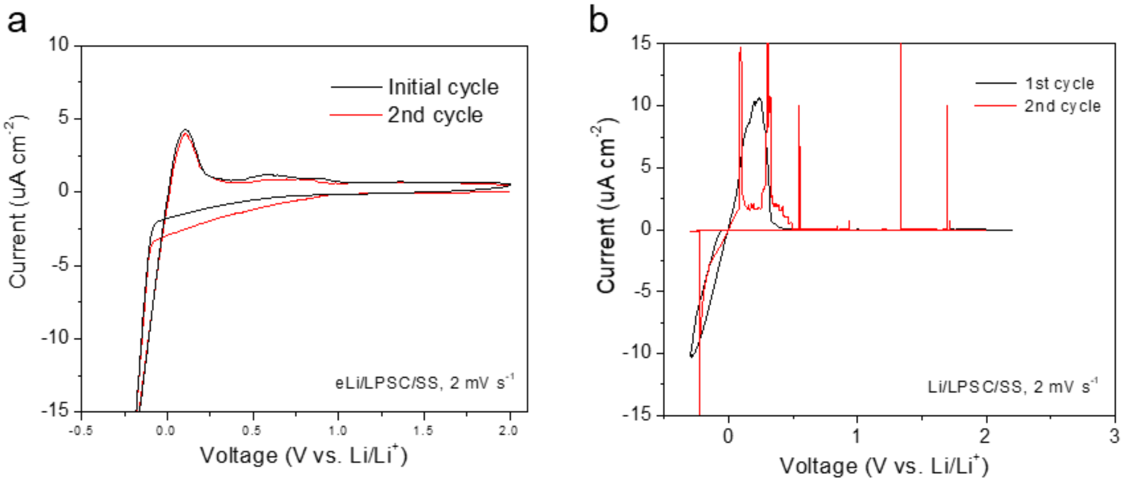

Figure 28. The first two cyclic voltammetry curves of (a) eLi|LPSC|SS and (b) Li|LPSC|SS cells at a scanning rate of 2 mV s^{-1} (−0.2 to 2.0 V). The thickness of LPSCl was controlled as 100 µm; SS = stainless steel.

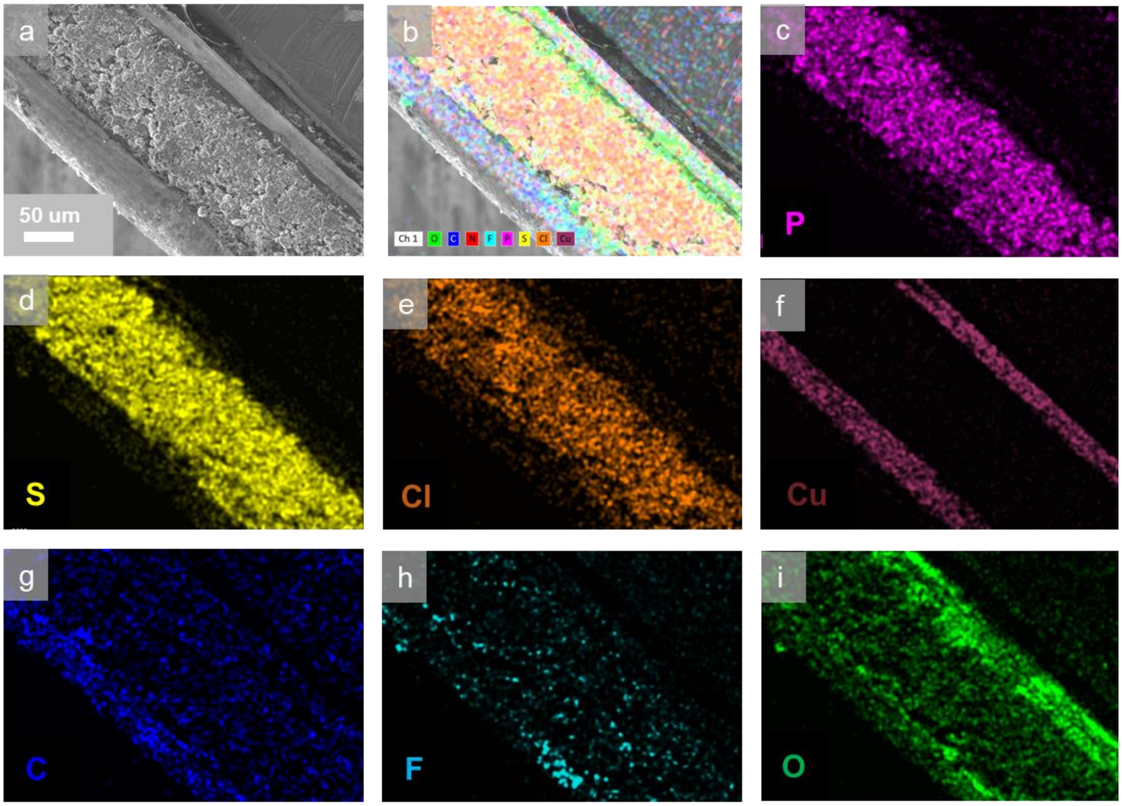

Figure 29. (a) Cross-sectional scanning electron microscopy (SEM) images of cycled eLi|LPSC|eLi symmetric cell. (b-i) SEM images: (b) selected area and corresponding energy dispersive spectroscopy elemental mapping of (c) phosphorus (LPSCl), (d) sulfur (LPSCl), (e) chlorine (LPSCl), (f) copper (current collector), (g) carbon (PTFE and interphase), (h) fluorine (PTFE and interphase), and (i) oxygen (interphase) collected from the eLi|LPSCl|eLi slides.

Patents/Publications/Presentations

Publication

- Wan, H., B. Zhang, S. Liu, J. Zhang, X. Yao, and C. Wang. “Understanding LiI-LiBr Catalyst Activity for Solid State Li_2S/S Reactions in an All-Solid-State Lithium Battery.” *Nano Letters* 21 (2021): 8488−8494.

Task 1.8 – Low Impedance Cathode/Electrolyte Interfaces for High-Energy-Density Solid-State Batteries
(Eric Wachsman and Yifei Mo, University of Maryland)

Project Objective. The project objective is to research, develop, and test Li-metal-based batteries that implement solid LICs equipped with NMC cathodes integrated into the Li-metal / Li-La-Zr (LLZ) tri-layer architecture. Specifically, the team will achieve the following: (1) identify and demonstrate interfacial layers to achieve low-impedance and stable NMC/LLZ interfaces; (2) develop novel processing techniques to fabricate NMC/LLZ composite cathodes with low interfacial resistance; and (3) enable high-performance ASSBs with an energy density of 450 Wh/kg and 1400 Wh/L and negligible degradation for 500 cycles.

Project Impact. Instability or high resistance at the interface of high-energy cathode materials with Li-garnet SEs limits the high-energy-density ASSLBs. This project will lead to a fundamental understanding of solid-electrolyte/solid-cathode interfaces and a unique and transformative LLZ framework to enable high-energy-density, safe Li-metal batteries approaching ~ 400 Wh/kg.

Approach. In this new project, the team will build on their demonstrated expertise with garnet electrolytes and ASSB cells to accomplish the following: (1) engineer interfaces to overcome high NMC/LLZ interfacial impedance and interfacial degradation; (2) develop processing and fabrication techniques to achieve high-loading NMC/LLZ composite cathodes with low resistance and high cyclability; and (3) integrate the NMC/LLZ cathodes into all-solid-state Li-metal/LLZ cells to achieve high-energy-density batteries.

Out-Year Goals. The project will solve the current challenges of integrating garnet SE with a cathode to achieve a high-performance ASSB using a high-energy-density Li-metal anode. The resultant high energy density and stability using both high-energy-density Li-metal anodes and NMC cathodes will open new applications in portable electronics, EVs, and beyond.

Collaborations. This project funds work at University of Maryland (UMD). The principal investigator (PI), E. Wachsman, will have management responsibility and will lead experimental efforts including garnet synthesis, interface processing, cell fabrication, and testing. The Co-PI, Y. Mo, will lead computational efforts on understanding stability between garnet and cathode and on identifying promising coating materials. In addition, E. Wachsman is actively collaborating with several universities and national laboratories through the U.S.–German cooperation on SSB interfaces.

Milestones

1. Experimentally determine thermochemical stability between interface-coated LLZ and infiltrated NMC. (Q1, FY 2021; In progress)
2. Perform computations of promising coating materials to determine appropriate compositions to stabilize the LLZ-NMC interface. (Q2, FY 2021; Completed)
3. *Go/No-Go Decision*: Demonstrate a 10-times reduction in interfacial impedance between coated and uncoated LLZ/NMC interfaces. Design capable of meeting performance requirements. (Q4, FY 2021; Completed)

Progress Report

Figure 30 shows XRD profiles of various NMC-LLZTO co-sintered samples at 800°C. As shown by the profile for a co-sintered pellet (in red), a reaction between $Ni_{0.6}Mn_{0.2}Co_{0.2}$ (NMC-622) and LLZTO can be observed by the appearance of decomposition products (Li_2MO_3, M = Ni, Mn, Co) at ~ 24° and ~ 32°. However, these peaks are not present in trilayer samples infiltrated by NMC-622 that were subjected to the same co-sintering conditions. This suggests that the surface contact between NMC and LLZTO is insufficient for XRD to be able to detect the decomposition products. The surface areas of NMC-622 and LLZTO that are in contact with each other are greater in the pellet due to the randomized mixing of the sample. Transmission electron microscopy (TEM) will be carried out to detect formation of these decomposition products at the interface next quarter.

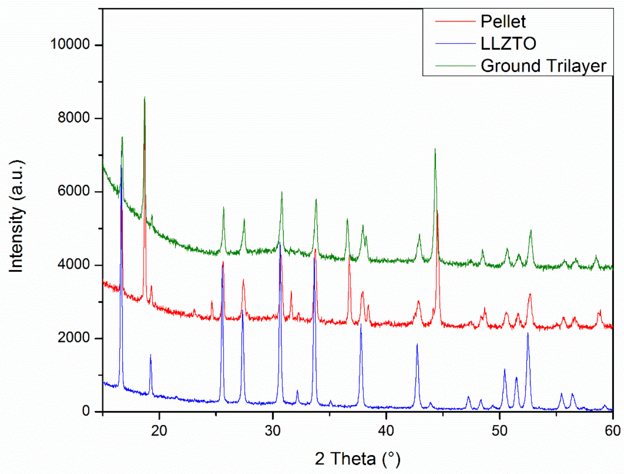

Figure 30. X-ray diffraction of NMC and LLZTO samples co-sintered at 800°C. Pellet: pressed powder mixture of NMC and LLZTO. Ground trilayer: ground assembly of LLZTO trilayer with NMC particles infiltrated into porous layers.

Figure 31 contains Nyquist and distribution of relaxation times (DRT) plots of the EIS results measured on symmetric NMC|LLZTO|NMC cells that were co-sintered at various temperatures (700°C, 800°C), demonstrating the benefit of using a ZnO interfacial layer coated by atomic layer deposition (ALD) in reducing the area specific resistance (ASR). Specifically, this demonstrated a significant reduction in the ASR when

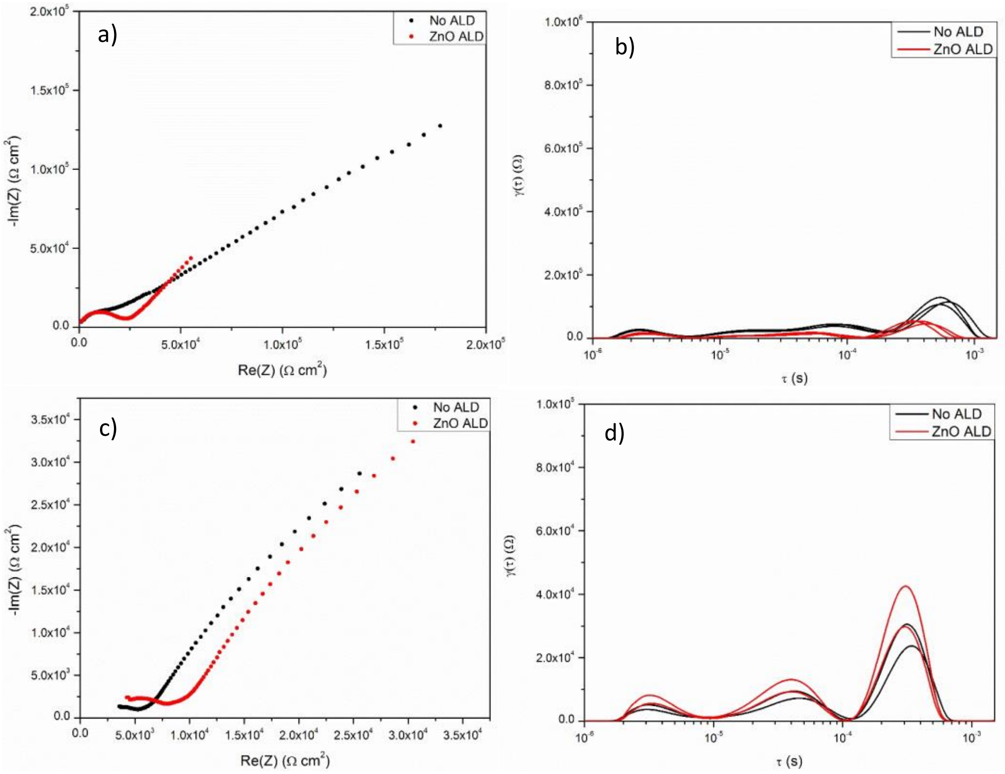

Figure 31. Electrochemical impedance spectroscopy for symmetric NMC-622|LLZO|NMC-622 cells co-sintered at various temperatures comparing uncoated and ALD-coated samples. (a) Nyquist plot and (b) distribution of relaxation times (DRT) analysis of samples co-sintered at 700°C. (c) Nyquist plot and (d) DRT analysis of samples co-sintered at 800°C.

co-sintered at 700°C; however, similar ASRs are obtained from ZnO coated and uncoated samples when co-sintered at 800°C. Last quarter, the team demonstrated that Al_2O_3-coated samples showed a 4-times decrease in the ASR compared to the uncoated sample at 800°C, indicating that Al_2O_3 is better than ZnO at improving interfacial impedance.

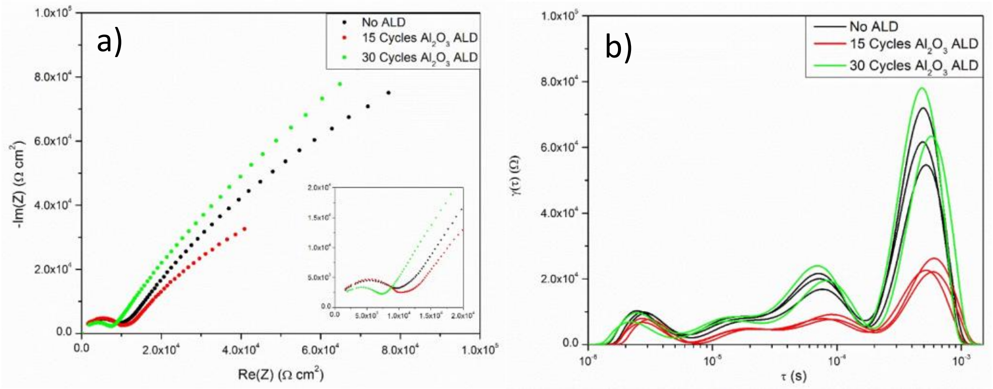

Figure 32. Electrochemical impedance spectroscopy for symmetric NMC-622|LLZO|NMC-622 cells co-sintered at 800°C comparing uncoated and Al_2O_3-ALD-coated samples. (a) Nyquist plot. (b) Distribution of relaxation times plot.

To determine the effect of the interlayer thickness on the ability to improve interfacial impedance of NMC symmetric cells, samples were coated with different thicknesses of ALD alumina and co-sintered at 800°C. Fifteen cycles of ALD correspond to approximately a 3-nm interlayer, and 30 cycles correspond to approximately a 6-nm interlayer. Figure 32 contains EIS results in the form of Nyquist and DRT plots. These demonstrate that the 3-nm interlayer has a 4-times reduction in the ASR, whereas the 6-nm interlayer appears to have similar ASR to the uncoated samples.

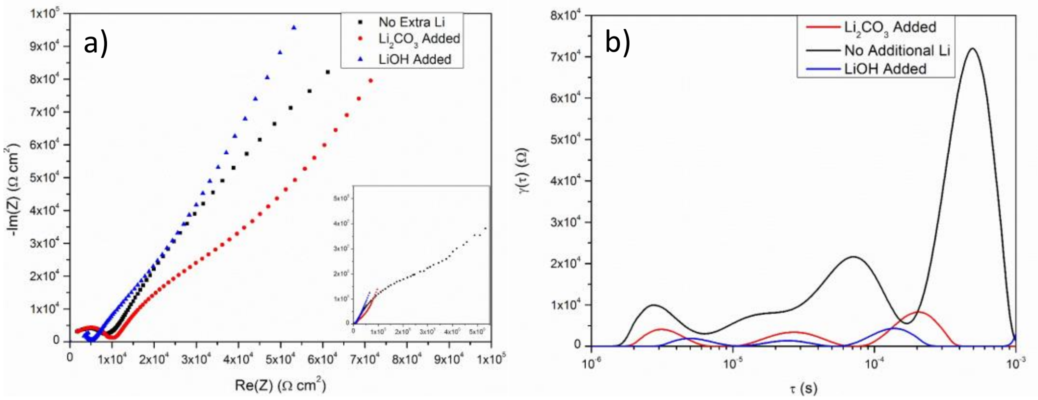

Figure 33. Electrochemical impedance spectroscopy for symmetric NMC-622|LLZO|NMC-622 cells co-sintered at 800°C comparing samples with and without extra lithium from various sources. (a) Nyquist plot. (b) Distribution of relaxation times plot.

Due to previous DSC results indicating that adding additional lithium would prevent the reaction of NMC and LLZTO, symmetric NMC cells were co-sintered at 800°C with additional lithium from either LiOH or Li_2CO_3 as the source in a molar ratio of 1:3 (Li:NMC). Figure 33 shows EIS results for these experiments, demonstrating a significant reduction of the ASR of more than 10-times, regardless of lithium source. This confirms the DSC results that increasing the amount of available lithium would reduce the reaction of NMC and LLZTO. Furthermore, this reduction can be integrated with the ALD interlayers for even greater reduction in interfacial impedance. To investigate this, lithium was added in the same 1:3 ratio to symmetric cells, where the garnet trilayer was coated with varying thicknesses of Al_2O_3. The EIS results from these samples are shown in Figure 34. Both the 3-nm and 6-nm interlayers have similar ASR. Given the previous results showing that the 6-nm interlayer had higher ASR than the 3-nm interlayer, this suggests that the thicker interlayer was insufficiently lithiated since the ionic conductivity of lithiated alumina is several orders of magnitude higher than that of unlithiated alumina.

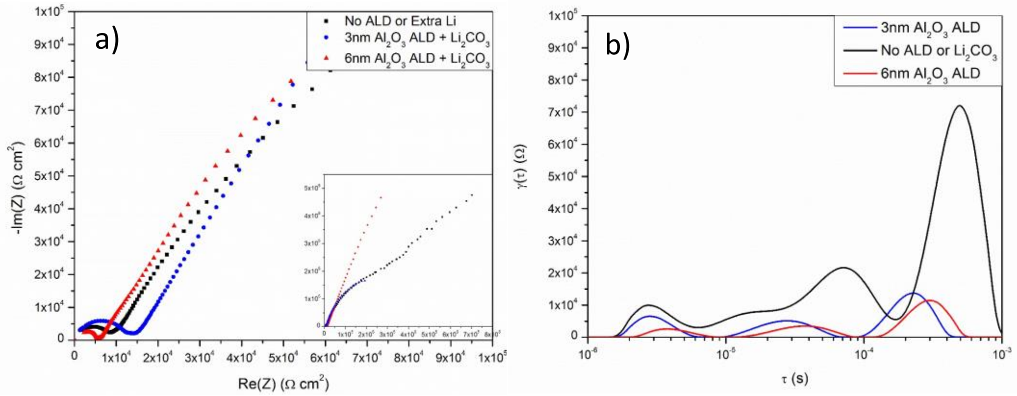

Figure 34. Electrochemical impedance spectroscopy for symmetric NMC-622|LLZO|NMC-622 cells co-sintered at 800°C comparing various thicknesses of ALD-coated samples, all with the same amount of extra lithium added. (a) Nyquist plot. (b) Distribution of relaxation times plot.

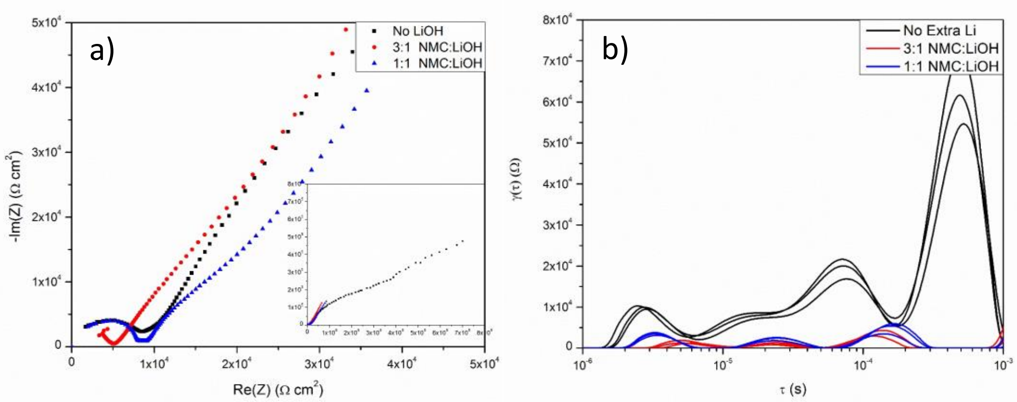

Figure 35. Electrochemical impedance spectroscopy for symmetric NMC-622|LLZO|NMC-622 cells co-sintered at 800°C comparing samples where the extra lithium ratio was increased from 1:3 Li:NMC to 1:1. (a) Nyquist plot. (b) Distribution of relaxation times plot.

Finally, the amount of extra lithium was increased to get a sense for how much additional lithium is beneficial to NMC/LLZTO co-sintering. The Li:NMC ratio was increased to 1:1, and the EIS results are shown in Figure 35. The Nyquist and DRT plots show that both ratios significantly decrease the ASR when compared to samples without extra lithium. However, increasing the amount of extra lithium past 1:3 (Li:NMC) shows similar ASR, so further reductions in ASR by lithiation alone are not realized.

Patents/Publications/Presentations

Publications

- Nolan, A. M., D. Wickramaratne, N. Bernstein, Y. Mo,* and M. D. Johannes.* "Li^+ Diffusion in Amorphous and Crystalline Al_2O_3 for Battery Electrode Coatings." *Chemistry of Materials* 33, No. 19 (2021): 7795–7804.
- Yang, M., and Y. Mo.* "Interfacial Defect of Lithium Metal in Solid-State Batteries." *Angewandte Chemie International Edition* 60 (2021): 21494.

Task 1.9 – Developing an *In Situ* Formed Dynamic Protection Layer to Mitigate Lithium Interface Shifting: Preventing Dendrite Formation on Metallic Lithium Surface to Facilitate Long Cycle Life of Lithium Solid-State Batteries

(Deyang Qu, University of Wisconsin, Milwaukee)

Project Objective. The objective of this project is to research, develop, and test Li-metal-based batteries that implement solid LICs equipped with a formed dynamic protection layer. The proposed project aims to enable safe, long-cycle lithium anodes to achieve cell performance targets of 400 Wh/Kg, over 100 cycles, with 15-year shelf life, and < $100/KWh cost.

Project Impact. Project efforts are to contribute an in-depth understanding of the lithium interface and dendrite growth prevention to the field of Li-metal batteries, which will pave the way for eventual development of high-energy-density, low-cost, and long-lasting lithium batteries. This advancement could be a crucial selling point for the greater adoption of EVs. This project will make possible the translation of fundamental research into practical implementation of high-energy lithium anodes, enabling eventual achievement of cell performance targets.

Approach. The novelty of this approach is that the team intends to mitigate the dendrite problem by creating a dynamic protection layer during the interface shift to prevent dendrite formation throughout battery operation.

Out-Year Goals. The project has three out-year goals: (1) *in situ* diagnostic tools are fully functional; (2) potential candidates for Li-anode modifications are identified; and (3) synthesis routes are designed.

Collaborations. The PI is the Johnson Control Endowed Chair Professor, who has close and frequent collaboration with Johnson Controls' scientists and engineers. The collaboration enables the team to validate the outcomes of fundamental research in pilot-scale cells. The PI also has been working closely with top scientists at Argonne National Laboratory (ANL), Brookhaven National Laboratory (BNL), LBNL, and Pacific Northwest National Laboratory (PNNL) and with U. S. industrial collaborators, for example, General Motors (GM), Millipore Sigma, and Clarios. In addition, the team works with international collaborators in China, Japan, and South Korea. These collaborations will be strengthened and expanded to give this project a vision with both today's state-of-the-art technology and tomorrow's technology in development, while incorporating feedback from material designers and synthesizers upstream, as well as from industrial end users downstream.

Milestones

1. Lithium anode electrochemical performance evaluation. Synthesis n-type polymer materials and evaluation of the electrochemical performance. (Q1, FY 2021; Completed)

2. Roll-press coating development. Complete the process development of roll-press coating. (Q2, FY 2021; Completed)

3. Polycyclic aromatic hydrocarbon (PAH) derivative structure identified. Identification of the synergy of the parameters and their impact on dendrite growth. (Q3, FY 2021; Completed)

4. Synthesis and test of PE with PAHs. Synthesis of PE with various PAH functionalities, and test with lithium anode in a half cell. (Q4, FY 2021; Completed)

5. Dendrite suppression demonstrated; interim cell performance verified. Dendrite suppression on coated lithium anode demonstrated, and analysis indicates technical approach capable of achieving performance targets. (Q4, FY 2021; Completed)

Progress Report

In past quarters, the team demonstrated a high-performance all-solid battery with $Ni_{0.8}Mn_{0.1}Co_{0.1}$ (NMC-811) and protected lithium anode with a bi-composition SSE (halide and sulfide). Along with their continuous investigation of the lithium surface protection in the bi-composition SE, this quarter, the team tried to better understand the Li/Li_6PS_5Cl interface. The energy cyclability, rate capability, and volume changes during cycles were studied.

To focus the electrochemical investigation on a lithium anode, the team aimed to find an adequate cathode with a high electrochemical reversibility and a low voltage (below 2.5 V) to ensure its compatibility to Li_6PS_5Cl. Working with their industry collaborator (Millipore Sigma; the compound is now available through Millipore Sigma catalog), the team found that a graphene (Gr)-doped poly (anthraquinonyl sulfide) (PAQS) was an excellent cathode for the test vehicle to investigate the lithium anode in a Li/Li_6PS_5Cl system. Prepared via a one-pot synthesis approach, which facilitated the dispersion and utilization of Gr during the polymerization process of PAQS, the PAQS-G nanocomposite was extremely conductive and electrochemically reversible.

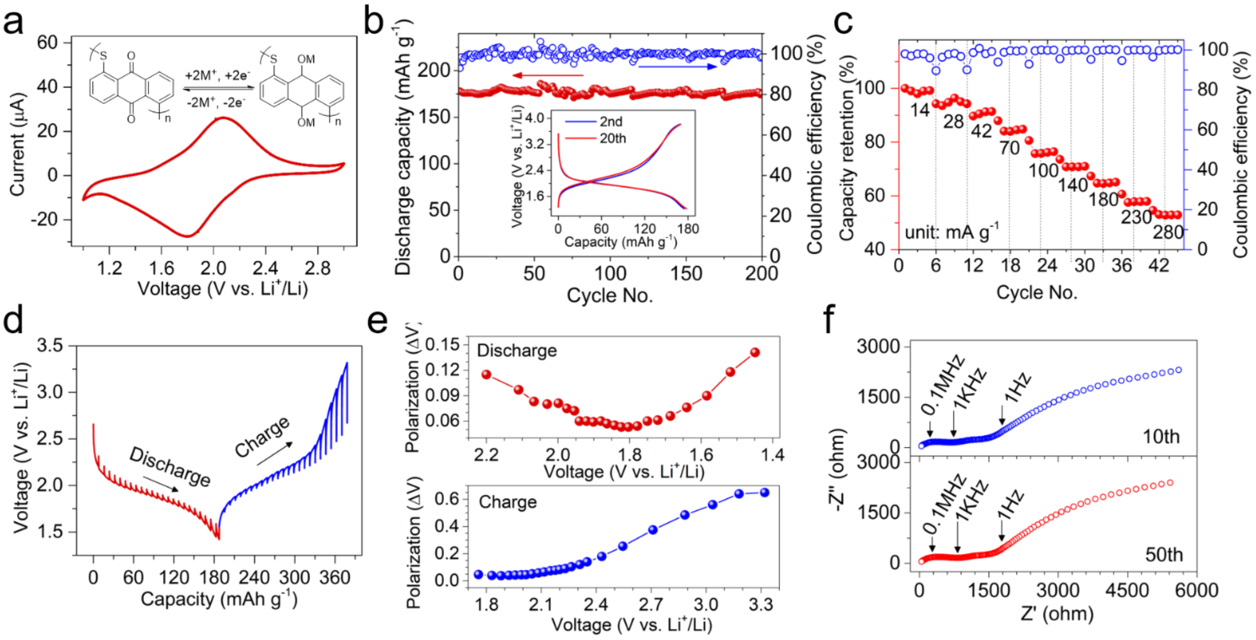

Figure 36. Electrochemical performance of PAQS-G/Li_6PS_5Cl/LiIn all-solid-state lithium battery. (a) Cyclic voltammetry profile at a scan rate of 0.05 mV s^{-1}. (b) Cycling performance at 0.1C (18 mA g^{-1}); inset shows galvanostatic voltage profiles at different cycles. (c) Rate performance. (d) Galvanostatic intermittent titration technique potential profile and (e) corresponding polarization plots during one charge/discharge cycle. (f) Electrochemical impedance spectra tested under fully discharged state of different cycles.

Figure 36a shows that a pair of broad peaks occur at 1.81 V and 2.08 V, representing the very reversible redox behavior of the anthraquinonyl group. The PAQS-G cathode delivers a reversible capacity of ~ 178 mAh g^{-1} at 60°C. Figure 36b shows the cyclability of the all-solid-state-electrolyte cell made with PAQS-G and protected lithium anode. After 200 cycles, the capacity retention was 94% and CE was nearly 100%. As shown in Figure 36c, the rate performance was tested from 0.042 mA/cm^2 (14 mA/g) to 0.84 mA/cm^2 (280 mA/g). About 53% of its initial capacity was maintained under 0.84 mA/cm^2 rate. Galvanostatic intermittent titration technique (GITT) was further employed to study the thermodynamic potential of the electrochemical reaction. A series of current pulses (10 mA) was applied, with each followed by a relaxation time of 4 hours. During relaxation, the cell tended to become homogenous by Li^+ diffusion and reached an equilibrium. As shown in Figure 36d, one voltage plateau is shown after the full relaxation, indicating a one-step solid-solid phase transition. As shown in Figure 36e, polarization curves are obtained from the iR drop during the relaxation, representing the evolution of interfacial resistance under different potentials. During the discharge process, the polarization was relatively small. By contrast, a build-up of polarization was observed at the end of the charge process, indicating that a large Li^+ concentration gradient was established across the cell. This result can be explained by a complete dissociation of Li^+ from PAQS backbone and, simultaneously, a partial delithiation (oxidation) of Li-rich Li_6PS_5Cl electrolyte. Thereby, the evolution of the interfacial resistance during one cycle was potential-dependent. As shown in Figure 36f, similar EIS patterns are displayed at the end of the discharge of the 10th and the 50th cycle, indicating that the evolution of interfacial impedance was very reversible from cycle to cycle, which was beneficial for the cycling stability of both anode and cathode.

Patents/Publications/Presentations

The project has no patents, publications, or presentations to report this quarter.

Task 1.10 – Molecular Ionic Composites: A New Class of Polymer Electrolytes to Enable All-Solid-State and High-Voltage Lithium Batteries

(Louis Madsen, Virginia Polytechnic Institute and State University)

Project Objective. Based on a newly discovered class of solid PE materials, that is, molecular ionic composites (MICs), the overall objective is to develop solid-state lithium conductors targeted for use in transportation applications. MICs form a mechanically stiff, electrochemically stable, and thermally stable matrix. Specific objectives include the following: (1) development of robust MIC electrolyte thin films (~ 20 µm) to serve as simultaneous nonflammable separators and dendrite-blocking Li^+ conductors, (2) electrochemical quantification of key performance metrics including electrolyte stability, interfacial reactions, and suitability/compatibility with a range of electrode materials, and (3) comprehensive investigation of ion transport mechanisms and electrode-electrolyte interfacial reactivity under practical operating conditions using NMR and synchrotron X-ray analyses.

Project Impact. Commercialization of Li-metal SSBs is hampered by lack of a functional nonflammable SE that can provide high ionic conductivity, wide electrochemical window, favorable mechanical properties to inhibit lithium dendritic growth, and low interfacial resistance. The tunable MIC materials platform has potential to fulfill these requirements with relatively simple fabrication techniques, and thus shows promise for enabling nonflammable SSBs that can be optimized for low cost and high energy density.

Approach. MICs rely on a unique polymer that is similar to Kevlar® in its strength, stiffness, and thermal stability, but with densely spaced ionic groups that serve to form an electrostatic network that permeates mobile ions in the MIC. The team can tailor the ion concentrations and types to yield MIC electrolyte films that are electrochemically compatible with Li-metal anode as well as a range of high-voltage layered cathodes. They are searching the composition space of lithium salts, electrochemically compatible ILs, and polymer [poly(2,2′-disulfonyl-4,4′-benzidine terephthalamide), or PBDT] molecular weight to determine best composition windows for MIC electrolytes. The team is also investigating best methods for casting thin films in terms of temperature, solvent/evaporation conditions, and control over the initial liquid crystalline gel formation point. Concurrently, they are testing MIC films in various electrochemical cells, quantifying transport and structural/morphology parameters with NMR and X-ray techniques, and measuring key mechanical (dynamic mechanical thermal analysis, stress-strain) and thermal [DSC, thermal gravimetric analysis (TGA)] properties.

Out-Year Goals. This year, the team will further optimize the film casting process to obtain thin MIC electrolyte films, but will focus primarily on detailed electrochemical quantification of key performance metrics including electrolyte stability, interfacial reactions, and suitability/compatibility with a range of electrode materials (with the focus on lithium metal and layered oxides). The team will understand and optimize the oxidative stability and interfacial impedance properties of MIC electrolytes. The team will develop and characterize working battery cells incorporating MIC electrolyte films with various cathode and anode materials, and will work to understand fundamental material compositions and interfacial compatibilities to choose favorable combinations for safe SSBs with high energy density.

Collaborations. The team is collaborating with T. J. Dingemans’ group at University of North Carolina, Chapel Hill, in which they are forming composites based on PBDT polymer and carbon materials such as Gr oxide, and are beginning to develop charged rigid-rod polymers building on the PBDT structure. The team is exploring shear rheology and broadband dielectric spectroscopy collaboration with R. H. Colby at Pennsylvania State University (PSU). They are collaborating with D. Nordlund at Stanford Linear Accelerator Center (SLAC) National Accelerator Laboratory to conduct synchrotron X-ray studies on MIC films.

Milestones

1. Determine parameter spaces for film formation, and develop design capable of meeting performance requirements for film casting process. (Q2, FY 2021; Completed, with ongoing improvements)
2. Optimize oxidative stability by using NMC/MIC/NMC and Li/MIC/NMC cell platforms to determine the upper limit of cycling voltage. (Q3, FY 2021; Completed)
3. Optimize electrolyte chemistry to achieve minimal interfacial impedance. (Q4, FY 2021; Completed)
4. Initial full cell integration and performance evaluation with Li/MIC/NMC and cycling under high current density. (Q1, FY 2022; In progress)

Progress Report

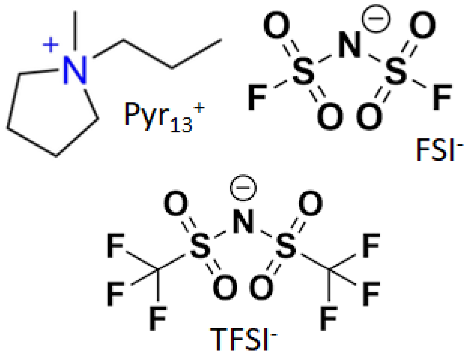

Figure 37. Chemical structures of Pyr$_{13}$FSI and TFSI anion. All three ions are present in the two systems studied with LiTFSI salt. The two systems using LiFSI salt had no TFSI anion.

This quarter, the team further explored solid MIC electrolyte membranes using *N*-propyl-*N*-methylpyrrolidinium bis(fluorosulfonyl)imide (Pyr$_{13}$FSI) as the base IL with one of two salts (LiTFSI and LiFSI), and over a range of different concentrations. Figure 37 shows the chemical structures of the base IL (Pyr$_{13}$FSI) and TFSI anion involved in these systems. Table 2 shows the composition of these three components (PBDT, salt, and Pyr$_{13}$FSI) in addition to the thickness of each system, the ionic conductivity, the Li-ion transference number (t_{Li+}), and the limiting current density measured at room temperature. As previously reported, these electrolytes exhibit an ionic conductivity up to 0.91 mS/cm, which is almost a factor of two higher than previously studied *N*-butyl-*N*-methylpyrrolidinium bis(trifluoromethanesulfonyl)imide (Pyr$_{14}$TFSI) based MIC system (0.52 mS/cm). Furthermore, the t_{Li+} of 0.35 for these newly measured systems is a factor of 3 larger than the previous MIC system (0.12). In addition, the team can now reach a current density of 0.60 mA/cm^2 for the MIC consisting of 100% bis(fluorosulfonyl)imide (FSI) anion in lithium symmetric cells. These cells are being long-term cycled at 0.20 mA/cm^2 at room temperature (for over 500 hours so far), and this is twice the current density as that reported for the Pyr$_{14}$TFSI-based MIC system. They expect further improvements in limiting current and cycling stability as they more finely optimize composition and cell assembly.

Table 2. Room-temperature conductivity and Li-ion transference number of Pyr$_{13}$FSI-based molecular ionic composites (MICs) with specified lithium salts and compositions. The highest conductivity value is almost a factor of 2 larger than that of the previously reported Pyr$_{14}$TFSI-based MIC, and each transference number is about a factor of 3 larger.

Composition (PBDT-salt-Pyr$_{13}$FSI, wt%)	Salt	Thickness (µm)	Conductivity at 25°C (mS/cm)	Li-ion transference number (t_{Li+})	Limiting Current Density (mA/cm^2)
10-10-80	LiTFSI	52.0	0.64	0.34	0.50
10-20-70	LiTFSI	40.2	0.44	0.39	0.20
10-10-80	LiFSI	48.8	0.91	0.33	0.60
10-20-70	LiFSI	43.1	0.17	-	0.40

The team has also prepared other MICs with a wide range of different ILs at the same fixed PBDT content (10 wt%) to continue optimizing and fundamentally understanding the ion transport properties while maintaining sufficient mechanical strength. Figure 38 shows the ionic conductivity of six MICs at 30°C as a function of the IL molecular volume (V_m). The MIC prepared with 1-butyl-3-methylimidazolium dicyanamide (BMIM DCA) shows the highest conductivity, reaching 6 mS/cm. Besides that, the MICs prepared with a smaller IL cation ($EMIM^+$) demonstrate higher conductivity. Overall, the conductivity of these MICs is larger than 1 mS/cm at 30°C, and is only slightly decreased (within a factor of 3) compared to the conductivity of their respective neat ILs. Uniaxial stress-strain tests reveal that the Young's moduli of these MICs range from 46 MPa to 490 MPa, which is significantly higher than any other PGEs with similar ionic conductivity. These basic studies are helping the team to expand the parameter space for MIC formation, with the goals of higher current density, superior mechanical properties, and electrochemical compatibility and stability with a range of high-energy-density cathode materials.

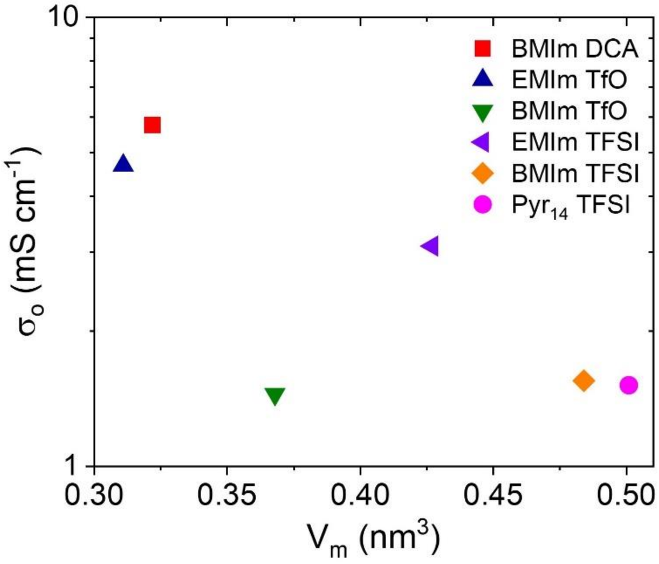

Figure 38. Ionic conductivity at 30°C of molecular ionic composites prepared with different ionic liquids (ILs) and 10 wt% PBDT as a function of IL molecular volume V_m. NOTE: BMIM: 1-butyl-3-methylimi-dazolium; EMIM: 1-ethyl-3-methylimid-azolium; Pyr_{14}: 1-butyl-1-methylpyrrolidinium; DCA: dicyanamide; TfO: trifluoro-methane-sulfonate; and TFSI: bis(trifluoromethylsulfonyl)imide.

The team has also made progress toward elucidating the ionic distribution inside the MIC electrolyte via sulfur K-edge X-ray absorption spectroscopy (XAS) at the BNL National Synchrotron Light Source (NSLS). In preliminary results, the team established a baseline to analyze the sulfur element in a MIC electrolyte, which will further enrich fundamental understanding of MIC-electrolyte-based ASSBs. Synchrotron XAS serves as a powerful tool to probe the MIC electrolyte in an elementally selective way and provides valuable information on the local environment and the oxidation state of specific atoms in the MIC electrolyte. Tender-energy XAS showed good results on X-ray absorption near-edge spectroscopy (XANES) and X-ray absorption fine structure (XAFS) without beam damage to the MIC electrolyte (Figure 39). With the team's extensive expertise in developing codes and methods to analyze synchrotron imaging data, they envision that XAS experiments as well as other complementary analysis methods on their novel electrolyte material will lay a foundation for improving the design principles for new MIC electrolytes.

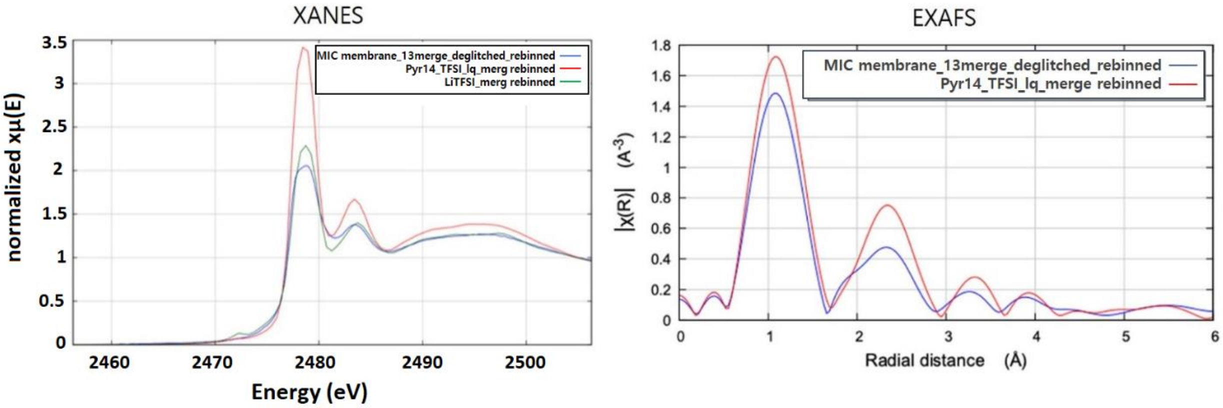

Figure 39. Preliminary results of sulfur K-edge X-ray absorption spectroscopy data. The extended X-ray absorption fine structure data have been obtained for the polymer membrane and ionic liquid samples without beam damage.

This quarter, the team has investigated specific pressure control for MIC battery assembly. Pressure control in Li-metal SSBs plays an important role in terms of the cell internal resistance and cycling performance. An appropriate stacking pressure is required to enhance contact between the electrodes and SSE, while, at the same time, not disrupting the inherent properties of the electrolyte. Considering the mechanical properties of these MIC electrolytes compared to ceramic-based electrolytes, to understand and engineer the stacking pressure will be meaningful to maximize the lifespan of MIC-based SSBs. Herein, the team adopts a polyether ether ketone (PEEK) mold using titanium plungers as the current collector (Figure 40) to finely control the applied stacking pressure through the adjustable torque, and they are beginning to investigate the corresponding electrochemical performance in NMC-811/MIC/Li cells. These cells are assembled and sealed inside the glovebox before measurements. The team has confirmed that under pressure-free conditions, the open circuit voltage (OCV) is comparable with the coin-cell platform (~ 3.4 V versus Li/Li$^+$). The follow-up is to change the pressure, while monitoring the OCV to find the critical pressure value to measure the electrochemical cycling performance within the proper pressure range and investigate the underlying mechanisms. The final target of these experiments is to determine the optimal stacking pressure in the NMC-811/MIC/Li system and achieve high-energy, stable SSBs.

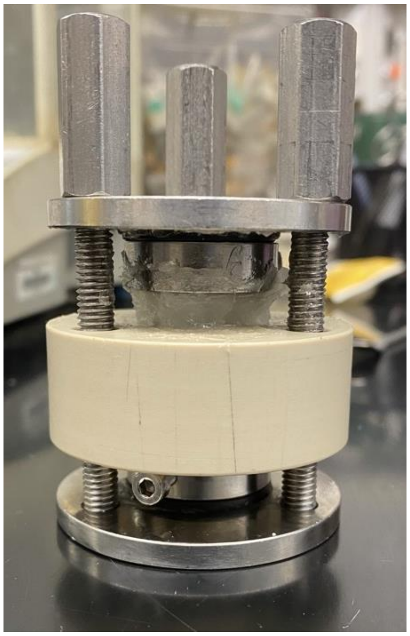

Figure 40. Experimental design of the polyether ether ketone (PEEK) cell (adapted from a cell developed in collaborator Y. Yao's group at University of Houston) to monitor the stacking pressure applied to the solid-state batteries. By tracking pressure applied on the batteries, the team can obtain an optimal stacking pressure in cell formation to achieve high-energy, stable MIC-based solid-state batteries.

Patents/Publications/Presentations

The project has no patents, publications, or presentations to report this quarter.

Task 1.11 – All-Solid-State Batteries Enabled by Multifunctional Electrolyte Materials (Pu Zhang, Solid Power Inc.)

Project Objective. The project objective is to develop Li-metal SSBs enabled by multifunctional SSEs for EV application. The ultimate goal is scalable production of large-format ASSBs able to deliver ≥ 350 Wh/kg specific energy, ≥ 1000 cycle life, and ≤ $100/kWh cost.

Project Impact. The project is enabling scalable production of large-format ASSBs required by the vehicle market and is building domestic battery manufacturers as leaders in the global vehicle ASSB production. The proposed technology will address key limitations of state-of-the-art lithium batteries to meet DOE EV battery targets and accelerate their adoption as large-format EV batteries for sustainable transportation technology.

Approach. The project will develop a high-performance Li-metal solid-state cell enabled by a multifunctional SSE. The new SSE will (1) have high conductivity (up to 10 mS/cm), (2) be stable against lithium metal and high-voltage cathode (0-4.5 V), (3) promote uniform lithium plating (enabling > 2C charge rate), and (4) be compatible with large-scale manufacturing processes. The specific cell chemistry to be demonstrated will be the SSE with Li-metal anode and high-nickel-content Li-metal oxide cathode. The solid-state cell will be assembled by scalable roll-to-roll processes developed by Solid Power.

Out-Year Goals. In Year 1, multifunctional SSE will be developed with lithium ionic conductivity of ≥ 3 x 10^{-3} S/cm. A CCD of ≥ 6 mA/cm^2 will be achieved in a symmetric lithium cell. The SSE design concept will be proven by demonstrating cycle life of ≥ 200 in a full cell. In Year 2, SSE material will be optimized with lithium ionic conductivity of ≥ 5 x 10^{-3} S/cm. Scalable cell assembly processes will be developed. Cycle life of ≥ 500 will be demonstrated in a full cell. In Year 3, large-format solid-state cells (> 2Ah) will be assembled/tested to meet the final goal: ≥ 350 Wh/kg, ≥ 1000 cycles, and ≤ $100/kWh cost.

Collaborations. The proposed team consists of Solid Power and a subcontractor, University of California, San Diego (UCSD). Solid Power (PI: P. Zhang) will develop the multifunctional SSE and other cell components, assemble cells, and conduct cell tests. UCSD (PI: Y. S. Meng) will carry out material characterization by using advanced techniques such as X-ray photoelectron spectroscopy (XPS), cryogenic – scanning transmission electron microscopy (cryo-STEM) imaging, cryo-STEM EDS, electron energy loss spectroscopy (EELS), and cryogenic – focused ion beam (cryo-FIB) milling. The UCSD team seeks to quantify the kinetics and evolution of each contributing factor and its impact on battery performance.

Milestones

1. Charge rate ≥ 0.5C. (Q1, FY 2021; Completed)
2. Pouch cell capacity ≥ 200 mAh. (Q2, FY 2021; Completed)
3. SSE CCD ≥ 18 mA/cm^2. (Q3, FY 2021; Completed)
4. SSE stability ≥ 0-4.5 V. (Q4, FY 2021; Completed)
5. SSE film ≥ 1 m and ≤ 60 µm. (Q4, FY 2021; Completed)
6. SSE Li-ion conductivity ≥ 5 mS/cm. (Q4, FY 2021; Completed)
7. Cycle life ≥ 500. (Q4, FY 2021; Completed)

Progress Report

SSE Stability at 4.5 V

Solid Power has developed multifunctional SE materials with high conductivity and stability. The high-voltage stability of the new electrolyte was evaluated in a Li-NMC full cell. An LPS electrolyte was also tested as a baseline. When tested at 2.5-4.5 V, C/10 – C/10, and 45°C, the new electrolyte cell is stable after 10 cycles, while the BE cell shows 20% resistance growth. The new electrolyte cell also shows 60% lower cell resistance than the baseline cell. Figure 41 shows the cell resistance growth comparison of the two electrolytes.

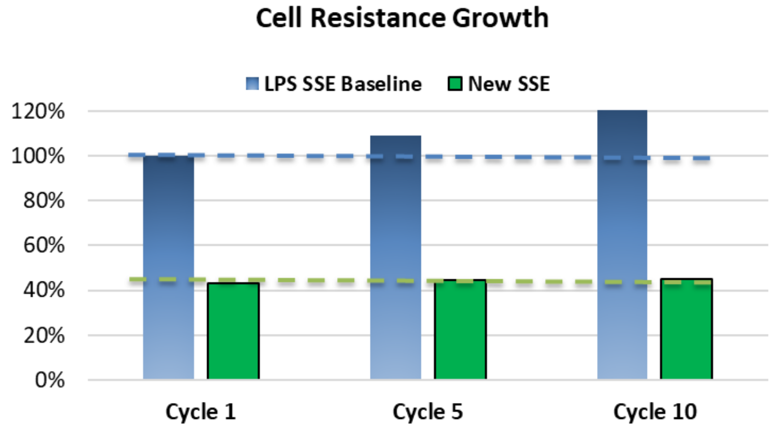

Figure 41. Li-NMC full-cell resistance growth: new multifunctional electrolyte versus baseline electrolyte. The cells were tested at 2.5-4.5 V, C/10 – C/10, and 45°C. The 0-4.5 V stability of the new electrolyte is demonstrated.

SSE Film Fabrication

The SSE separator coating process has been developed at pilot scale. A separator slurry was prepared by mixing the SSE powder, a binder, and a solvent by using a planetary mixer. The slurry was then cast on a carrier film on a slot-die coater. The separator length and thickness target (≥ 1 m and ≤ 60 µm) has been met this quarter. Figure 42 shows images of the separator film on the coater and the separator inside a lithium cell.

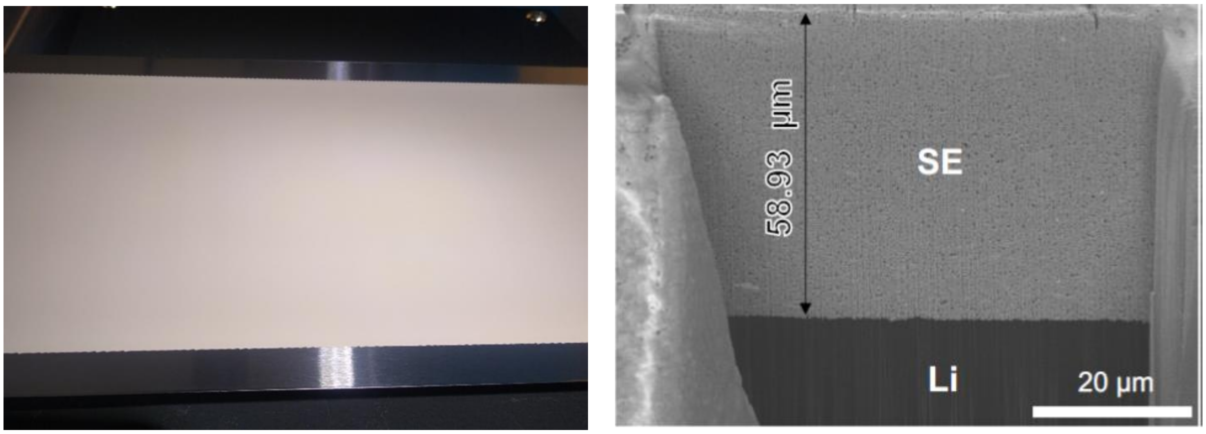

Figure 42. Solid-state electrolyte separator film: (left) on the coater and (right) inside a Li-metal cell.

Full-Cell Cycle Life Demonstration

The cycle life of the electrolyte was evaluated in a Li-NMC pouch cell. When tested at 2.8-4.2 V, C/5 – C/5, and ambient temperature (~ 25°C), the pouch cell showed 90% capacity retention after 500 cycles (in Figure 43). The cycle life of 500 has passed the *Go/No-Go Decision* point. It should be noted that the capacity fluctuation was due to the ambient temperature change.

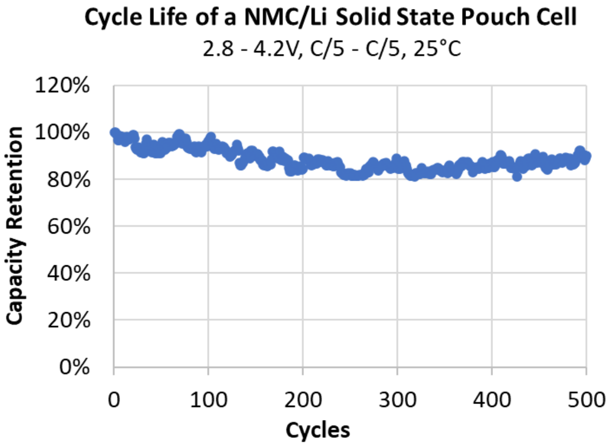

Figure 43. Cycle life of an NMC/Li-metal solid-state pouch cell with the multifunctional solid-state electrolyte at 25°C.

Patents/Publications/Presentations

The project has no patents, publications, or presentations to report this quarter.

Task 1.12 – Developing Materials for High-Energy-Density Solid-State Lithium-Sulfur Batteries (Donghai Wang, Pennsylvania State University)

Project Objective. The project objectives are to develop materials involving advanced S-C composite materials, solid additives, and sulfide-based SSEs, and to acquire knowledge for Li-S ASSBs. Li-S ASSBs with large areal sulfur loading (≥ 5 mg cm^{-2}) and high sulfur content (≥ 50 wt% in cathode), pairing with lithium or lithium alloy anode, will deliver a high initial specific capacity of over 1200 mAh g^{-1} at high charge/discharge rate (> 0.3 C) for 500 cycles with over 80% capacity retention.

Project Impact. This project aims to develop new materials to enable Li-S ASSBs with high energy density, excellent cycling stability, and good rate performance, and thus to build knowledge for fabrication of prototype Li-S ASSBs. Specifically, the developed new materials will greatly increase the specific capacity of sulfur and sulfur utilization at high areal sulfur loading, alleviate the interfacial problem between S-C composite and SSE within sulfur cathode, boost Li-ion conductivity, and improve moisture stability of glass and glass-ceramic sulfide-based SSE. Meeting the technical targets will potentially promote development of high-energy-density Li-S ASSBs and their practical application in EVs and plug-in hybrid EVs (PHEVs) and will also reduce petroleum consumption in the transportation sector by helping battery-powered vehicles become more accepted by consumers as a reliable source of transportation.

Approach. The project goal will be accomplished through developing new materials, together with in-depth characterization of sulfur cathode. Specifically, approaches to realize the project objectives include the following: (1) development of new carbon material with unique structure, high surface area, and large pore volume; (2) development of new S-C and S-C-M_xS_y materials (M = Li, Co, Ti, Mo, etc.) to facilitate electron/ion transport; (3) development of novel additives to tune interfacial behavior among components in the cathode; (4) development and optimization of new SSE through cation and anion doping with superior properties such as high ionic conductivity, good moisture, and stability; and (5) diagnostics, characterization, and cell tests on the developed new material or advanced sulfur cathode.

Out-Year Goals. The out-year goals are as follows: (1) develop new S-C-M_xS_y hybrid materials, new cathode additives, and anion-doped SEs (ionic conductivity above 3 mS cm^{-1} at room temperature), and (2) conduct characterization and performance tests on both material and electrode levels. The *Go/No-Go Decision* will be demonstration of all-solid-state sulfur cathode with over 1000 mAh g^{-1} discharge capacity at 0.1 C discharge rate and 50 wt% sulfur content for 100 cycles at room temperature.

Collaborations. There are no active collaborations.

Milestones

1. Demonstrate sulfur cathode with > 1000 mAh g^{-1} capacity at 0.2 C at 60°C. (Q1, FY 2021; Completed)
2. Demonstrate new anion-doped electrolyte with ionic conductivity > 2 mS cm^{-1} at 25°C, and sulfur cathode with > 1000 mAh g^{-1} using additives (≤ 3 wt%) at 0.3 C for 50 cycles. (Q2, FY 2021; Completed)
3. Demonstrate sulfur cathode with > 1000 mAh g^{-1} at 0.3 C for 50 cycles at 60°C using hybrid conductive materials. (Q3, FY 2021; Completed)
4. Demonstrate sulfur cathode with > 1000 mAh g^{-1} at 0.1 C for 100 cycles at room temperature, and anion-doped SEs with ionic conductivity > 3 mS cm^{-1} at 25°C. (Q4, FY 2021; Completed)

Progress Report

New Sulfur Cathode for All-Solid-State Li-S Batteries (ASSLSBs)

This quarter, the team has been developing an advanced sulfur cathode that can cycle under 0.1 C for more than 100 cycles at room temperature with high sulfur utilization. Their previous findings revealed that an efficient ionic and electronic network within sulfur cathodes plays a vital role in their electrochemical performance. Thus, they prepared a new sulfur cathode with 50 wt% sulfur content. This sulfur cathode composite was synthesized by the high-energy ball-milling method, which provides superior uniform distributions of active material and conductive additives. The cycling performance of the new sulfur cathode was electrochemically activated under 0.05 A g^{-1} (based on the weight of the whole sulfur cathode) for the first three cycles and then subsequently cycled at 0.1 A g^{-1} (= 0.12 C) between 0.5 and 2.5 V at room temperature (Figure 44). During the activation cycles, the specific discharge capacity (based on the weight of sulfur) could reach above 1200 mAh g^{-1}. After the 3rd cycle, the capacity initially dropped to ~ 1100 mAh g^{-1} due to the higher current rate. It soon recovered to ~ 1200 mAh g^{-1} in a few cycles and maintained stably for more than 100 cycles. It is worth noting that the performance meets the target of the milestone for this quarter and the corresponding *Go/No Go Decision*.

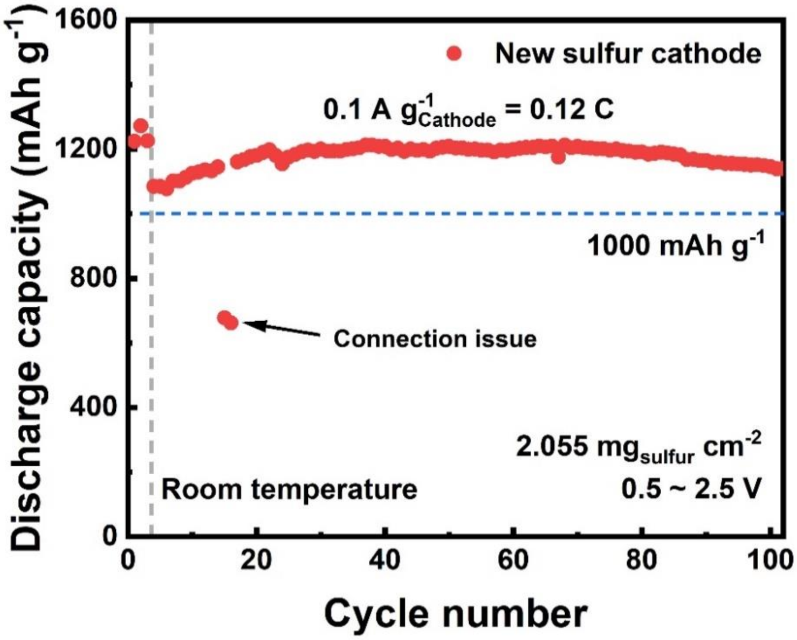

Figure 44. Cycling performance of the new sulfur cathode under 0.1 A g^{-1} (= 0.12 C) and 0.5 to 2.5 V at room temperature. The discharge capacity is based on the weight of sulfur.

Anion-Doped SSE

Besides developing the advanced sulfur cathode composite, the team developed a new anion-doped solid-state electrolyte using the liquid-phase method. The new anion-doped glass-ceramic SSE was successfully synthesized by optimizing compositions, synthesis conditions, annealing temperature, and annealing time. The ionic conductivity of the new SE was measured at different temperatures, namely, 25°C, 40°C, 60°C, 80°C, and 100°C. The Arrhenius plot and Nyquist impedance plot are depicted in Figure 45. The new SSE delivered a high ionic conductivity of 6.09 mS cm^{-1} at 25°C with a low activation energy of 0.222 eV. This superior ionic conductivity of the new anion-doped SSE fulfills the milestone requirement this quarter.

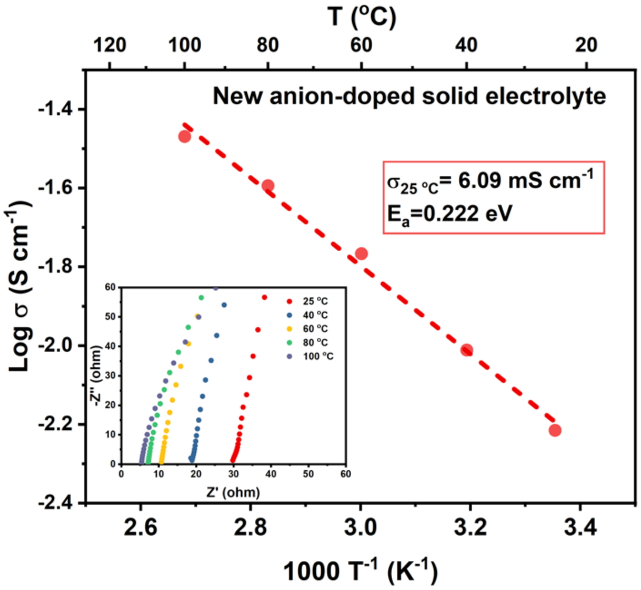

Figure 45. The Arrhenius plot and Nyquist impedance plot of the new anion-doped solid-state electrolyte.

Patents/Publications/Presentations

The project has no patents, publications, or presentations to report this quarter.

TASK 2 – DIAGNOSTICS

Team Lead: Guoying Chen, Lawrence Berkeley National Laboratory

Summary and Highlights

To meet the goals of the VTO programs on next-generation EVs, low-cost and abuse-tolerant batteries with higher energy density, higher power density, better safety, and longer lifetimes are needed. In pursuit of these goals, high cell operating voltages and demanding cycling conditions are used, which leads to unprecedented chemical and mechanical instabilities in cell components. Successful implementation of promising electrode materials (such as silicon anode and high-voltage cathodes) and new cell chemistry (such as high-energy Li-metal cells combined with SSEs) requires better understanding of fundamental processes, especially those at the interface/interphase of both anode and cathode. Identifying and understanding structure-property-electrochemical performance relationships in materials and various failure modes in cell chemistry are therefore more pressing than ever, not only in guiding battery development activities but also the scale-up efforts needed for commercialization.

Task 2 takes on these challenges by combining model systems, *ex situ*, *in situ*, and *operando* approaches, with an array of state-of-the-art analytical and computational tools. Numerous subtasks are tackling the chemical processes and reactions at the electrode/electrolyte interfaces in Li-metal batteries. Researchers at LBNL use surface- and bulk-sensitive techniques, including FTIR, attenuated total reflectance (ATR)-FTIR, near-field infrared (IR) and Raman spectroscopy/microscopy, and scanning probe microscopy (SPM) to characterize changes in materials and the physicochemical phenomena occurring at the interface of Li-metal electrode. GM is developing *in situ* diagnostic techniques, including atomic force microscopy (AFM), nano-indentor, dilatometer, and stress-sensor, to be combined with atomic/continuum modeling schemes to investigate the coupled mechanical/chemical degradation of the SEI layer as well as the microstructural evolution at the interface/interphase of Li-metal anode. ANL aims to develop high-conductivity ceramic electrolytes through cation doping and to identify mechanistic barriers that limit chemical, mechanical, and electrochemical durability of solid/solid interfaces. University of Houston (UH) is developing multidimensional diagnostic tools, including FIB-SEM, time-of-flight secondary ion mass spectrometry (TOF-SIMS), and in-SEM nanoindentation, to probe structural, chemical, and mechanical evolution at the interfaces of SSLBs. At LBNL, model systems of electrode, SSE, and their interfaces with well-defined physical attributes are being developed and used for advanced diagnostic and mechanistic studies at both bulk and single particle levels. These controlled studies remove the ambiguity in correlating a material's physical properties and reaction mechanisms to its performance and stability, which is critical for further optimization. Subtasks at BNL and PNNL focus on the understanding of fading mechanisms in electrode materials, with the help of synchrotron-based X-ray techniques [diffraction and hard/soft X-ray absorption (XAS)] at BNL and high-resolution transmission electron microscopy (HRTEM) / STEM and related spectroscopy techniques at PNNL. The final subtask at Stanford/SLAC develops and utilizes an integrated X-ray characterization toolkit to investigate and generate insights on SSBs, by tracking the evolution of nanoscale chemistry as well as structure, microstructure, and transport properties. The diagnostics team not only produces a wealth of knowledge key to developing next-generation batteries, they also advance analytical techniques and instrumentation with a far-reaching effect on material and device development in various fields.

Highlights. The highlights for this quarter are as follows:

- The UH (Y. Yao) group developed an *operando* SEM observation platform suitable for investigation of morphological evolution and failure mechanisms at the electrolyte-electrode interface in solid-state micro-cells.
- The LBNL (G. Chen) group demonstrated stable cycling of all-solid-state Li-metal battery (ASSLMB) cells employing an NMC-811 cathode and a Li_3YCl_6 SSE for well over 100 cycles.

Task 2.1 – Characterization and Modeling of Lithium-Metal Batteries: Model-System Synthesis and Advanced Characterization

(Guoying Chen, Lawrence Berkeley National Laboratory)

Project Objective. This project will use a rational, non-empirical approach to design and develop SSE materials and interfaces for next-generation Li-metal batteries. Combining a suite of advanced diagnostic techniques with carefully prepared model-system samples, the project will perform systematic studies to achieve the following goals: (1) obtain understanding on the role of SSE grain and grain boundaries (GBs) on ion conduction and dendrite formation, (2) obtain fundamental knowledge on rate- and stability-limiting properties and processes in SSEs when used in Li-metal batteries, (3) investigate the reactivities between SSE and electrodes, and gain insights on the dynamic evolution of the interfaces, and (4) design and synthesize improved SSE materials and interfaces for safer and more stable high-energy Li-metal batteries.

Impact. The project will focus on fundamental understanding of SSE and relevant interfaces to enable its use in Li-metal batteries. Knowledge gathered from model-system-based studies will guide the design and engineering of advanced materials and interfaces. The use of the non-empirical, rational-design approach will develop high-energy battery systems with improved commercial viability.

Approach. The project will combine model-system synthesis and advanced diagnostic studies to investigate ion conduction and interfacial chemistry of SSE in Li-metal batteries. Single crystalline (SC), polycrystalline, and amorphous model SSE samples with various grain and GB properties will be synthesized. Model interfaces between the SSE and electrodes with controlled properties will also be developed. Both bulk-level and single-grain-level characterization will be performed. Global properties and performance of the samples will be established from the bulk analyses, while the single-grain-based studies will utilize time- and spatially-resolved analytical techniques to probe the intrinsic redox transformation processes and failure mechanisms under battery operating conditions.

Out-Year Goals. In the out-years, the project will deliver fundamental knowledge on the role of SSE microstructure in Li^+ conduction and lithium dendrite formation/propagation. Insights on performance-limiting physical properties and phase transition mechanisms as well as dynamic evolution of SSE/electrode interfaces will be obtained. Mitigating approaches, such as use of surface coating or “buffer layer” in stabilizing SSE/electrode interfaces, will be evaluated. Further, advanced SSE materials and interfaces for improved high-energy Li-metal batteries will be designed and synthesized.

Collaborations. This project collaborates with the following PIs: G. Ceder, K. Persson, M. Doeff, B. McCloskey, R. Kostecki, and R. Prasher (LBNL); W. Yang (Advanced Light Source, ALS); D. Nordlund and Y. Liu (Stanford Synchrotron Radiation Lightsource, SSRL); C. Wang (PNNL); and J. Nanda (Oak Ridge National Laboratory, ORNL).

`Milestones

1. Develop SSE/Li model interfaces for studying the reactivities and dendrite formation at the Li-metal anode interface. (Q1, FY 2021; Completed)
2. Synthesize SSE model samples and model interfaces for studying reactivities and dendrite formation at Li-metal anode. (Q2, FY 2021; Completed)
3. Advance the diagnostic studies of SSE/Li-metal anode interfaces. (Q3, FY 2021; Completed)
4. Obtain mechanistic understanding and deliver design strategies to mitigate reactivities at SSE/Li anode interface. (Q4, FY 2021; Completed)

Progress Report

Previous theory work has shown that LYC SE can react with Li-metal anode to form LiCl, Y_2Cl_3, and/or Y, leading to unstable halide SE/anode interface in ASSB cells. However, the kinetics of these reactions and their implications on cycling stability are unclear. This quarter, the team investigated changes at the interface of LYC and lithium anode after prolonged cycling. ASSB cells with NMC-811 – LYC|LYC|Li-In were assembled and cycled between 3.0 V and 4.3 V (V versus Li^+/Li). To eliminate intergranular cracking associated with volume expansion/contraction of conventional NMC secondary particles, SC NMC-811 was used in this study. Composite cathodes were prepared by combining SC NMC-811, LYC, and carbon in a weight ratio of either 80:20:0 (without carbon) or 57:40.5:2.5 (with 2.5 wt% carbon). Figure 46 compares electrochemical performance of both cells cycled at 0.2 C. The 1st-cycle voltage profiles (Figure 46a-b) show large irreversible capacity loss, indicating side reactions on initial charge and discharge. Reversibility drastically improved in the following cycle, with both cells achieving excellent CE of ~ 99% over 100 cycles. Figure 46c-d further compares discharge capacity as a function of cycle number. While the cell without carbon delivered ~ 140 mAh/g, a discharge capacity of ~ 170 mAh/g was obtained on the cell with 2.5 wt% carbon. The results show the positive effect of introducing carbon on cathode active material utilization, demonstrating the importance of better connected electronic pathways and improved conductivities in ASSB performance.

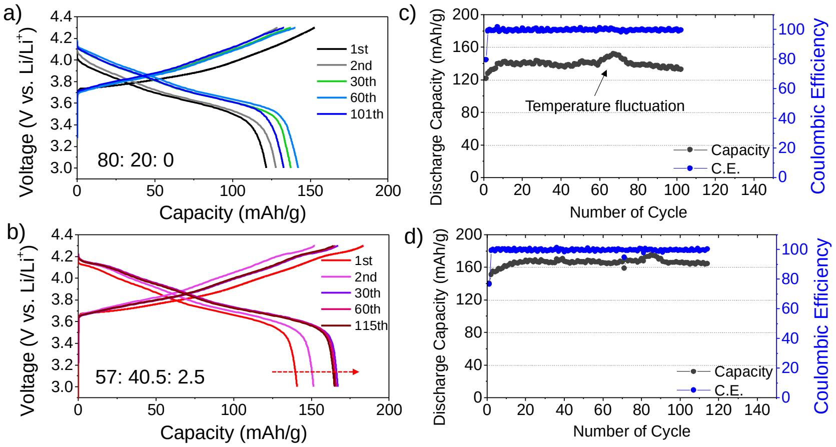

Figure 46. Charge and discharge voltage profiles (a-b), discharge capacity retention and Coulombic efficiency (c-d) of all-solid-state battery cells with a cathode composite consisting of SC-NMC-811, LYC, and carbon in an 80:20:0 weight ratio (a/c) and 57:40.5:2.5 weight ratio (b/d).

EIS was used to monitor impedance evolution in the cell with the carbon-containing cathode composite. Data were collected at the charged state of the indicated cycle number, each after 2 hours of rest at the OCV (Figure 47a). There is a small impedance increase during the initial cycles; however, the cell largely stabilizes on further cycling, suggesting possible formation of passivation layer(s) at the SE/electrode interfaces. Here, the team compares the SEM cross-sectional images collected at LYC/Li-In anode interface before and after cycling (Figure 46b-d). The pristine interface (Figure 46b) shows a clean boundary between LYC and Li-In anode. After 115 cycles, a distinct interlayer with a thickness of ~ 3-5 µm is clearly seen between the separator and the anode. The chemical nature and its dynamic evolution, as well as the role of the interlayer in ASSB cycling, will be further investigated.

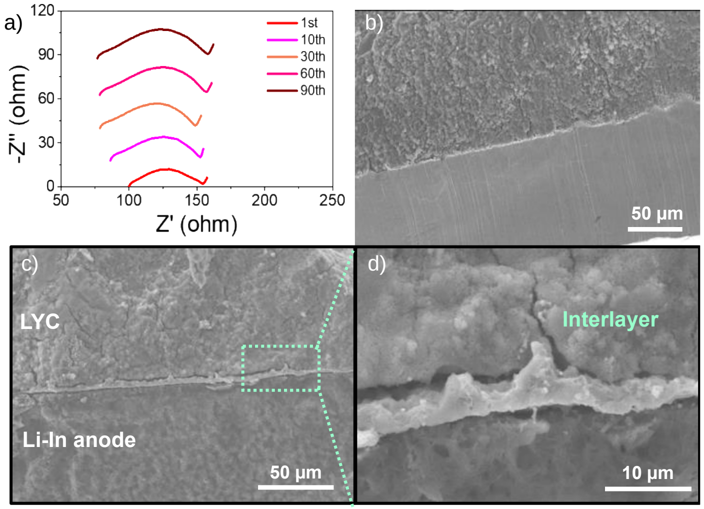

Figure 47. (a) Nyquist plots from the electrochemical impedance spectroscopy measurement of an all-solid-state battery cell with the cathode containing 2.5 wt% carbon. (b-d) Cross-sectional scanning electron microscopy images collected at the LYC/Li-In anode interface of the cell before (b) and after (c/d) cycling.

Patents/Publications/Presentations

Patent

- Kim, S., Y. Lu, and G. Chen. "High-Energy and High-Power Composite Cathodes for All Solid-State Batteries." LBNL ROI 2021-176, September 2021.

Publication

- Chen, D., J. Zhang, Z. Jiang, C. Wei, J. Burns, L. Li, C. Wang, K. Persson, Y. Liu, and G. Chen. "Role of Fluorine in Chemomechanics of Cation-Disordered Rocksalt Cathodes." *Chemistry of Materials* 33, No. 17 (2021): 7028–7038. doi: 10.1021/acs.chemmater.1c02118.

Presentation

- 72nd Annual Meeting of the International Society of Electrochemistry, Virtual (August 2021): "Improving Stability of High-Energy Disordered Rocksalt Cathodes"; G. Chen. Invited.

Task 2.2 – Interfacial Processes – Diagnostics
(Robert Kostecki, Lawrence Berkeley National Laboratory)

Project Objective. The objective of the proposed research is to establish specific design rules toward the next generation of low-impedance Li-metal rechargeable batteries that are capable of performing 1000 deep discharge cycles at CE > 99.9% and suppressing lithium dendrite formation at high current densities (> 2 mA/cm^2). This project aims at the following: (1) establishing general rules between Li$^+$ transport properties in novel liquid/solid electrolytes, and (2) determining the mechanism of the SEI layer (re)formation. The other goal is development and application of far- and near-field optical probes and synchrotron-based advanced X-ray techniques to obtain insight into the mechanism of Li$^+$ transport and interfacial reactions in lithium/liquid model systems. Through an integrated synthesis, characterization, and electrochemistry effort, this project aims to develop a better understanding of lithium/LE interface so that rational decisions can be made as to their further development into commercially viable Li-metal cells.

Project Impact. Chemical instability and high impedance at the interface of Li-metal electrodes limits electrochemical performance of high-energy-density batteries. A better understanding of the underlying principles that govern these phenomena is inextricably linked with successful implementation of high-energy-density materials in Li-metal-based cells for PHEVs and EVs. New state-of-the-art techniques to identify, characterize, and monitor changes in materials structure and composition that take place during battery operation and/or storage will be developed and made available to the Program participants. The proposed work constitutes an integral part of the concerted effort within the BMR Program, and it supports development of new electrode materials for high-energy, Li-metal-based rechargeable cells.

Approach. The pristine and cycled composite electrode and model thin-film electrodes will be probed using various surface- and bulk-sensitive techniques, including FTIR, ATR – FTIR, near-field IR and Raman spectroscopy/microscopy, and SPM to identify and characterize changes in materials structure and composition. Novel *in situ / ex situ* far- and near-field optical multi-functional probes in combination with standard electrochemical and analytical techniques are developed to unveil the structure and reactivity at interfaces and interphases that determine electrochemical performance and failure modes of materials.

Out-Year Goals. In the out-years, the project aims to achieve the following: (1) understand factors that control performance and degradation processes, (2) unveil structure and reactivity at hidden or buried interfaces and interphases that determine electrochemical performance and failure modes, and (3) propose effective remedies to address inadequate Li-metal-based battery calendar/cycle lifetimes for PHEV and EV applications.

Collaborations. The diagnostic studies will be carried out in sync with other diagnosticians (G. Chen, B. McCloskey, R. Prasher, and L-W. Wang) and theory and computational scientists (G. Ceder and K. Persson).

Milestones

1. Acquire near-field spectra from Gr/SEI. (Q1, FY 2021; Completed)
2. Determine composition of SEI on lithium via *in situ* near-field FTIR measurements. (Q2, FY 2021; Completed)
3. Complete preliminary near-field FTIR and XPS investigations of surface reactivity of lithium in LE and SE. (Q3, FY 2021; Completed)
4. Develop a valid mechanism for non-uniform current distribution on lithium/electrolyte interface. (Q4, FY 2021; Completed)

Progress Report

This quarter, the team has investigated non-uniform lithium plating on Gr electrodes at the solid polymer electrolyte (SPE) interface using *in situ* near-field FTIR nano-spectroscopy (nano-FTIR). Monolayer Gr is atomically thin and transparent for infrared light, which allows recording nano-FTIR signals from the subsurface of Gr. With the resolution, provided by nano-FTIR, the team was able to observe two distinct regions of lithium plated on a Gr electrode. They found that structural properties of the polymer (chain orientation) and chemical composition (polymer/salt ratio) directly influence local Li$^+$ transport properties, which then give rise to inhomogeneous SEI formation on a congruent spatial scale—triggering and continuously aggravating non-uniform current distribution and non-uniform lithium plating and at the electrode/SEI interphase in following cycles. This completes efforts toward this quarter's milestone.

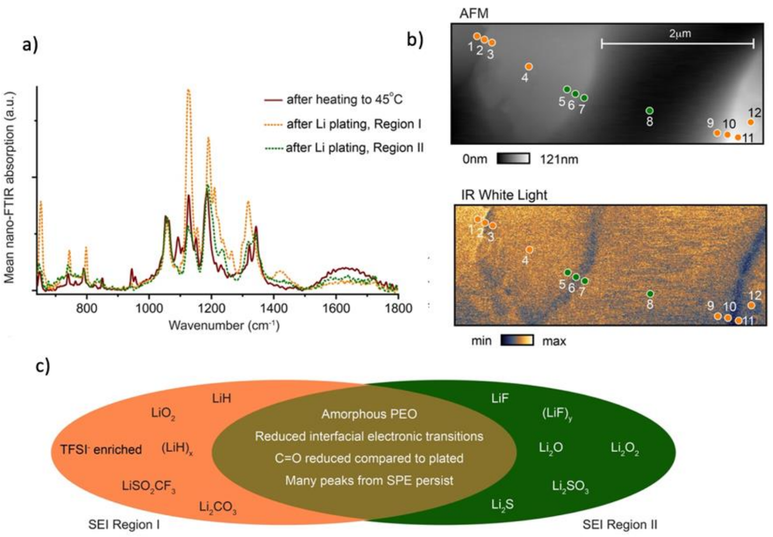

Figure 48. Characterization of the graphene-solid polymer electrolyte (SPE) interface after lithium plating. (a) Averaged nano-Fourier transform infrared (FTIR) absorption from two different regions of formed SEI after lithium plating. (b) Atomic force microscopy and infrared white light images of the analyzed graphene subsurface. (c) Venn diagram depicting key similarities and differences between the two predominate SEI regions on the graphene/Li electrode.

As for investigation of non-homogeneity at the LE interface, the team has optimized the *in situ* electrochemical cell that will allow performing *in situ* studies via nano-FTIR. They have addressed issues with the previous design, such as wetting of electrodes and more room for the AFM cantilever in nano-FTIR. The cell must allow having a Gr window to analyze subsurface interfaces. The proposed cell design and a digital photograph of machined parts are presented in Figure 48.

The 2-electrode electrochemical cell was machined from PEEK and is compatible with both LEs and SEs. A copper current collector can accommodate a Li-metal electrode, while a SS current collector is designed to accommodate LFP electrodes. The slurry of LFP will be drop casted and dried on a SS current collector. The choice of LFP as a cathode material is explained by the wide plateau of delithiation of LFP in GEN 2 electrolyte, which allows controlled plating of lithium without change of the cell potential in a 2-electrode cell configuration. Figure 48 shows electrochemical data obtained from the assembled electrochemical cell with Li-metal and copper electrodes in GEN 2 electrolyte. The CV shows two peaks corresponding to lithium plating (negative current) and lithium stripping (positive current). Further testing will be done using a LFP slurry drop casted onto a SS current collector.

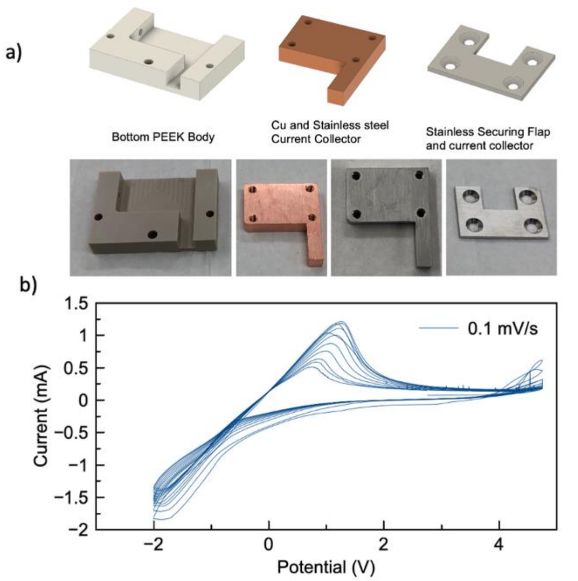

Figure 49. (a) 3D schematics and digital photographs of the cell designed for performing nano-Fourier transform infrared experiments at the liquid electrolytes – graphene interface. (b) Cyclic voltammetry of the assembled cell with Li-metal and copper electrodes in a GEN 2 electrolyte.

Patents/Publications/Presentations

The project has no patents, publications, or presentations to report this quarter.

Task 2.3 – Advanced *In Situ* Diagnostic Techniques for Battery Materials (Xiao-Qing Yang and Enyuan Hu, Brookhaven National Laboratory)

Project Objective. The primary objective of this project is to develop new advanced *in situ* material characterization techniques and to apply these techniques to support development of new cathode and anode materials with high energy and power density, low cost, good abuse tolerance, and long calendar and cycle life for beyond Li-ion battery systems to power PHEVs and battery electric vehicles (BEVs). The diagnostic studies will focus on issues relating to capacity retention, thermal stability, cycle life, and rate capability of beyond Li-ion battery systems.

Project Impact. The VTO Multi-Year Program Plan describes the goals for battery: "Specifically, lower-cost, abuse-tolerant batteries with higher energy density, higher power, better low-temperature operation, and longer lifetimes are needed for development of the next-generation of HEVs [hybrid electric vehicles], PHEVs, and EVs." The results of this project will be used for development of technologies that will significantly increase energy density and cycle life, and reduce cost. This will greatly accelerate deployment of EVs and reduce carbon emission associated with fossil fuel consumption.

Approach. This project will use a combination of synchrotron XRD and pair distribution function (x-PDF) and of neutron diffraction (ND) and pair distribution function (n-PDF); x-ray spectroscopies including hard/soft XAS, X-ray photon emission spectroscopy (PES); and imaging techniques including X-ray fluorescence (XRF) microscopy, transmission X-ray microscopy (TXM), and TEM.

Out-Year Goals. The out-year goals are to develop spectro-tomography, XRD, XAS, and PDF techniques, and to apply these techniques on Li-ion battery cathode, Na-ion battery cathode, and SSE.

Collaborations. The BNL team will work closely with material synthesis groups at ANL (Y. Shin and K. Amine) for the high-energy composite, at PNNL for the S-based cathode and Li-metal anode materials, and with ORNL on neutron scatterings. This project will also collaborate with industrial partners at GM and Johnson Controls, as well as with international collaborators.

Milestones

1. Complete three-dimensional (3D) spectro-tomography studies of Li-rich layered material $Li_{1.2}Ni_{0.13}Mn_{0.54}Co_{0.13}O_2$ at various states of charge (SOCs). (Q1, FY 2021; Completed)
2. Complete XRD, PDF analysis, and XAS studies of single-crystal sodium cathode material $Na_xNi_{0.76}Mn_{0.14}Co_{0.1}O_2$. (Q2, FY 2021; Completed)
3. Complete XRD/x-PDF/XAS studies of O3-type Na-cathode material $Na_xLi_{1.2-y}Mn_{0.54}Ni_{0.13}Co_{0.13}O_2$. (Q3, FY 2021; Completed)
4. Complete sulfur and phosphorus XAS studies of SSE $Li_{10}GeP_2S_{12}$ (LGPS) from various SOCs during the 1st cycle. (Q4, FY 2021; Completed)

Progress Report

This quarter's milestone was completed. BNL has been focused on developing new diagnostic techniques to study and improve performance of high-energy-density Li-ion batteries and Na-ion batteries, as well as SSBs. SSE is the key component of SSBs. Sulfur-based ceramic SSEs have spurred great interest due to their high ionic conductivity. Amongst them, ceramic sulfide SEs were reported with conductivities of 12-25 mS/cm, which is similar to or even higher than traditional LEs. Unfortunately, the intrinsic voltage window of ceramic sulfide SEs is narrow (1.7-2.1 V). However, previous works have reported that LGPS-based batteries can be stable up to 5 V. These seemingly contradictory results remain one of the most pressing issues facing the SE field. It has been reported that the stability window of ceramic sulfides can be controlled, and substantially widened, using mechanical constraints to induce metastabilities; understanding the mechanism of this will provide valuable information for developing high-voltage SSEs. An XAS technique was applied to this study in collaboration with X. Li at Harvard University. Figure 50g1-g2 shows the phosphorus and sulfur XAS peaks of pristine LGPS compared with those after CV scan up to 3.2 V and 9.8 V in liquid or solid-state batteries. In the conditions of no mechanical constraint in the liquid battery (denoted as 3.2 V-L), both phosphorus and sulfur show obvious peak shift toward the high energy and the shape change, indicating significant global oxidation reaction and rearrangement of local atomic environment in LGPS. In contrast, the phosphorus and sulfur peaks do not show obvious signs of oxidation in SSBs, as no peak shift is observed. However, it is noticeable that the shoulder intensity increases at 2470 eV and 2149 eV in phosphorus and sulfur spectra, respectively. An *ab initio* multiple scattering simulation of the phosphorus XAS peak from LGPS with various strain applied to the unit cell is shown in Figure 50h. A comparison between experiment and simulation suggests that the increase of shoulder intensity in XAS here might be caused by the negative strain, that is, the compression experienced by crystalline LGPS after CV scan and holding at high voltages. If the team connects the strain broadening in XRD with the shoulder intensity increase in XAS, and simultaneously considers that no obvious decomposition current was observed in the CV test up to 10 V, a physical picture emerges about the small local decomposition-induced compression to nearby crystalline LGPS.

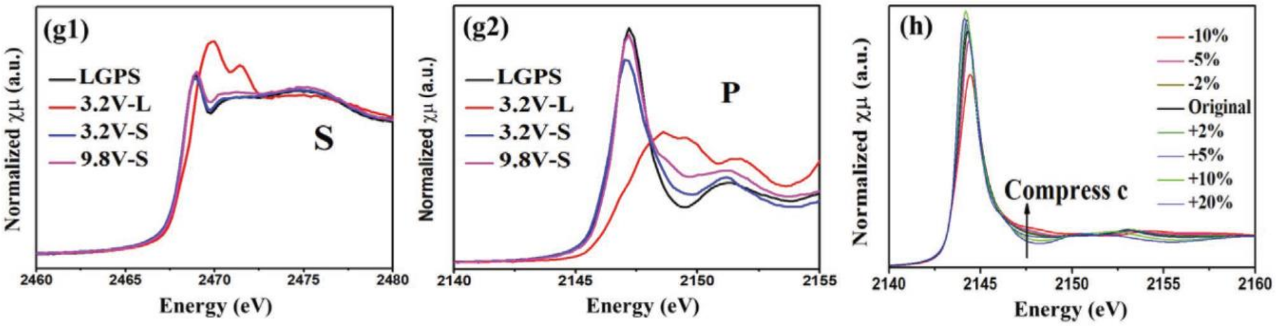

Figure 50. X-ray absorption spectroscopy (XAS) measurements of sulfur (g1) and phosphorus (g2) peaks from LGPS after cyclic voltammetry scans and holds at 3.2 V in liquid cell (3.2 V-L), 3.2 V in solid cell (3.2 V-S), and 9.8 V in solid cell (9.8 V -S), compared with pristine LGPS. (h) The simulation of phosphorus XAS peak changes by applying different strains in the *c*-direction of LGPS.

Patents/Publications/Presentations

Publication

- Wu, Z., S-M. Bak,* Z. Shadike, S. Yu, E. Hu, X. Xing, Y. Du, X-Q. Yang, H. Liu,* and P. Liu. "Understanding the Roles of the Electrode/Electrolyte Interface for Enabling Stable Li||Sulfurized Polyacrylonitrile Batteries." *ACS Applied Materials & Interfaces* 13 (2021): 31733–31740.

Task 2.4 – Probing Interfacial Processes Controlled Electrode Stability in Rechargeable Batteries (Chongmin Wang, Pacific Northwest National Laboratory)

Project Objective. The main objective is to explore interfacial phenomena in rechargeable Li-ion batteries of both SSE and LE configuration, to identify the critical parameters that control the stability of interface and electrodes as well as SE. The outcome will be establishing correlations between structural-chemical evolution of active components of batteries and their properties. These correlations will provide insight and guidance to battery materials development groups for developing high-performance battery materials.

Project Impact. The proposed characterization work focuses on atomic-level structural and chemical analysis and direct correlation with battery fading properties. The work can be directly used to guide design of electrode materials with tailored microstructure and chemistry for enhanced properties of increasing the energy density of Li-ion batteries and to accelerate market acceptance of EVs, especially for PHEVs as required by the EV Everywhere Grand Challenge.

Approach. The project will use integrated advanced microscopic and spectroscopic techniques, including *in situ* and *ex situ* STEM, environmental STEM, cryo-electron microscopy, and *in situ* liquid secondary ion mass spectrometry (SIMS) to directly probe the structural and chemical information during lithium deposition and stripping. Cryo-STEM with analytical tools, such as EDS and EELS, will be used to gain chemical and electronic structural information at the interface between lithium metal and electrolyte of both solid-state and liquid configuration, which will allow direct correlation between the morphology and chemistry. STEM – high-angle annular dark-field (HAADF) atomic-level imaging and EDS/EELS will be used to probe the interface and bulk lattice stability of cathode and SE in SSB. The work will be in close collaboration with the battery development group within the BMR and U. S.–Germany Collaboration on Energy Storage.

Out-Year-Goals. This project has the following out-year goals:

- Atomic-level multi-scale *ex situ* / *in situ* and *operando* STEM and cryo-STEM investigation on the fading mechanisms of energy-storage materials and devices in the system of both LE and SE; develop a fundamental understanding of electrochemical energy-storage processes and kinetics of electrodes.
- Develop new *in situ* and *ex situ* STEM capability for probing challenging questions related to energy storage technology for both SSE and LE energy storage systems.

Collaborations. This project collaborates with G. Chen (LBNL); J. Nanda (ORNL); Y. Yao (UH); K. Amine (ANL); D. Wang (PSU); A. Manthiram (University of Texas, or UT, Austin); W. Tong (LBNL); Y. Cui (Stanford); J. Zhang (PNNL); J. Liu (PNNL); W. Xu (PNNL); X. Jie (PNNL); D. Lu (PNNL); X. Xiao (GM); Y. S. Meng (UCSD); and M. S. Whittingham (State University of New York, Binghamton).

Milestones

1. Measure the electronic properties of SEI layer and identify dependence on the electrolyte chemistry. (Q1, FY 2021; Completed)
2. Identify the structure and chemistry of surface layer formed on lithium metal when it contacts with LE. (Q2, FY 2021; Completed)
3. Reveal the nature of reaction product and the fading mechanism of NMC cathode when in contact with SE. (Q3, FY 2021; Completed)
4. Identify the structural and chemical difference of SEI on lithium dendrite and spherical particle to gain the correlation between SEI and lithium morphology. (Q4, FY 2021; Completed)

Progress Report

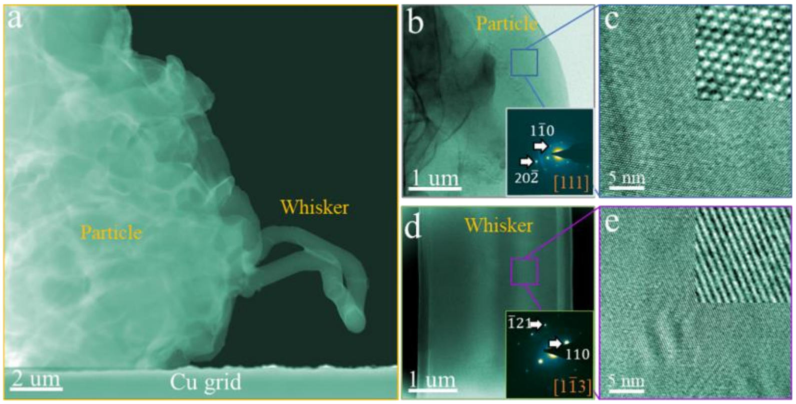

Figure 51. Microstructure of lithium deposits as particle and whisker formed in ether-based localized high-concentration electrolyte (LHCE). (a-e) Cryo – (scanning) transmission electron microscopy (STEM) images of lithium deposits formed in the ether-based LHCE: (a) high-angle annular dark-field – STEM image of lithium deposits with two typical morphologies; bright-field TEM image of (b) particle-shaped lithium deposit and (c) corresponding high-resolution TEM (HRTEM) image; and bright-field TEM image of (d) whisker-shaped lithium deposit and (e) corresponding HRTEM image. Insets: selected area electron diffraction patterns and enlarged area from lithium deposits.

A fundamental question for lithium deposition is delineation of the critical factors that control lithium morphology. Given the complexity of operation of electrochemical cells, it is often hard to isolate how a specific factor affects lithium morphology because an intended change of one parameter will, unavoidably, cause a change of other parameters. The team notices that, using LHCE, the deposited lithium is dominated by particle morphology, while simultaneously with the formation of a certain fraction of lithium whisker within the same coin cell (Figure 51). Detailed probing of the differences in the SEI layer on the lithium particle and the lithium whisker within the same coin cell will lead to correlation between lithium morphology and the structural and chemical features of the SEI layer.

In this study, the team probes the SEI that formed on lithium whisker and lithium particle in the same coin cell, to search the intrinsic correlation between the microstructure and chemistry of SEI layer with the morphology of lithium deposits. LHCE—composed of LiFSI salt, DME solvent, and 1,1,2,2-tetrafluoroethyl-2,2,3,3-tetrafluoropropyl ether (TTE) as the diluent at a molar ratio of 1:1.2:3— was used to deposit lithium at the current density of 0.1 mA cm^{-2}. The team uses cryogenic HRTEM, EDS, and EELS to characterize the detailed structure, chemical composition, and elemental distribution of SEI layers formed on the lithium particle and lithium whisker within the same coin cell using LHCE. These results provide insight for correlating features of the SEI layer with lithium morphology (Figure 52).

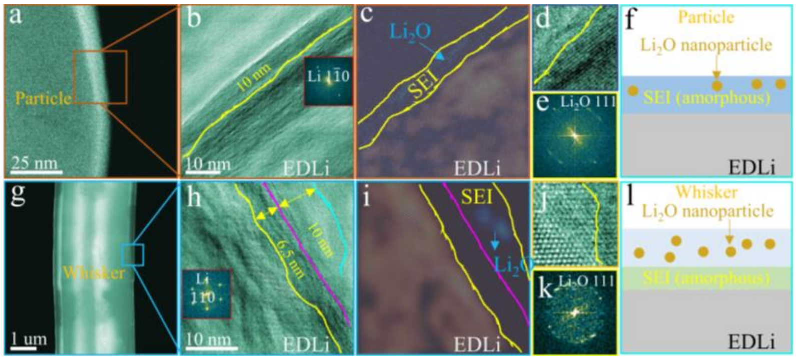

Figure 52. Nanostructures of SEIs formed on lithium particle and lithium whisker in ether-based localized high-concentration electrolyte. (a) Scanning transmission electron microscopy (STEM) – high-angle annular dark-field (HAADF) image of lithium particle. (b) Transmission electron microscopy (TEM) image shows the SEI layer. (c) Filtered image shows Li_2O in the SEI layer. (d) High-resolution TEM (HRTEM) image. (e) Fast Fourier transform (FFT) of (d), and (f) schematic drawing to illustrate SEI layer structure on lithium particle. (g) STEM-HAADF image of lithium whisker. (h) HRTEM image shows SEI layer on lithium whisker is a bilayer structure. (i) Filtered image shows spatial distribution of Li_2O. (j) HRTEM image. (k) FFT of (j), and (l) schematic drawings of the SEI layer on lithium whisker.

The team reveals that the SEI layer on the lithium particle is a mosaic structure, featuring an amorphous matrix with embedded Li_2O nanoparticles. Compositionally, the SEI on the lithium particle is enriched with sulfur, especially at the outer layer of the SEI. The SEI layer on lithium whisker displays a bilayer structure, featuring an inner amorphous layer that is dominated by oxygen and a mosaic outer layer with fluorine. Based on this structural and compositional information, it is further inferred that the diffusivity of lithium ion in SEI layer on lithium particle is higher than that in the lithium whisker. Those results establish the likely correlation between the SEI layer and the morphology of the lithium deposits.

Even the present work cannot lead to a conclusive result regarding the root cause as to why some lithium grows as particle, while other lithium grows as whisker within the same coin cell, the distinctive difference of SEI on lithium particle and lithium whisker from the same coin cell delineates insight on the correlation between features of the SEI layer with lithium morphology.

Patents/Publications/Presentations

Publications

- Jia, H., X. H. Zhang, Y. B. Xu, L. F. Zou, J-M. Ki, P. Y. Gao, M. H. Engelhard, Q. Y. Li, C. J. Niu, B. E. Matthews, T. L. Lemmon, J. T. Hu, C. M. Wang, and W. Xu. "Towards Practical Use of Cobalt-Free Lithium Ion Batteries by an Advanced Ether-Based Electrolyte." *ACS Applied Materials & Interfaces* 13 (2021): 44339–444347.
- Chae, S., Y. B. Xu, R. Yi, H-S. Lim, D. Velickovic, X. L. Li, C. M. Wang, and J-G. Zhang. "Micron-Sized Silicon/Carbon Composite Anode Synthesized by Impregnation of Pitch in Nano-Porous Silicon." *Advanced Materials* 33 (2021): 2103095.
- Han, X., S. Y. Wang, Y. B. Xu, G. M. Zhong, Y. Zhou, B. Liu, X. Y. Jiang, X. Wang, Y. Li, Z. Q. Zhang, S. Y. Chen, C. M. Wang, Y. Yang, W. Q. Zhang, J. L. Wang, J. Liu, and J. H. Yang. "All Solid Thick Oxide Cathodes Based on Low Temperature Sintering for High Energy Solid Batteries." *Energy & Environmental Science* 14, No. 9 (2021): 5044–5056.

Presentation

- Microscopy and Microanalysis Virtual Meeting (August 3, 2021): "Sweeping Potential Regulated Structural and Chemical Evolution of Solid-Electrolyte Interphase on Cu and Li as Revealed by Cryogenic Transmission Electron Microscopy"; Y. B. Xu, H. P. Wu, H. Jia, J-G. Zhang, W. Xu, and C. M. Wang.

Task 2.5 – Integrated Atomic-, Meso-, and Micro-Scale Diagnostics of Solid-State Batteries (Yi Cui, William Chueh, and Michael Toney; Stanford University / SLAC National Accelerator Laboratory)

Project Objective. By developing a characterization toolkit that tackles length scales (Å to mm), cell pressure (1-100 bars), and dynamics (during synthesis, fabrication, and cycling), the project aims to generate insights to engineer SSBs for deployment in EVs. This interdisciplinary team aims to achieve this objective by merging a broad range of characterization approaches as well as modeling to track the evolution of nanoscale chemistry and structure, microstructure, and transport.

Project Impact. The project will have an impact in several areas: (1) accelerate rational design of coatings and artificial SEIs in SSBs; (2) inhibit the root causes leading to cell shorting, and enable high current cycling; (3) accelerate design of cathode coating and composite electrode architectures; and (4) reduce degradation and variability during SSB manufacturing via composition and surface engineering.

Approach. The project has a multi-fold approach that will encompass the following: (1) resolve nanoscale structure and chemistry of SEIs via cryo-TEM; (2) track SE and lithium microstructure evolution in 3D via X-ray micro and diffraction tomography; (3) visualize nanoscale ionic and electronic transport at GBs via conducting AFM; (4) map current distribution in cathodes via scanning TXM; and (5) monitor nanoscale SE evolution with gas impurity via *in situ* environmental TEM.

Out-Year Goals. The project will develop an integrated characterization toolkit to characterize SSBs within a single cycle and over hundreds of cycles, spanning a wide range of relevant length scales.

Collaborations. Project collaborations include work with SSRL, ALS, and Advanced Photon Source (APS) synchrotron light sources.

Milestones

1. Demonstrate *operando* X-ray microscopy to track lithium reactivity with LPS SE at open circuit as a function of pressure. (Q1, FY 2021; Completed)
2. Achieve 20-nm resolution for electrochemical impedance AFM for recording ionic and electronic conductivity. (Q2, FY 2021; Completed)
3. Determine composition of reacted phase between LPS and NMC cathodes after 10 cycles using various microscopy methods. (Q3, FY 2021; Completed)
4. Demonstrate *operando* SEM and FIB to record sub-surface microstructure in LLZO during lithium plating. (Q4, FY 2021; Completed)

Progress Report

A comprehensive investigation into the short-circuiting mechanism in LPS during lithium plating and stripping has been completed. Electrochemical cycling, *operando* X-ray imaging, optical imaging and XRD were combined to elucidate the lithium plating and stripping mechanism in LPS. The team focused on three areas. First, they examine cycling parameters that correlate strongly with the CCD. Second, they investigate how the LPS morphology evolved during lithium plating and stripping. Finally, they investigate the calendar aging mechanism of Li/LPS.

On cell cycling, the team varied the amount of lithium plated/stripped as well as the current density. Through a careful correlation analysis, they show that current density does not uniquely correlate to the CCD. The amount of lithium plated per cycle, in addition, was an important contributor.

On the lithium plating mechanism, *operando* XRT revealed very few and extremely small cracks (microns). In most cells, only one small fracture was observed. This contrasts with many literature reports that showcase massive change in the SE microstructure during lithium plating. The team believes that the literature reflects the extent of pre-existing defects in the pellet, particularly, porosity. In the project's cells, they used high pressure during testing to eliminate the possibility of significant porosity. Electrical measurement after the short is consistent with the tomography results: the resistance of the short suggests a filament on the order of a few microns in diameter.

Finally, in terms of calendar aging, the team shows that short-circuiting can occur without current being passed, especially when the cell is subjected to large uniaxial pressure. *Operando* tomography showed that, during calendar aging, lithium reacts with LPS, which is visible microstructurally. They believe this reflects the intrinsic reactivity between lithium metal and LPS, and the reacted phase is likely Li_2S, which is consistent with XRD results and optical imaging.

Patents/Publications/Presentations

Presentations

- SLAC National Accelerator Laboratory, Scientific Advisory Committee, Virtual (September 15, 2021); W. C. Chueh.
- Meeting of the Electrochemical Society (ECS), Virtual (June 1, 2021); W. C. Chueh.

Task 2.6 – Investigating the Stability of Solid/Solid Interface
(Zonghai Chen, Argonne National Laboratory)

Project Objective. The project objective is to characterize the physical/chemical properties of species at the solid/solid interfaces and to fundamentally understand the critical issues that limit the mechanical, chemical, and electrochemical stability of solid/solid interfaces at the cathode and the anode.

Project Impact. The project will lead to several areas of impact: (1) to generate knowledge that supports the rational design of materials and process development; (2) to establish structure-properties relationship of the interface; and (3) to understand the formation mechanism of lithium dendrite and to predict potential solutions.

Approach. The project approach is multi-fold: (1) understanding the physics behind the transformation between the low conductivity phase and the high conductivity phase; (2) investigating the bonding strength of the CEI using model systems; and (3) developing electrolytes with high ionic conductivity and good bonding to cathodes through cation doping.

Out-Year Goals. The project has the following out-year goals:

- Developing synchrotron-based diagnosis tools to investigate physical/chemical properties of solid/solid interface.
- Identifying mechanistic barriers that limit the chemical/mechanical/electrochemical durability of solid/solid interface.
- Developing model systems to validate the failure mechanism of solid/solid interface.

Collaborations. The project works with ANL collaborators A. Ngo, L. A. Curtiss, V. Srinivasan, Y. Ren, J. Libera, and Y. Z. Liu, and with BNL collaborators F. Wang and X. H. Xiao.

Milestones

1. *In situ* electron microscopic characterization of the dendrite formation on LLZO. (Q1, FY 2021; Completed)
2. Investigation of electronic conducting path in LLZO pellet. (Q2, FY 2021; Completed)
3. Investigation of the mechanical stability of cathode/LLZO interface using model system. (Q3, FY 2021; Completed)
4. Microscopic study of the mechanical stability of cathode/LLZO interface. (Q4, FY 2021; Completed)

Progress Report

Last quarter, *ex situ* SEM was deployed to observe the morphological change of NMC cathode materials after cycling. After electrochemical testing in coin cells, the NMC particles were harvested from the cycled electrode, and *ex situ* SEM experiments revealed severe cracks inside the NMC particles. This quarter, the team has conducted an *in situ* SEM experiment to confirm their observation in the *ex situ* experiment.

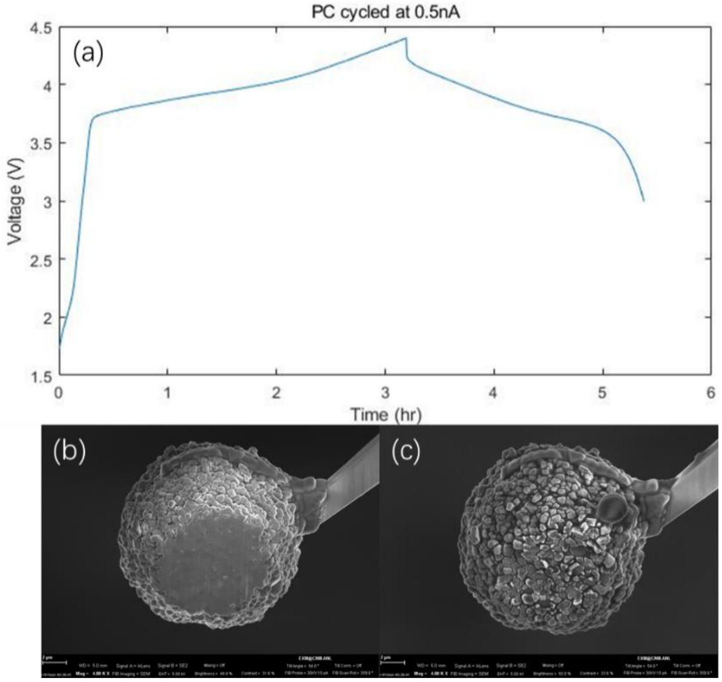

Figure 53. (a) Voltage profile of a single NMC particle being charged/ discharged with a constant current of 0.5 nA. (b) Scanning electron microscopy (SEM) image of single particle electrode (a corner of the particle was cut off to show interconnection among primary particles). (c) SEM image of single particle electrode after one charge/discharge cycle, clearly showing cracks at the boundary between primary particles.

To conduct the single particle *in situ* SEM experiment, a NMC particle was physically attached to a tungsten tip by applying carbon coating between the NMC particle and the tungsten tip. At the same time, a FIB was utilized to remove a corner of the NMC particle to reveal interconnection among the primary particles. As shown in Figure 53b, the NMC particle is closely packed with primary particles, and the GBs among primary particles can be observed by SEM. A single particle battery was then assembled using lithium as the counter electrode, and an ionic LE was used. Figure 53a shows the voltage profile of the single particle battery when charged/ discharged with a constant current of 0.5 nA. The SEM image was taken on the single particle electrode after completing one charge/discharge cycle. A crack along the GB is clearly visible in Figure 53c. In this case, when LE was used, the crack between primary particle could be filled with LE so that the transport of Li^+ was not disrupted due to formation of cracks. However, in the case of a liquid-free SSB, the electrolyte is not able to diffuse into the cracks; such cracks can pose a significant challenge for maintaining functionality of the SSBs. Therefore, the team also investigated a single-crystal NMC cathode to minimize the amount of GB, hoping to alleviate the negative impact of cracking.

Figure 54a-b compares the morphology of single crystal and polycrystalline $LiNi_{0.6}Mn_{0.3}Co_{0.1}O_2$. It can be seen that the single crystal material has an average particle size of ~ 2 µm, which is much bigger than the size of primary particles in polycrystalline NMC (generally ~ 200 nm) and is smaller than the size of secondary particles of polycrystalline material (~ 10 µm, see Figure 53b). The size of the single crystal NMC is a compromise between the specific surface area and the length of diffusion pathway for Li^+ to get in and out of the single crystals. To get a clear idea on the interfacial stability of $LiNi_{0.6}Mn_{0.3}Co_{0.1}O_2$ cathodes, high-precision leakage current was measured for both materials. In this experiment, regular NMC/Li half cells were assembled. The cells were formatted at C/10 for 2 cycles between 3.0 V and 4.4 V for 2 cycles. After the formation cycles, the cells were charged at constant voltage to different potentials for 20 hours, and the steady leakage was measured at each working potential. In principle, the measured steady leakage current is the rate of electron transfer rection at the CEI, which is a quantitative indicator of interfacial stability. Figure 54c shows that the steady leakage current increases with the working potential for both cathode materials. Meanwhile, the polycrystalline $LiNi_{0.6}Mn_{0.3}Co_{0.1}O_2$ shows a smaller leakage current than the single crystal counterpart.

However, at the potential higher than 4.3 V, the single crystal material shows better stability. In addition, the team also conducted *in situ* high-energy XRD using focused X-ray beam (see Figure 54d for a picture of the newly developed *in situ* electrochemical cell). Figure 54e-f compares the evolution of (003) for both materials during charging/discharging. After completion of the charge/discharge cycle, the cells were held at open-circuit for 4 hours to observe the relaxation of crystal structure of both cathode materials. Clearly, a slower Li^+ removal/insertion kinetics were observed for the single crystal material, probably due to its bigger particle size than the primary particles of polycrystalline counterpart. Even during the relaxation period, a continuous relaxation behavior was observed (see Figure 2f).

Although single crystal materials can be desired for SSBs from the perspective of preventing particle cracking, slow Li^+ kinetics can be an issue for high-rate applications. Further investigation for potential use of single crystal cathode for SSBs will be conducted in future work.

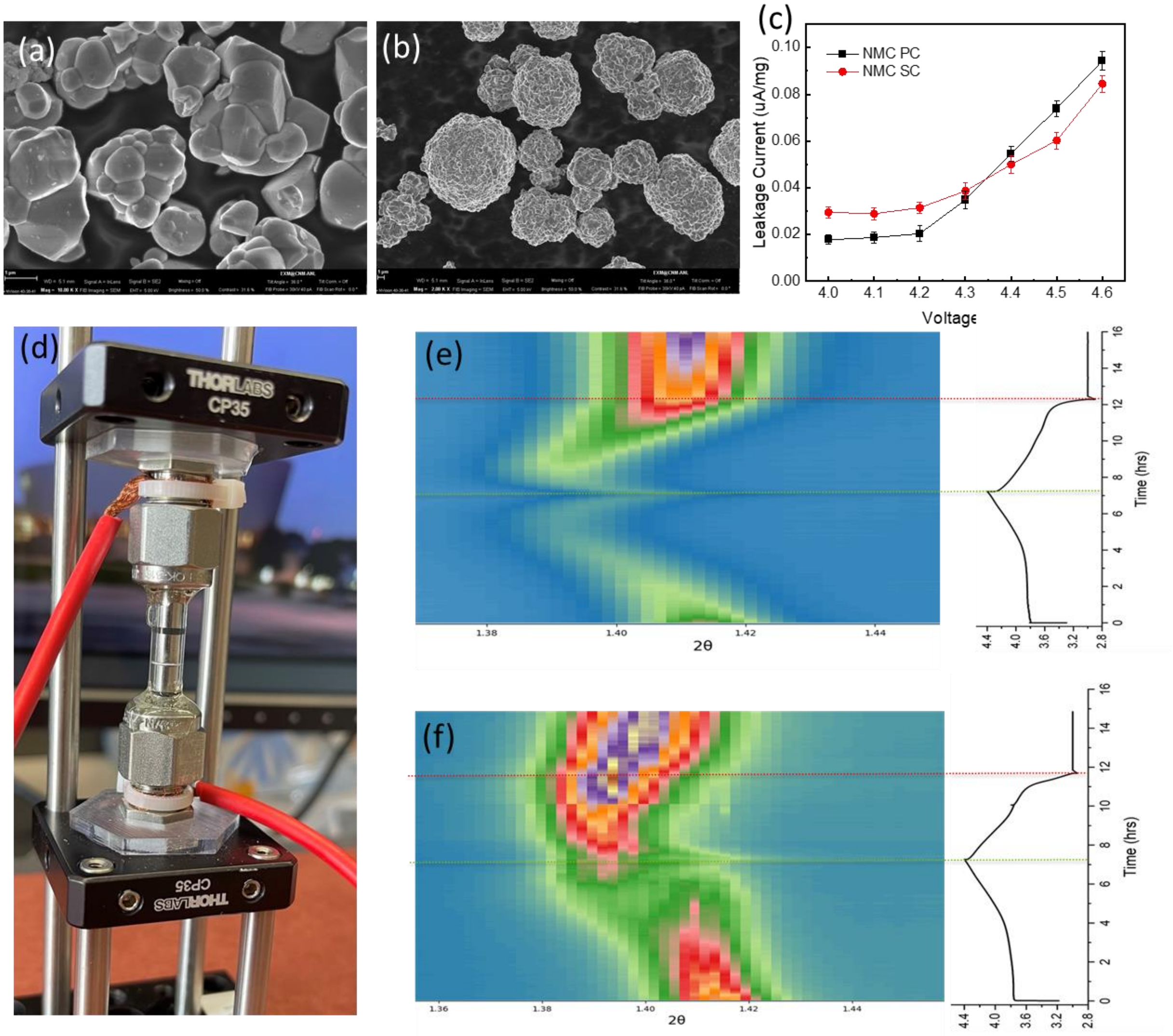

Figure 54. (a) Scanning electron microscopy (SEM) image of single crystal $LiNi_{0.6}Mn_{0.3}Co_{0.3}O_2$. (b) SEM image of polycrystalline $LiNi_{0.6}Mn_{0.3}Co_{0.1}O_2$. (c) Comparison of steady leakage current for single crystal and polycrystalline $LiNi_{0.6}Mn_{0.3}Co_{0.1}O_2$. (d) Photo of an *in situ* electrochemical cell to be used for focused beam X-ray diffraction. (e) Evolution of (003) peak for polycrystalline $LiNi_{0.6}Mn_{0.3}Ni_{0.1}O_2$ during charging/discharging. (f) Evolution of (003) peak for single crystal $LiNi_{0.6}Mn_{0.3}Ni_{0.1}O_2$ during charging/discharging.

Patents/Publications/Presentations

Publication

- Liang, Y. J., J. Y. Cai, D. H. Liu, and Z. H. Chen. "Surface Modification of Nickel-Rich Cathode Materials by Ionically Conductive Materials at Room Temperature." *Energy Technology* 9, No. 10 (2021): 2100422.

Task 2.7 – Fundamental Understanding of Interfacial Phenomena in Solid-State Batteries (Xingcheng Xiao, General Motors)

Project Objective. The project objective is to develop a comprehensive set of *in situ* diagnostic techniques combined with atomic/continuum modeling schemes to investigate and understand the coupled mechanical/chemical degradation associated with dynamic interfacial phenomena in SSBs. Specifically, *in situ* observations and characterizations of lithium plating-stripping processes, lithium dendrite formation, interphase formation, and the induced interfacial stresses, as well as the mechanical and electrochemical properties of interfaces and interphases, are paramount. The study will provide useful guidelines for optimizing cell structure design and engineering interfaces and interphases to enable SSBs.

Project Impact. The project will provide fundamental understanding of the dynamic interfacial phenomena and the coupled mechanical and chemical degradation. In addition, it will establish a critical guideline to design safe and durable SSBs with energy density > 500 wh/kg for EV applications.

Approach. The multi-scale *in situ* diagnostic tools, including AFM, nanoindentation, dilatometer, stress sensors, and pressure cells, will be used to investigate mechanical behavior and microstructure evolution at interface/interphase during lithium plating and stripping. The information (along with Li-ion transport properties and microstructure evolution obtained using the advanced spectroscopic ellipsometry, and *in situ* TEM) will be correlated with electrochemical performance toward high cycle efficiency and dendrite-free SSBs. The goal of this understanding is to develop strategies for surface and interface engineering, apply them to commercially available SEs (including powder, pellets, and foils), and assemble SSBs for further validation and optimization, eventually extending cycle life for EV application.

Out-Year Goals. The project seeks to develop SSB model systems to capture critical mechanical properties and probe the coupled mechanical-chemical degradation by further developing comprehensive *in situ* diagnostic tools. All results obtained from these *in situ* studies, combined with advanced *postmortem* analysis and modeling, will be correlated with the cycling stability of SSBs. The *in situ* tools developed will be applied to the following two periods to deeply understand the coupled mechanical and chemical degradation of interface/interphase.

Collaborations. The co-PIs involved in experiments and simulation will be as follows: B. W. Sheldon and Y. Qi (Brown University), Y-T. Cheng and A. Seo (University of Kentucky), and Q. Zhang (GM).

Milestones

1. Correlation between interfacial mechanical failure mechanisms and current density and pressure. (Q1, FY 2021; Completed)
2. Summary of the thickness, chemical bonding, and structural information of the interphases between anode and SE and between cathode and SE. (Q2, FY 2021; Completed)
3. Identified mechanisms of ionic transport through the interface/interphase. (Q3, FY 2021; Completed)
4. Multi-scale modeling framework to describe the coupled mechanical/chemical degradation. (Q4, FY 2021; Completed, made *Go Decision*)

Progress Report

Modeling of Impact of Alloying Elements on Li-Stripping Morphology. The Li-Mg alloy has been reported to show better rate capability and less severe dendrite issues than the pure lithium metal. These advantages make the Li-Mg alloy a good candidate for the anode in the SSBs, but the mechanism to explain the better performance of the Li-Mg alloy is not well established. Some groups assume that the Li-Mg framework is fixed and functions as the host (skeleton) for the plating of lithium atoms without considering the interdiffusion in the Li-Mg alloys.

This quarter, the project's developed density functional theory (DFT) – kinetic Monte Carlo (KMC) simulation scheme was employed to simulate the hopping of both lithium and magnesium atoms to understand the dynamics and stripping morphology in the Li-Mg alloy.

DFT calculations showed that the hopping barrier for lithium exchanging with a vacancy is only 0.055 eV, which is only slightly higher (~ 0.061 eV) with the presence of a nearby magnesium atom; the hopping barrier for magnesium to exchange with a vacancy is 0.102 eV. Although this is about twice that of a lithium hopping, it is still low enough for significant hopping events to occur at room temperature.

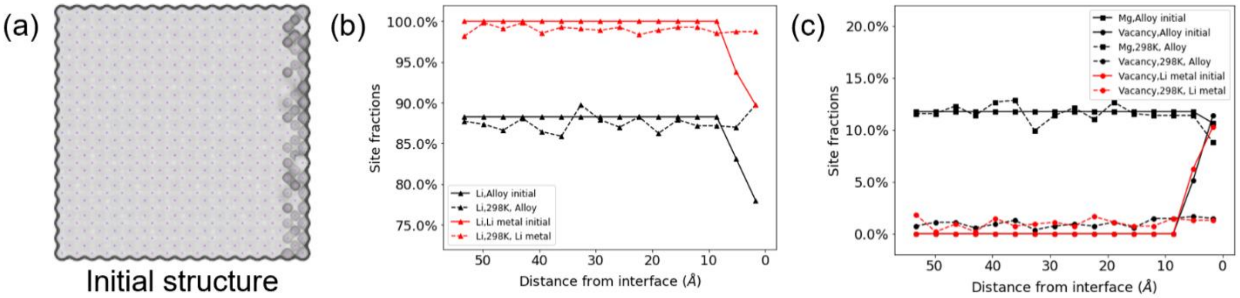

Figure 55. (a) The initial structure. (b) The site fractions of the lithium atoms (triangles). (c) Magnesium atoms (squares) and vacancies (circles) in the lithium metal (red curves) and the Li-Mg alloy (black curves). The solid lines represent the initial site fractions before the kinetic Monte Carlo (KMC) simulation, while the dashed lines stand for the site fractions after 10^5 steps of KMC simulations.

The KMC simulations therefore considered both lithium and magnesium hopping, with different hopping rates toward the lithium surface after stripping (as shown in Figure 55a). Figure 55b-c shows site fractions of lithium atoms, magnesium atoms, and vacancies in the pure lithium (red) and the Li-10%Mg alloy (black) in every two atomic layers parallel to the surface. In pure lithium, the site fraction is $f_{Li} + f_V = 1$; for Li-Mg alloy, it is $f_{Li} + f_{Mg} + f_V = 1$. In the initial structure of pure lithium metal (red curves in Figure 55b), 10% of the sites are vacancies near the interface (0-5 Å). After KMC simulation, both the site fractions of vacancies and lithium atoms became uniform. For the Li-Mg alloy, although the site fraction of vacancies also decreases to a uniform bulk value after KMC simulations, the site fractions of lithium and magnesium atoms near the surface change in opposite directions. For lithium atoms, the site fraction increases from 80% to ~ 90%, which is even higher than the site fraction of lithium atoms (88%) in the bulk. In contrast, the site fraction of magnesium atoms in the first two atomic layers decreases from 10% to 8% (Figure 55c, squared black lines). Therefore, the surface has a higher Li-to-Mg ratio near the surface after inter diffusion. The effective diffusion of lithium is faster toward the interface in the Li-Mg alloy. These phenomena may account for the better rate performance with the presence of the magnesium atoms (which can also diffuse) during the stripping process.

The next step is to develop an analytical model to get the concentration profiles of lithium, magnesium, and vacancies to extend the observations in the KMC model to larger length and time scales to compare with experimental observations. The interdiffusion in multicomponent Li-alloys should be a general phenomenon for Li-alloy anode with better rate performance.

Pressure Effect on the Interface between LLZO and Li-Metal Electrodes. The effect of external pressure on the interfacial resistance between Ta-doped LLZO SE and Li-metal electrodes was investigated using EIS. Prior to electrochemical cycling, a Li-metal symmetric pouch cell was placed in a homemade pressure device. An external pressure of 1.81 MPa was then applied for less than 1 minute, and an EIS measurement was taken to record the contact resistance while under this max pressure. The external pressure was then removed. After removing the pressure, EIS measurements were taken as a function of time to study the cell's response. An intriguing new observation was seen on removing the external pressure. The interfacial resistance continued to decrease even without the driving force of stack pressure. As seen in Figure 56, interfacial resistance decreases over the course of seven days after the initial pressure of 1.81 MPa is removed.

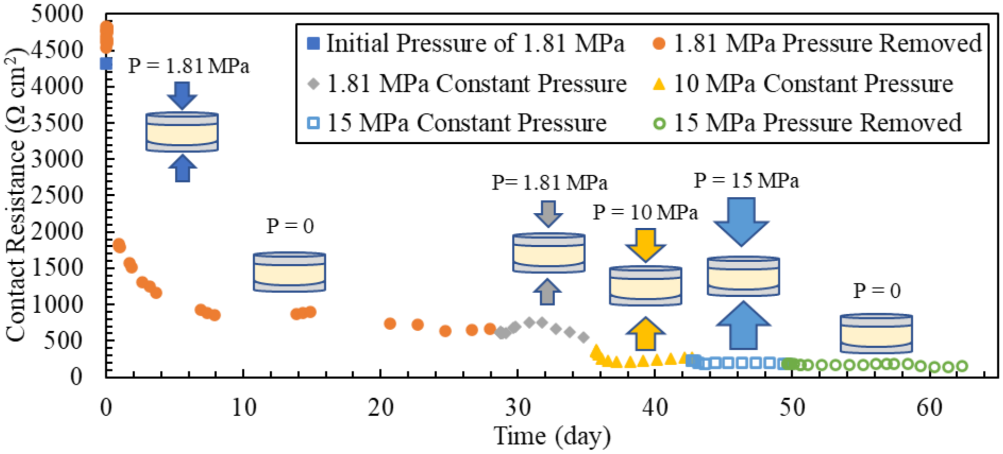

Figure 56. Contact resistance versus time plotted out under various pressure conditions. The initial pressure of 1.81 MPa was applied at time zero.

The team proposes that after the pressure is removed, the interfacial resistance decreases further as a result of the power-law creep of lithium metal, which increased its contact area with the LLZTO, as schematically shown in Figure 57. The dislocations form during the initial application of pressure and start to move once pressure is removed because of the back-stress in the dislocation substructures.[2] The dislocations find their way to the surface, reducing stress and creating more contact area with LLZTO. In addition to the driving force due to creep, growing the contact area between lithium and LLZTO is energetically favorable since LLZTO is lithiophilic.[3-5] The team proposes that the lithium metal continues to flow even after the pressure is removed to reduce surface energy of lithium metal and LLZTO, as well as the strain energy in the dislocation substructure. However, this proposal should be examined in the future.

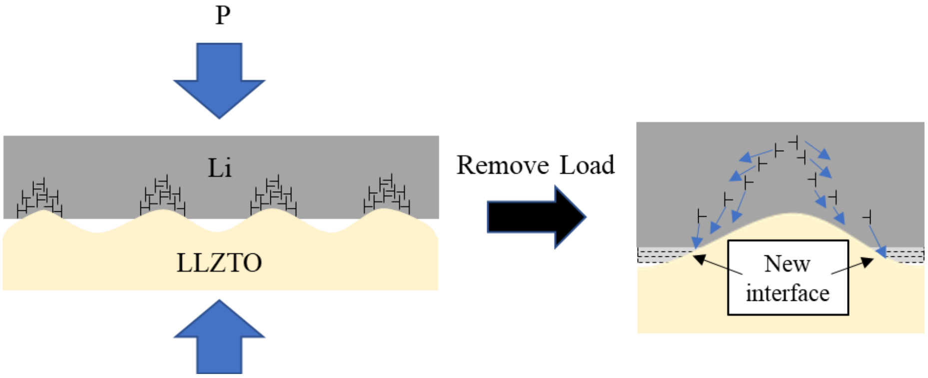

Figure 57. Conceptual diagrams depicting the cross section of lithium and LLZTO interface. The formation of dislocation substructures, and the movement of dislocations after removing the external pressure, cause an increase in the contact area with LLZTO.

Patents/Publications/Presentations

Publications

- Meyer, A., X. Xiao, M. Chen, A. Seo, and Y-T. Cheng. “A Power-Law Decrease in Interfacial Resistance between LLZO and Lithium Metal After Removing Stack Pressure.” *Journal of the Electrochemical Society* 168, No. 10 (2021): 100522.
- Feng, M., J. Pan, and Y. Qi. “Impact of Electronic Properties of Grain Boundaries on the Solid Electrolyte Interphases (SEIs) in Li-ion Batteries.” *Journal of Physical Chemistry C* 125, No. 29 (2021): 15821–15829.
- Yang, C-T., and Y. Qi. “Maintaining a Flat Li Surface during the Li Stripping Process via Interface Design.” *Chemistry of Materials* 33, No. 8 (2021): 2814–2823.

Presentations

- KLA Instruments Nanoindentation eUser Meeting, China and East Asia (September 15–16, 2021): “Understanding the Coupled Electrochemical-Mechanical Behavior of Materials for Improving the Performance and Durability of Lithium Ion Batteries”; Y-T. Cheng. See: http://iuniversity.kla.com/.
- WEKU (Public Radio) Interview, Richmond, Kentucky (August 12, 2021): “UK Materials Science Professor Sees Interest In Biden’s Electric Vehicle Goal.” Available online: https://www.weku.org/2021-08-12/uk-materials-science-professor-sees-interest-in-bidens-electric-vehicle-goal.

Task 2.8 – Multidimensional Diagnostics of the Interface Evolutions in Solid-State Lithium Batteries (Yan Yao, University of Houston)

Project Objective. The project objective is to develop a platform combining FIB-SEM tomography, TOF-SIMS, and in-SEM nanoindentation-based stiffness mapping for structural, chemical, and mechanical characterizations in SSLBs. Assessment of the influence of cell design and testing conditions (external pressure, current density, temperature) on the evolutions of interfaces will be performed.

Project Impact. The consolidated *in situ* structural–chemical–mechanical diagnostic platform established in this project will provide unprecedented insights into the failure mechanisms of SSLBs.

Approach. Space- and time-resolved structural, chemical, and mechanical characterizations of the cathode–electrolyte and anode–electrolyte interfaces will be performed on lithium ASSBs using FIB-SEM, TOF-SIMS, and in-SEM nanoindentation. Tasks include the following: (1) development of solid-state cell thin stacks and test-cell configurations that are suitable for *in situ* characterizations; (2) quantitative characterization and *in situ* tracking of interfacial voids formation within composite cathode and electrolyte layer; (3) identification and *in situ* tracking of the chemical composition, spatial distribution, and mechanical properties of electrolyte decomposition products at the lithium- and cathode-electrolyte interfaces; and (4) visualization, chemo-mechanical properties detection, and *in situ* tracking of lithium dendrites grown within the SE layer.

Out-Year Goals. In the out years, the project will develop thin-stack solid-state cells, micro-cells, in-SEM nanoindentation, and testing protocols. The correlation between structural evolution, electrolyte decomposition, and interfacial resistance increase will be investigated.

Collaborations. The UH team (Y. Yao, Z. Fan, and Y. Liang) works closely with the Rice University team (J. Lou and H. Guo).

Milestones

1. Cell optimization and electrochemical benchmarking. (Q2, FY 2021; Completed)
2. Nano-cell development. (Q4, FY 2021; Completed)
3. Multi-scale structural investigations. (Q1, FY 2022; In progress)
4. Composition and spatial distribution study. (Q2, FY 2022; In progress)
5. Selected region mechanical property probing. (Q3, FY 2022; In progress)

Progress Report

As a part of ongoing multiscale structural investigations, the team has improved their micro-cell setup to be ready for *operando* observations. Figure 58 shows the *operando* SEM observation of a solid-state micro-cell with NMC cathode, LPSCl electrolyte, lithium anode, and an interlayer of Ag–C to mitigate lithium dendrite formation. In this example, the team focused on the morphology evolution of the electrolyte–anode interface, which is highlighted in Figure 58a. Figure 58b–d shows the temporal evolution of the interface during the discharge of the cell. A representative structural feature in the lithium anode is highlighted in the bottom part of Figure 58b. As discharge proceeds, the feature is seen moving toward the interface, a clear indication of the bulk consumption of the lithium layer near the interface. No notable change is found in the electrolyte layer (the upper half of the images) and the interlayer in the middle. A gap forms between the Ag–C interlayer and lithium shortly after the start of the discharge (Figure 58c), and the morphology of the gap continuously changes throughout the discharge, ending in a totally different appearance in Figure 58d.

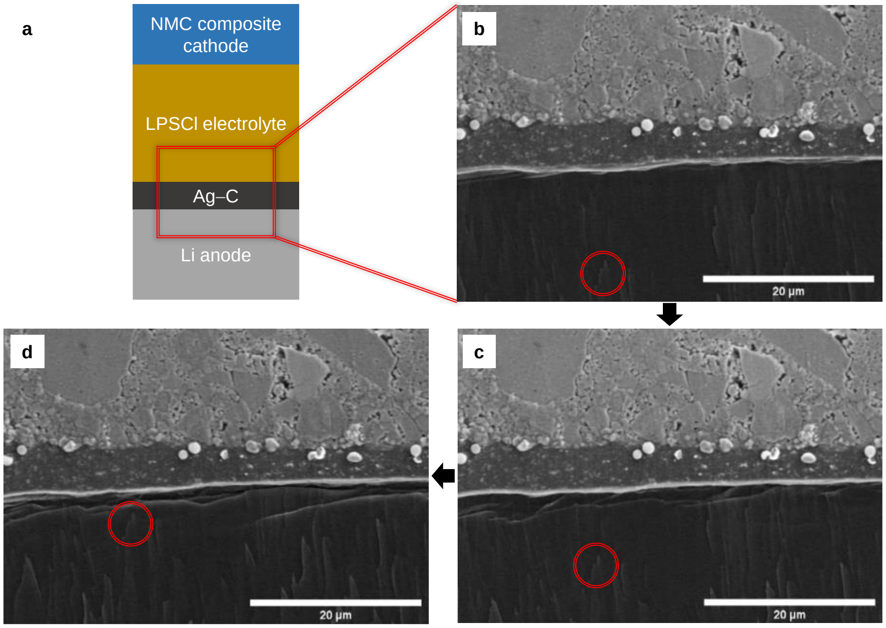

Figure 58. Structure (a) and *in operando* morphology characterization (b–d) of an NMC|LPSCl|Ag–C|Li micro-cell during discharge. The imaging area in (a) is highlighted with a rectangle. A moving structural feature in (b-d) is highlighted with a circle.

The team has also monitored morphology evolution during the charge process (Figure 59). In particular, they want to highlight an area where the contact between the electrolyte (the top, lighter layer in Figure 59a) and the interlayer (the middle, darker layer) is not intimate. A line crack quickly propagates into a gap as charging starts (Figure 59b). As charging continues, the gap becomes wider, and bright particles pop up from the interlayer throughout the thickness of the layer (Figure 59c). The bright particles are most likely lithium metal. Toward the end of the charge, lithium fibrils grow out of the further-widened gap (Figure 59d), at which point the cell short-circuits. It appears that the initial crack is what leads to the eventual cell failure.

This *operando* observation platform allows the team to probe the failure mechanism of solid-state cells from multiple angles. Clearly many potential factors governing the longevity of the cells are involved from the limited examples presented herein. The relationship between the interfacial contact and cell performance is therefore a focus of the team's future study.

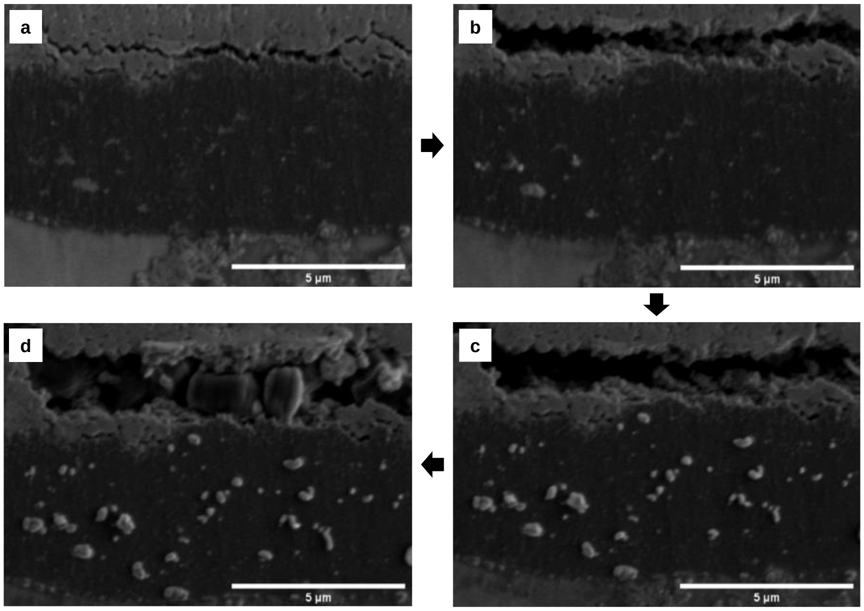

Figure 59. *In operando* morphology characterization of an NMC|LPSCl|Ag–C|Li micro-cell during charge.

Patents/Publications/Presentations

Presentation

- Lindsay Seminar of Chemical Engineering, Texas A&M University (TAMU), College Station, Texas, (September 29, 2021): "Next-Generation Batteries for Electric Vehicles and Stationary Storage." Invited.

TASK 3 – MODELING

Team Lead: Venkat Srinivasan, Argonne National Laboratory

Summary and Highlights

Achieving the performance, life, and cost targets outlined by VTO will require moving to next-generation chemistries, such as higher capacity Li-ion intercalation cathodes, silicon and other alloy-based anodes, Li-metal anode, and sulfur cathodes. However, numerous problems plague development of these systems, from material-level challenges in ensuring reversibility to electrode-level issues in accommodating volume changes, to cell-level challenges in preventing cross talk between the electrodes. In this task, a mathematical perspective is applied to these challenges to provide an understanding of the underlying phenomenon and to suggest solutions that can be implemented by the material synthesis and electrode architecture groups.

The effort spans multiple length scales, from *ab initio* methods to continuum-scale techniques. Models are combined with experiments, and extensive collaborations are established with experimental groups to ensure that the predictions match reality. Efforts also focus on obtaining parameters needed for the models, either from lower-length scale methods or from experiments. Projects also emphasize pushing the boundaries of the modeling techniques used to ensure that the task stays at the cutting edge.

A major focus of the effort is around Li-metal-based SSBs. While these chemistries hold promise, numerous challenges such as reactivity, conductivity, and mechanical stability prevent their commercialization. Mathematical models are ideal to provide the guidance and insights needed to solve these issues.

In the area of Li-metal anodes, the focus is on understanding how materials can be designed to prevent dendrite growth using continuum modeling approaches, combined with calculations on mobility in solid conductors. The results are used to guide materials development by providing the properties needed to prevent dendrites, while also achieving the energy and power goals. Models examine the role of the SEI on the morphology of the dendrite and describe the mechanical-electrochemical coupled effects that are critical for dendrite formation. Finally, efforts are focused on discovery of new solid ion conductors with properties that far exceed existing materials. The focus is on using these models as a guide before embarking on extensive experimentation.

Lithium metal with SEs will be paired with cathode materials, often intercalative in nature. Models are being developed to examine the solid-cathode interface in Li-metal based systems, where side reactions and interface debonding issues are known to limit cycling. These models are being used to understand how to prevent chemo-mechanical failure at the interface. Coatings, an effective strategy for high-voltage operation, are being explored with the aim of providing a rational design approach for new coating materials. In addition, focus is paid to porous electrodes with cathode particles to predict the impact of heterogeneities on electrode behavior.

Highlight. The highlight for this quarter is as follows:

- Full SSBs suffer from interfacial delamination challenges related to the volume change in the cathode during lithiation/delithiation. Delamination results in decreased area for charge transfer and leads to impedance rise and capacity fade. The extent of this issue depends on the partial molar volume of lithium in the cathode particles and elastic modulus of the SEs. V. Srinivasan and co-workers have investigated the impact of these properties using mesoscale models. Simulations suggest that the soft sulfide-type electrolytes show greater tendency to accommodate volume change compared to LLZO-type electrolytes. A phase map was developed that shows the region where such delamination effects can be eliminated.

Task 3.1 – Characterization and Modeling of Lithium-Metal Batteries: First-Principles Modeling and Machine Learning

(Kristin Persson, Lawrence Berkeley National Laboratory)

Project Objective. This project supports VTO programmatic goals by developing next-generation, high-energy cathode materials and enabling stable cathode operation at high voltages through target particle morphology design, functional coatings, and rational design of electrolytes. The end-of-project goals include the following: (1) understanding of the factors that govern charge transport in nonaqueous, superconcentrated LEs, (2) critical surface and coating design and optimization strategies that will improve cycling of Li-ion battery cathodes by reducing cathode degradation from oxygen loss, and (3) simulation and machine learning (ML) of the early formation of the SEI on Li-metal electrodes.

Project Impact. This project is aimed at providing fundamental insights into the atomistic mechanisms underlying surface reactivity and performance of Li-ion cathode materials and electrolytes with the ultimate goal to suggest improvement strategies, such as coatings, surface protection, novel electrolyte formulations, and particle morphology design. Transport modes as a function of solvent and salt concentrations will be clarified, and a data-driven reaction network framework will be designed and implemented to predict early SEI formation on lithium metal.

Approach. First-principles calculations, both static and dynamic approaches, are used to model SSE material thermodynamics and kinetics. LEs are modeled through coupled classical molecular dynamics (CMD) and first-principles methods to accurately capture solvation structure as well as reactivity of the liquid system. The reaction network is built on large-scale first-principles data, using graph theory and ML models.

Out-Year Goals. Electrolyte work will be aimed toward understanding the atomistic interactions underlying performance of lithium electrolytes, specifically elucidating conductivity (as a function of salt concentration) and impact on the charge transport mechanisms at play. Amorphous coatings will be evaluated based on ionic transport metrics and thermodynamic stability. The reaction network will be tested against known interfacial species forming on lithium metal in $LiPF_6$/EC electrolytes.

Collaborations. This project is highly collaborative between BMR PIs G. Chen (LBNL), G. Ceder (University of California, Berkeley, UCB), and R. Kostecki (ANL). Improved coating formulations will be examined by Chen and Ceder, and interfacial reactivity insights will be corroborated by Kostecki.

Milestones

1. Preliminary insights into the SEI composition and reaction pathways for BEs. First approximative reaction scheme proposed. (Q3, FY 2020; Completed)
2. Develop a valid model for amorphous structure as compared to experimental radial distribution function (RDF) data. (Q3, FY 2021; Completed)
3. Quantify the effect of co-solvents to at least one superconcentrated electrolyte. (Q4, FY 2021; In progress)
4. Correlation of electrolyte chemistry and Li/SEI compositional structure determined. (Q1, FY 2022; In progress)

Progress Report

The superconcentrated LE project aims at understanding and identifying which LE formulations using high salt concentrations may allow for improved electrochemical performance. One particular focus is the use of co-solvents to improve transport properties, with one case study involving use of co-solvents for $LiPF_6$ in propylene carbonate (PC) electrolytes. $LiPF_6$ in PC is a previously investigated and characterized system.[1] In this work, the co-solvent is a "diluent" that has been chosen for reducing viscosity while avoiding direct coordination with the electroactive cation.[2]

To investigate such a system, one particular fluorinated diluent was chosen and then added to PC-$LiPF_6$ for two concentrations: one that would allow a high concentration electrolyte (HCE; ~ 3 M of salt, ratio of Li:PC:diluent 1:2:0.3), and one that could potentially allow the LHCE (ratio Li:PC:diluent 1:3:3), at 1 M.[3] To this end, CMD simulations were employed to investigate the change in solvation structure and transport resulting from addition of the diluent co-solvent (methods following Reference 1).

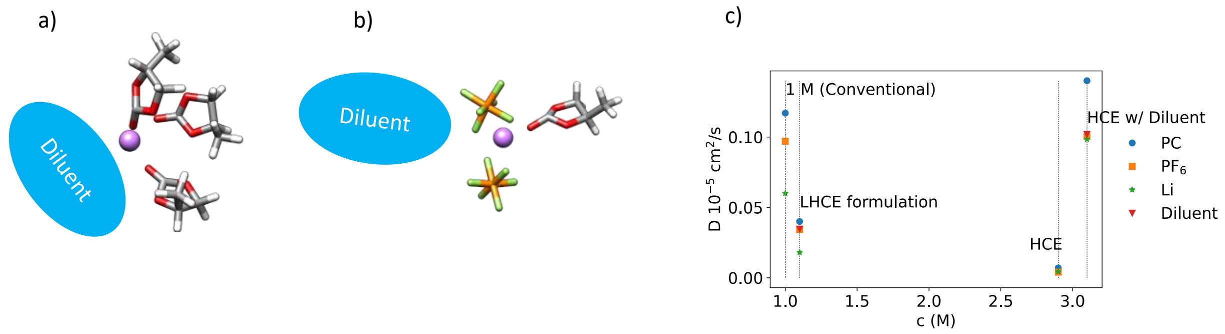

Figure 60. (a) Molecular dynamics "snapshot" of the solvation structure of a lithium cation in the localized high concentration electrolyte (LHCE) formulation. (b) Molecular dynamics "snapshot" of the solvation structure of a lithium cation in the HCE formulation with the fluorinated diluent. Atoms are shown in purple (lithium), red (oxygen), white (hydrogen), green (fluorine), and orange (phosphorus). (c) Diffusion coefficients of the various species as a function of concentration. HCE formulation is $LiPF_6$ in PC; HCE + diluent denotes $LiPF_6$ in PC and diluent. Vertical lines are for visual ease.

Figure 60a-b shows snapshots of solvation structures of the lithium cation for the two studied concentrations (LHCE and HCE, respectively). It is found that in the LHCE concentration, the true LHCE regime is not in fact attained. More specifically, the diluent co-solvent is found in the first solvation shell of the electroactive cation. This indicates that this particular diluent is more-so a conventional co-solvent than a non-coordinating species in this case. In addition, this suggests that the success of the LHCE strategy is likely system-specific and may not work for polar carbonate electrolyte solvents such as PC. In fact, the diffusion constants of the various species were not improved for the LHCE formulation, as shown in Figure 60c, where they decrease from the formulation at a similar concentration without the diluent. In the case of the HCE with the diluent, the lithium cation is less often directly solvated by the diluent. Moreover, the diffusion constants of the various species are greatly increased (Figure 60c), suggesting success of the chosen diluent as viscosity reducing co-solvent. Further characterization, both in silico and experimental, is planned.

References

[1] Self, J., K. D. Fong, and K. A. Persson. "Transport in Superconcentrated $LiPF_6$ and $LiBF_4$ / Propylene Carbonate Electrolytes." *ACS Energy Letters* 4 (2019): 2843-2849.

[2] Cao, X., et al. "Effects of Fluorinated Solvents on Electrolyte Solvation Structures and Electrode/Electrolyte Interphases for Lithium Metal Batteries." *Proceedings of the National Academy of Sciences* 118, No. 9 (2021): e2101899118. doi: 10.1073/pnas.2020357118.

[3] Ren, et al. "Localized High-Concentration Sulfone Electrolytes for High-Efficiency Lithium-Metal Batteries." *Chem* 4, No. 8 (2018): 1877-1892.

Patents/Publications/Presentations

The project has no patents, publications, or presentations to report this quarter.

Task 3.2 – Electrode Materials Design and Failure Prediction
(Venkat Srinivasan, Argonne National Laboratory)

Project Objective. The main project objective is to develop computational models for understanding the various degradation mechanisms for next-generation Li-ion batteries. This year's goal is to use the continuum-based mathematical model to investigate interfacial stability between Li-metal electrodes and SEs during deposition and dissolution of lithium under externally applied currents. Both soft polymer and hard ceramic type electrolytes will be investigated. The team also aims to develop a computational model for understanding the interdiffusion of ions and its impact on other degradation mechanisms at the CEI. Ceramic-based SEs are expected to enable high-energy-density and liquid-free, safe, next-generation Li-ion batteries. Li-metal anodes should be incorporated due to their substantially larger volumetric and specific capacity, as compared to present day graphite-based anodes. During charge, lithium dendrites are observed through the SEs, which are supposed to occur because of the non-uniform current distribution at the Li/electrolyte interface. Interfacial detachment between the lithium electrode and SE has been observed during electrochemical dissolution of lithium (or, the stripping process), which can lead to nonhomogeneous contact and substantially higher charge transfer resistance between the electrode and electrolytes. Similar issues have also been observed at the Li/PE interface during lithium stripping, which will be investigated thoroughly. On the cathode side, diffusion of transition metals (TMs) into the SEs, along with delamination between cathode and SE, leads to increased interfacial resistance. The side reaction between cathodes and SEs is a bigger issue for the sulfides as compared to the oxide-based ceramics, whereas the delamination is supposed to be more dominant within the oxides. The developed computational model will be used to investigate the impact of physicochemical and transport properties of the SE on the overall interfacial degradation observed at both the cathode and anode sides. The main focus will be to elucidate interfacial issues and devise strategies to enable successful implementation of SE in next-generation Li-ion batteries.

Project Impact. Findings from this research will give a better understanding of the factors, at the electrode/SE interface, limiting the cycle life of SE-based Li-ion batteries. These results will help to enable all-solid-state Li-ion batteries.

Project Approach. The approach used here is to develop mesoscale models based on governing principles at the continuum level to describe the critical processes occurring in the materials. Electrochemical, microscopic, and spectroscopic data from experiments are combined with theories for parameter estimation and model validation. The model is then used to provide insights and guidance for design of new materials.

Out-Year Goals. At the end of this project, a computational framework will be presented that is capable of estimating lithium stripping and interdiffusion of ions at electrode/electrolyte interface.

Collaborations. This project collaborates with L. A. Curtiss, A. T. Ngo, and C. M. Phatak at ANL.

Milestones

1. Develop a mesoscale model to capture the void formation at the Li/LLZO interface during dissolution. (Q1, FY 2021; Completed)
2. Compare the lithium dissolution results as predicted by the mesoscale computations (conducted at ANL) with the experimental results obtained from the German group (J. Janek at Justus Liebig University, Giessen). (Q2, FY 2021; Completed)
3. Understand current distribution around a dendritic protrusion during lithium dissolution. (Q3, FY 2021; Completed)
4. Develop computational model for sulfide electrolytes. (Q4, FY2021; Completed)

Progress Report

Develop Computational Model for Sulfide Electrolytes. A computational model, in the continuum level, has been developed this quarter for capturing the interfacial delamination and space charge layers that form at the interface between sulfide electrolytes and oxide cathodes. Capacity fade experienced by sulfides due to these issues has also been compared with that of LLZO. It is well known that sulfide-based SEs (Young's modulus ~ 20 GPa) are much softer than garnet-type LLZO (Young's modulus ~ 150 GPa), and the fracture energy between sulfides and cathodes (~ 0.8 J/m^2) has been reported to be slightly smaller than that between cathode and LLZO (~ 2.0 J/m^2). Figure 61a demonstrates the voltage versus capacity curves during the charge and discharge processes for NMC cathodes with LLZO (black) and LPSCl (magenta) SEs. The blue dashed line indicates discharge capacity without any interfacial delamination. The extent of detachment at NMC/LLZO interface is 73%; the NMC/LPSCl interface is much less, only 45%. Hence, the delamination-induced capacity fade experienced by LPSCl is smaller than that experienced by LLZO. The extent of interfacial detachment depends on the partial molar volume of lithium within the cathode particles and elastic modulus of the SEs. Accordingly, a phase map is demonstrated in Figure 61b for various cathode and SE materials. The stability limits for LLZO-based and LPSCl-based SEs are clearly demonstrated, where the difference can be attributed to the mismatch in their fracture energies. The green and yellow regions within the phase map indicate stable operation and complete detachment, respectively.

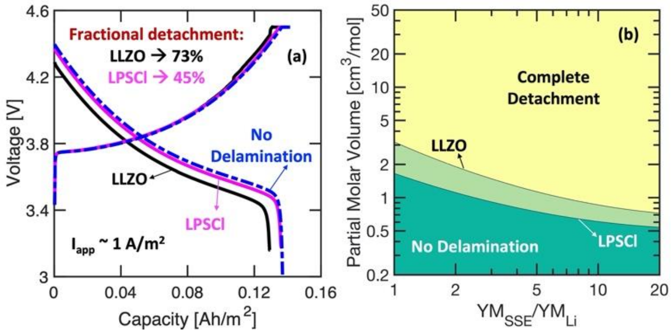

Figure 61. (a) Voltage versus capacity performance curves for NMC/LLZO (black) and NMC/LPSCl (magenta) during the 1st charge and discharge process. The blue dashed line indicates performance curves without any interfacial delamination. NMC/LPSCl experiences much less detachment, and capacity fade, than NMC/LLZO. (b) Phase map between partial molar volume of lithium within cathodes and Young's modulus of solid electrolytes indicating the domains of stable operation (green) and complete detachment (yellow). Two different stability limits for LLZO and LPSCl are shown.

Evolution of a space charge layer between cathode and SE is also modeled. Difference in relative permittivity of NMC cathode, LLZO SE, and LPSCl SE dictates the extent of space charge layers at the charged and discharged state. Evolution of potential and concentration at the NMC/LLZO and NMC/LPSCl interfaces is demonstrated in Figure 62a-b.

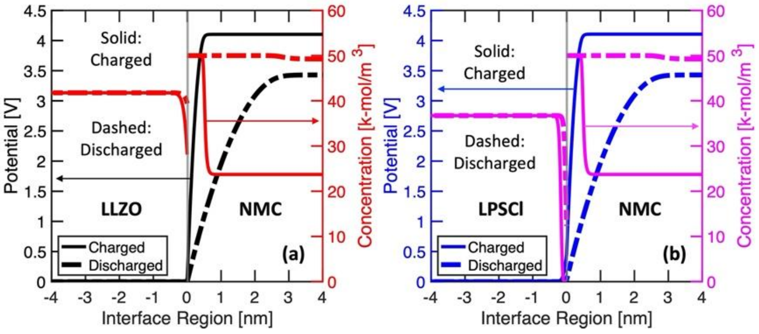

Figure 62. Distribution of potential and concentration within the space charge layer at (a) NMC/LLZO and (b) NMC/LPSCl interface. The solid and dashed lines indicate the space charge layer under fully charged and discharged conditions, respectively. Due to its higher relative permittivity, the space charge layer within LLZO is much thinner than that observed within LPSCl. For both LLZO and LPSCl, the space charge domain in the cathode is substantially thicker under the fully discharged condition.

Discharge capacity fade due to the space charge layer is shown in Figure 63a-b. This computational model development for sulfide electrolytes successfully completes the milestone for the fourth quarter.

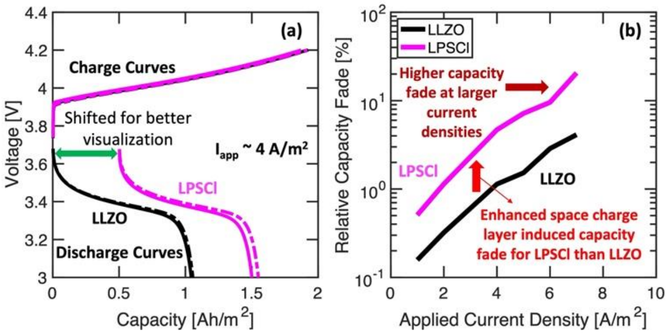

Figure 63. Influence of the space charge layer on the charge/discharge process is captured through the decrease in exchange current density due to decrease and increase in lithium concentration on the electrolyte and cathode, respectively. A strong space charge layer increases the charge transfer resistance between the cathode and electrolytes. (a) Voltage versus capacity performance curves under applied current density of 4 A/m^2 for NMC cathodes with LLZO and LPSCl. (b) Ratio of space charge layer induced capacity fade over the initial capacity as observed under different applied current densities. Due to its stronger space charge layers, LPSCl experiences more capacity fade than LLZO.

Patents/Publications/Presentations

The project has no patents, publications, or presentations to report this quarter.

Task 3.3 – Modeling of Amorphous Solid-State Conductors
(Gerbrand Ceder, University of California, Berkeley)

Project Objective. SSBs are promising to achieve high energy density. The project objective is to determine the design principles needed to create SSEs with high Li-ion conductivity, while also achieving stability against common Li-ion cathodes and Li-metal anodes.

Project Impact. The project will lead to understanding the factors that control Li-ion motion in crystalline and amorphous solids and will develop strategies to create stable interfaces against lithium metal and high-voltage cathode materials. The understanding of such processes is necessary to determine design principles to develop reliable ASSBs.

Approach. HT computation is used to screen suitable SE with high electrochemical stability and high ionic conductivity, by incorporating nudged elastic band (NEB) and an *ab initio* molecular dynamics (AIMD) method. Meanwhile, DFT is used to calculate bulk elastic constants of materials, surface energies, and interface decohesion energies of GBs. Thermodynamic interface stability is assessed from *ab initio* computed grand potential phase diagrams in which the lithium voltage can be controlled. Kinetic limits for SE decomposition are assessed by topotactic lithium insertion and removal from the SE.

Out-Year Goals. Future goals include the following: (1) gain insight into what creates high Li-ion conduction in sulfide and oxide solids, and (2) develop stable, processable solid-state conductors that can be applied in ASSBs.

Collaborations. There are no collaborative activities this quarter.

Milestones

1. Finite T phase diagram of L-P-S system. (Q1, FY 2021; Completed)
2. Develop model for electronic conductivity in SEs. (Q2, FY 2021; Completed)
3. Evaluate effect of ionic and electronic conductivity on lithium plating in SE. (Q3, FY 2021; Completed)
4. Develop a valid model for amorphous structure, and compare to spectroscopy data. (Q4, FY 2021; Completed)

Progress Report

Identification of Activated Diffusion Network

While experimental[1] and theoretical[2] investigations have pointed at the interaction between lithium ions being an important factor for high lithium ionic conductivity, the mechanism behind this effect has not been clearly demonstrated. By observing the diffusion network of garnet frameworks and sodium super ionic conductor (or NASICON) frameworks, a common pattern of activated diffusion networks has been discovered. Specifically, three topological features of the diffusion network that are beneficial for fast lithium migration are identified: 3D percolation network, short distance between occupied lithium sites, and homogeneity of the transport path. Figure 64 illustrates that in garnet and NASICON frameworks, these three features allow for 3D percolation of activated local environment and non-dissipation of such an environment, resulting in their superionic conductivities.

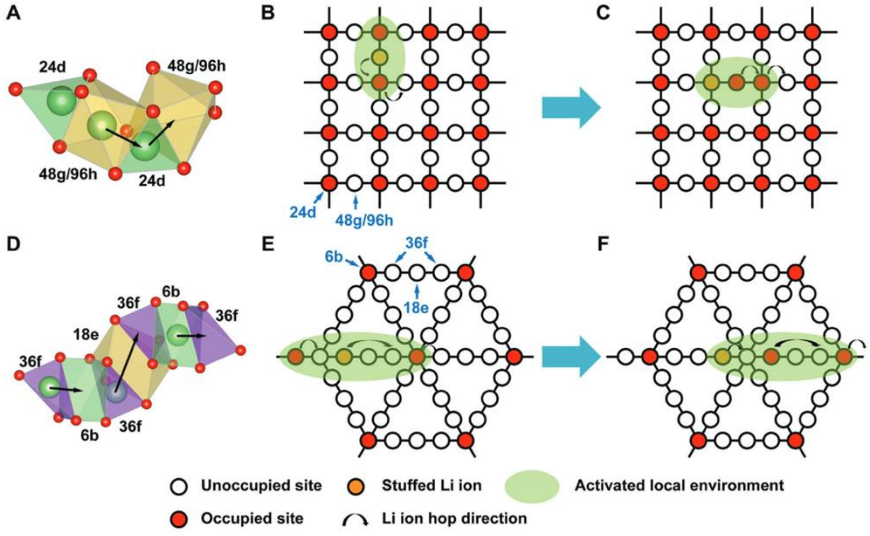

Figure 64. Diffusion mechanism in Li-stuffed Li_3 garnet (a) and NASICON (d) by cooperative hopping of Li-ions in activated local environment. Diffusion network of NASICON before (b) and after (c) cooperative migration. Diffusion network of garnet before (e) and after (f) cooperative migration is illustrated.

HT Screening of Superionic Conductors with Similar Features

The activated diffusion network and its three key features can be directly used as screening criteria to discover novel oxide superionic conductors. By performing HT screening from the Materials Project database,[3] seven novel frameworks that allow high ionic conductivity are discovered. AIMD simulation results show that these materials exhibit 0.1 mS/cm or higher at 300 K. One example of the predicted candidate is Li_2TeO_4 with a distorted inverse spinel structure. While the activation energy for lithium motion in the stoichiometric structure is 1.13 eV,[4] on lithium stuffing by doping Nb^{5+} into Te^{6+} site, face-sharing tet-oct (Li1-Li4 and Li2-Li3 in Figure 65) environments form. This lowers the activation energy to 0.21 eV, allowing high ionic conductivity of 3.2 mS/cm at 300 K. This result clarifies how the interaction between lithium ions within close proximity can drastically enhance ionic conductivity.

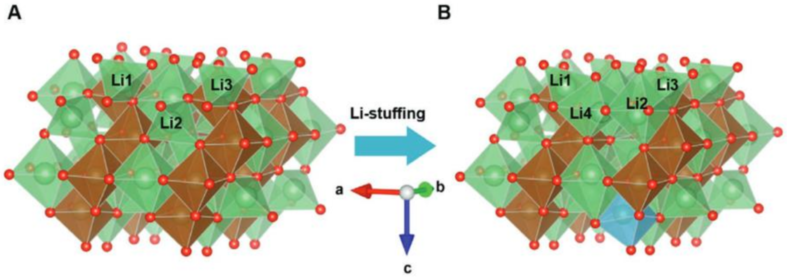

Figure 65. Example of lithium oxide superionic conductor candidate: Li_2TeO_4 before (a) and after (b) lithium stuffing via Nb^{5+} doping into Te^{6+} site.

References

[1] Arbi, K., et al. *Chemistry of Materials* 14 (2002): 1091–1097.
[2] Xu, M., et al. *Physical Review B* 85, No. 5 (2012): 052301.
[3] Jain, A. et al. *APL Materials* 1 (2013): 011002.
[4] González, C., et al. *Materials Research Bulletin* 29 (1994): 903–910.

Patents/Publications/Presentations

Publication

- Xiao, Y., K. Jun, G. Ceder, et al. "Lithium Oxide Superionic Conductors Inspired by Garnet and NASICON Structures." *Advanced Energy Materials* 11, No. 37 (2021): 2101437. doi: 10.1002/aenm.202101437.

Task 3.4 – Characterization and Modeling of Li-Metal Batteries: Force Field Theory and Lithium-Sulfur Battery Simulations
(Lin-Wang Wang, Lawrence Berkeley National Laboratory)

Project Objective. The project objective is to develop force field (FF) based on *ab initio* calculations to study Li-S cathode and lithium LE. It also includes designs for Li-S cathode systems for high gravimetric and volumetric capacities. Lithium diffusion in both LE in a confined space and in Li-S cathode systems is a main focus of this project. To enable calculation of large systems, ML-FF trained on *ab initio* calculation data will also be developed. The success of this new approach will greatly expand the capability of theoretical simulation for battery systems. ML-FF can also be used in combination with traditional classical FF to deal with the nonreactive parts of the system.

Project Impact. Making the Li-S battery a commercial reality will have a major impact on society and also help to realize the VTO goal of 500 km per charge for EV. However, the nature of chemical reaction makes it different from the traditional intercalation-based Li-ion battery. The molecular nature of Li_2S_n also allows solvation in the electrolyte. To address these problems, it is essential to have fundamental studies and understandings of the underlying mechanisms. Theoretical simulations can play an important role in discovering and designing new cathode materials. However, traditional *ab initio* calculations are limited by their computational size, while the classical FF simulations are limited by their accuracy and the lack of adequate FF. The development of ML-FF can overcome these problems by bridging the size gap between the *ab initio* simulation and the real systems that need to be studied.

Approach. ML-FF will be developed by first running *ab initio* simulations, which can generate hundreds of thousands of datasets. The project has a unique capability of decomposing the total energy of a DFT calculation into the energy of each atom. Compared to conventional DFT calculations, this increases the number of data by hundreds of times, an important requirement for ML model training. The dependence of the atomic energy to the local atomic bonding environment will be captured using ML methods. Three ML approaches will be: linear fitting; neural network (NN) model; and Gaussian process regression model. The team will compare the efficacies of these models. Meanwhile, they will also deal with the long-range Coulomb interactions existing in the electrolyte system and the ionic species in LE. The idea is to first fit the charge density of the system and also remove the long-range electrostatic energy before the fitting of the local energy on each atom. The team will design new Li-S and Na-S cathode materials. In particular, they will design an amorphous Li-S mixture, with other materials such as CNT, black carbon, or electric conductive two-dimensional (2D) materials.

Out-Year Goals. In outgoing years, the project will further develop computational methods for more accurate entropy and interaction energy calculations for the electrolyte, as well as for Li-S cathode systems.

Collaborations. The project will collaborate with G. Liu and Y. Cui for cathode design. It has also collaborated with F. Pan of Beijing University for lithium battery research in general.

Milestones

1. Lithium charge density fitting in electrolyte, to fit long-range Coulomb interaction. (Q1, FY 2021; Completed)
2. Study of electrolyte behaviors, including their stability problems. (Q2, FY 2021; In progress)
3. Incorporation of Coulomb interaction in local energy calculation; ML-FF fitting. (Q3, FY 2021; Completed)
4. Further study of Li-S cathode with polymer, to study electric conductivity in such a system. (Q4, FY 2021; In progress)

Progress Report

This quarter, the team fully developed the polarization model in the density-based machine-learning force field (DB-ML-FF) for electrolyte calculation. As shown in Figure 66, many points are taken, first to probe the polarization of the molecule from DFT calculation. The calculated polarization energy is then used to develop the polarization model. The polarization model is an energy term which is a second order function of the electric fields on different atoms. The electric fields are calculated in different ways, based on the total potential in the system. Through their study, the team shows that it is possible to have a polarization model that can induce a polarization energy in the order of 1 eV.

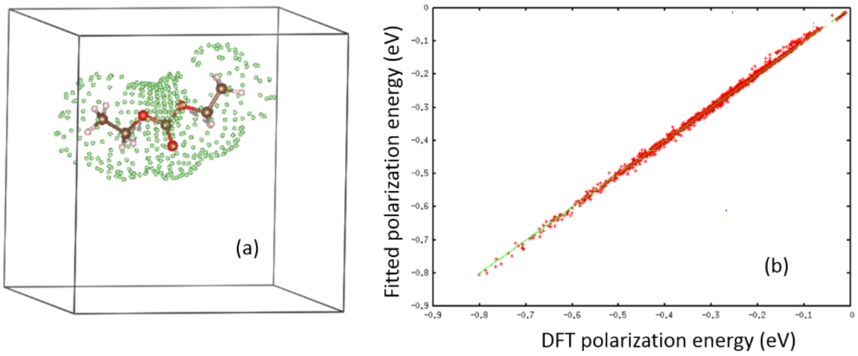

Figure 66. Polarization model: (a) Probing point for electrolyte diethyl carbonate molecule. (b) Density functional theory calculated polarization energy versus polarization model predicted polarization energy.

They have now added together the different energy terms for the DB-ML-FF model, including: the intra-molecule ML-FF term, the inter-molecule density-based Coulomb and exchange interaction term, and the inter-molecule polarization term. They have carried out molecular dynamics (MD) of the model for a large 5000-atom electrolyte system, as shown in Figure 67 (left). Although there is much to improve for efficiency of the code, this does demonstrate that it is feasible to perform large-system MD based on this method. Finally, they show in Figure 67 (right) that the DB-ML-FF model calculated atom-atom correlation function does agree with the direct DFT-simulated correlation function. This comparison is done in a small (~ 200 atom) system to allow the DFT simulation to be finished in a reasonable time.

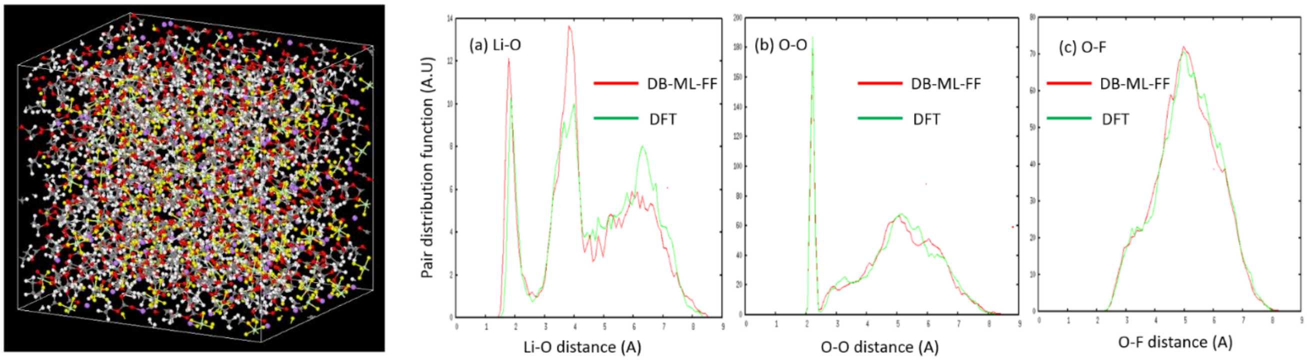

Figure 67. (left) The molecular dynamics (MD) simulation based on density-based machine learning force field (DB-ML-FF), for a 5000-atom electrolyte system, consisting of ethylene carbonate, diethyl carbonate, Li$^+$, and PF_6^-. (right) The atom-atom pair distribution functions based on MD simulations, based on density functional theory method, and the DB-ML-FF method.

Patents/Publications/Presentations

The project has no patents, publications, or presentations to report this quarter.

Task 3.5 – *In Situ* and *Operando* Thermal Diagnostics of Buried Interfaces in Beyond Lithium-Ion Cells
(Ravi Prasher, Lawrence Berkeley National Laboratory)

Project Objective. Transport at various interfaces in *beyond lithium ion* cells will play a major role in electrochemical performance and reliability. It has not yet been possible to thermally profile a Li-metal cell during operation to provide a spatially resolved map of thermal transport properties throughout the cell. The objective of this research is to create a metrology capable of spatially resolved *in operando* thermal property profiling, and then to relate thermal property to the quality of electrodes and interfaces, and to use the developed thermal metrology to understand electrochemical processes in Li-metal batteries, such as dendrite growth, interface kinetics, and ionic transport.

Project Impact. Characterizing electrochemical processes in Li-metal cells such as lithium deposition and dendrite growth at interfaces is of great significance for understanding and enhancing their electrochemical performance and reliability. *In situ* and *operando* micro electrothermal sensors can provide significant information regarding the impact of buried interfaces as a function of time, material, voltage, current, temperature, etc. Therefore, it is important to develop *operando* micro electrothermal sensors and develop models relating those signals to electrochemical performance for *beyond lithium ion* cells. The physics-based model relating thermal and electrochemical properties based on these measurements can facilitate future design of Li-metal batteries.

Approach. To accomplish project goals, the team will utilize an in-house adapted 3-omega (3ω) technique to probe thermal properties of a Li-metal cell while it is in operation, without affecting the operation of the cell. The 3ω sensors will be deposited and fabricated on Li-metal cells based on previous learning on 3ω sensor fabrication. The characteristic depth of the thermally probed region is defined by the wave's "thermal penetration depth," $\delta_p = \sqrt{D/2\omega}$, where D is the sample's thermal diffusivity, and 2ω is the heating frequency of the thermal wave. By depositing the project's 3ω sensors on the battery's outer surface and adjusting ω, the team controls δ_p to span the full range from the top to the bottom layer, thereby noninvasively probing the thermal transport in subsurface layers and interfaces within the bulk of the battery. Thermal transport can be related to quality of the interfaces. By doing concurrent thermal transport and electrochemical performance measurements, the team plans to relate thermal transport to electrochemical performance. As frequency-based thermal measurement techniques provide excellent spatial resolution within the cell, the team also plans to study heat generation at the electrolyte – Li-metal interface and to relate the thermal signals to the interface kinetics and ionic transport. The frequency dependence of heat generated due to transport resistance is different from that due to kinetic resistance. The team plans to utilize this difference to separate the contributions of kinetic and transport resistance at the interface, which will enable understanding of interface kinetics and transport at the Li-metal – SSE interface.

Out-Year Goals. The project will design, build, and implement the adapted 3ω metrology to examine thermal properties and a general frequency-dependent thermal metrology to examine heat generation. This will involve developing and testing the metrology itself along with accompanying theory, designing compatible battery samples, and applying the technique to live cells. The team will measure thermal transport properties of battery materials provided by collaborators. Combined with the electrochemical performance measurement, this will provide significant information relating the thermal signal to the electrochemical process.

Collaborations. This project collaborates with two LBNL groups: V. Battaglia's for cell assembly for 3ω studies, and R. Kostecki's for pristine battery active material growths for studies of thermal signals related to electrochemical process.

Milestones

1. Iteration of electrothermal sensor design. (Q1, FY 2021; Completed)
2. Fabrication of Li-symmetric test cells with incorporated electrothermal sensors. (Q2, FY 2021; Completed)
3. Sensitivity analysis and sample design optimization to maximize measurement sensitivity to target electrochemical properties. (Q3, FY 2021; Completed)
4. Baseline impedance spectroscopy of cells for ion and electron mobility. (Q4, FY 2021; Completed)

Progress Report

This quarter, the team assembled and cycled symmetric lithium-LLZO cells and performed simultaneous impedance spectroscopy and 3ω measurements as a function of the number of cycles. They primarily used two types of LLZO, one sintered in-house by their collaborator in Berkeley lab and another sintered by a commercial supplier (MSE Supplies). Representative impedance spectra for the in-house and commercial cells are shown in Figure 68a-b, respectively. As seen, the impedance of the in-house cells is on the order of kilohms, while that of the commercial cells was on the order of megaohms. According to the supplier (MSE Supplies), such drastic reduction in conductivity (increase in resistance) was most likely due to excess lithium loss during the sintering process. Nevertheless, the team was able to cycle the cells at a reasonably high voltage. The cells were cycled maintaining a constant current of 20 μA/cm^2 and to a capacity of 400 μAh. Above that current, the in-house LLZO cells tended to short, while the commercial LLZO cells required unreasonably high voltage. As seen in Figure 68, the impedance of the newly assembled cell is less than a cycled one. This can occur either due to an increase in the SEI resistance or a change in lithium surface morphology leading to contact loss between lithium metal and the electrolyte. Next quarter, they will compare these EIS results with the 3ω measurements, as 3ω measurements tell about the lithium morphology evolution. By combining the EIS and 3ω results, they will have a better idea of the factors leading to the increase in interface resistance on cycling.

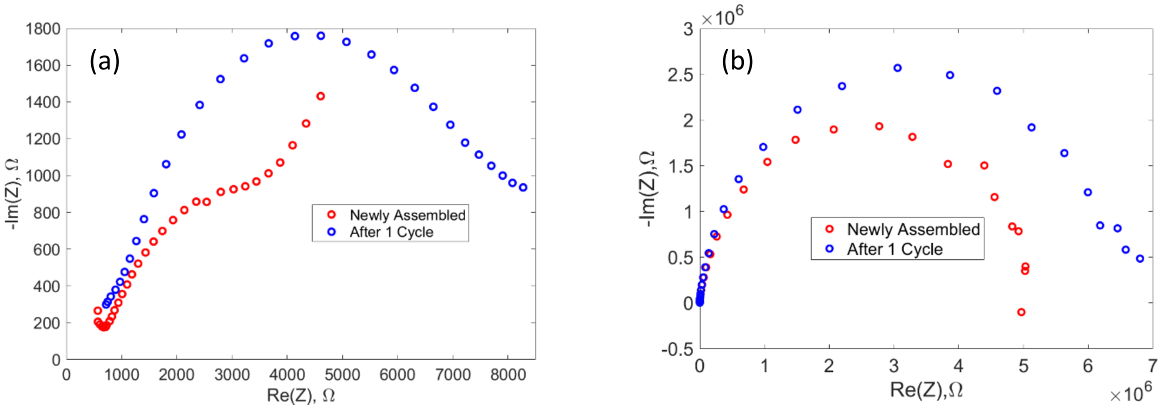

Figure 68. Electrochemical impedance spectra of symmetric lithium solid-state cells using LLZO electrolyte (a) sintered in-house and (b) commercially purchased. The interface resistance of both cells increases after cycling, suggesting interface degradation. Additionally, the commercial LLZO (b) shows much higher resistance, most likely due to lithium loss during sintering.

Patents/Publications/Presentations

The project has no patents, publications, or presentations to report this quarter.

Task 3.6 – Multi-Scale Modeling of Solid-State Electrolytes for Next-Generation Lithium Batteries (Anh Ngo, Larry A. Curtiss, and Venkat Srinivasan, Argonne National Laboratory)

Project Objective. This project is part of a multi-scale modeling effort to obtain an in-depth understanding of the interaction of the electrode and the SE aimed at developing highly efficient SSE batteries for vehicle applications. Input parameters needed for mesoscale (continuum) level calculations are being obtained from atomistic calculations including DFT and CMD simulations. This atomistic input will enable a multi-scale computational procedure for SSEs that is capable of successfully capturing the physicochemical aspects during charge and discharge process, including lithium transport mechanisms, interfacial phenomena during the insertion and extraction of lithium ions, and mechanical deformation of SSE.

Project Impact. A major safety concern experienced with commercially available Li-ion batteries under some scenarios is leakage of the LE, which can potentially catch fire. Replacement of the LE is necessary to decrease the fire hazard and improve safety associated with present-day Li-ion batteries. In addition, use of SEs provides a path to prevent dendrites in Li-metal anodes, thereby leading to batteries with significantly higher energy density. The impact of this project will be to help in development of good SSEs as a replacement for the commercially used organic LEs to improve safety and energy density in Li-ion batteries.

Approach. Parameters needed for mesoscale modeling of grain interior, GB, and electrode-electrolyte interface will be calculated by DFT-based calculations along with Monte Carlo (MC) and MD simulations. The calculations will be used to determine properties of the electrode with the SE as well as in GB regions of the SE. This will include calculations of structure, stability, ionic conductivity, Young’s modulus, fracture toughness, exchange current density, and other properties.

Out-Year Goals. The out-year goals of this work are to calculate other properties such as fracture toughness and include other SSEs and coatings in the multi-scale modeling.

Collaborations. This project collaborates with Y. Cui at Stanford.

Milestones

1. Determine stable surface of the LPSCl SSE and the NMC-811/LPSCl interface. (Q1, FY 2021; Completed)
2. Conduct AIMD study of electrochemical interface between NMC-811/LPSCl. (Q2, FY 2021; Completed)
3. Investigate Li-ion transport of the NMC-811/LPSCl interface, and calculate exchange current density. (Q3, FY 2021; Completed)
4. Incorporate information obtained from the atomistic calculations into the mesoscale model, and predict the impact of performance. (Q4, FY 2021; Completed)

Progress Report

Incorporate Information Obtained from Atomistic Calculations into Mesoscale Model, and Predict Impact on Performance

In the last few quarters, the team conducted detailed analysis of the interface between NMC cathode and LPSCl SE, which led to successful estimation of the lithium exchange current density and fracture energy between the cathode and the SE. These numbers were incorporated into a mesoscale-level model, which simulated the Li-metal anode, LPSCl SEs, and NMC cathode particles. The computational domain is shown in Figure 69a, where evolution of fracture at the CEI during charge-discharge operation is shown by black cross symbols. The voltage versus capacity curves during the charge and discharge process, as predicted by the computational model, are shown in Figure 69b. Mechanical degradation and subsequent loss of electrochemically active surface area leads to a decrease in discharge capacity for NMC/LPSCl systems. Figure 69c demonstrates evolution of interfacial delamination during the charge and discharge process. It is evident that substantial delamination occurs during the end of the charge process, which eventually leads to an increase in overpotential during discharge. This can be attributed to the delithiation-induced shrinkage of cathode particles and subsequent generation of tensile stress at the CEI. It is noted that increase in volume of the Li-metal anode applies some compressive stress on the NMC/LPSCl interface, but that it is insufficient to prevent delamination. Negligible interfacial detachment during the discharge process is also shown in Figure 69c.

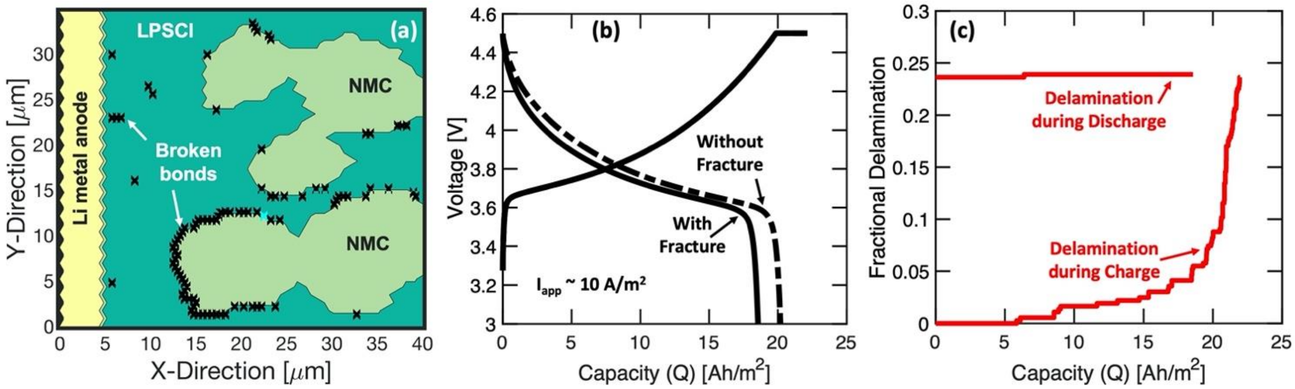

Figure 69. (a) Demonstration of the computational domain used to investigate the extent of interfacial delamination within NMC/LPSCl cathode/solid-electrolyte systems. Li-metal anode has also been incorporated in the left side. (b) Comparison of voltage versus capacity curves during the charge and discharge process for NMC/LPSCl systems with and without interfacial delamination. Applied current density is maintained constant at 10 A/m^2. (c) Evolution in interfacial delamination during the first charge and discharge process for NMC/LPSCl systems under applied current density of 10 A/m^2.

Decrease in discharge capacity and increase in cathode/electrolyte delamination over multiple cycles is shown in Figure 70a-b for two applied current densities of 10 A/m^2 and 100 A/m^2. Due to higher kinetic potential drop under larger current densities, smaller magnitude of discharge capacity is extracted at higher current densities. Interfacial delamination is almost independent of the applied current due to the constant current / constant voltage (CCCV) charge protocol. These mesoscale simulations complete the milestone for the fourth quarter.

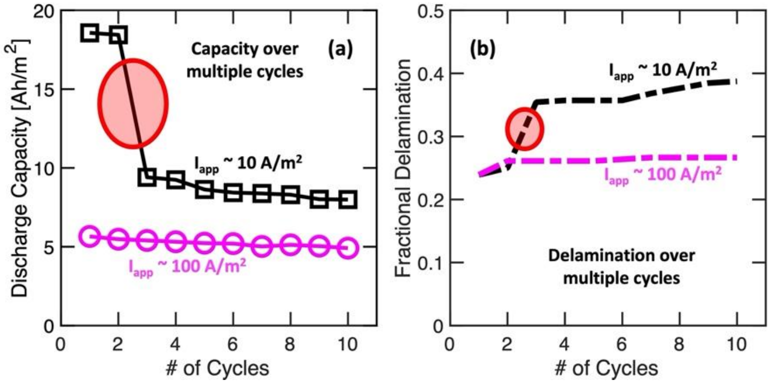

Figure 70. (a) Comparison of discharge capacity over multiple cycles under two applied current densities of 10 A/m^2 and 100 A/m^2. Constant current / constant voltage (CCCV) charge and CC discharge protocols have been implemented in the reported cycles. (b) Extent of delamination over the 10 cycles under two applied current densities. For 10 A/m^2, the sudden drop in discharge capacity can be attributed to the sudden increase in interfacial delamination, which is highlighted by the red circles.

Patents/Publications/Presentations

Publication

- Barai, P., T. Rojas, B. Narayanan, A. T. Ngo, L. A. Curtiss, and V. Srinivasan. “Investigation of Delamination-Induced Performance Decay at the Cathode/LLZO Interface.” *Chemistry of Materials* 33, No. 14 (2021): 5527–5541.

Task 3.7 – Integrated Multi-Scale Modeling for Design of Robust 3D Solid-State Lithium Batteries (Brandon Wood, Lawence Livermore National Laboratory)

Project Objective. This project will develop a multi-scale, multi-physics modeling framework for probing the effects of materials microstructure and device architecture on ion transport within 3D ceramic SSB materials, with the goal of enhancing performance and reliability. The project has three primary objectives: (1) integrate multi-physics and multi-scale model components; (2) understand interface- and microstructure-derived limitations on ion transport; and (3) derive key structure-performance relations for enabling future optimization.

Project Impact. This project will lead to understanding interfacial losses and instabilities that impede performance and promote failure of SSBs. The multi-scale and multi-physics modeling framework developed in this work will address shortcomings of existing modeling strategies that either lack coupling of the multi-physics nature of various processes active in 3D batteries or fail to incorporate processes at different length scales to understand function. Ultimately, the tools and understanding generated by this project can be utilized to realize optimization of interface-dominated 3D batteries.

Approach. The project approach integrates simulations at three scales to predict ion transport limitations within the ceramic SSE LLZO, as well as across the interface between LLZO and $LiCoO_2$ (LCO) cathodes. A particular focus is on understanding the effects of microstructures and architectures resulting from processing of 3D SSBs, as well as their mechanical and chemical evolution at different stages of cycling. First-principles and CMD simulations are used to compute fundamental Li-ion diffusion within bulk SE and cathode materials, along/across GBs of the electrolyte, and along/across electrolyte/cathode interfaces. Next, phase-field simulations are used to generate digital representation of realistic microstructures of the materials, which are combined with the atomistic simulation results to parameterize mesoscale effective property calculations and to establish microstructure-property relationships for ion transport. Finally, these relationships inform a cell-level macroscopic electro-chemo-mechanical modeling framework, which can be used to optimize performance of ceramic 3D SSLBs based on LLZO SEs.

Out-Year Goals. The current phase of the project is complete. Subject to funding and renewal, future activities will focus on computing mechanical properties of internal and multiphase interfaces using a multiscale approach that builds on previous quarters' activities.

Collaborations. This project collaborates with N. Adelstein from San Francisco State University on atomistic diffusion modeling, and J. Ye from Lawrence Livermore National Laboratory (LLNL) on 3D printing of SSB materials. They also partner with T. Danner and A. Latz from Deutsches Zentrum für Luft- und Raumfaurt (DLR) on impedance modeling and electro-chemo-mechanical interface models, with P. Zapol from ANL on modeling of interfaces in LLZO, and with D. Fattakhova-Rohlfing from Forschungszentrum Jülich (FZJ) and E. Wachsman from UMD on properties of LLZO with varying densities and microstructures as part of the U. S.–Germany partnership on SSB research.

Milestones

1. Demonstrate microstructural model of stress effect on ion transport. (Q1, FY 2021; Completed)
2. Compute barriers for ion transport across LCO/LLZO interface. (Q2, FY 2021; Completed)
3. Integrate polycrystalline diffusion model with EIS simulations. (Q3, FY 2021; Delayed by staffing issues and redirected)
4. Demonstrate full multi-scale EIS model using ion transport simulations of CEIs. (Q4, FY 2021; Delayed by staffing issues and redirected)

Progress Report

ML Interatomic Potentials for Accelerated Atomistic Simulations of Interfaces. The team's focus has shifted to extending the reach of atomistic simulations to larger, more complex interface configurations with intrinsic disorder. Accordingly, they have developed the ML potential that can compute configurations with far greater efficiency compared to AIMD. Results from these computations are being integrated into the team's mesoscale modeling framework to estimate microstructure-dependent transport across both internal (GB) and multiphase interfaces between the cathode and electrolyte.

This quarter, the team improved the ML potential to properly simulate transport through an internal LLZO GB by including in the training data amorphous LLZO structures with expanded volumes. They found that the potential presents quantum-level accuracy for energies and forces for *NPT* MD simulations up to 2500K, with root mean squared errors (RMSE) for energies and forces < 10 meV/atom and < 0.2 eV/Å, respectively. To validate the performance and extract useful parameters for their mesoscale models, the team performed atomic simulations with the ML potential at various conditions and evaluated RDFs, mechanical properties, lithium transport parameters, and atomic vibrational characteristics. Figure 71 shows that the RDFs from MD simulation with the ML potential (MLMD) for amorphous LLZO with volume expansions at 3000 K are nearly identical to those calculated by the trajectory from AIMD simulations and much better than those computed using a CMD simulation approach that relies on a simpler empirical potential. The bulk, shear, and Young's moduli for crystalline LLZO predicted by the ML potential were 123.2 GPa, 65.1 GPa, and 166.0 GPa, respectively, which are close to those computed using quantum DFT simulations (114.7 GPa, 65.2 GPa, and 164.5 GPa, respectively), with overall errors below 7.5%. Also, the equilibrium lattice constant and bulk modulus of amorphous LLZO (broadly representative of high-angle GBs) predicted by the ML potential were 13.43 Å and 76.9 GPa, which are similar to those calculated by DFT (13.47 Å and 78.0 GPa) with errors below 1.5%.

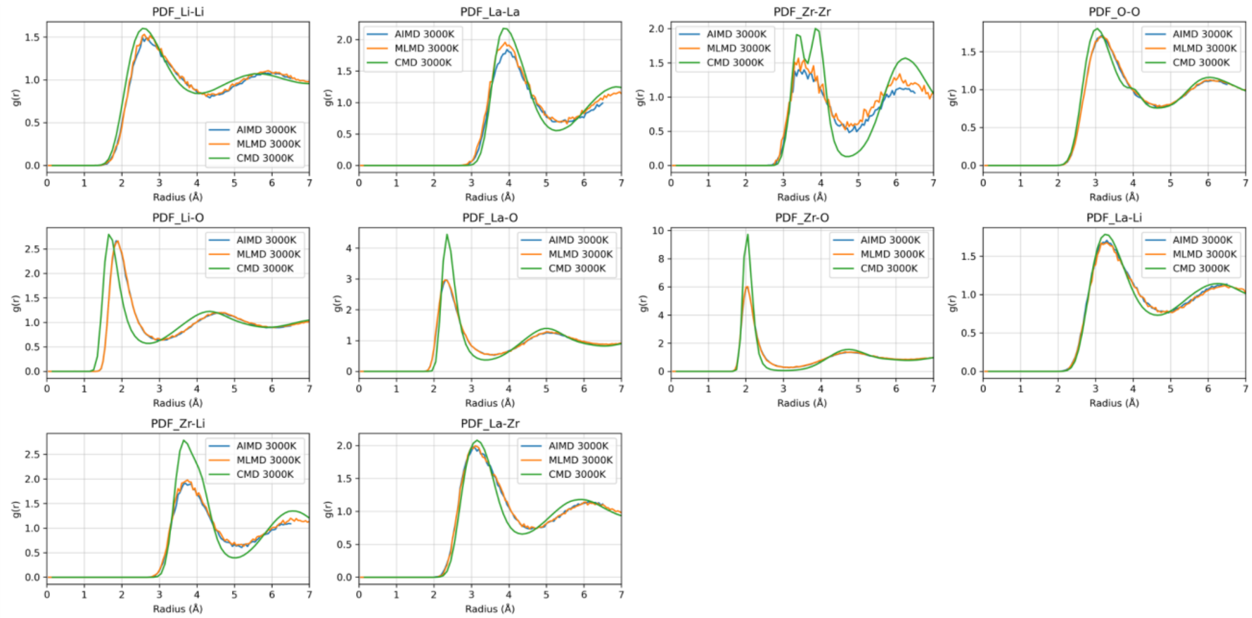

Figure 71. Comparison of radial distribution functions (RDFs) of atomic pairs between *ab initio* molecular dynamics (AIMD, blue), molecular dynamics with machine-learning force field (MLMD, orange), and classical molecular dynamics with an empirical potential (CMD, green) for (a) amorphous LLZO at 3000 K with 33% increase in volume and (b) crystalline LLZO at 1273 K with 10% increase in volume. MLMD and CMD simulations (NVT ensemble) were performed using a 2×2×2 supercell for 100 ps. AIMD simulations (NVT ensemble) were performed using a unit cell for 30 ps.

In addition to the static properties, Figure 72 shows that the new ML potential predicts lithium transport parameters close to AIMD for both crystalline and disordered variants. For example, the error in the activation energy (E_a) for diffusion is only 1.7% with respect to AIMD, and estimated diffusivities by MLMD and AIMD are nearly identical across a range of temperatures. The higher activation energy for the amorphous variant reflects the blocking effect of GBs, which is known to lead to increased impedance in LLZO. The team also confirmed that the phonon density of states (DOS) of each element was well predicted by the ML potential for amorphous LLZO.

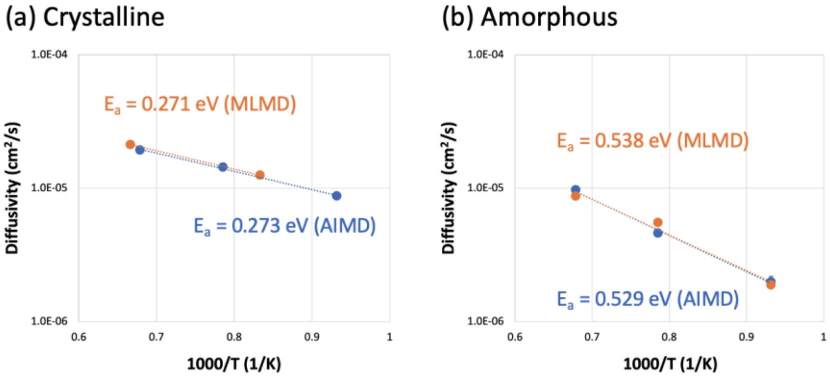

Figure 72. Lithium diffusivities predicted by molecular dynamics with machine-learning force field (MLMD, orange) and *ab initio* molecular dynamics (AIMD, blue) for (a) crystalline and (b) amorphous LLZO with activation energies (Ea) evaluated by fitting diffusivities to the Arrhenius relation (dotted lines). Molecular dynamics simulations (NVT ensemble) with the machine-learning force field (MLFF) were performed for 100 ps using a 2x2x2 supercell and AIMD simulations (NVT ensemble) were performed for 30 ps using a unit cell.

Having validated the approach and validity of the ML potentials, the team proceeded to construct models of GBs and interphase boundaries to compute Li^+ transport. These computations are refinements of calculations from previous quarters, which were performed using either CMD approaches or on simpler representations using full AIMD. As an illustration, Figure 73 presents the trajectory of Li^+ ions transporting through a LLZO ∑5(210)/[001] GB model at 2000 K. The ML potential permits analysis of Li^+ migration in such large GB models for long simulation times with quantum-level accuracy, which AIMD simulations cannot handle. The team has performed similar computations for the LLZO|LCO interface by collecting additional structural training data using small interface models that mimic atomic interactions at the interface with various local compositions. In addition, analysis of the local environments that promote rapid diffusion or act as diffusion blockers (and hence increased impedance) was aided by development of new analytical techniques that rely on discretizing jumps and sites to examine spatiotemporal correlation effects. These techniques were reported and applied in two new publications this quarter (see Publications section).

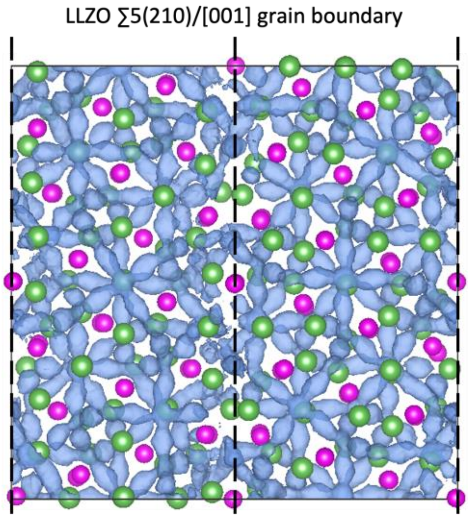

Figure 73. Ionic probability density plot (blue isosurface) for lithium in LLZO ∑5(210)/[001] coherent grain boundary model (40 formula unit, 960 atoms). Molecular dynamics simulations (NVT ensemble) with the machine-learning force field were performed for 100 ps at 2000 K. Magenta and green atoms are zirconium and lanthanum, respectively; for simplicity, oxygen atoms are not shown.

Patents/Publications/Presentations

Publications

- Shi, R., M. Wood, T. W. Heo, B. C. Wood, and J. Ye. "Towards Understanding Particle Rigid-Body Motion during Solid-State Sintering." *Journal of the European Ceramic Society* 41 (2021): 211.
- Wood, B. C., J. B. Varley, K. E. Kweon, P. Shea, A. T. Hall, A. Grieder, M. Ward, V. P. Aguirre, D. Ringling, E. L. Ventura, C. Stancill, and N. Adelstein. "Paradigms of Frustration in Superionic Solid Electrolytes." *Philosophical Transactions of the Royal Society A* 379 (2021): 20190467.
- Mehmedovic, Z., V. Wei, A. Grieder, P. Shea, B. C. Wood, and N. Adelstein. "Impacts of Vacancy-Induced Polarization and Distortion on Diffusion in Solid Electrolyte Li_3OCl." *Philosophical Transactions of the Royal Society A* 379 (2021): 20190459.

Task 3.8 – First-Principles Modeling of Cluster-Based Solid Electrolytes (Puru Jena, Virginia Commonwealth University)

Project Objective. The objective of the project is to use cluster-ions, which are stable atomic clusters that mimic the chemistry of individual atoms, as the building blocks of new SEs for Li-ion batteries and the corresponding battery system. The advantages of using cluster-ions to replace elemental ions is that the size, shape, and composition of the former can be tailored to achieve higher superionic conductivity, electrochemical stability, and charge transfer across the solid-state ions (SSIs) than the conventional materials. More specifically, the goal is to develop superior SEs based on cluster-ions and to model these SEs and their interfaces with electrodes, especially with the Li-metal anode, for successful integration into high-performance SSBs for EVs. The team will model and screen cluster-based solid electrolytes (CSEs) that, compared to conventional SEs, have low activation energies, practical room-temperature ionic conductivities, wide electrochemical stability windows, and desired mechanical properties that, for example, can inhibit the Li-metal anode dendrite growth. They will provide a fundamental understanding of the ionic conduction mechanism in the newly developed CSEs and will identify means to further improve property metrics via chemical and defect engineering. The team will model the interfacial properties, such as the structural, chemical, electrochemical, and ion/charge transfer properties, between the CSEs and electrodes at the atomic level, as well as find the interfacial coating materials with desired properties. Based on accumulated data from modeling, they will establish links between the basic parameters of the cluster-ions and the bulk/interface properties, which can directly guide experiments. Meanwhile, the team will work closely with experimentalists in the BMR Program to complement the project's theoretical efforts and to guide them in focused development of the predicted CSEs and the interfaces.

Project Impact. The proposed project will open a new avenue for guiding experiments in the synthesis of SSBs equipped with CSEs and capable of operating over a wide temperature range. Modeling and understanding of the ionic conduction of CSEs and their interfacial properties with electrodes, especially with Li-metal anode, will enrich current battery science and also train the future workforce in SSB development for next-generation EVs by supporting postdoctoral fellows.

Approach. This project will employ multi-scale theoretical methods and computational techniques.

Out-Year Goals. The out-year goals involve modeling development of new CSE materials and database.

Collaborations. The team is working with J. Nanda of ORNL, Y. Wu of Ohio State University (OSU), and D. Mitlin of UT, Austin, on SEs.

Milestones

1. Complete development of new CSE materials with a database. (Q4, FY 2021; Completed)
2. Structural studies of the chemically mixed systems containing both cluster-ions and elemental ions. (Q2, FY 2021; Completed)
3. Characterizations of the chemically mixed systems. (Q3, FY 2021; Completed)
4. Cation doping in the CSE systems. (Q4, FY 2021; Completed)
5. Optimizing the chemical mixing and cation doping for the cluster-ion-based SE materials with enriched database. (Q4, FY 2021; Completed)

Progress Report

Both milestones for this quarter have been completed. Based on the CSEs in the project's database, the cation-doped systems are studied. Multi-valence metal elements in +2 and +3 states have been selected according to their compatible ionic radii with that of Li^+ (0.9 Å). The ground-state configurations of the cation-doped systems are identified using the project's developed program that was used to study the halogen-cluster mixed systems in the last quarter. For demonstration, Figure 74 shows the optimized ground-state structures of one typical CSE doped with three different multi-valence metal cations.

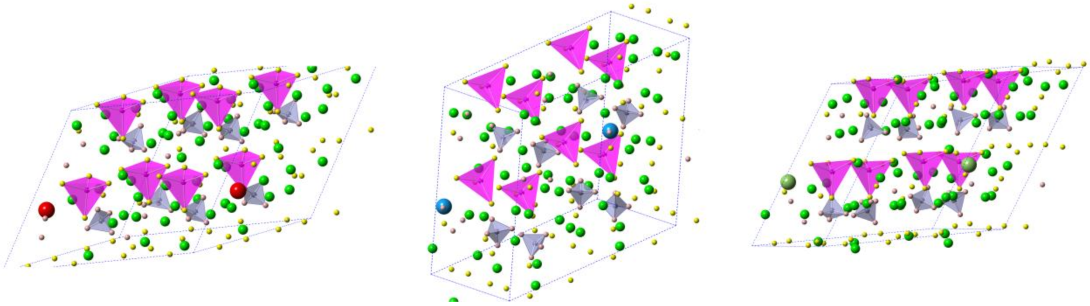

Figure 74. Optimized ground-state structures of a cluster-based solid electrolyte from the project's database doped by three kinds of multi-valence metal cations. The doped cations are shown in big size and in red, blue, and light green, respectively (from left to right). In each case, the structure contains two types of cluster-ions: one is represented by the small tetrahedra in grey, and the other by the big tetrahedra in magenta.

The major findings include the following:

- Li^+ vacancies are always present adjacent to the doped multi-valence metal ion to lower the energy, and the doping can lead to orientational disorder of the cluster-ions in the ground-state structure, as shown in Figure 74.
- The doping elements that lead to optimized ionic conduction properties are different for different CSEs. As demonstrated in the calculated diffusivities in Figure 75, Mg^{2+} doping leads to the highest diffusivities, especially at room temperature, for three cases in CSE_1, CSE_4, and CSE_5; Al^{3+} leads to the highest diffusivity for CSE_2, and Ga^{3+} for CSE_3.

For each studied doped CSE, AIMD simulations are carried out using a large supercell containing hundreds of atoms. In each case, AIMDs are performed at four temperatures. A typical AIMD lasts around 100 ps with a 2 fs time step, where 5-10 ps is allowed for the system to reach thermal equilibrium before the data are collected to calculate the mean squared displacement (MSD) for all the atomic species in the system. The diffusivity at each temperature is then calculated from the MSD. The calculated diffusivities at a few temperature points are fitted to the Arrhenius relation and extrapolated to other temperatures, especially the room temperature (300 K). The activation energy is extracted from the fitting. The ionic conductivity and activation energy of each CSE doped with multi-valence cations are then optimized against the doping species.

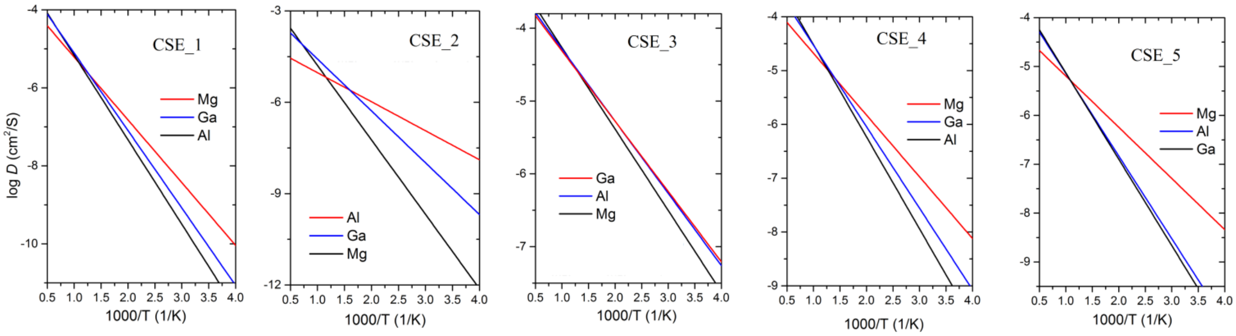

Figure 75. Calculated diffusivities at different temperatures for the studied cation-doped cluster-based solid electrolytes (CSE).

The optimized halogen-cluster mixing of the CSEs (in terms of the halogen concentration) and the optimized cation-doping in the CSEs (in terms of the doping species and the charge states) have been obtained. The results are added to the project's database of CSEs. The team will provide detailed results and the updated data in their Research Performance Progress Report.

Patents/Publications/Presentations

Publications

- Fang, H., P. Jena, J. Nanda, D. Mitlin, et al. "Heavily Tungsten Doped Sodium Thioantimonate Solid State Electrolytes with Exceptionally Low Activation Energy for Ionic Diffusion." *Angewandte Chemie International Edition* 60 (2021): 26158–26166. doi: 10.1002/anie.202110699.
- Fang, H., P. Jena, Y. Wu, et al. "Antiperovskite K_3OI for K-Ion Solid State Electrolyte." *Journal of Physical Chemistry Letters* 12 (2021): 7120–7126.

Presentation

- Michigan Technological University (October 7, 2021): "Design and Understanding Novel Solid Electrolytes"; H. Fang. Invited.

Task 3.9 – Predictive Engineering of Interfaces and Cathodes for High-Performance All-Solid-State Lithium-Sulfur Batteries
(Badri Narayanan, University of Louisville)

Project Objective. The primary goal of this project is to leverage data-driven methods and ML strategies to develop accurate multi-physics models for ASSLSB materials that can capture electrochemical and transport phenomena over atomic-to-mesoscopic length/timescales; these models will be rigorously validated by synthesis and advanced characterization experiments. The team will leverage the predictive power of these models, alongside synthesis/characterization experiments and battery fabrication, to address longstanding issues at the electrode/electrolyte interfaces in ASSLSBs. The project's proposed technology involves the following: (1) halide-doped solid sulfide electrolytes that can concurrently provide high Li^+ ion conductivity and suppress dendrite growth; (2) novel mesoporous cathode composed of interconnected carbon nano-cages (CNCs) co-infiltrated with sulfur and sulfide electrolyte, which hold potential to allow high sulfur loading and optimal ion/electron pathways; and (3) functionalization of sulfide electrolyte with ILs to improve physical contact and minimize impedance at the CEI.

Project Impact. ASSLSBs remain far from commercialization due to poor understanding of fundamental electrochemical/chemical and transport processes that occur at the interfaces, especially at atomic to mesoscopic scales. Successful development of proposed predictive models (at multiple scales) will bridge this knowledge gap and will advance fundamental understanding of reaction chemistry, kinetics, charge transfer, and dendrite growth at electrified SSIs. This will enable predictive design of effective strategies to mitigate interfacial problems in ASSLSBs, including poor interfacial contact, interfacial impedance to Li^+ ion transport, and poor electron/ion conduction within cathodes. Ultimately, the fundamental knowledge gained will lead to development of high-performance ASSLSBs that meet DOE targets of specific energy (350 Wh/kg @C/3), sulfur loading (> 6 mg/cm^2), and high cycle life (1000).

Approach. The project brings together innovative solutions in multi-scale materials modeling, electrolyte synthesis, fabrication of cathode architecture, and electrolyte functionalization to overcome the issues at electrode/electrolyte interfaces in ASSLSBs. The central idea is to employ a data-driven and ML-based approach to develop accurate multi-physics battery models at atomic-to-mesoscopic scales. This approach overcomes critical problems with existing model development methods by foregoing the need for pre-defined functional forms, introducing deep-learning technique to describe reactivity, and employing optimization methods that do not require human intuition. Multi-scale simulations based on the newly developed models will provide insights into electrochemical phenomena at electrode/electrolyte interfaces.

Out-Year Goals. In Year 2, the goal is to gain atomic-scale understanding of interfacial reactions in ASSLSBs, and to assess the effectiveness of functionalizing CEIs with ILs.

Collaborations. The team collaborates with the groups under A. Ngo and L. A. Curtiss at ANL for quantum simulations of battery systems; they plan to collaborate with J. Nanda at ORNL for advanced spectroscopic *in situ* characterization of interfaces.

Milestones

1. Extend reactive interatomic potential models to include interfaces. (Q1, FY 2021; Completed)
2. Advance characterization of CEIs to understand their reactivity, stability, and structure; validate predictions of reactive interatomic potentials. (Q2, FY 2021; Completed)
3. Utilize reactive MD to gain insights into interfacial processes, and predictively design stable interface with good ion transport. (Q3, FY 2021; Completed)
4. Fabricate batteries that meet interim performance metrics. (Q4, FY 2021; Completed)

Progress Report

This quarter, the team made good progress on (a) gaining fundamental understanding of interfacial reactions that occur between the functionalizing liquid (containing IL and diluent) with cathode and sulfide SSE, and (b) fabrication of Li-S coin cells that provide good cyclability at high sulfur loading.

Atomic-Scale Understanding of Effect of Functionalizing Liquid on Chemical Reactions at Cathode/SE Interface. Battery fabrication efforts showed that interfacial resistance across the CEI in ASSLSBs (with $Li_6PS_5F_{0.5}Cl_{0.5}$ electrolyte, lithium anode, and Super-P cathode) can be alleviated significantly by functionalizing with an IL [LiTFSI in N-butyl-N-methyl pyrrolidinium (PYR-14)]. This, in turn, can enable stable cycling of solid-state, albeit with a somewhat low initial discharge capacity (~ 600 mAh/g) owing to high viscosity of IL. Both initial discharge capacity and cycle life can be significantly enhanced by diluting IL with DOL. The team found that a 0.04 mL solution containing 2 M LiTFSI in 1:1 (volume) PYR_{14}:DOL gives the most optimal performance with $Li_6PS_5F_{0.5}Cl_{0.5}$ electrolyte, lithium anode, and Super-P cathode (at low S-loading of 0.7 mg/cm^2) – 1100 mAh/g initial discharge capacity, with a retention of 400 mAh/g after 50 cycles (@C/20) with excellent CE. Adding sulfide SSE to the Super-P cathode improves capacity retention to 480 mAh/g, but with slightly diminished CE. Clearly, ILs show much promise in enhancing performance of ASSLSBs. Nevertheless, the effect of IL functionalizing liquid on the chemical reactions at the CEI remains unclear.

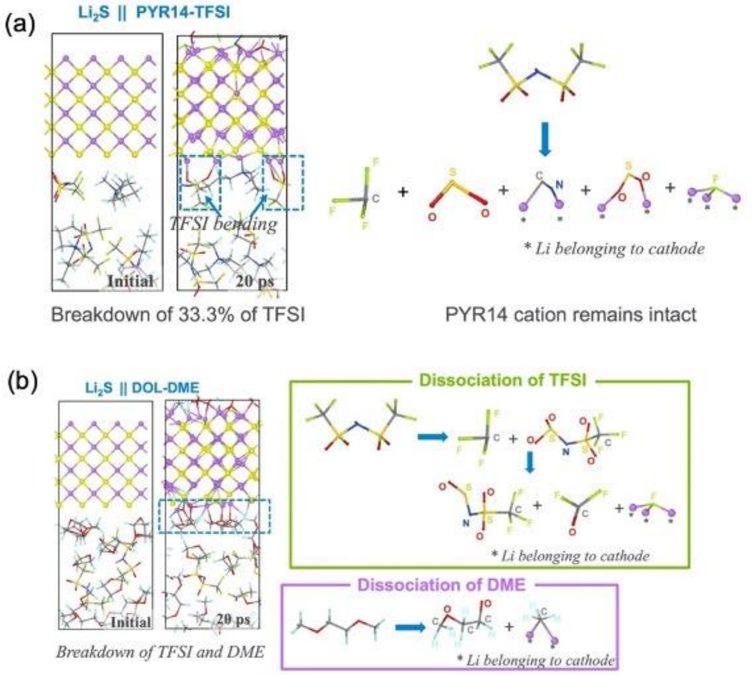

Figure 76. Decomposition reactions of (a) PYR_{14}-TFSI ionic liquid, and (b) LiTFSI in DOL-DME near the cathode in its fully discharged state (Li_2S) obtained from *ab initio* molecular dynamics (AIMD) simulations under ambient conditions. Both panels (a-b) show the atomic snapshots of the interface in the beginning and end of the AIMD trajectory. Note, both Li_2S and $Li_6PS_5F_{0.5}Cl_{0.5}$ are oriented such that their crystallographic [001] directions are aligned normal to the interface. In all cases, TFSI anion dissociates, resulting in Li-F bonds. DOL does not dissociate, as opposed to DME.

This quarter, the team employed AIMD simulations to identify the effect of two types of functionalizing liquid, namely (a) IL ([PYR_{14}][TFSI]), and (b) glyme (2 M LiTFSI in DOL:DME = 1:1 by volume) on the interfacial reactions with representative sulfide SSE ($Li_6PS_5F_{0.5}Cl_{0.5}$) and cathode. For the cathode, the team considered two extreme cases: (a) Li_2S (fully discharged), and (b) S_8 (fully charged). For all cases, the cathode (Li_2S and S_8), and sulfide SSE were oriented such that their crystallographic [001] directions are aligned normal to the interface. The typical supercell sizes were ~ 1 nm × ~ 1 nm × ~ 3-5 nm (~ 300 atoms). The team's AIMD calculations show that both [PYR_{14}][TFSI] and DOL-DME do not react with sulfide SSE ($Li_6PS_5F_{0.5}Cl_{0.5}$). Notably, the ethereal oxygen of DOL and DME coordinates with lithium of sulfide SSE at the DOL-DME || sulfide SSE interface without decomposition; in contrast, the PYR_{14} does not coordinate with the sulfide SSE. Similarly, no decomposition reactions were observed between the functionalizing liquid ([PYR_{14}][TFSI] or DOL-DME) and the cathode in its fully charged state.

Detailed analysis of the project's AIMD trajectories shows that both [PYR$_{14}$][TFSI] and DOL-DME react with the cathode in its fully discharged state (that is, Li_2S) via breakdown of the TFSI anions facilitated by the lithium atoms in Li_2S (Figure 76). However, both the extent of decomposition and the reaction products are strongly dependent on the nature of the functionalizing liquid. At the interface between [PYR14][TFSI] and Li_2S-cathode, ~ 33.3% of [TFSI] dissociates to form -CF_3, -SO_2, and -CN species (Figure 76a). The [PYR14] cations remain stable throughout the simulation time (20 ps). On the other hand, at the DOL-DME || Li_2S interface, ~ 50% of the [TFSI] anions dissociate, forming -CF_2O and -SO-N-SO_2-CF_3 species. Additionally, ~ 20% of DME breaks down, forming -O-CH_2-CH_2-O-CH_3 and -CH_3 species. Interestingly, DOL does not dissociate against Li_2S—making it a better diluent than DME—consistent with the team's experiments. In both cases ([PYR14][TFSI] and DOL-DME with Li_2S-cathode), the fluorine atoms obtained from the dissociation of [TFSI] bind with lithium of the cathode to form new Li-F bonds, which could enhance interfacial stability.

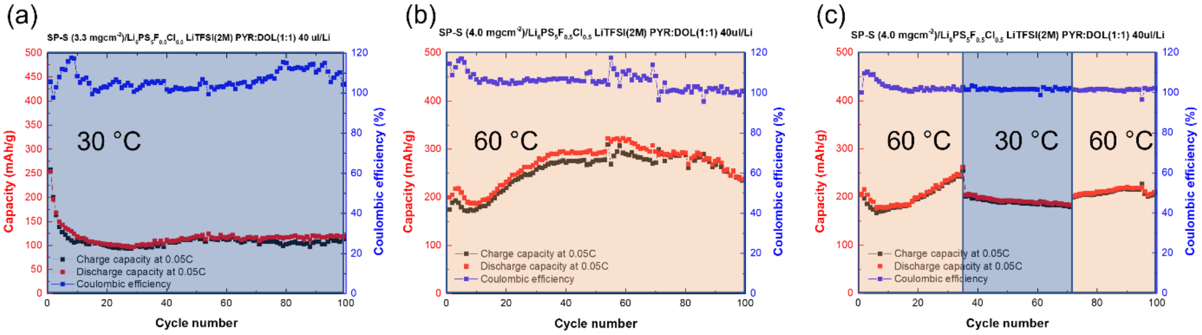

Figure 77. Performance of battery with Super-P cathode at high S-loading (4 mg/cm^2) functionalized with 40 µL functionalizing liquid containing 2 M LiTFSI in PYR14:DOL (1:1), $Li_6PS_5F_{0.5}Cl_{0.5}$ sulfide solid-state electrolyte, and lithium anode cycled at (a) 30°C, (b) 60°C, and (c) temperatures alternating between 60°C and 30°C. All batteries cycled at C/20 rate.

Fabricate Battery with Optimized Cathode, Sulfide SSE, and Lithium Anode. To achieve high S-loading (> 4 mg/cm^2), the team employed two strategies, namely (a) water-based binder chemistry, and (b) engineering cathode architecture (using CNCs to host sulfur or sulfide SSE)—both also using porous aluminum collectors.

The team first used a cathode architecture consisting of Super P-S (1:3) 88 wt%, CNT 8 wt%, and carboxymethyl cellulose (CMC) 4 wt%. Figure 77 compares the electrochemical performance of batteries with Super P-S cathode with 4.0 mg/cm^2 sulfur loading, $Li_6PS_5F_{0.5}Cl_{0.5}$ sulfide SSE, and lithium anode with 40 µL

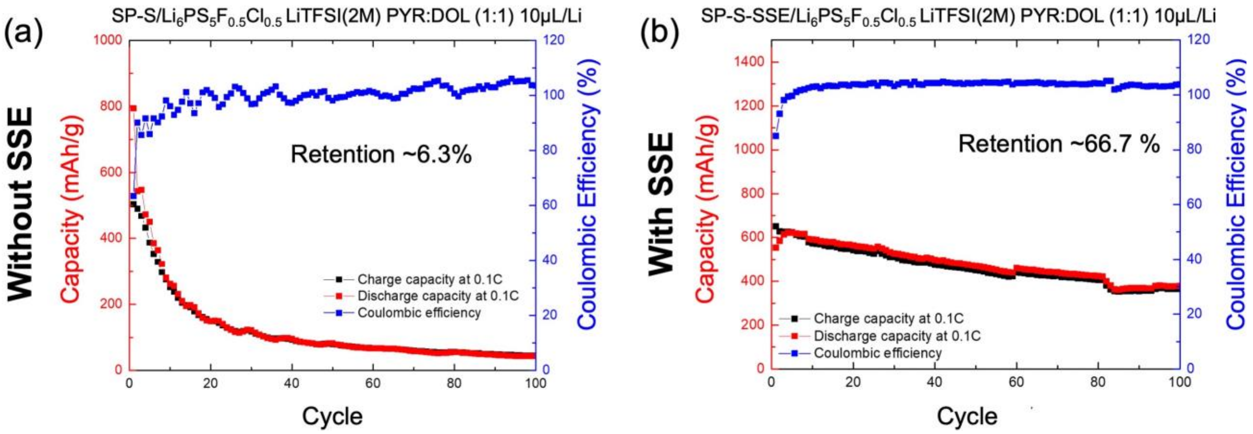

Figure 78. Electrochemical performance of battery consisting of Super P-S cathode with 0.7 mg/cm^2 loading functionalized with 10 µL functionalizing liquid containing 2 M LiTFSI in PYR14:DOL (1:1), $Li_6PS_5F_{0.5}Cl_{0.5}$ sulfide solid-state electrolyte (SSE), and lithium anode (a) without any sulfide SSE in cathode and (b) when SSE is drop casted onto the cathode.

functionalizing liquid containing 2 M LiTFSI in PYR_{14}:DOL(1:1) at 30°C and 60°C. At 30°C, the battery shows an initial discharge capacity of ~ 250 mAh/g, which fades away quickly (within first 10 cycles) to ~ 100 mAh/g. However, after this initial fade, the capacity remains steady at ~ 100 mAh/g, even after 100 cycles (Figure 77a). Interestingly, cycling tests at 60°C showed an increase in capacity from an initial value of ~ 200 mAh/g to ~ 250 mAh/g at 100 cycles (Figure 77b). This anomalous behavior is likely due to the temperature-induced lowering in viscosity of functionalizing IL, and the consequent favorable reaction kinetics. This hypothesis is supported by the team's electrochemical tests alternating between 30°C and 60°C (Figure 77c). Over the initial 30 cycles when the battery is cycled at 60°C, they observe a steady increase in capacity. This is followed by a capacity fade when the temperature is lowered to 30°C (cycles 35-72), and by a slight increase in capacity when the temperature is subsequently increased to 60°C. A detailed spectroscopic analysis of the interfaces is ongoing to understand the effect of temperature on the interfacial reactions.

To make rapid advances in ASSLSBs, it is crucial to minimize the amount of functionalizing liquid. Incorporating sulfide SSE in the cathode on the battery performance can provide ion conduction pathways and enable much lower amounts of functionalizing liquid. To optimize the process of incorporating sulfide SSE in the cathode, the team first fabricated batteries with low sulfur loading of ~ 0.7 mg/cm^2 and a low amount of functionalizing liquid (10 µL), as shown in Figure 78. Indeed, the team observes that in the absence of any sulfide SSE in the cathode, the scarcity of IL functionalization drives a rapid capacity fade, from an initial value of ~ 800 mAh/g to ~ 50 mAh/g, yielding a poor capacity retention (~ 6%), as shown in Figure 78a. On drop casting 100 µL of solution of sulfide SSE in anhydrous ethanol (10 wt%) onto the cathode, capacity retention improves dramatically, yielding a capacity of ~ 400 mAh/g after 100 cycles (Figure 78b). This clearly suggests that incorporating sulfide SSE into the cathode provides an excellent route to reduce the amount of functionalizing liquid. However, it is challenging to extend this technique to high S-loading, owing to the need for water-based binders at high S-loading.

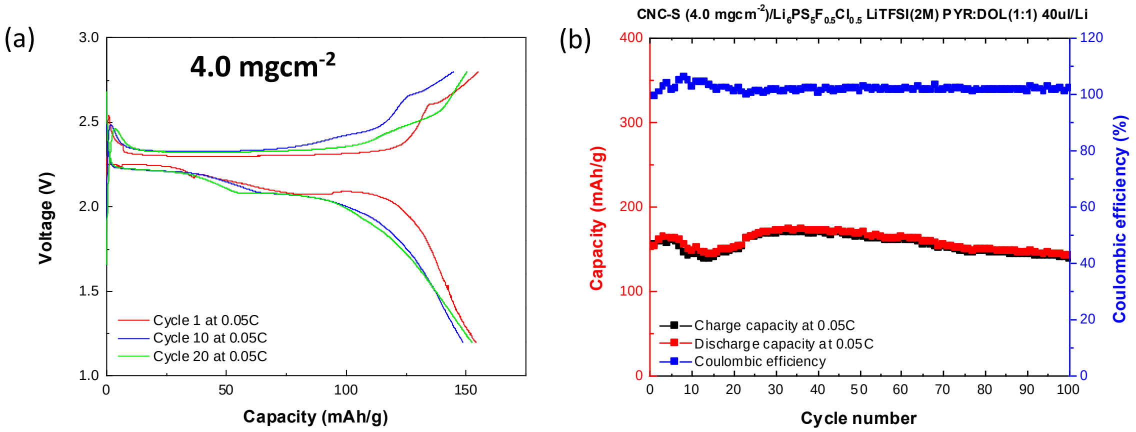

Figure 79. Performance of battery with carbon nanocages cathode at high S-loading (4 mg/cm^2) functionalized with 40 µL functionalizing liquid containing 2 M LiTFSI in PYR14:DOL (1:1), $Li_6PS_5F_{0.5}Cl_{0.5}$ sulfide solid-state electrolyte, and lithium anode cycled at 60°C at C/20 rate. (a) Charge-discharge curve at 1, 10, and 20 cycles. (b) Charge/discharge capacity (shown in black/red) and Coulombic efficiency (shown in blue) during battery cycling.

An effective way to concomitantly achieve good sulfide SSE incorporation and high S-loading is to employ mesoporous cathode architectures made up of interconnected CNCs. Such a network can provide necessary electronic conductivity; additionally, the size of the hollow CNCs can be tuned to achieve desired S-loading and incorporation of sulfide SSE. This quarter, the team first focused on fabricating batteries with CNC cathodes at high S-loading without any sulfide SSE incorporation. They prepared a cathode consisting of CNC-S (1:3) 85 wt%, CNT 10 wt%, CMC 5 wt%, and coated onto an aluminum current collector using the doctor blading technique. Figure 79 shows the performance of a battery with CNC-S cathode with 4.0 mg/cm^2 sulfur loading and functionalized with 40 µL 2 M LiTFSI in PYR:DOL (1:1), $Li_6PS_5F_{0.5}Cl_{0.5}$ sulfide SSE, and lithium anode at 60°C. It showed an initial discharge capacity ~ 150 mAh/g, with a slight decrease of the capacity in the first 10 cycles. Then, the capacity started to increase again, retaining its value at ~ 140 mAh/g after 100 cycles

(Figure 79). Although these results show promise, further engineering of ionic/electronic conductivity of cathode is essential to improve battery performance. The team is exploring several strategies including (a) adding more CNT to improve electronic conductivity of cathode, (b) engineering porosity of the cathode, and (c) adding sulfide SSE into cathode to improve its ionic conductivity and minimize the amount of functionalizing IL.

Patents/Publications/Presentations

Publication

- Kempaiah, R., H. Chan, S. Srinivasan, S. Sankaranarayanan, B. Narayanan, and A. Subramanian. “Impact of Stabilizing Cation on Lithium Intercalation in Tunneled Manganese Oxide Cathodes.” *ACS Applied Energy Materials* 4, No. 11 (2021): 12099–12111. doi: 10.1021/acsaem.1c01598.

Task 3.10 – Predicting the Nucleation and Evolution of Interphases in All-Solid-State Lithium Batteries

(Sabrina (Liwen) Wan, Lawrence Livermore National Laboratory)

Project Objective. The goal of this project is to develop and apply a suite of new computational tools to predict early-stage formation of metastable interphases in SSBs. To achieve this goal, this project focuses on meeting three primary objectives corresponding to different regimes within the early-stage interphase formation: (1) identify chemical motifs for pre-nucleation; (2) predict possible interphase structures; and (3) model the kinetics of interphase formation.

Project Impact. Degradation of SSE and formation of undesired secondary interphases at the solid electrolyte/electrode interfaces are some of the key issues that limit SSB technology from practical applications. The computational tools developed in this project will allow modeling of nucleation and formation of interphases with quantum-level accuracy and significantly improved efficiency compared to currently available methods. Completion of this project will also provide valuable insights into the correlation between local chemistry and interphase formation, which can be used to inform design of interfacial structures to lower interfacial resistance and to extend cycling life of SSBs.

Approach. The project approach centers on close integration of *ab initio* simulations, ML, and stochastic methods to probe chemistry and nucleation across broad ranges of time and length scales. First, the team will identify chemical motif, which acts as chemical precursor for pre-nucleation based on ML and large-scale AIMD simulations. Second, they will predict possible interphase structures based on stochastic minimizations of population-weighted chemical motifs identified from the MD simulations. Third, they will model the kinetics of interphase formation and evolution using KMC. To test the general applicability of the proposed computational methods, the team considers a variety of commercially viable SE and cathode materials, including cubic LLZO and LiPON SEs, and LCO and LFP cathodes. These materials also represent a range of degrees of stability arising from their intrinsic properties—in particular, LiPON|LCO, LLZO|LCO, and LLZO|LFP are expected to form stable, less stable, and reactive interfaces, respectively.

Out-Year Goals. The future goal is to predict practical strategies either to facilitate formation of the desired interphase that allows for fast Li^+ diffusion and is stable on cycling or to suppress the formation of undesired interphase to reduce interfacial impedance of ASSBs.

Collaborations. There are no collaborative activities this quarter.

Milestones

1. Identify chemical precursors for interphase formation. (Q1 FY 2021; Completed)
2. Construct initial interphase structures. (Q2, FY 2021; Completed)
3. Identify proper constraints for global optimization. (Q3, FY 2021; Completed)
4. Obtain possible interphase structures and compositions. (Q4, FY 2021; In progress)

Progress Report

Global Optimization to Identify Formation of Secondary Phases at the Solid Electrolyte/Cathode Interface. This quarter, the team continued efforts to characterize distinct interphase structures for LLZO|LCO interfaces. From last quarter, they identified optimum parameters for global energy minimization using the Basin Hopping algorithm. This allows them to efficiently sample the potential energy surfaces of random structures with an aim to identify low-energy meta-stable phases for distinct interphase nuclei identified in the previous quarter. Here, they present results for identifying a stable $LaCoO_3$ phase using the global energy minimization algorithm. To speed up the sampling of complex potential energy surfaces of $LaCoO_3$, they generated seven distinct starting $LaCoO_3$ configurations with varying cell symmetries. Figure 80a-c shows examples of three distinct starting configurations for $LaCoO_3$. Figure 80d-f shows the energy variations for distinct random structures sampled through the Basin Hopping algorithm, starting from the generated initial configurations in Figure 80a-c, respectively. The inset shows some of the identified local minima from sampling the potential energy surface of $LaCoO_3$. The random structures are generated by perturbing the cobalt and lanthanum cations by 0.1 Å for every consecutive structure starting from the initial structures.

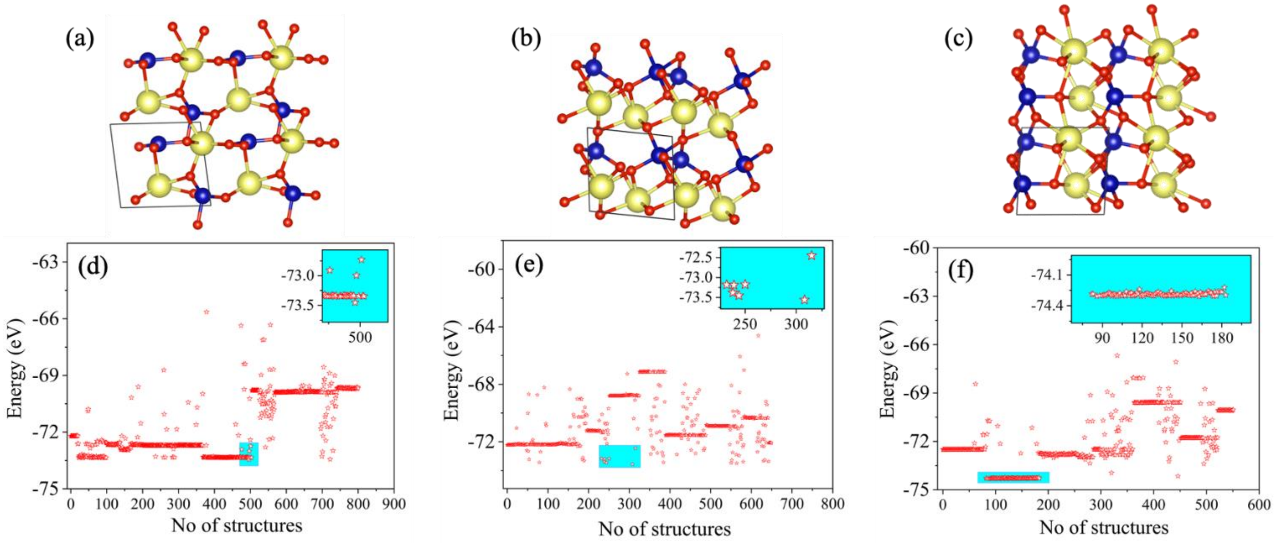

Figure 80. (a-c) Three distinct initial $LaCoO_3$ configurations for the interphase formation nuclei identified from the *ab initio* molecular dynamics sampling of the LLZO|LCO interfaces. (d-f) Energy variations during Basin Hopping for the random structures generated from the initial configurations. The inset in (d-f) shows identified local minima among the sampled random structures. Lanthanum, cobalt, and oxygen ions are represented by yellow, blue, and red spheres, respectively, in the structure representations.

Overall, the team has sampled more than 8000 random structures for $LaCoO_3$, from which more than 50 local minima (based on the energy) were collected from the energy variation plots, as shown in Figure 80d-f. These local minima were further relaxed to identify the lowest energy meta-stable phases of $LaCoO_3$. Figure 81 shows examples of structural evolution, from initial configuration to the identified meta-stable phases during Basin Hopping, and to the final fully relaxed meta-stable phase of $LaCoO_3$. Solid-state NEB calculations are being performed to compute the activation energies for such phase transformation from a random seed to a meta-stable phase. A continued search for identifying other meta-stable interphase structures as well as obtaining the corresponding activation energies will allow the team to better understand the kinetics of interphase nucleation and formation at the LLZO|LCO interfaces and the relation to processing and cycling conditions.

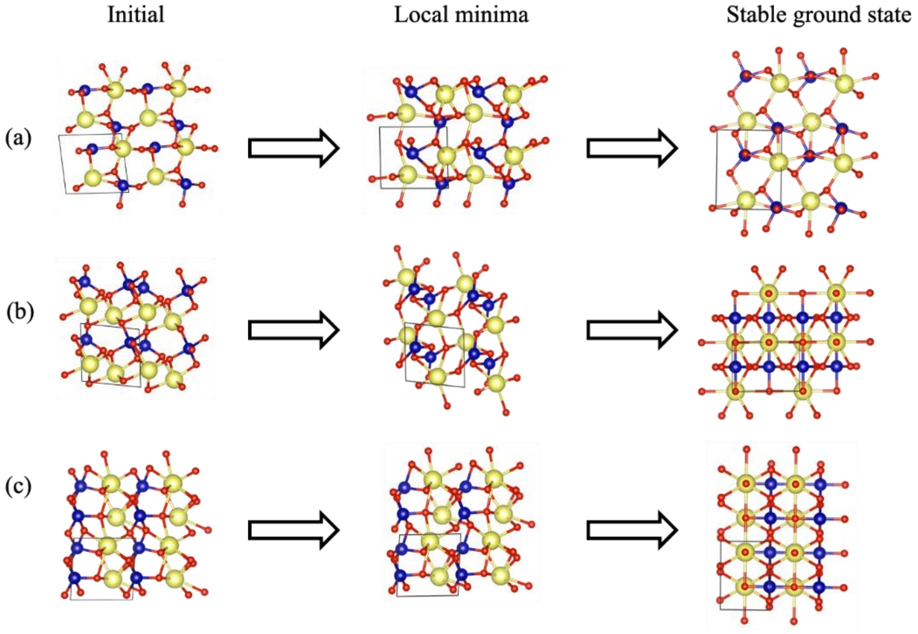

Figure 81. Hypothetical phase transformation pathways to form various meta-stable $LaCoO_3$ phases.

Patents/Publications/Presentations

The project has no patents, publications, or presentations to report this quarter.

Task 3.11 – Design of Strain Free Cathode – Solid-State Electrolyte Interfaces Using Chemistry-Informed Deep Learning
(Hakim Iddir, Argonne National Laboratory)

Project Objective. The main objective of this project is to use state-of-the-art ML techniques and high-performance computing (HPC) to model complex oxide materials that will allow the team to develop cathode – SE interfaces that exhibit minimal or no strain as well as provide chemical stability at the interface between the cathode material and the SSE. A deep understanding and control of the cathode/SSE interface (including its chemical and mechanical stability) is needed to develop an effective SSB. The active cathode material changes volume during cycling, particularly at high task SOC. This volume change leads to strained interfaces triggering loss of contact and delamination, and hence reduction/elimination of electron and ion transport pathways. The increased strain could also generate cracks within the SSE, creating new paths for lithium dendrite growth channels. These structural changes degrade the electrochemical performance of the battery. Several strategies have had limited success in alleviating these drawbacks, including mixed SSE, buffer layers between the cathode and the SSE, and dopants to improve chemical stability of the interface. These approaches, although promising, could not resolve issues with both the chemical and mechanical stability of the interface. In this project, the team proposes a new approach that takes advantage of well-established ML techniques and HPC to screen for candidate dopants of high-Ni-content NMC cathodes that would both reduce the volume expansion and the chemical reactivity (mixing) at the interface, with minimum impact on electrochemical performance and energy density of the cathode.

Project Impact. Structure-property relationships are at the heart of most fundamental scientific approaches. However, the link between structure and property remains a challenge in the materials science of complex systems, such as the oxides that form battery components. In particular, the chemical and mechanical stability of the cathode-SSE interface presents a challenge to development of SSBs. High-performance DFT calculations provide the necessary framework to understand such systems. Unfortunately, given the limited number of atoms and time scales accessible by the method, along with the myriad calculations required to achieve satisfactory results, the computational cost of simulating all the possible configurations of a multicomponent oxide is prohibitive. In this work, the team augments the DFT data with ML (especially deep learning) techniques that allow them to access the large system sizes and longer time scales necessary to build thermodynamic models. They focus on understanding the nature of benchmark $Li_{1-\alpha}Ni_{1-x-y-z}Mn_xCo_yM_zO_2$ structures (M dopant, α, x, y, $z < 1$), their volume change with lithium content, the nature and concentration of the dopants, and chemical stability of the SSE-cathode interface. The DFT and ML approach will provide new cathode compositions that will reduce the strain of the SSE-cathode interface and hence improve its mechanical and chemical stabilities.

In this project, the team aims at developing a methodology that will allow them to explore and expand the configurational space using HPC approaches in a systematic and efficient way. The methodology will encompass DFT, AIMD, MD, and ML. The methodology will also take advantage of various software already developed at ANL and at other DOE laboratories (for example, Balsam) to automate, manage, and control the large number of calculations needed to achieve the project goal.

Approach. All calculations will be performed by spin-polarized DFT as implemented in the Vienna *ab initio* simulation package (VASP). After geometry optimization within the DFT+U framework, electronic relaxation will be performed using a single-point calculation with the hybrid functional HSE06. For production calculations, they will use the message-passing interface (MPI) parallelized version of VASP.

Exploration of the potential energy surface is needed to predict the structure of solid materials and interfaces. Such calculations are infeasible using MD or DFT calculations alone. Thankfully, the potential energy surface of a system can be represented by the sum of the energies of the local neighborhoods surrounding each atom. This enables the use of ML surrogate models trained with DFT calculations to capture the energies in local neighborhoods. The input to the ML surrogate must be a unique representation of the system under study.

Consequently, the local environment of each ion is described using a local environment descriptor that renders the atomic configuration invariant to rotations, translations, and permutations of the atoms. In recent years, several different descriptors have come to prominence with advantages and disadvantages. Once the ML surrogate is trained, the total energy and forces over all the ions of any structural configuration can be determined. Such information can be used for atomistic simulations, namely, MD and MC.

In this project, the team proposes to use the open-source DeepMDkit python/C++ package to construct the ML potential energy surface and FFs. The promise of DeepMDkit in this work is to provide near-DFT accuracy at orders-of-magnitude lower computational expense, comparable to traditional MD simulations. Efficiency in training is facilitated through integration with TensorFlow and MPI / graphics processing unit support.

One of the challenges of developing ML potential energy surface is achieving accurate predicted forces and energies across the entire configurational space, while minimizing the total number of calculations required for training. In recent years, active learning has been highlighted for its ability to target training examples most likely to improve the model quality or to achieve some other objective (that is, maximizing a predicted material property). DP-GEN, an open source python package based on DeepMDkit, implements a similar active learning scheme with HPC support, and has been employed to construct ML potential energy surface with accuracy approaching DFT and sometimes exceeding embedded atom potential for experimentally measured properties of interest. In this work, the team proposes to leverage DeepMDkit and DP-GEN to efficiently generate ML potential energy surfaces for cathode-electrolyte systems including a variety of dopants.

Out-Year Goals. One out-year goal involves developing a DFT-trained ML model on NMC/LLZO interface, ready to use for large screening of new cathodes, SSE compositions, and cathodes/SSE interfaces. A second is to provide fundamental understanding on critical parameters limiting performance and stability of the cathode/SSE interface and hence of the SSB.

Collaborations. Project collaborators include J. Croy, C. Johnson, and E. Lee from ANL Chemical Sciences and Engineering Division for the synthesis phase of the project.

Milestones

1. Determine volume changes and phase transformation during charging for $LiNiO_2$ using the developed DFT-trained ML model. (Q1, FY 2021; Completed)
2. Determine elemental segregation, volume changes, and phase transformation during charging of $Li(Ni_{0.8}Mn_{0.1}Co_{0.1})O_2$ using the developed DFT-trained ML model. (Q2, FY 2021; Completed)
3. Extend solid bulk models to include surfaces and dopants. (Q3, FY 2021; Completed)
4. Apply ML model to understand mechanical and chemical interactions on CEIs. (Q4, FY 2021; In progress)

Progress Report

Effect of Dopants on Ni-Rich Cathode Volume Change on Delithiation

The team has submitted the manuscript on $LiNiO_2$ anisotropic volume change. They are now modeling mitigation strategies to avoid excessive strain caused by the collapse of the lattice on delithiation, using $LiNi_{0.8}Mn_{0.1}Co_{0.1}O_2$ (NMC-811) as a benchmark material. Since low-cobalt or no-cobalt materials are desirable, they focus on dopants that substitute cobalt ions first. Dopants can change the lithium and cation distribution. To accomplish this task, they have developed a software to automatically dope and generate configurations under certain constraints, to limit the search space to a more manageable extent. They generated configurations for the doped material with a Li/Ni exchange up to 9%, cobalt and manganese confined to the TM layer, and the dopant located in either the TM layer or the lithium layer. The simulation cells for NMC-811 are smaller than what the team used originally for the TM configurations in previous calculations, to allow them to cover a wide array of possible configurations, including some highly symmetric cells that generated new low-energy configurations. These cells are four times smaller, 108 versus 432. In the large cell, it was possible to include 3 cobalt and 3 manganese per TM layer. The real composition of these large cells is 83.4% nickel, 8.3% cobalt, and 8.3% manganese. In the small cell, the team can only include 2 cobalt and 2 manganese per TM (keeping the composition constant per layer), and the overall composition is 77.8% nickel, 11.1% cobalt, and 11.1% manganese. Given the size and imposed constraint, they were able to generate all configurations of the search space (more than 60 million). All the algorithms have been coded in python. The ML model fitting is being performed using DeepMDkit, as indicated in previous reports. The approach is shown in the schematic in Figure 82. During an undergraduate summer internship program, the team trained an undergraduate intern and performed a test of this workflow on Nb-doped and Al-doped NMC (432 atom cell) on a subset of 700,000 configurations for a dopant composition of 1 niobium or 1 aluminum substituting for 1 cobalt; they found that Al-doped NMC mitigated the volume change slightly better than Nb-doped NMC. This test showed that the ML-based approach could arrive at a DFT-verified lower energy configuration out of 700,000 configurations within a couple of days.

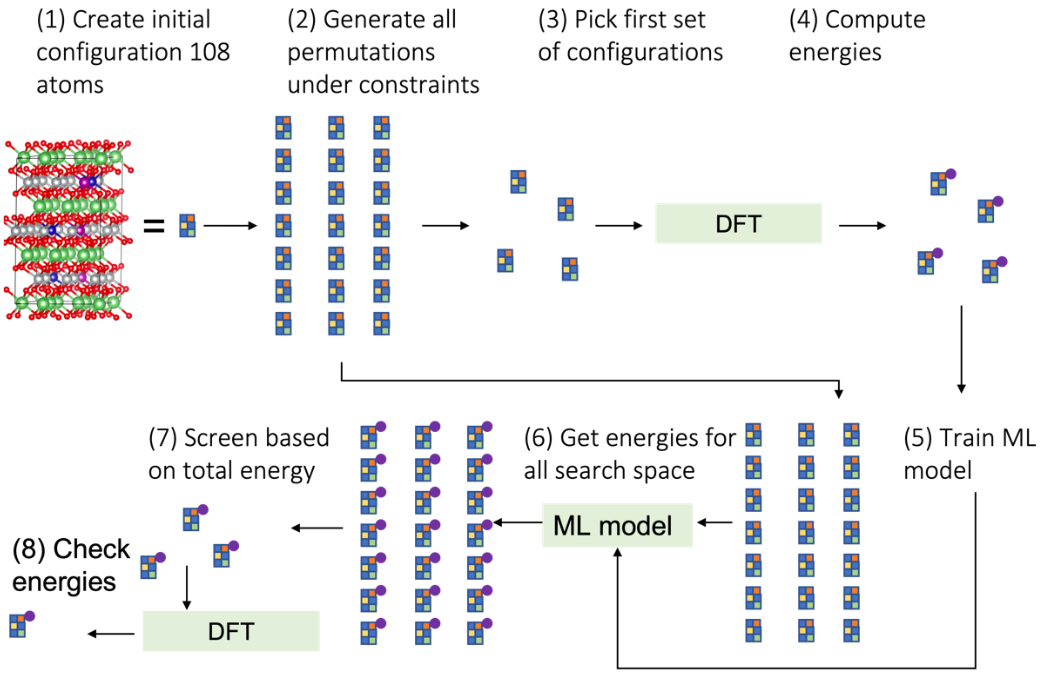

Figure 82. Schematic of workflow to obtain the lowest energy configurations of fully lithiated doped NMC-811.

Cells with the lowest energy configurations will be delithiated to ~ 4% lithium content, and distribution of lithium within the material will be tested in a similar fashion. Finally, volume change and other properties will be computed. The effect of temperature will be considered using MD simulations with the ML potential.

It is important to highlight that, given the large number of dopants planned for the screening, the GGA+U approach presents new challenges, such as finding the most appropriate U values for dopants, which are not always available. Hence, the team tested and set up a DFT procedure using the novel "r^2SCAN"[1] plus Van der Waals corrections D3/D4. This is a regularized variant of the strongly constrained and appropriately normed semi-local density functional "SCAN" that includes semi-classical London dispersion corrections. It has the speed of generalized gradient approximations, while approaching the accuracy of hybrid functionals. The team found that if they start from a previously optimized geometry and wavefunction using the functional optB86b-vdW, the convergence of the r^2SCAN-D3 simulation is reliable and fast. Also, they are taking advantage of the GPU nodes on Argonne's Laboratory Computing Resource Center (LCRC) Swing cluster to speed up the calculations.

Cathode Solid Electrolyte Interfaces Analysis

To understand the strain issues on solid-state Li-ion batteries, the team built simulation cells with minimum initial strain between the materials. Using a proprietary software, they generated a total of 2517 interfaces between LZO/LLZO and LNO/NMC cathodes. The interfaces span various conditions, as cathode facets (104)/(012)/(001), planar (ab) strain, buffer space between materials, vacuum space surrounding the materials, and slab thickness. To make the ML model flexible and accurate, the team needs to explore as many different systems as possible. A representative model interface is shown in Figure 83. The model has 243 atoms and is composed of three layers of LNO and half a unit cell for LLZO surrounded by vacuum space. The initial average misfit in the *ab* plane is ~ 2%. Given the size of these supercells (even with all compromises taken), the team also built smaller LZO-cathode interfaces to generate more training data for the ML model. DFT simulations are running in the team's available computational clusters at Argonne's LCRC (Bebop/Swing) and NREL HPC facilities (Eagle/Swift). Software that automates all the workflow, including the ML training, has been developed within the group.

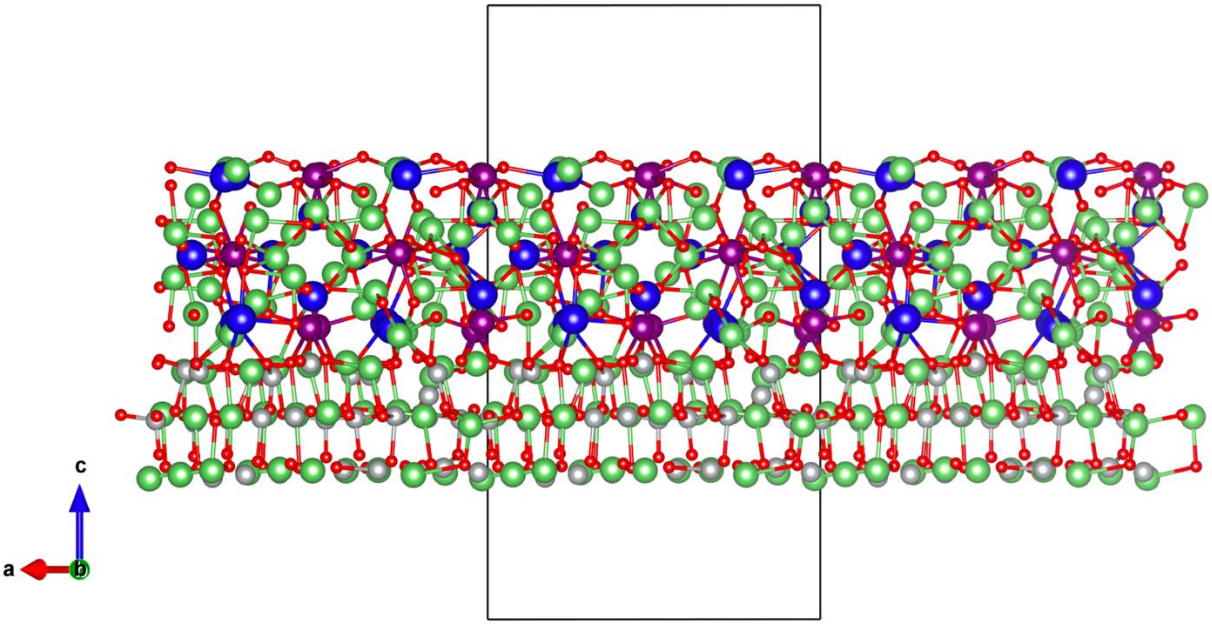

Figure 83. Representative $LiNiO_2$-LLZO interface model. Green, grey, red, blue, and purple spheres represent lithium, nickel, oxygen, lanthanum, and zirconium, respectively.

Reference

[1] Ehlert, S., U. Huniar, J. Ning, J. W. Furness, J. Sun, A. D. Kaplan, J. P. Perdew, and J. G. Brandenburg. “r^2SCAN-D4: Dispersion Corrected Meta-Generalized Gradient Approximation for General Chemical Applications.” *Journal of Chemical Physics* 154, No. 6 (2021): 061101. doi: 10.1063/5.0041008.

Patents/Publications/Presentations

Publication

- Garcia, J. C., J. Gabriel, N. H. Paulson, J. Low, M. Stan, and H. Iddir.* “Insights from Computational Studies on the Anisotropic Volume Change of Li_xNiO_2 at High States of Charge ($x < 0.25$).” *Journal of Physical Chemistry C* 125, No. 49 (2021): 27130–27139.

Presentation

- Northwestern – Argonne Institute of Science and Engineering (NAISE) Undergraduate Interns Symposium (August 1–16, 2021): “Exploring Solid-State Cathode Materials Space”; A. Tai, J. Gabriel, N. Paulson, J. Garcia, J. Low, and H. Iddir.

Task 3.12 – Tackling Solid-State Electrochemical Interfaces from Structure to Function Utilizing High-Performance Computing and Machine-Learning Tools

(Shinjae Yoo, Feng Wang, and Deyu Lu, Brookhaven National Laboratory; Nongnuch Artrith and Alexander Urban, Columbia University)

Project Objective. This project aims at elucidating the structural evolution and other dynamic properties of the interphases at the SSIs in SSBs under processing and electrochemical cycling conditions that strongly impact cell performance. By leveraging synergies of first-principles theory, HPC, ML, and computational/experimental spectroscopy, this project involves a comprehensive investigation of SE systems and SSIs that may enable the practical use of lithium anodes and high-nickel NMC cathodes in SSBs. Specific project objectives are as follows: (1) develop realistic atomic-scale structure models of the heterostructural SSIs, (2) determine the impact of structural evolution on the stability and transport properties of the SSIs, and (3) identify the coating/doping chemistry that may stabilize SSIs during formation and electrochemical cycling.

Project Impact. Interfacial properties and the dynamical evolution of interphase structures are crucial for the stability and performance of SSBs. This project will lead to fundamental understanding of current materials limits and will identify key materials parameters for optimizing the performance of SSBs. By corroborating atomic-scale theory with experiment, the project will identify structure–property relationships of the heterostructural SSIs in SSB systems that are relevant for EVs. The outcomes of this project will therefore accelerate development of high-energy-density, safe SSBs for EVs.

Approach. Accurate ML potentials will be trained on an extensive database from DFT calculations to simulate the structure evolution and electrochemical properties of the SSIs. Using a second ML model, key physical descriptors will be extracted from EELS and XAS measurements. This spectral fingerprinting will enable the automated interpretation of spectroscopy measurements, thereby bridging between atomistic modeling and experiment. An experimental platform will be developed to integrate experimental/computational spectroscopy and modeling of SSIs. In combination, the two ML models and the spectroscopic data will facilitate the construction of a physics-based model to unravel the structure-property relationships of the SSIs.

Out-Year Goals. The project will progress toward establishing dynamic composition-structure-property relationships for interface stability and transport within and across the electrochemical SSIs in SSBs. The ML approach will be further developed to a general model for thermodynamic and transport properties of dynamic heterostructural electrochemical interfaces and will eventually be applied to the practical SSB systems.

Collaborations. The project is collaborating with Y. Du at BNL.

Milestones

1. Complete mapping of the phase diagram and structure-stability-conductivity relationships in the glass/ceramic (*gc*) $Li_2S–P_2S_5$ (LPS) system. (Q1, FY 2021; Completed)
2. Characterize initial stages of the interfacial reaction of *gc*-LPS with lithium metal using ML-augmented DFT and XAS spectroscopy. (Q2, FY 2021; Completed)
3. Correlate characteristic structural motifs of *gc*-LPS and the *gc*-LPS/Li interface with XAS spectral features using ML. (Q3, FY 2021; Completed).
4. Determine formation and evolution mechanisms of *gc*-LPS/Li interphases using XAS measurements and ML models. (Q4, FY 2021; Completed)

Progress Report

This quarter, the team used a combination of electrochemistry, X-ray spectroscopy, and data analytics to investigate electrochemical decomposition of *gc*-LPS electrolyte outside its electrochemical stability window, and formation and evolution of the *gc*-LPS/Li interphases. XPS studies revealed the oxidative sulfur and phosphorus species from LPS decomposition. Trends in the experimental sulfur K-edge XANES spectra of the *gc*-LPS/Li interphases were correlated with the computational spectral databases (reported in the previous two quarters), suggesting that oxidative sulfur species likely contain corner sulfur atoms with low lithium CNs and bridging S-S motifs. Evidence of forming resistive Li_2S species in the *gc*-LPS/Li interphases was also obtained by X-ray spectroscopy, providing insights into the impedance increase of the LPS/Li interface during cycling.

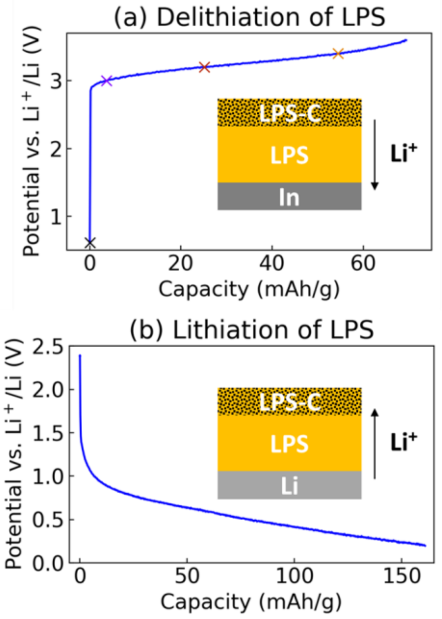

Figure 84. Constant current delithiation (a) and lithiation (b) of LPS-C composite. Insets show cell configuration. The markers in (a) indicate the states that the samples were prepared for X-ray absorption spectroscopy measurement.

Spectroscopic Studies of Electrochemical Instability of LPS Electrolyte

Sulfide-based SEs undergo oxidative (reductive) decomposition when the potential is above (below) the electrochemical stability window. In this study, the team focused on the potential-dependent reactivity of LPS electrolyte itself, that is, LPS works as the active material instead of as an electrolyte in a battery cell, as illustrated in the inset of Figure 84. Similar redox reactions of LPS are expected to occur at the anode-electrolyte or cathode-electrolyte interfaces in SSBs, so this study will help to understand the mechanism of SSI formation and evolution. To improve the signal-to-noise ratio in the XAS measurement, LPS powder was mixed with carbon black (a non-active material), and the LPS-C composite electrodes were fabricated. In the composite, the interface reaction occurs at the surface of each LPS particle, which greatly enhances the spectral signal of the reaction products, as compared to samples without carbon black, where the reaction occurs only in the first few tens of nanometers over the entire electrolyte pellet surface.

Galvanostatic cycling with potential limitation (GCPL) was conducted on the LPS-C composite, as shown in Figure 84a-b. In the delithiation experiment (Figure 84a), LPS-C was cycled versus indium foil and oxidized; in the lithiation experiment (Figure 84b), LPS-C was cycled versus lithium foil and reduced.

The team performed XPS measurements on pristine and delithiated samples, as shown in Figure 85. The delithiated samples were measured at the end of the process, where most of the chemical changes have occurred. They observed oxidative changes in both sulfur 2p and phosphorus 2p spectra, as shown by the emergence of new doublet peaks at higher binding energies corresponding to oxidized sulfur and phosphorus species.

The change in sulfur 2p is more pronounced than that in phosphorus 2p spectra. The binding energy of the new doublets in the fits indicates the formation of bridging sulfur bonds, possibly associated with the phosphorus- and sulfur- containing species like S_8, P_2S_5, $P_2S_8^{4-}$, $P_2S_7^{4-}$, and $P_2S_6^{2-}$, as reported in literature.[1-3]

To further elucidate the delithiation reaction and identify the reaction products, sulfur K-edge XANES spectra were taken from LPS samples cycled to different potentials, as indicated by the markers in Figure 84a. Figure 86a shows the measured spectra of the delithiated (oxidative decomposition) samples. The XANES spectrum of the pristine sample has three pronounced features, including a main peak near 2470 eV, a smaller peak near 2471.5 eV, and a broad peak at 2475 eV, consistent with the team's previous results (as in the second quarter report). During delithiation, the intensity of the peak at 2470 eV decreases, while the small peak at 2471.5 eV becomes stronger as the voltage increases. This spectral feature has been attributed to an increasing number of S-S bonds in the literature.[4]

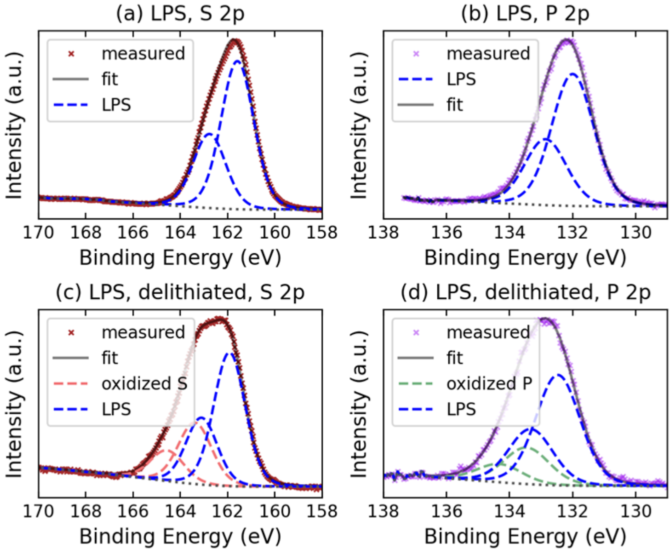

Figure 85. X-ray photoelectron spectroscopy measurements and fitting of the sulfur 2p and phosphorus 2p for the pristine LPS (a-b) and delithiated LPS (c-d), respectively.

Further atomic scale insights can be drawn by correlating the trend in the sulfur K-edge XANES spectra during the LPS redox reactions with the computational LPS structure and spectral databases developed in the second and third quarters. The project's structure database contains a large variety of $(Li_2S)_x(P_2S_5)_{1-x}$ compounds in the LPS phase diagram. As this database does not contain any (de)lithiated LPS structures, the team focuses their analysis on the local chemical environment of the sulfur atoms, because XANES measurement is well known as a local probe.

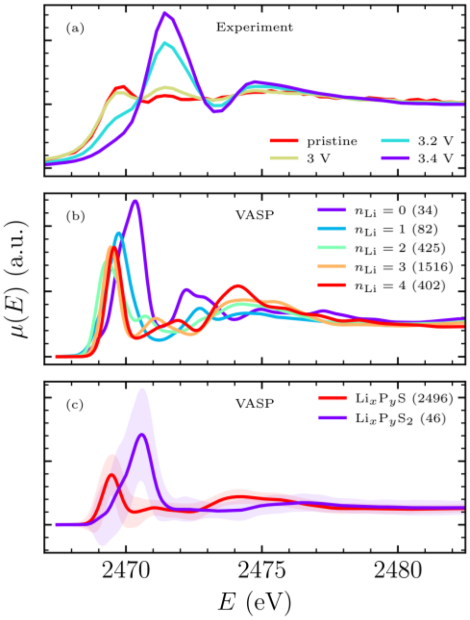

Figure 86. (a) Experimentally measured sulfur K-edge X-ray absorption spectra of LPS in the fluorescence mode, including pristine LPS and samples at different states of oxidation decomposition (as marked in Figure 84). (b) Average VASP spectra binned by the number of lithium neighbors adjacent to the absorbing site. (c) Average VASP spectra for absorbing sulfur atoms that have no adjacent sulfur atoms, and those that contain an S-S bond. Error regions (shaded areas) correspond to a single standard deviation.

At the beginning of the LPS delithiation, corner sulfur atoms may lose their lithium neighbors. As the oxidative reaction progresses, under-coordinated sulfur atoms in nearby phosphorus tetrahedra are likely to form S-S bonds.[4] To validate this hypothesis, the team analyzed two local structure descriptors, that is, the lithium and sulfur CNs of the sulfur absorbers, which are correlated with the trend in sulfur K-edge XANES, as presented in Figure 86. As shown in Figure 86b, the team found that as the local lithium coordination increases, the main peak at ~ 2470 eV moves to lower energies with decreasing intensity (n_{Li} from 4 to 2). At an even lower lithium coordination (n_{Li} = 1 and 0), the peak moves to higher energy with increasing intensity. Although the position of the higher energy peak is lower in energy as compared to the experiment, the overall trend is in qualitative agreement with the experiment. In Figure 86c, they analyzed the spectral signature of S-S bonds. Structures with S-S bond on average exhibit a stronger peak at higher energies (near 2471 eV) than those without S-S bond.

Note that the team's analysis is not exhaustive, as it is possible that new local structure motifs outside their structure database may emerge in the delithiated LPS compounds. Nevertheless, their sulfur K-edge XANES analysis suggests that corner sulfur atoms with low lithium CNs and bridging S-S motifs are possible oxidative sulfur species, which belong to the products of the LPS decomposition on electrochemical oxidation. These products are detectable by XAS from above 3 V versus Li^+/Li. Since the changes in XAS spectra can only be distinguished when the reaction products accumulate to bulk level, the onset of the reaction could start below 3 V, which is in agreement with the fact that the galvanostatic cycling in Figure 84a shows ~ 4 mAh/g capacity before reaching 3 V. The study of the intrinsic redox reactions helps to explain the high resistance in cathode-LPS composite electrodes and provides a basis for determining the functional voltage range of LPS. The method used here should be generally applicable to the characterization of other sulfide electrolytes, such as argyrodite sulfides that the team plans to study next fiscal year. They have also collected sulfur K-edge XANES data on LPS with different lithiation states, and work is in progress to analyze these data. Next quarter, they plan to also collect phosphorus K-edge XAS data to help further resolve the reaction of LPS decomposition.

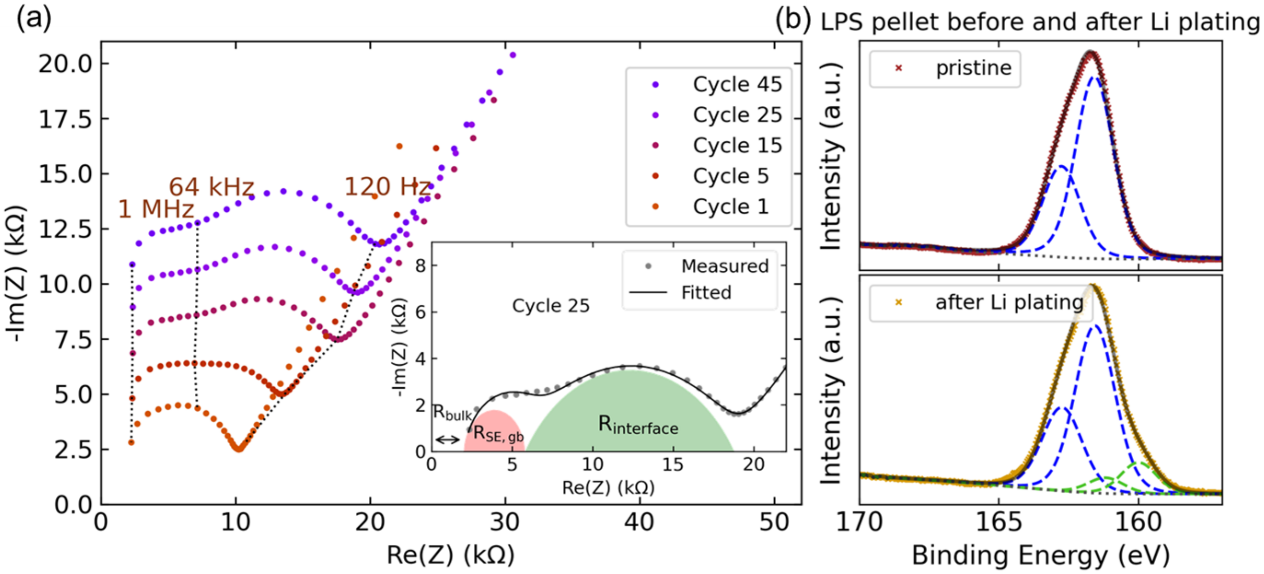

Figure 87. (a) Impedance spectra of a Cu|Li|LPS|Cu cell at different cycle numbers. The spectra are vertically shifted for clarity. An example of the fitting of the Nyquist plot using the equivalent circuit model (R(RQ)(RQ)Q) is shown in the inset. (b) Sulfur 2p spectra from LPS pellets. Top: Pristine LPS pellet. Bottom: LPS pellet after lithium plating. In each subfigure, markers indicate the measured data, the solid black line is the fitting result, and dashed lines are from the different species used in the fitting.

Interface Reaction between Lithium Anode and LPS Electrolyte

EIS and XPS were used to study formation and evolution mechanisms of the *gc*-LPS/Li interphases. A Cu|Li|LPS|Cu cell was assembled to measure the LPS/Li interface reaction at different cycles, where the lithium electrode was on one side of the LPS pellet, and the other side only had the copper current collector. After lithium is plated onto the copper current collector, this cell is equivalent to the symmetric cell.

EIS measurements were performed to monitor the increase in interfacial resistance during cycling, with spectra recorded in the frequency range from 1 MHz to 100 mHz. Figure 87a shows the evolution of cell impedance with cycling, and the inset shows the equivalent circuit fit of the spectrum at cycle 25. The team observed that the cell's bulk resistance (frequency > 1MHz) and the GB resistance of the electrolyte (high-frequency range) changed very little, while the interface resistance (low-frequency range) increased significantly with cycle number, indicating the formation of a highly resistive interphase layer. Additionally, most of the increase in the interfacial resistance occurred in the first 15 cycles rather than in cycles 15-45. They infer that this is caused by the substantial growth of the interphase layer in the early cycles and slows down after tens of cycles.

The team used XPS to characterize the reaction products in LPS after lithium plating. During cycling, lithium is electrochemically deposited on the copper foil side and reacts with the sulfide SE. They peeled off the copper foil after 30 cycles and measured the reacted SE surface by XPS. Figure 87b shows the sulfur 2p spectra of pristine and cycled LPS. In the pristine sample, the doublet peak at ~ 161.5 eV is attributed to non-bridging sulfur (S^-) from LPS.[5] In the Li-plated sample, a shoulder is observed at the lower binding energy side, indicating the formation of reduced sulfur species. The fitted doublets at 159.9 eV binding energy are attributed to sulfide ions (S^{2-}), which could be the formation of Li_2S. This explains the highly-resistive interphase between lithium and LPS observed in the EIS study. The team will extend this study next fiscal year to track the formation and growth of the interphase layer, and to investigate how coating/doping can limit the formation of resistive interphase layers and mitigate adverse effects on cell performance.

References

[1] Koerver, R., I. Aygün, T. Leichtweiß, C. Dietrich, W. Zhang, J. O. Binder, P. Hartmann, W. G. Zeier, and J. Janek. "Capacity Fade in Solid-State Batteries: Interphase Formation and Chemomechanical Processes in Nickel-Rich Layered Oxide Cathodes and Lithium Thiophosphate Solid Electrolytes." *Chemistry of Materials* 29. No. 13 (2017): 5574–5582.

[2] Swamy, T., X. Chen, and Y-M. Chiang. "Electrochemical Redox Behavior of Li Ion Conducting Sulfide Solid Electrolytes." *Chemistry of Materials* 31, No. 3 (2019): 707–713.

[3] Koerver, R., F. Walther, I. Aygün, J. Sann, C. Dietrich, W. G. Zeier, and J. Janek. 'Redox-Active Cathode Interphases in Solid-State Batteries." *Journal of Materials Chemistry A* 5, No. 43 (2017): 22750–22760.

[4] Hakari, T., M. Deguchi, K. Mitsuhara, T. Ohta, K. Saito, Y. Orikasa, Y. Uchimoto, Y. Kowada, Y. Hayashi, and A. Tatsumisago. "Structural and Electronic-State Changes of a Sulfide Solid Electrolyte during the Li Deinsertion–Insertion Processes." *Chemistry of Materials* 29, No. 11 (2017): 4768–4774.

[5] Wang, Y., T. Matsuyama, M. Deguchi, A. Hayashi, A. Nakao, and M. Tatsumisago. "X-Ray Photoelectron Spectroscopy for Sulfide Glass Electrolytes in the Systems $Li_2S–P_2S_5$ and $Li_2S–P_2S^5$–LiBr." *Journal of the Ceramic Society of Japan* 124, No. 5 (2016): 597–601.

Patents/Publications/Presentations

The project has no patents, publications, or presentations to report this quarter.

TASK 4 – METALLIC LITHIUM

Team Lead: Jagjit Nanda, Oak Ridge National Laboratory

Summary and Highlights

The use of a metallic lithium anode is required for advanced battery chemistries like Li-ion, Li-air, and Li-S to realize dramatic improvements in energy density, vehicle range, cost requirements, and safety. However, use of metallic lithium with liquid and solid polymer or ceramic electrolytes has so far been limited due to parasitic SEI reactions and dendrite formation that eventually short circuit the battery. Adding excess lithium to compensate for such losses negates the high-energy-density advantage of a Li-metal anode and leads to further concern for battery safety. For a long lifetime and safe anode, it is essential that no lithium capacity is lost either (1) to physical isolation by roughening, dendrites, or delamination processes, or (2) to chemical isolation from side reactions. The key risk, and current limitation, for this technology is the gradual loss of lithium over the cycle life of the battery.

BMR, Battery500, and other DOE programs are addressing this challenge with many innovative and diverse approaches. Key to all is the need for a much deeper analysis of the degradation processes and new strategies to maintain a dense, fully connected lithium and a dendrite-free electrolyte so that materials can be engineered to fulfill the target performance metrics for EV application, namely 1000 cycles and a 15-year lifetime, with adequate pulse power. Projecting the performance required in terms of just the lithium anode, this requires a high rate of lithium deposition and stripping reactions, specifically about 30 µm of lithium per cycle, with pulse rates up to 10 and 20 nm/s (15 mA/cm^2) charge and discharge, respectively, with little or no excess lithium inventory. This is daunting in the total mass and rate of material transport that must be achieved without failures.

The efficient and safe use of metallic lithium for rechargeable batteries is then a great challenge, and one that has eluded R&D efforts for years. This project takes a broad look at this challenge for both SSBs and batteries continuing to use LEs. Electrolytes reported here include nonflammable liquid solutions, gel type polymer-in-a-salt, composites of ceramic polymer phases, common and novel PEs, and both oxide and sulfide ceramic electrolytes. In most studies, the electrolyte phases were modified by addition of plasticizers or interface coatings to improve transport, stability, and ease of manufacturing. Researchers are typically working toward cycling of full cells with relevant and balanced capacities for the lithium anode and cathode using measures of CE, interface resistance, and post-cycling observation of the disassembled cell components to assess stability of the Li-metal anode and chosen electrolyte.

Highlights

The highlights for this quarter are as follows:

- The Stanford-SLAC team (Y. Cui) reports a prelithiation process by fabricating ultra-thin Li-metal in a graphene oxide host of controllable thickness. When used in model graphite-LFP full cell, the 1st cycle efficiency improves from 87% to 96%, providing an effective method for preventing loss of Li-inventory.
- At ORNL (J. Nanda and team), the project reports electrochemical performance of Li/LPS/NMC-811 all-solid-state cells as a function of stack pressure. Changing the stack pressure from 5 Mpa to 50 Mpa does not improve cell performance, providing insights of a limiting external stack pressure beyond which mechanical constriction alone cannot address interfacial contact resistance between electrode/SE.
- The LLNL team (J. Ye) has developed low-binder LLZTO and LLZTO/NMC-622 ink formulations for 3D printing that aid densification during sintering, and they successfully printed cathode/electrolyte bilayer films. Further decreasing the LLZTO/NMC-622 ratio to 25:75 wt% and adding sintering aids substantially improves the electrochemical performance of these co-sintered composite cathodes in full cells.

Task 4.1 – Lithium Dendrite Prevention for Lithium Batteries
(Wu Xu and Ji-Guang Zhang, Pacific Northwest National Laboratory)

Project Objective. The objective of this project is to enable lithium metal to be used as an effective anode in rechargeable Li-metal batteries with good stability and high safety. The investigation this fiscal year will focus on two aspects. First, develop nonflammable polymer composite electrolytes (NPCEs) and investigate effects of various flame-retardant solvents and polymers on ionic conductivity, lithium CE, lithium anode morphology, flammability, and battery performances in terms of long-term cycling stability and rate capability at various temperatures. Second, establish correlation of morphologies of SEI layer and deposited lithium with electrolyte formulation, current density, and lithium deposition/stripping cycling.

Project Impact. Lithium metal is an ideal anode material for high-energy-density rechargeable batteries; however, the application of Li-metal anode is hindered by safety concerns and short cycle life. The safety concerns of Li-metal batteries mainly arise from lithium dendrite growth and electrolyte flammability, while the short cycle life is related to low lithium CE. Although much progress has been achieved in suppressing lithium dendrites and increasing lithium CE in LEs, most LEs are flammable and may pose safety hazards in case of extreme conditions. Therefore, development of electrolytes with improved safety for advanced battery chemistry is imperative. An ideal electrolyte for Li-metal anode should not only suppress lithium dendrite growth and have high CE, but also be intrinsically nonflammable. This fiscal year, the team will develop NPCEs that have high lithium CE, suppress lithium dendrites, and are stable with high-voltage cathodes. The success of this project will increase safety of Li-metal and Li-ion batteries and accelerate market acceptance of EVs, as required by the EV Everywhere Grand Challenge.

Approach. The approach will encompass several areas: (1) develop NPCEs that can enable long-term cycling with significantly improved safety features of Li-metal batteries, (2) develop current collectors with 3D structure for Li-metal anode to suppress lithium dendrite growth, increase lithium utilization, and extend cycle life of Li-metal batteries, and (3) conduct mechanistic studies on lithium deposition behavior to lay groundwork for future improvement of electrolytes (salts, solvents, and additives) for Li-metal batteries.

Out-Year Goals. The long-term goal of the proposed work is to enable Li-metal and Li-ion batteries with a specific energy of > 350 Wh/kg (in cell level), 1000 deep-discharge cycles, 15-year calendar life, and less than 20% capacity fade over a 10-year span to meet the goal of EV Everywhere Grand Challenge.

Collaborations. This project collaborates with C. Wang of PNNL on characterization by TEM/SEM; K. Xu and M. Ding of U. S. Army Research Laboratory (ARL) on DSC measurements; and B. Polzin at ANL on coated electrode sampling.

Milestones

1. Evaluate properties of NPCEs and cycling performance of Li||NMC cells using the NPCE. (Q1, FY 2021; Completed, December 31, 2020)
2. Elucidate influencing factors on lithium deposition behavior by *in situ* AFM. (Q2, FY 2021; Completed)
3. Fabricate 3D-structured current collectors and characterize their physical properties. (Q3, FY 2021; Completed)
4. Evaluate influence of 3D-structured current collector on Li-metal deposition behavior and cycling performance of Li||NMC cells. (Q4, FY 2021; Completed)

Progress Report

This quarter, the effectiveness of composite separators of polyimide and polyethylene in Li||NMC-622 coin cells was further studied using an electrolyte of LiFSI-1.1DME–3TTE (DME-LHCE). Two kinds of arrangements of polyimide (11-µm thick) and polyethylene (7-µm thick) were used—polyimide/polyethylene with polyimide contacting Li-metal anode, and polyethylene/polyimide with polyethylene contacting Li-metal anode. Single-layer polyethylene (20-µm thick) was also investigated as a baseline.

Figure 88 shows the long-term cycling performance of the Li||NMC-622 cells comprising the single-layer polyethylene separator and the two (polyimide/polyethylene and polyethylene/polyimide) composite separators. It is seen that the cell using polyethylene/polyimide composite separator exhibits excellent cycling stability in both discharge capacity and CE. After 350 cycles, the capacity retention of polyethylene/polyimide based cell amounted to 83.5%, whereas those of single-layer polyethylene and polyimide/polyethylene composite separator only reached 49.3% and 1.9%, respectively. The polyethylene/polyimide-based cell maintained a CE of 99.8% at the 350th cycle. The cell based on single polyethylene showed slightly lower and decreased CE with cycling. In contrast, the cell based on polyimide/polyethylene composite separator exhibited a large fluctuation in CE after about 150 cycles. The cell with polyimide/polyethylene separator (polyimide is in direct contact with lithium) exhibits the worst cycling performance, mainly due to the reactivity between lithium and polyimide.

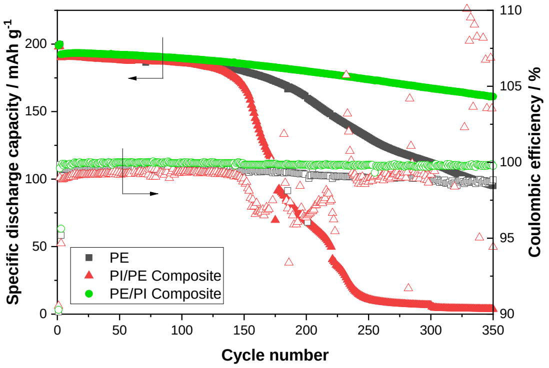

Figure 88. Room-temperature cycling performance of Li||NMC-622 coin cells with three separator assemblies, that is, polyethylene (PE), polyimide (PI) / PE, and PE/PI. The cells contained 50-µm-thick lithium, 4.2 mAh cm^{-1} NMC-622, and 75 µL DME-LHCE (LiFSI:DME:TTE = 1:1.1:3 by mol.); they were cycled in 2.5-4.4 V at: C/10 charge and C/5 discharge after three formation cycles at C/10, where 1C = 4.2 mA cm^{-2}.

Figure 89a-b shows the surface morphologies of lithium electrodes after 250 cycles in Li||NMC-622 cells comprising single-layer polyethylene and polyethylene/polyimide composite separator. It is seen that the lithium electrode from the cell with polyethylene/polyimide composite separator exhibited denser morphology than that from single polyethylene separator. Although polyethylene is in contact with Li-metal anode in both cases, the uniform distribution of the highly ordered pores in the 3DOM polyimide membrane (Figure 89d) can better regulate the Li-ion flux in the cell than the single polyethylene separator (Figure 89c), thus reducing inhomogeneity of lithium deposition. Another possible reason for the longer cycling performance of Li||NMC-622 cells with polyethylene/polyimide composite separator is that polyimide may act as a TM cation scavenger in the electrolyte. To verify this hypothesis, corresponding experiments have been devised, and results will be reported later. Besides the electrochemical performance evaluations, safety of the cells using single-layer polyethylene and polyethylene/polyimide composite separator will be investigated.

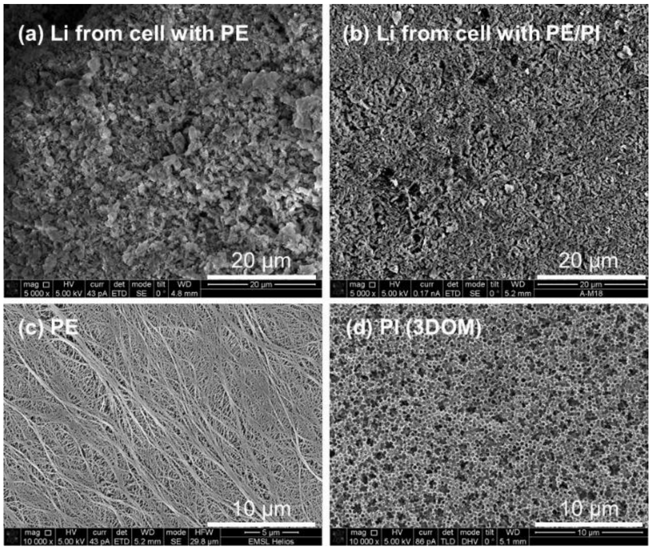

Figure 89. Scanning electron microscopy images of surface morphologies of (a-b) lithium electrodes after 250 cycles in Li||NMC-622 cells with (a) polyethylene (PE) and (b) PE / polyimide (PI) separators and (c-d) separators of (c) PE and (d) PI (3DOM structure).

Patents/Publications/Presentations

Publication

- Jia, H., X. Cao, J-G. Zhang, and W. Xu.[*] "Electrolytes for Lithium-Ion and Lithium Metal Batteries." In *Encyclopedia of Energy Storage* (2021). doi: 10.1016/B978-0-12-819723-3.00106-2. Publisher: Elsevier Inc.

Task 4.2 – Composite Electrolytes to Stabilize Metallic Lithium Anodes
(Nancy Dudney and X. Chelsea Chen, Oak Ridge National Laboratory)

Project Objective. The project has several objectives: (1) prepare novel polymer and ceramic electrolyte materials that can work together to achieve thin membranes that have the unique combination of electrochemical and mechanical properties required for practical manufacturing and to stabilize the metallic lithium anode for good power performance and long cycle life, (2) identify key features of the composite composition, architecture, and fabrication that optimize performance, and (3) fabricate thin electrolyte membranes to use with a thin metallic lithium anode that provides good power performance and long cycle life.

Project Impact. A stable lithium anode is critical to achieve high energy density with excellent safety, lifetime, and cycling efficiency. This study will identify key design strategies that should be used to prepare composite electrolytes to meet the challenging combination of physical, chemical, and manufacturing requirements to protect and stabilize the Li-metal anode for advanced batteries. By utilizing well characterized and controlled component phases, design rules developed for composite structures will be generally applicable toward substitution of alternative and improved SE component phases as they become available. Success will enable DOE technical targets: 500-700 Wh/kg, 3000-5000 deep discharge cycles, and robust operation.

Approach. This project seeks to develop practical SEs to provide stable, long-lived protection for Li-metal anode. Current electrolytes have serious challenges when used alone: oxide ceramics are brittle, sulfide ceramics are air-sensitive, polymers are too resistive and soft, and many electrolytes react with lithium. Composites provide a clear route to address these issues. While work continues to emphasize study of ceramic electrolyte / PE interfaces, this effort has expanded to address the following: (1) practical processing routes to fabricate full batteries using better composite electrolytes with a composite cathode and thin Li-metal anode, and (2) introduction of alternative polymer and ceramic phases to replace well-known model materials and develop improved composite electrolytes. In addition to solid-state devices, hybrid batteries are investigated using a fluid or gel catholyte within the porous cathode. Coatings have also been employed to stabilize electrode interfaces. These directions increase complexity of the studies, but are needed to improve cycling stability and rate performance and to advance practical implementation of the SE and Li-anode technology.

Out-Year Goal. The goal is to use advanced manufacturing processes where the architecture of the composite membrane can be developed and tailored to maximize performance and cost-effective manufacturing.

Collaborations. Work is conducted by B. Armstrong, S. Kalnaus, A. Ullman, and X. C. Chen. Ceramic electrolyte powders (LICGC™) are obtained from Ohara Corporation. J. Libera from ANL provided a large quantity of LLZO powders.

Milestones

1. Sinter and characterize porous LLZO network by different processes. (Q1, FY 2021; Completed)
2. Compare polymer-LLZO ceramic composites with four different ceramic loadings. (Q2, FY 2021; Completed)
3. Elucidate the Li-ion path through at least two distinct polymer-ceramic composites. (Q3, FY 2021, Completed)
4. Measure Li^+ transference number with at least two different anion receptors. (Q4, FY 2021; Completed)

Progress Report

Optimization of Self-Standing 3D Interconnected Composite Electrolyte

Last quarter, the team successfully made a flexible 3D interconnected composite electrolyte. This quarter, they first obtained 3D interconnected LICGC™ ceramic network of different porosities to eventually understand its impact on the flexibility of the polymer-filled composites. This was done by partially sintering LICGC™ (1-µm size particles) using different sintering conditions, described in Table 3. Ionic conductivity of partially sintered tapes (PSTs) as a function of sintering conditions was measured for the various porosities (Table 3). The conductivity of PST obtained via the team's standard sintering protocol (PST_01) led to almost two orders lower ionic conductivity compared to the fully dense LICGC™ plate provided by Ohara, that is, 2.6×10^{-6} S/cm versus 2.9×10^{-4} S/cm. Increasing the dwell time at 1000°C from 3 hours to 6 hours and 9 hours did not lead to any significant changes in the ionic conductivity (PST_02, 03; structure shown in Figure 90b). Increasing the sintering temperature from 1000°C to 1100°C led to complete collapse of the porous structure and much smaller porosity (PST_04; Figure 90c), with much higher ionic conductivity, although still one order magnitude lower than the dense Ohara plate. Sintering at an intermediate temperature of 1050°C did not lead to a complete collapse, but the tape turned severely wavy after sintering, making it difficult to measure its ionic conductivity (PST_05; Figure 90d-e). To address this issue, a two-step sintering procedure after the binder burn-off step at 600°C was successfully applied (PST_06, 07; Figure 90f). The discs remained flat; ionic-conductivity measurements are pending.

Two hypotheses behind the two-orders of magnitude lower ionic conductivity of PSTs were tested. First, a slower burn-off of the binders in the tape was tried in case there was an incomplete burn-off that caused a poorer sintering. The slow burn-off procedure corresponds to different weight loss stages according to the project's TGA data. However, no significant increase in conductivity was observed (PST_08). As a comparison, binder-free pellets made via hydraulic pressing of LICGC™ powders were sintered alongside (LICGC™_Pellet). Significantly higher ionic conductivity was observed. However, it turned out to be not a direct comparison, as the porosity of sintered pellet was much lower (44.9 % versus 52.3 %), likely due to dense packing of particles in the green pellet versus green tape. The team will measure the conductivity of PST_06 and _07, which have similar porosity to LICGC™_Pellet, to confirm this hypothesis. In the second hypothesis, tapes were sintered by burying in mother powder in case lithium loss at the surface was behind the observed lower ionic conductivities. However, the ionic conductivity remained unchanged (PST_09), indicating lithium loss is not the cause of the low ionic conductivity. At this point, the team's third hypothesis is that due to the porous nature of the PSTs, the true conductivity of the interconnected structure may not be equal to the apparent conductivity as measured by the alternating current (AC) impedance spectroscopy assuming full contact area with the electrodes. They will proceed to assess the ionic conductivity of polymer-filled PSTs where full contact with the electrodes can be achieved.

Table 3. Porosity and ionic conductivity of partially sintered LiCGC™ tapes as a function of sintering conditions.

Sample ID	Sintering Conditions	Vol% of Porosity in PSTs	Wt% of Ceramic if Porosity is Filled with xPEO	Ionic Conductivity of PSTs (S/cm)
PST_01	600°C for 2 h, 1000°C for 3 h (*baseline sintering protocol*)	52.4 %	66.5 %	2.6×10^{-6}
PST_02	600°C for 2 h, 1000°C for 6 h	48.9 %	69.5 %	7.9×10^{-6}
PST_03	600°C for 2 h, 1000°C for 9 h	51.1 %	67.5 %	4.1×10^{-6}
PST_04	600°C for 2 h, 1100°C for 3 h	9.3 %	90.7 %	4.8×10^{-5}
PST_05	600°C for 2 h, 1050°C for 2 h	35.9 %	79.6 %	Could not be measured
PST_06	600°C for 2 h, 1000°C for 3 h, 1050°C for 0.5 h	46.2 %	71.8 %	Not yet measured
PST_07	600°C for 2 h, 1000°C for 3 h, 1050°C for 1 h	45.6 %	72.3 %	Not yet measured
PST_08	200°C for 1 h, 300°C for 1 h, 200°C for 1 h, 350°C for 1 h, 450°C for 1 h, 500°C for 1 h, 1000°C for 3 h (*slow burn-off of binder*)	52.3 %	66.5 %	4.3×10^{-6}
PST_09	600°C for 2 h, 1000°C for 3 h (*buried in mother powder*)	Not measured	-	4.0×10^{-6}
LICGC™_ Pellet	200°C for 1 h, 300°C for 1 h, 200°C for 1 h , 350°C for 1 h, 450°C for 1 h, 500°C for 1 h, 1000°C for 3 h (*slow burn-off of binder*)	44.9 %	72.8 %	1.8×10^{-5}
LICGC™_ Dense Plate	From supplier	No porosity	-	2.9×10^{-4}

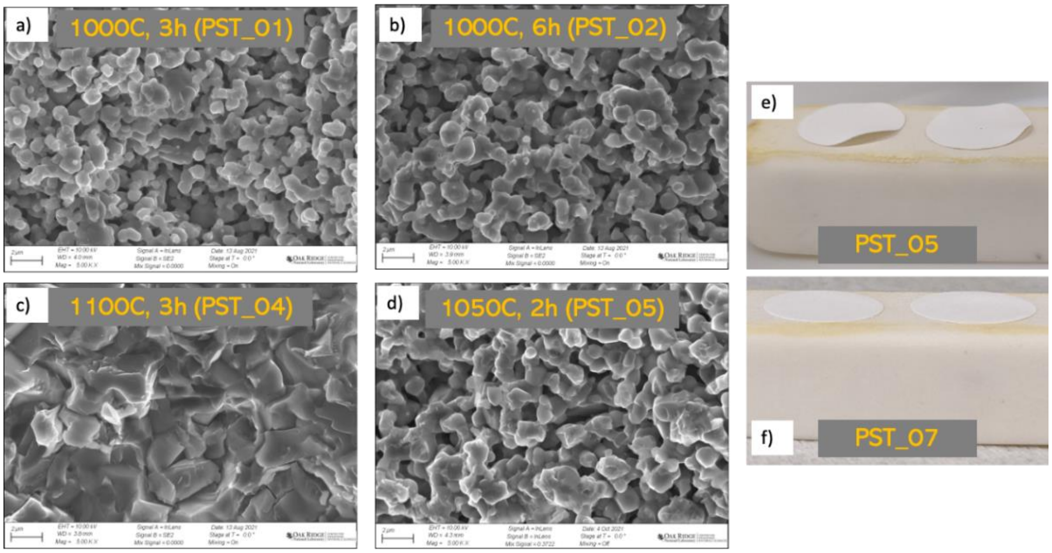

Figure 90. (a-d) Microstructures of partially sintered tapes (PSTs) sintered under various conditions. (e-f) Photographs to highlight the flatness of tapes after sintering under conditions.

Second, they also optimized the formulation of cross-linked PEO (xPEO) used for filling the PSTs. Changing the molecular weight of one of the precursor molecules (Jeffamine) from 900 to 2000 (Table 4) led to significantly lower interfacial resistance and overpotentials during cycling of Li//Li symmetric cells made with purely PE membranes (no ceramic; Figure 91).

Table 4. Composition and interfacial impedance with lithium metal of the cross-linked PEO electrolytes evaluated.

Sample ID	PEGDGE M.W. (g/mol)	Jeffamine M.W. (g/mol)	[EO + PO] : LiTFSi	Initial Li//Li Interfacial Resistance at 70°C (Ω·cm^2)
xPEO-previous	500	900	16.0	230
xPEO-current	500	2000	16.0	55

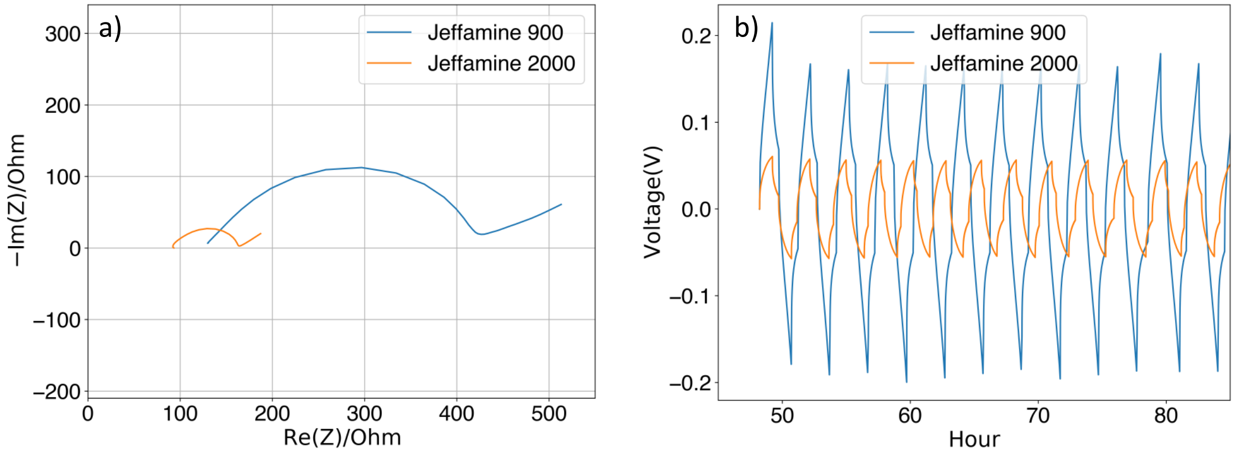

Figure 91. (a) Impedance spectra and (b) voltage profile of Li//Li symmetric cells made with the two xPEO formulations (no ceramic). Cells were cycled galvanostatically at 50 μA/cm^2, 70°C.

Third, the team carefully monitored the changes in flexibility of the PSTs as they were filled with xPEO PE. In the previous report, they had shown that the xPEO-filled PST (sintering conditions were the same as for PST_01) became flexible after it was plasticized with tetraethylene glycol dimethyl ether (TEGDME) liquid plasticizer. They observed similar behavior again when tried with PST_03 (Figure 92). In addition, they found that the disc increased in its area after plasticization without showing any apparent cracks or fractures (Figure 92). As the plasticizer was dried-off, the disc shrank back to its original size, which strongly suggests that the 3D ceramic network had not broken after plasticization (Figure 92). The team is studying the effect of porosity of PST on its flexibility after plasticization. Initial results suggest that PSTs with more sintering (less porosity) do not exhibit this flexibility with plasticization.

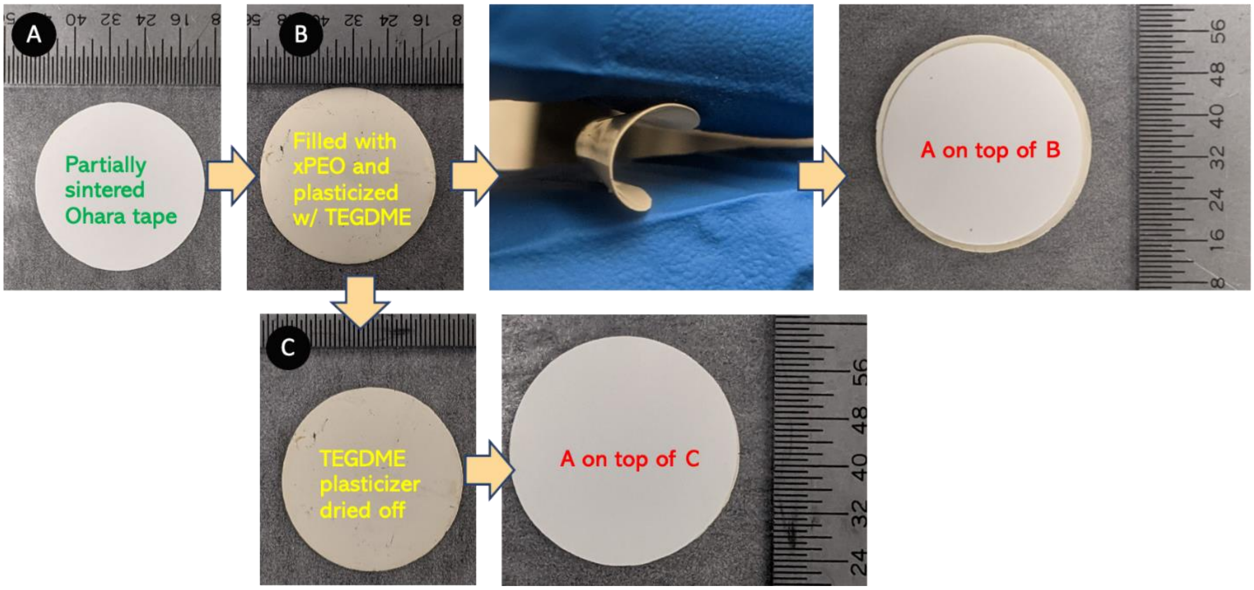

Figure 92. (Top row) Photographs showing increase in flexibility and area of partially sintered LICGC™ tape (PST_03) as it was filled with xPEO polymer electrolyte and plasticized with TEGDME liquid plasticizer. (Bottom row) As the plasticizer was dried-off from the composite electrolyte, the disc returned to being brittle and shrank to its original size.

Modeling of Li-Ion Concentration Gradients in Composite Electrolytes

Numerical simulations continued for the three electrolyte arrangements in Figure 93. In the previous report, the team described the ions distribution in each case, demonstrating lower concentration gradients in the geometry where the PE domain is divided by a fully dense SIC wall (Figure 90b). In the current investigation, they study the transient behavior of the system and its convergence to the steady state; they then qualitatively compare the results with the experimental measurements (Figure 91). Due to the small domain size in the simulations, the steady state is reached rather quickly compared to the experimental measurements of the current density in cells with the thickness orders of magnitude larger. However, the qualitative comparison is still valid; overall, the modeling results follow the experimentally measured current trends. It can be seen that in the case of trilayer arrangement with the fully dense LATP plate, the steady state is reached faster than in other scenarios, as the developed concentration gradients are minimal.

The transport number (often also called transference number) for lithium (t_+) is defined as the portion of the total ionic current carried by cations. In the case of homogeneous binary electrolyte, calculation of the t_+ is rather straightforward as the ionic flux is uniform and the calculation can be done over any orthogonal cross-section in the electrolyte domain. This approach will not be valid in composite electrolytes. Here, the team calculates the transport number using the volume averaged migration flux of cations and anions with the resulting effective value of t_+ for the entire domain. With this approach, the transport number for lithium in PE and in PE with the CPE in the middle is 0.3 and 0.33, respectively. The transference number increases to 0.53 when the LATP plate is placed in the middle of the PE domain, Figure 90b.

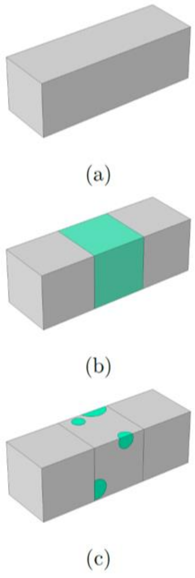
(a)
(b)
(c)

Figure 93. The three electrolyte configurations considered in the simulations.

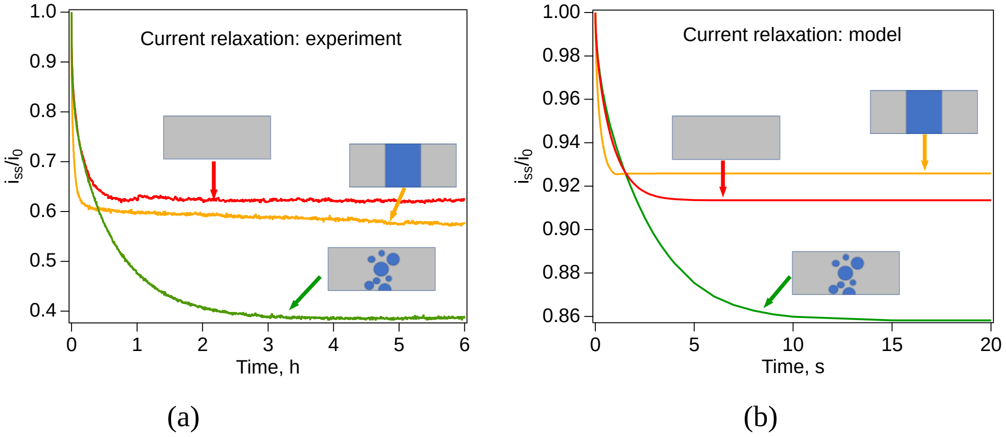

Figure 94. Transient behavior of the electrolyte arrangements corresponding to Figure 93: (a) experiment, and (b) model.

Patents/Publications/Presentations

Patent

- "Method of Manufacturing a Thin Film Composite Solid Electrolyte"; U. S. Patent Application 17/497,023; Filed October 8, 2021.

Task 4.3 – Enabling Solid-State Batteries through Characterization and Modeling
(Sanja Tepavcevic and Larry A. Curtiss, Argonne National Laboratory)

Project Objective. The project objectives are multi-faceted, including development of a new mechanically and chemically stable and Li-ion conductive ($\geq 2 \times 10^{-4}$ S/cm at 298 K) crystalline/amorphous SE for SSB. The anode and cathode are composed of lithium metal and a Li-based oxide, respectively, allowing operation at cathode potentials > 5 V (denoted as a S_{Li}-S_{EL}-S_C system).

Project Impact. Protective organic and inorganic compounds can enhance stability of the interface, improve Li-ion interfacial transport, minimize dendrite formation, and increase safety in Li-ion batteries.

Approach. The project proposes to develop and use interdisciplinary, atomic-/molecular-level insight obtained from integrating both experimental- and computational-based methodologies to define the landscape of parameters that control interfacial properties for a new generation of the Li-ion SSB systems. The strategy will involve transferring knowledge gained from well-characterized thin-film materials to real-world materials. This strategy forms a closed loop wherein the knowledge gained from model systems is used to design more complex, real-world materials, and vice versa. The work will focus on utilizing existing in-house synthesis and characterization methods to enable rapid transition from fundamental science to realistic cells.

Out-Year Goals. The out-year goals are to use and develop the physical and chemical synthesis methods for design of SSI with unique chemical/mechanical/conductivity properties. The proposed work will develop and exploit a variety of *ex situ* and *in situ* experimental optical and surface sensitive techniques and electrochemical methods to explore and explain bulk and interfacial properties of the selected materials. The results will serve to unravel many puzzling bulk and interfacial properties of S_{Li}-S_{EL}-S_C systems, including various types of ceramic and glass materials.

Collaborations. This project funds work at ANL and collaboration with J. Sakamoto at UM.

Milestones

1. Evaluating chemical stability and correlating with interfacial reactivity for vacuum-deposited Li/Al -doped LLZO interfaces. (Q1, FY 2021; Completed)
2. Understanding impact of different dopants in LLZO (aluminum versus gallium) on chemical and electrochemical reactivity with metallic lithium by surface and bulk sensitive techniques and computational tools. (Q2, FY 2021; Completed)
3. Modifying energy barrier for Li^+ transport in Al-doped LLZO by controlling the chemistry of the GBs via additives. (Q3, FY 2021; Completed)
4. Optimizing nanoLLZO+PEO composite and characterizing chemical and electrochemical reactivity with metallic lithium by surface and bulk sensitive techniques. (Q4, FY 2021; Completed)

Progress Report

Development of Large-Scale LLZO SSEs from Ultrafine-Grain Nanofibers. Cubic LLZO has been considered a promising candidate for SEs due to its relatively high ionic conductivity (~ 10^{-3}-10^{-4} S/cm), stability against Li-metal anodes, and wide voltage stability window (> 5 V versus Li/Li^{+}). Conventional LLZO synthesis processes generate green powders (for example, solid-state reaction, co-precipitation, plasma pyrolysis, and citrate combustion) and require high sintering temperatures of > 1100°C as well as a long sintering time of > 24 hours. Recently, LLZO nanofibers prepared by electrospinning method demonstrated a low sintering temperature of 700-800°C, opening the possibility of low-temperature synthesis of LLZO electrolytes. With roll-to-roll technology that is scalable, the electrospinning approach reduces processing steps, shortens manufacturing time, and increases production energy efficiency, leading to a novel and cost-effective manufacturing pathway to synthesize large-area SSEs.

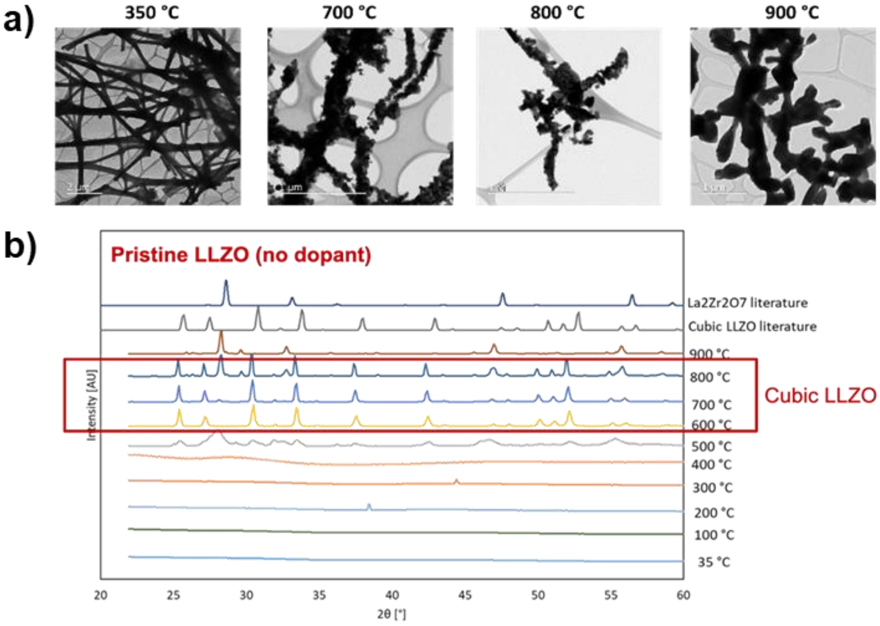

Figure 95. Annealing of the LLZO Nanofibers. (a) Transmission electron microscopy images of nanofibers annealed at 350°C, 700°C, 800°C, and 900°C. (b) *In situ* wide angle X-ray scattering (WAXS) performed at APS 12-ID-B at different temperatures for ultrafine grain LLZO nanofibers formed using the electrospinning method.

Using electrospinning methods, the team managed to obtain cubic LLZO, even without doping elements usually needed to stabilize the cubic phase. This effect was attributed to the low surface energy associated with nanocrystalline LLZO grains crystallized from thin electrospun precursor fibers, which favors the low surface energy cubic phase over the high surface energy tetragonal phase. The as-spun nanofibers are amorphous polymer nanofibers with metal ions uniformly dispersed in carrier polymers. No excess lithium salts were added in the precursor solution to compensate for lithium loss. During annealing, the nanofibers were heated to the target temperature with a heating rate of 10°C/min, annealed for 30 minutes, and then furnace cooled to room temperature. During the post-annealing step, the polymers are removed as CO_2 gas, while the crystalline LLZO fibers are formed through LLZO nucleation and grain coalescence. By adjusting the annealing temperature and time, LLZO fibers with various grain sizes and morphologies can be achieved.

Figure 95 shows the results of LLZO nanofibers annealed at different temperatures. As can be seen from Figure 95a, the nanofibers annealed up to 350°C are amorphous. After heating to 700°C for 30 minutes, the nanofibers begin to show a rough surface, attributed to formation of nanocrystalline grains in the nanofibers, whose grain size is around 10 nm. A similar nanofiber morphology was observed when nanofibers were annealed at 800°C, showing an average grain size of 20 nm. When the nanofibers were annealed at 900°C, an interconnected network was observed where the individual “nanofibers” were “welded” at the joints due to sintering. This observation indicates that with annealing temperature, the team can distinctly separate the cubic and tetragonal phases (Figure 95b) and select the desirable phase by controlling the nanofiber grain size. The fact that the favorable cubic phase forms at lower annealing temperatures provides a process window for ultra-fine-grain nanofiber synthesis. They will also examine lower annealing temperatures as well as higher heating and cooling rates to achieve smaller grain sizes.

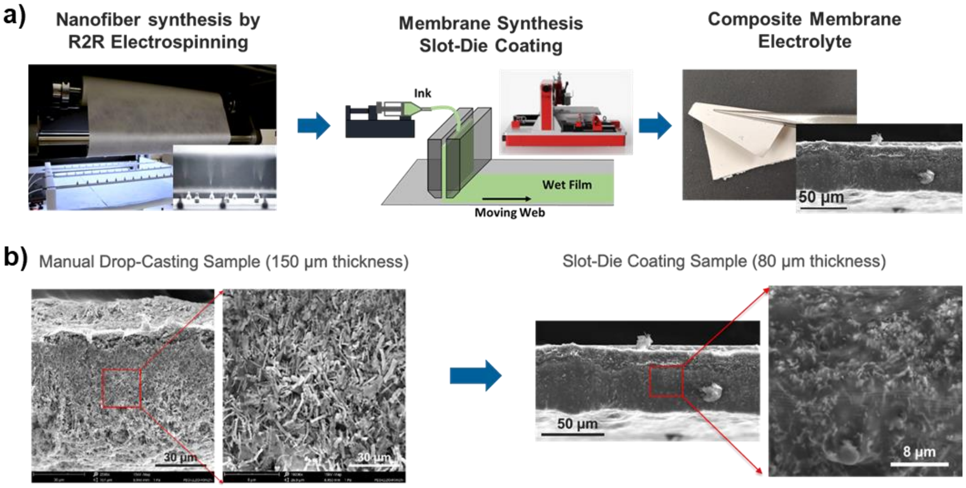

Figure 96. Composite synthesis and optimization. (a) Roll-to-roll (R2R) nanofiber fabrication by electrospinning; slot-die coating process; and final composite membranes. (b) Drop-cast membranes are heterogenous and porous, while slot-die coated membranes are uniform and can be made thinner.

Figure 96a shows the roll-to-roll electrospinning tool and a slot-die coating process for nanofiber LLZO-PEO CPE membrane fabrication. During this process, LLZO fibers of a desired loading ratio are mixed with a LiTFSI-doped PEO solution, and the well-dispersed slurry is then coated on a fast-moving web to form a thin membrane. By accurately controlling coating pressure and gap, as well as web moving speed, uniform membranes of designed thickness (≤ 20-150 µm) can be obtained. Figure 96b presents cross-sectional SEM images of coated membranes. While traditional membranes from drop-cast samples are heterogenous and porous, slot-die coated samples are dense, uniform, and show good ductility and uniform fiber distribution in the polymer. Ideally, interconnected LLZO nanofiber networks are the basis of the composite, with the polymer present within the fiber "scaffold" to increase flexibility and provide soft interfacial contacts for the anode and cathode. Both intrinsic Li^+ conductivity and nanowire morphology are needed for optimal performance. High LLZO loadings are required to achieve this percolation network and thus high room-temperature conductivity. Thus, they will adjust nanofiber distribution to form a good percolation network to achieve high room-temperature conductivity.

Al-doped LLZO nanofiber/PEO/LiTFSI composites are the starting system to optimize microstructure with respect to nanofiber loading and spatial distribution, coating defect control, and membrane thickness. The team believes moving to undoped cubic LLZO nanofibers will be beneficial in the long term, as aluminum dopant segregation is known to limit CCD and their synthetic methods are uniquely suited to enable dopant-free cubic LLZO. Ongoing work will optimize ink composition, mechanical fluidic properties, and coating process parameters to ensure dense and low-defect membranes with good LLZO fiber percolation networks.

Electrochemical Reactivity of Composite with Metallic Lithium. The team tested three composite compositions with LLZO loadings at 41%, 50%, and 56 wt% LLZO. Symmetric Li||Li cells were used to test the electrolytes' performance with galvanostatic cycling and impedance measurements. Figure 97a shows cycling of three samples from 0.05 mA/cm^2 up to 4.0 mA/cm^2 with capacities up to 4 mAh/cm^2. All cells show a general decrease in polarization voltage with increased cycling over time. Figure 97b shows that this is due to large decreases in interfacial impedance, as repeated stripping and plating provides better contact between the lithium electrode and composite electrolyte. Impedance also shows that as LLZO content increases, more high-frequency impedance is resolved, as seen by the emergence of a second semicircle; this is likely due to the contribution of LLZO to overall conductivity.

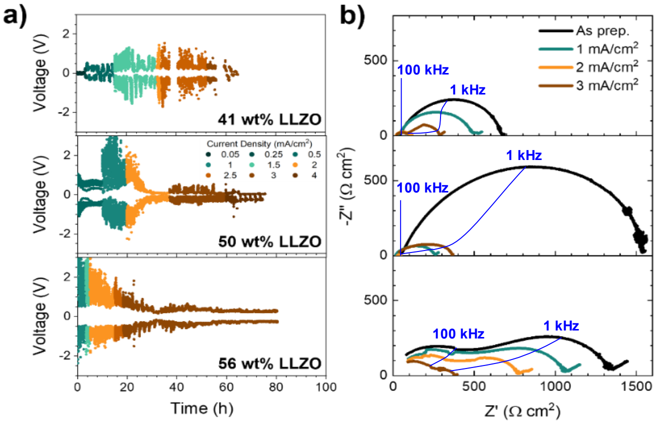

Figure 97. Symmetric cells electrochemical characterization. (a) Symmetric Li||Li cycling of composite polymer electrolytes with different LLZO loadings. Cycling up to 3-4 mA/cm^2 and up to 4 mAh/cm^2 is possible without cell shorting. (b) Impedance spectra of the corresponding cells as prepared and after cycling at given current densities.

Patents/Publications/Presentations

Patent

- The combined application of inventions IN-21-049 (Solid-State Nanofiber-Polymer Multilayer Composite Electrolytes) and IN-21-052 (Development of Dual-Fiber and Fiber-Powder Composite Solid-State Lithium Batteries). “Solid-State Nanofiber Polymer Multilayer Composite Electrolytes and Cells”; filed September 30, 2021; application 17/490,956.

Publication

- Liu, P., M. J. Counihan, Y. Zhu, J. G. Connell, D. Sharon, S. N. Patel, P. C. Redfern, P. Zapol, N. M. Markovic, P. F. Nealey, L. A. Curtiss, and S. Tepavcevic. “Increasing Ionic Conductivity of Poly(ethylene oxide) by Reaction with Metallic Li.” *Advanced Energy and Sustainability Research* (2021). doi: 10.1002/aesr.202100142.

Task 4.4 – 3D Printing of All-Solid-State Lithium Batteries
(Jianchao Ye, Lawrence Livermore National Laboratory)

Project Objective. This project has three objectives: (1) tuning microstructures of 3D-printed SSE separators, (2) determining material and processing compatibilities with cathode printing, and (3) 3D printing of sintering-free SSE separators.

Project Impact. ASSLBs are difficult to process due to the brittleness of ceramic materials, poor solid-solid contact, and electrolyte-electrode stability issues. As a result, the energy and power density and also cycling stability are far from satisfying. This project will address fabrication difficulties by using state-of-the-art 3D-printing techniques that can introduce 3D interfaces and architectures to enhance solid-solid contact and reduce charge transfer resistance. Success will benefit the DOE by establishing the best manufacturing methods for ASSBs to achieve VTO goals on the performance of beyond Li-ion batteries.

Approach. The project employs 3D-printing techniques to manufacture SSEs and related components for ASSBs. The team starts with direct ink writing (DIW) to develop ink recipes with desired rheological properties and to explore post-sintering approaches to achieve high densification. In parallel with DIW 3D printing, the team also explores other 3D printing options, such as projection microstereolithography. Both sintering and sintering-free approaches can gain benefit from 3D printing and therefore will be investigated.

Out-Year Goals. The team will determine the co-sintering stability of printed NMC/LLZTO films and compare with that of hydraulic-pressed NMC/LLZTO pellets. They will print SSE/cathode bilayer structures with controlled interfaces and determine their electrochemical performance with or without post sintering process.

Collaborations. Microstructures, ionic conductivities, and mechanical properties will be provided to the LLNL simulation team, led by the PI, B. Wood, for establishing and validating phase-field modeling methods.

Milestones

1. Evaluate new commercial LLZTO powder sources. (Q1, FY 2021; Completed)
2. Determine performance of ASSBs based on 3D-architected LLZTO structure. (Q2, FY 2021; Completed)
3. Determine performance of ASSBs based on composite PE. (Q3, FY 2021; Completed)
4. Evaluate ASSBs based on co-sintering approach. (Q4, FY 2021; In progress)

Progress Report

Low-Binder Ink Formulations

More than 40 different LLZTO ink formulations were evaluated as part of the development of a low-binder ink for 3D printing. The polymer binder can either be burned out in air prior to sintering the LLZTO, or carbonized in argon as part of the sintering process. Either way, when the binder is removed, voids are left between the LLZTO particles that make it more difficult for the LLZTO to fully densify during sintering. Therefore, ideally the ink should contain as little binder as possible. All of the inks tested here used polyvinyl butyral (PVB) as a binder and benzyl butyl phthalate (BBP) as a plasticizer in varying ratios with two different solvent systems [7:3 wt 1-butanol/alpha terpineol, and N-methyl-pyrrolidone (NMP)]. The team successfully developed two different low-binder ink formulations and printed small 1 cm × 1 cm square films using each ink, as shown in Figure 98a. The ink made with the 1-butanol/alpha terpineol solvent was much stiffer and produced freestanding films, whereas the ink made with NMP was much less viscous and produced conformal films. The formulations for these two inks were as follows: (1) 94.6 wt% LLZTO / 0.7 wt% PVB / 4.7 wt% BBP in 3:7 wt 1-butanol/alpha terpineol (freestanding), and (2) 95.3 wt% LLZTO / 0.8 wt% PVB / 4.0 wt% BBP in NMP (conformal). The printed samples were sintered at 1100°C for 6 hours in argon to determine how well they would densify under conditions typically used to successfully densify pressed pellets. The cross-section SEM images shown in Figure 98a confirm that the films printed from these low-binder content inks densified well after sintering.

Co-Sintered Cathode/Electrolyte Bilayers

Composite cathode inks made with LLZTO and NMC-622 in either a 50/50 wt% ratio or a 25/75 wt% ratio were then prepared based on these same low-binder formulations. These inks were printed and dried, and then the previously developed LLZTO NMP ink was printed on top of the dried cathode to create a cathode/solid electrolyte bilayer (Figure 98b). Bilayers with the reverse configuration (LLZTO on bottom and composite cathode on top) were also prepared, but printing the LLZTO on top of the cathode proved to be easier since the conformal nature of the LLZTO ink facilitated wetting on the bottom layer.

Since the printed bilayer films are quite thin, these same composite cathode inks were also tape-cast on top of pre-sintered LLZTO pellets for easier electrochemical testing. These bilayer pellets were then co-sintered again at 900°C for 2 hours in argon. The LLZTO and NMC-622 were mixed in a 50/50 wt% ratio, and no conductive additives were included in the first iteration, as the polymer binder in the ink is carbonized during the sintering process. The SEM cross-sections are shown in Figure 99a. Although the composite cathode layer is not fully

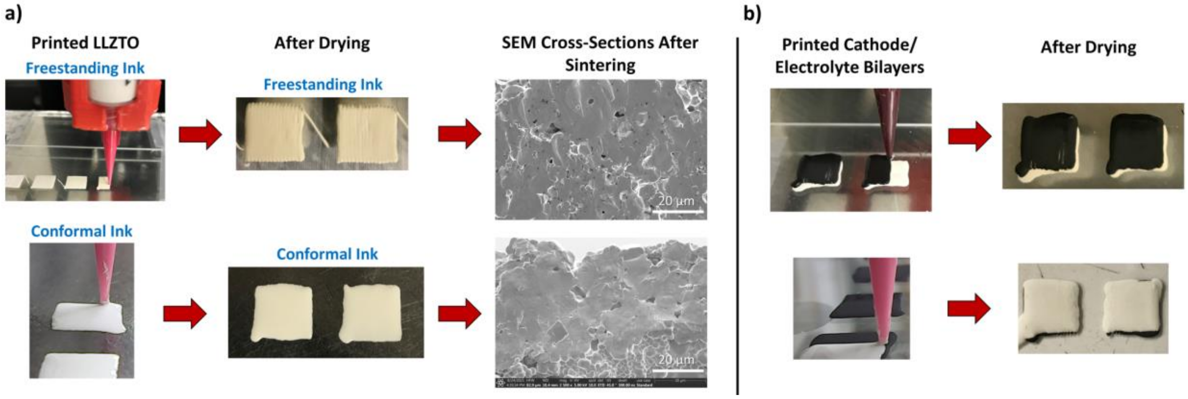

Figure 98. (a) Low-binder LLZTO inks printed by direct ink writing (250-µm nozzle). The formulations were as follows for the freestanding and conformal inks, respectively: 94.6 wt% LLZTO / 0.7 wt% PVB / 4.7 wt% BBP in 3:7 wt 1-butanol/alpha terpineol, and 95.3 wt% LLZTO / 0.8 wt% PVB / 4.0 wt% BBP in NMP. Cross-section scanning electron microscopy images show the printed films after sintering at 1100°C for 6 hours in argon with mother powder. (b) NMC-622 / LLZTO bilayers printed by direct ink writing (250-µm nozzle) in two configurations: (1) cathode on top / electrolyte on bottom; and (2) electrolyte on top / cathode on bottom.

densified, it appears that some sintering occurred between the LLZTO particles, and the spherical cathode particles remained fully intact. In addition, a separate bilayer pellet sample was prepared, but with 2.5 wt% carbon black added to the composite cathode ink to help with electrical conductivity. Interestingly, after co-sintering, the pre-sintered LLZTO pellet turned blue throughout its entirety, suggesting that the carbon caused a reaction that led to the diffusion of some species into the LLZTO. Indeed, the spherical NMC-622 particles can no longer be seen in the SEM cross-sections (Figure 99b), suggesting some degree of degradation. To try and prevent any reaction between the carbon black and the cathode material, another sample was prepared with NMC-622 that had been ALD-coated with Al_2O_3. However, after co-sintering the LLZTO pellet was green throughout.

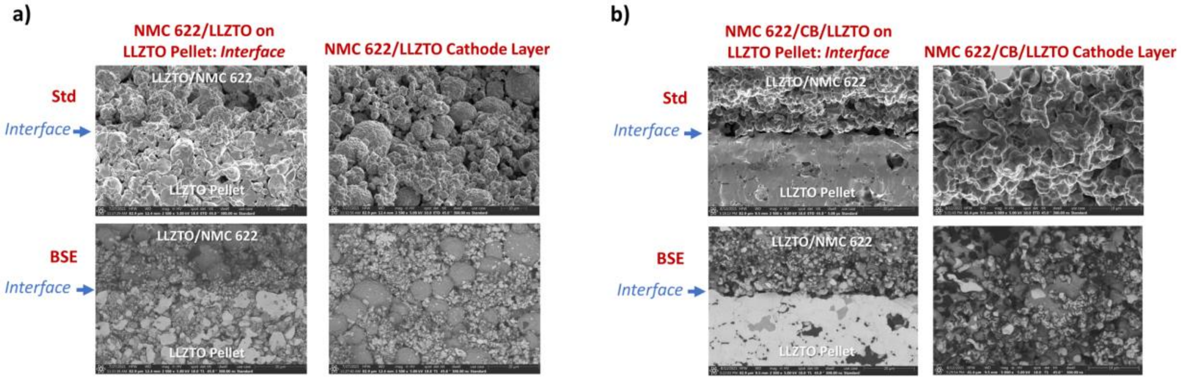

Figure 99. (a) Standard and backscattered (BSE) scanning electron microscopy cross-sections of LLZTO/NMC-622 composite cathodes (50/50 wt%) coated on pre-sintered LLZTO pellets and co-sintered at 900°C for 2 hours in argon: (a) without carbon black, and (b) with 2.5 wt% carbon black.

Each of these bilayer pellet samples was assembled into a full cell using lithium metal as the anode and graphite foil as the cathode current collector. The EIS results and the 1st charge/discharge cycle (at ~ C/50) are shown in Figure 100. Although the charge and discharge cycle was much shorter than it should be, the sample without carbon black had the lowest resistance and performed the best, lasting the longest before hitting the upper cutoff voltage. The two samples with carbon black both showed higher resistance and much worse cycling performance. The sample without the ALD coating reached the cutoff voltage in less than 1 second, indicating a high degree of internal cell resistance. The sample with the ALD coating performed slightly better, but still reached the cutoff voltage after a little over 2 minutes. To try and improve the performance, another set of samples was prepared with a different ratio of LLZTO to NMC and the addition of sintering aids (Li_3BO_3, or LBO, and SiO_2) based on the following formulation: 22.9 wt% LLZTO / 72.2 wt% NMC-622 / 1.0 wt% LBO / 0.2 wt% SiO / 1.0 wt% PVB / 2.8 wt% BBP. One sample was made with 2.5 wt% carbon black, and one was made with 10 wt% ITO to try to increase the conductivity without causing degradation reactions. In each case, the LLZTO pellets still turned green during sintering. However, the electrochemical performance was greatly improved relative to the first set of samples, as shown in Figure 100. The best-performing sample from this set was the one with no conductive additives, which showed a low resistance and charged for ~ 28 hours before hitting the upper cutoff voltage. The sample with carbon black also performed quite well, but showed a slightly higher resistance and hit the upper cutoff voltage earlier (~ 22 hours). The sample with ITO showed worse performance than the original 50/50 wt% LLZTO/NMC-622 sample, indicating that ITO is not a very effective conductive additive for co-sintering. The team is working to further improve the charge and discharge capacities of these cells.

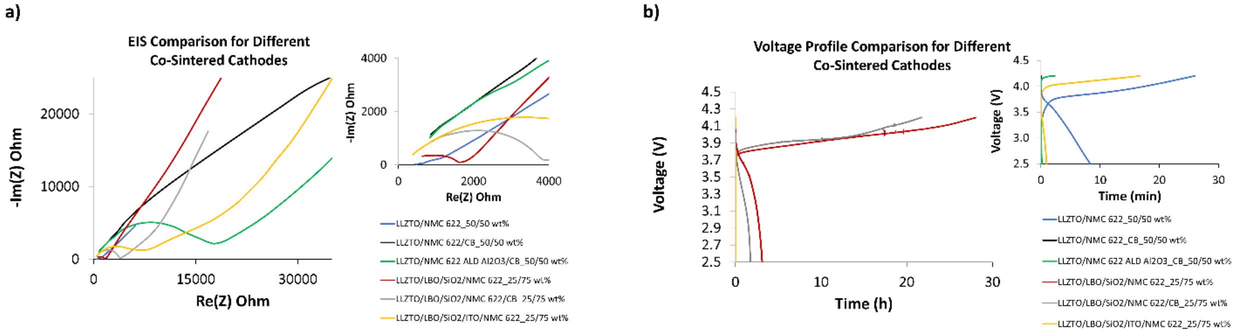

Figure 100. Comparison of electrochemical impedance spectroscopy results (a) and 1st cycle charge/discharge voltage profiles at ~ C/50 (b) for different composite cathodes coated on pre-sintered LLZTO pellets and co-sintered at 900°C for 2 hours in argon.

Overall, these results show significant progress toward successfully co-sintering the NMC-622 cathode and LLZTO SE to give good electrochemical performance. The team developed low-binder LLZTO and LLZTO/NMC-622 ink formulations for 3D printing that aid densification during sintering, and successfully printed cathode/electrolyte bilayer films. In addition, they found that decreasing the LLZTO/NMC-622 ratio to ~ 25:75 wt% and adding sintering aids substantially improves electrochemical performance of these co-sintered composite cathodes in full cells.

Patents/Publications/Presentations

The project has no patents, publications, or presentations to report this quarter.

Task 4.5 – Interfacial Studies on Lithium Thiophosphate Based Solid Electrolytes and Cathodes (Jagjit Nanda, Oak Ridge National Laboratory)

Project Objective. Capacity fading and the underlying interfacial side reactions between thiophosphate SEs and cathode active materials are not well understood. A key project deliverable is to combine EIS measurements with complementary *in situ* and *ex situ* spectroscopy and microscopy to identify decomposition reaction products at the CEI. Ultimately, this work will enable a mechanistic understanding of factors that limit the rate performance and capacity loss of SSBs. The goal here is to combine the information from these techniques to provide a unified overview of the interfacial layer's composition, structure, and morphology. In this multi-year work, the team will investigate a number of SEs [LPS, LGPS, and $Li_{9.54}Si_{1.74}P_{1.44}S_{11.7}Cl_{0.3}$ (LSiPCl)] and cathode compositions belonging to different structural families [LFP (olivine), FeS_2 (sulfide-based conversion cathode), and $LiNi_{0.6}Mn_{0.2}Co_{0.2}O_2$ (NMC-622, layered oxide)].

Project Impact. SSBs are poised to be the next-generation battery technology for meeting EV goals in terms of energy density, cycle life, and safety. Among other technical barriers, the success of this technology relies on design of stable electrode/electrolyte interfaces. Sulfide-based SEs have high ionic conductivity ($> 10^{-4}$ S/cm) and are mechanically soft, which simplifies processing compared to their oxide counterparts. Furthermore, sulfide SEs are comprised of earth abundant materials (for example, sulfur and phosphorus) and can be easily synthesized using scalable, low-temperature, solution-based routes.

Approach. A low-temperature (< 350°C) solution-based synthesis method will be used to synthesize the LPS family of SEs. The structure of these materials is characterized using XRD, Raman spectroscopy, and neutron scattering. Standard AC/DC electrochemical methods are used to characterize ionic conductivity, electrochemical stability, and CCD. The work scope includes using various *in situ* and *ex situ* electrochemical, microscopic, and spectroscopic tools for characterizing the structure, morphology, and kinetics of the interfacial reaction layer formed between thiophosphate SEs and cathodes.

Out-Year Goals. Develop thiophosphate SEs – sulfide cathode interfaces with low ASR for ASSBs.

Collaborations. This project will collaborate with G. Ceder (UCB) and P. Jena (Virginia Commonwealth University) on modeling and synthesis guideline, as well as with S. Greenbaum on solid-state NMR to measure ion-diffusivity and local bonding.

Milestones

1. Demonstrate and test hot-sintering method to fabricate composite thiophosphate SE-NMC cathodes. (Q1, FY 2021; Completed)
2. Optimize synthesis and processing conditions (for example, interfacial coatings and stack pressure) to minimize the ASR between argyrodite SEs and NMC cathodes. (Q2, FY 2021; Completed)
3. Perform Raman microscopy, NMR, and electron microscopy to characterize bulk argyrodite SE and cathode SE interfaces to investigate capacity loss and degradation mechanisms. (Q3, FY 2021; In progress)
4. Select and optimize a few solid-state cathode compositions to demonstrate room-temperature cycling with LPS and/or argyrodite SEs. Stretch Goal: 50 cycles with < 20% capacity fade. (Q4, FY 2021; In progress)

Progress Report

SSB literature reports often employ large external stack pressures (>1 MPa) to encourage stable solid-solid contacts during cycling. Furthermore, some studies have suggested that applying very high pressures (tens of MPa) extends the oxidative stability of sulfide-based SEs beyond 5 V versus Li/Li^+. Motivated by these prior investigations, Q4 activities evaluated how external stack pressure impacts the cycling performance of pellet-type SSBs containing ultra-high purity, thermally evaporated Li-metal anodes (~ 2.5 mAh/cm^2 on copper foil), ß-Li_3PS_4 separators (LPS, ~ 0.9 mm thick), and composite NMC-811 + LPS + C cathodes (60 wt% NMC, 6.6 mg_{NMC}/cm^2). Cells were constructed and tested in an Ar-filled glovebox as detailed in prior reports.

Figure 101a-b shows galvanostatic voltage profiles for SSBs tested under stack pressures of 5 MPa and 50 MPa, respectively. Both cells had an open-circuit potential of 2.41 ± 0.01 V and exhibited a sloping voltage profile ~ 2.6-3.7 V during the 1st charge due to oxidative decomposition of LPS. These results clearly show that high stack pressures have negligible impact on the thermodynamic stability of LPS and extent of LPS decomposition (~ 0.30 mAh/cm^2 for both cells). Surprisingly, the cell tested at 50 MPa had a slightly lower discharge capacity (113 mAh/g versus 128 mAh/g at 5 MPa), indicating that mechanical confinement does not necessarily promote better active material utilization. During extended cycling (Figure 101c), both cells exhibited gradual capacity fade (for example, 74 ± 1% capacity retention after 10 cycles), presumably due to formation of a resistive cathode/electrolyte interface and/or loss of solid-solid contact. Notably, the cell design implemented here is not prone to internal shorting from lithium dendrites during 50+ cycles at room temperature.

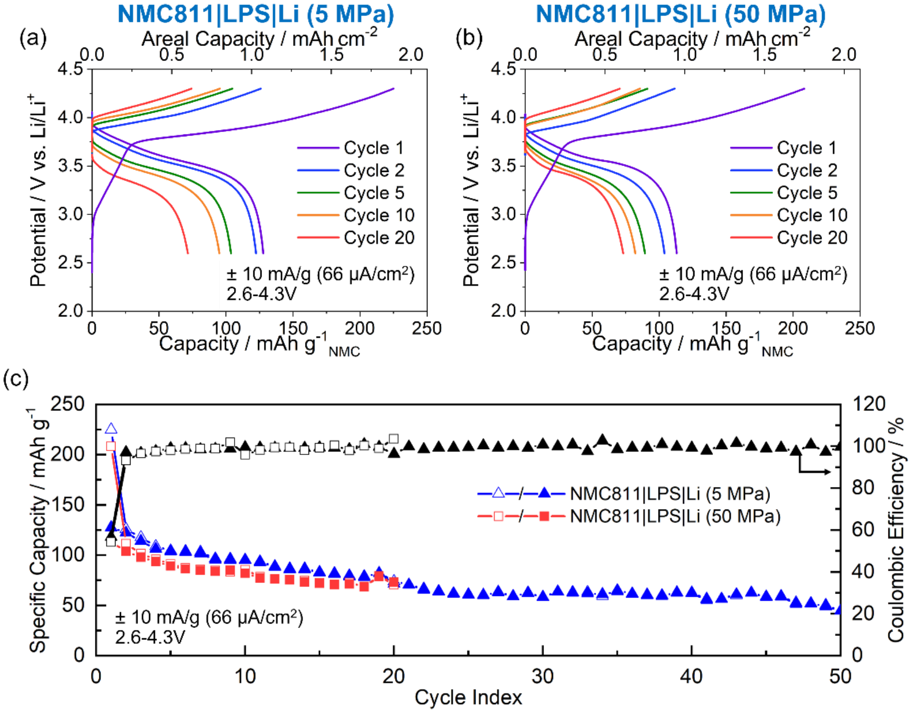

Figure 101. Galvanostatic cycling performance of SSBs containing thermally evaporated Li-metal anodes, LPS separators, and composite NMC cathodes. (a-b) Voltage profiles for cells tested using stack pressures of (a) 5 MPa and (b) 50 MPa. (c) Long-term cycling performance. The cell tested at 50 MPa is still cycling, and additional data on this sample will be reported in FY 2022.

Overall, these results indicate that simply applying large external forces is not sufficient to enable high-performance solid-state cathodes. To increase CE and reversible capacity of SSBs containing sulfide-based SEs, studies next fiscal year will focus on: (1) replacing LPS with halide-containing SEs (for example, $Li_6PS_5Cl_xBr_{1-x}$) with improved oxidative stability, (2) applying cathode coatings to promote more stable cathode/SE interfaces, and (3) developing high-capacity conversion cathodes such as FeS_2 and FeF_2. To screen various cathode compositions and coatings, testing capabilities will be expanded to cycle up to 10 SSBs simultaneously in an Ar-filled glovebox.

Patents/Publications/Presentations

Publication

- Vishnugopi, B. S., E. Kazyak, J. A. Lewis, J. Nanda, M. T. McDowell, N. P. Dasgupta, and P. P. Mukherjee. "Challenges and Opportunities for Fast Charging on Li-Metal Batteries." *ACS Energy Letters* 6 (2021): 3734−3749.

Presentation

- Interdisciplinary Topics in Materials Science (ITAM), (July 27–29, 2021): "Next Generation Materials and Systems for Electrochemical Energy Storage"; J. Nanda. Invited.

Task 4.6 – Prelithiation of Silicon Anode for High-Energy Lithium-Ion Batteries
(Yi Cui, Stanford University)

Project Objective. Prelithiation of high-capacity electrode materials is an important means to enable those materials in high-energy batteries. This study pursues three main directions: (1) development of facile and practical methods to increase 1st-cycle CE of anodes, (2) synthesis of fully lithiated anode to pair with high-capacity, Li-free cathode materials, and (3) prelithiation from the cathode side.

Project Impact. Prelithiation of high-capacity electrode materials will enable those materials in the next generation of high-energy-density Li-ion batteries. This project's success will make high-energy-density Li-ion batteries for EVs.

Approach. Silicon electrode film will be prepared by coating the slurry of silicon nanoparticles, carbon black, and binder mixture on copper foil through a doctor-blading method. The silicon electrode film will be prelithiated by pressing a Li-metal foil on top of it and heating it in an argon glovebox for a certain time. Then, Li_xSi electrode film can be obtained by removing the redundant lithium foil through a peeling-off approach. The redundant lithium foil is reusable for the next prelithiation. The structure, morphology, and other properties can be analyzed by SEM, TEM, XPS, Raman spectroscopy, XRD, etc. In the first year, the team aims to fabricate Li_xSi freestanding electrode film and improve its air stability. In the second year, the team aims to improve the electrochemical stability in full cells.

Out-Year Goals. Materials containing a large quantity of lithium will be synthesized for pre-storing lithium ions inside batteries. Materials and processes will be developed to be compatible with battery electrode and cell fabrication. First-cycle CE of anodes will be improved and optimized by prelithiation materials. Materials for prelithiation from the cathode side will be developed.

Collaborations. This project engages in collaboration with the following: BMR PIs; SLAC: M. Toney *(in situ* X-ray); and Stanford: W. Nix (mechanics).

Milestones

1. Produce ultra-thin lithium foil as a new dry prelithiation reagent. Produce lithium foil of different thicknesses to match the varied anode capacity. (Q1, FY 2021; Completed)
2. Demonstrate controllable initial CE improvement by prelithiation with ultra-thin lithium foil of different thicknesses. (Q2, FY 2021; Completed)
3. Demonstrate the microstructural and chemical evolution of silicon anode during ultra-thin lithium foil prelithiation. (Q3, FY 2021; Completed)
4. Demonstrate the role of ultra-thin lithium foil prelithiation to improve good cycle capacity retention in full battery. (Q4, FY 2021; Completed)

Progress Report

Substantial improvements on energy density of Li-ion batteries require development of high-capacity electrodes. Silicon anodes that have high theoretical capacities (3579 mAh/g)—ten times higher than the conventional graphite anodes (372 mAh/g)—hold great potential for application in high-energy Li-ion batteries. However, silicon anodes exhibit a low initial CE of 50-80%, which means 20-50% of battery capacity will be lost after 1st cycle due to side reactions. Therefore, a strategy to compensate the initial active lithium loss and improve initial CE is urgently needed to prevent battery capacity degradation.

In the previous report, the team presents a new prelithiation reagent of reduced Gr oxide (rGO)-hosted ultra-thin lithium [Li@eGF, (exfoliated Gr fluoride)] foils compatible with dry prelithiation. They applied Li@eGF foils for silicon anode prelithiation and to achieve controllable initial CE improvement from ~ 80% to ~ 100%. They further investigated morphological and chemical evolution after Li@eGF prelithiation. Here, they continue to pair Li@eGF prelithiated anodes with cathodes to demonstrate improved capacity retention in full cells after prelithiation.

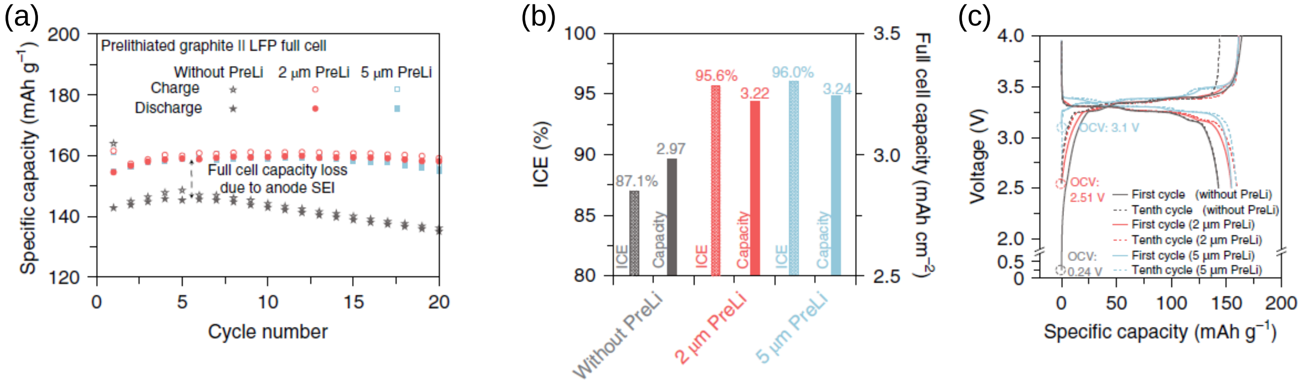

Figure 102. (a) Galvanostatic cycling of graphite || LFP full cells at 0.05 C using different thicknesses of Li@eGF film for prelithiation in the anode. For this graphite || LFP full cell, 1C = 150 mA g^{-1}. (b) Comparisons of the initial Coulombic efficiency and areal capacity (after five activation cycles) of graphite || LFP full cells using different thicknesses of Li@eGF film for anode prelithiation. (c) Voltage profiles of graphite || LFP full cells at 0.05 C using different thicknesses of Li@eGF film for prelithiation.

Here, the team uses graphite || LFP full cells as a model to investigate Li@eGF prelithiation in full cells. Similar to silicon, graphite meets the same problem of relatively low initial CE of ~ 93%, suggesting ~ 7% of battery capacity is lost after the initial cycle. In the team's demonstration, graphite anodes with designed capacity of 3.22 mAh cm^{-2} are paired with LFP cathodes with designed capacity of 3.22 mAh cm^{-2}. Therefore, the constructed battery has a theoretical capacity of 3.22 mAh cm^{-2}. However, without prelithiation, the 1st discharge capacity of the cell is only ~ 2.97 mAh cm^{-2}. The initial loss of 7% of battery capacity is mainly due to the initial SEI formation on the anode, and leads to irreversible battery capacity degradation (Figure 102a). To address this problem, the team applies Li@eGF prelithiation to the graphite anodes to compensate for the initial capacity loss. They coat a 2-µm-thick and a 5-µm-thick Li@eGF film, respectively, on a graphite anode. In both cases, the full-cell initial CE improves from 87% to ~ 96% (Figure 102b). Correspondingly, the capacities of Li-ion full cells are fully recovered and stabilized at the theoretical capacity (~ 3.22 mAh cm^{-2}). This result illustrates that this prelithiation function significantly improves cell capacity and compensates for initial loss of lithium in the anode. In addition, the appropriate prelithiation amount is important to avoid excessive lithium deposition on the anodes, which prevents poor battery performance and safety hazards. Prelithiation with 5-µm-thick Li@eGF (0.853 mAh cm^{-2}) exceeds the initial lithium loss amount of the graphite anode (0.25 mAh cm^{-2}). Expectedly, the full cell suffers from metallic lithium plating because the graphite cannot accommodate all lithium ions from the cathode during cell charging. As shown in Figure 102c, this plating induces higher-voltage plateaus, presenting metallic lithium deposition. By contrast, the graphite || LFP full cell prelithiated with 2-µm-thick Li@eGF has similar voltage profiles compared to the cell without prelithiation, showing no evidence of metallic lithium plating. These results demonstrate the importance of tunable thickness in Li@eGF, to well match the prelithiation capacity with initial capacity loss.

Patents/Publications/Presentations

Publication

- Chen, H., Y. Yang, D. Boyle, Y. K. Jeong, R. Xu, L. S. de Vasconcelos, and Y. Cui. “Free-Standing Ultrathin Lithium Metal–Graphene Oxide Host Foils with Controllable Thickness for Lithium Batteries.” *Nature Energy* 6 (2021): 790–798.

TASK 5 – SULFUR ELECTRODES

Team Lead: Prashant Kumta, University of Pittsburgh

Summary

The collected work of the projects in this Task encompasses the following areas:

- Conducting focused fundamental research on the mechanism of "shuttle effect" inhibition for rechargeable Li-S batteries.
- Developing electrode and electrolyte systems that can mitigate the "shuttle effect" so the low self-discharge and long cycle life can be achieved.
- Synthesizing sulfur composite materials with an emphasis on polymer sulfur composite materials.
- Developing creative electrode-making processes to improve processability and aerial capacity; for example, polymeric sulfur composites may not be suitable for the traditional slurry casting process.
- Developing a novel S_xSe_y cathode material for rechargeable lithium batteries with high energy density and long life, as well as low cost and high safety.
- Delivering an electrochemically responsive self-formed hybrid LIC as a protective layer for Li-metal anodes, enabling Li-metal anodes to cycle with a high efficiency.
- Developing high-energy, low-cost Li-S batteries with long lifespan.

Highlights. The highlights for this quarter are as follows:

- Task 5.1 led by K. Amine's group at ANL focused on conducting computational modeling in collaboration with L. Cheng of the Materials Science Division at ANL to understand the interaction between the formed lithium polysulfides and their experimentally synthesized ZnS, Co-N-C double-end binding (DEB) catalytic hosts. The calculations showed that the binding energies of Li_2S_4, Li_2S_6, and Li_2S_8 on the ZnS, Co-N-C surface are all ~ 1 eV higher than the single-end binding (SEB) carbon-based sulfur electrodes due to the hypothesized synergistic catalytic effect of Co-N-C and ZnS. This enhanced binding of the catalyst to the formed lithium polysulfides results in suppression of the dissolution and migration of lithium polysulfides from the cathode into the electrolyte. They also showed the efficacy of the DEB catalyst when cycling the cathodes in $LiNO_3$ free electrolytes, delivering a stable specific capacity of ~ 930 mAh g^{-1} after 100 cycles. The computational modeling studies also demonstrated that the Co-N-C single-atom catalyst (SAC) surface is more favorable for binding the formed lithium polysulfides compared to the Gr surface, thus preventing migration into the electrolyte. Further studies are under way. Results of these studies show validity of the DEB catalytic function of the ZnS, Co-N-C sulfur cathode hosts for achieving high-capacity sulfur electrodes.
- D. Lu and J. Liu's group at PNNL demonstrated a protocol to realize large-scale preparation of sulfur electrodes with both high mass loading and low porosity using a lubricant-assisted rolling method incorporating PTFE binder. They utilize a unform mixed paste of sulfur / Ketjenblack (KB), Super-P conductive additive, and PTFE binder prepared with the assistance of isopropanol (IPA) serving as a lubricant. They rolled the paste into electrode films of different thicknesses followed by vacuum drying into free-standing electrodes. Utilizing this method, they were able to generate electrodes with a sulfur loading of 4.3 mg cm^{-2} with an electrode thickness of ~ 55 μ yielding a high electrode density of 1.1 g cm^{-3}. Furthermore, the IPA enables the PTFE binder to be deformed into long fibers distributed evenly in the electrode, reducing the binder content to a low level of 1 wt% and elevating sulfur content to greater than 80 wt%. Using this protocol and system, they were able to generate electrodes with sulfur loadings

> 7 mg cm^{-2} and high areal capacities of > 9 mAh cm^{-2}. Further studies are under way. Results of these studies demonstrate this novel electrode processing method for large-scale fabrication of dense and high-loaded sulfur electrodes with lean amounts of binder.

- Y. Cui's group at Stanford reports on the continuing studies validating the catalytic efficacy and polysulfide capture of nanoscale encapsulation in ASSLSBs by testing the electrochemical performance of the $Li_2S@TiS_2$ cathodes in SPEs. They have demonstrated specific capacity as high as ~ 910 mAh g^{-1} Li_2S at 0.2C at 60°C, which is more than twice higher than that exhibited by bare Li_2S. Additionally, the $Li_2S@TiS_2$ cathode with a total cathode mass of 8.6 mg cm^{-2} sans the current collector. The system also exhibited a much better rate capability, achieving a discharge capacity of 660 mAh g^{-1}, 488 mAh g^{-1}, and 309 mAh g^{-1} based on Li_2S at 0.3C, 0.4C, and 0.8C, respectively. Moreover, the $Li_2S@TiS_2$ cell exhibits stable cycling at 0.8C at 80°C. After an initial discharge capacity of 490 mAh g^{-1} at 80°C, the cells retain 79%, 71%, and 68% of their initial capacity after 50, 100, and 150 cycles, respectively. The system also shows an average CE of 98.6% after 150 cycles, showing reduced shuttle effect owing to efficient polysulfide trapping by TiS_2 encapsulation. The team plans to further study the system. Results to date demonstrate the effectiveness of using TiS_2 encapsulation enabling polysulfides entrapment while also enhancing oxidation kinetics to achieve high-performing ASSLSBs.
- D. Qu's group at University of Wisconsin has conducted a systematic study of influence of sulfur in polyacrylonitrile (PAN) electrodes and tested them in coin cells to verify their earlier conclusions of sulfur containing organic polymers. They accordingly studied different sulfur (S_8) to PAN ratios. They observed that for very low sulfur content, the initial and subsequent discharge curves were very similar. With increasing sulfur content, the initial discharge curves were very different to subsequent discharge curves. In fact, for 8:1 (S_8:PAN) ratio, a clear two-step discharge curve was evident, confirming the existence of long-chain polysulfides or elemental sulfur. They also observed, as known in the literature, that PAN sulfur electrodes do not cycle well in ether-based electrolyte traditionally used for elemental sulfur cathodes; they do cycle well in carbonate-based electrolytes. The team plans to further investigate the influence of solvents on the cyclability of these S-PAN electrodes. The results of these studies demonstrate the role of sulfur interactions with nitrogen-containing polymers such as PAN and their influence in achieving high energy density in Li-S batteries.
- G. Liu's group at UCB has been studying use of amphiphilic hydrofluoroether (HFE) in electrolytes to further improve sulfur electrode cycling and also stabilize lithium metal. They showed that lithium anode corrosion and dendrite formation can be much reduced in the electrolyte with the presence of this fluoro-based amphiphilic electrolyte with highly concentrated salt solution resulting in high CE. The HFE molecules have a bi-functional amphiphilic structure comprised of a fluorocarbon lithiophobic moiety and an ethylene oxide (EO) lithiophilic moiety on each end. The system studied is 1,1,1,2,2,3,3,4,4-nonafluoro-6-(2-methoxyethoxy)hexane (F_4EO_2). The salt is 0.5 M LiTFSI. The base solvent is TTE with F_4EO_2:TTE weight ratio of 1:5. The resulting micellar structure of lithium salts in the EO cores is dispersed in the TTE solvent. The addition of a small amount (5-15% by weight) of DOL helps to dissolve polysulfides while also facilitating Li_2S_x formation, improving the utilization of sulfur. Controlling the DOL amount and LiTFSI, the team was able to demonstrate a Li-S cell operating above 1200 mAh g^{-1}, yielding over 99.5% CE. They plan to further investigate these systems. Results of these studies show the benefit of developing novel micellar electrolytes that are polysulfide resistant and prevent dendrites at the Li-metal anode while also inhibiting Li-metal corrosion for Li-S batteries.

Task 5.1 – Novel Chemistry: Lithium Selenium and Selenium Sulfur Couple (Khalil Amine, Argonne National Laboratory)

Project Objective. The project objective is to develop a novel S_xSe_y cathode material for rechargeable lithium batteries with high energy density and long life, as well as low cost and high safety.

Project Impact. Development of a new battery chemistry is promising to support the goal of PHEV and EV applications.

Approach. The dissolution of lithium polysulfides in nonaqueous electrolytes has been the major contribution to the low energy efficiency and short life of Li-S batteries. In addition, insulating characteristics of both end members during charge/discharge (sulfur and Li_2S) limit their rate capacity. To overcome this problem, sulfur or Li_2S is generally impregnated in a carbon-conducting matrix for better electronic conductivity. However, this makes it difficult to increase the loading density of practical electrodes. It is proposed to solve these barriers using the following approaches: (1) partially replace sulfur with selenium, (2) nano-confine the S_xSe_y in a nanoporous conductive matrix, and (3) explore advanced electrolytes with suppressed shuttle effect.

Out-Year Goals. This new cathode will be optimized with the following goals:

- A cell with nominal voltage of 2 V and energy density of 600 Wh/kg.
- A battery capable of operating for 500 cycles with low capacity fade.

Collaborations. This project engages in collaboration with the following: Y. Ren and C. Sun of APS at ANL, and L. A. Curtiss and L. Cheng at ANL.

Milestones

1. Build in-house Li-S pouch cell fabrication line, and demonstrate > 100-mAh pouch-cell performance using Se-doped sulfur cathode and fluorinated ether-based electrolytes. (Q1, FY 2021; Completed)
2. Design and characterize novel cathode host for Li-S and Li-Se/S batteries. (Q2, FY 2021; Completed)
3. Validate electrochemical performance of new cathode host. (Q3, FY 2021; In progress)
4. Conduct *operando* and *ex situ* characterization on developed cathodes during charge/discharge. (Q4, FY 2021; In progress)

Progress Report

This quarter, the team collaborated with L. Cheng at the Materials Science Division at ANL. The team conducted computational modeling to understand interaction between lithium polysulfides and generated ZnS/Co-N-C DEB host.

The dimension of the rectangular Gr layer was chosen to be 12.30 Å × 12.78 Å with 60 carbon atoms. Three carbon atoms on the Gr surface were replaced by one cobalt and two nitrogen atoms to form the Co–N–C surface shown in Figure 103a (b1). ZnS was placed near the CoN site to explore the synergistic effect between the two sites. This ZnS, Co–N–C surface is shown in Figure 103a (c1). The lithium polysulfide clusters were then placed on different positions on the Gr and the Co-N-C surface to explore the most stable structure favoring adsorption.

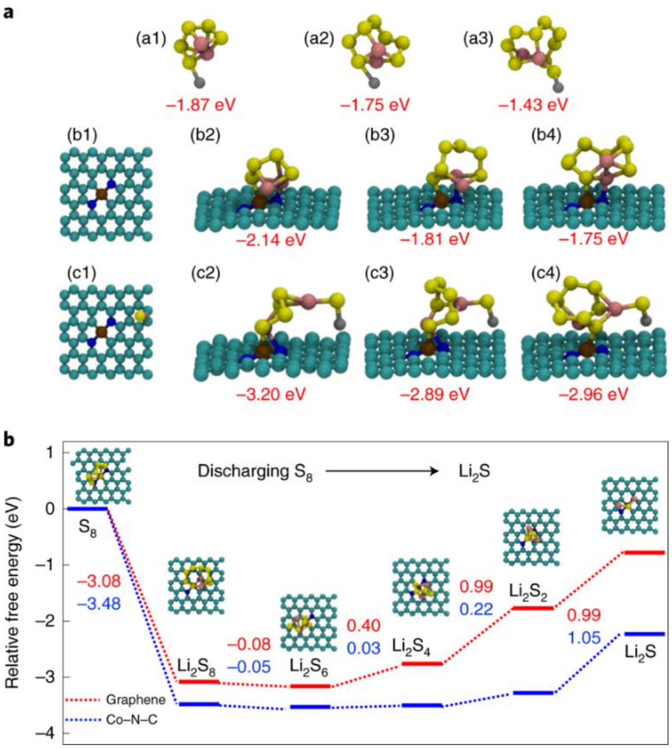

Figure 103. (a) Optimized configurations of Li_2S_4, Li_2S_6, and Li_2S_8 absorption on ZnS (a1-a3), the Co-N-C surface (b1-b4), and the ZnS, Co-N-C surface (c1-c4). The yellow, pink, silver, brown, blue, and cyan balls denote the sulfur, lithium, zinc, cobalt, nickel, and carbon atoms, respectively. (b) Relative free energy for the discharging process from S_8 to Li_2S on the bare graphene and Co-N-C surfaces. The optimized structures of the intermediates on the Co-N-C surface are shown as the insets. Same color coding for atomic structure as in (a).

The binding energy of lithium polysulfides on Co-N-C surface is calculated using equation (1) as:

$$E_{Li_2S_x+Co-N-C} - E_{Co-N-C} - E_{Li_2S_x} \qquad (1)$$

where $E_{Li_2S_x}$, E_{Co-N-C}, and $E_{Li_2S_x+Co-N-C}$ are the energies of the lithium polysulfides, Co-N-C surface, and lithium polysulfides – Co-N-C adsorption complex. Similarly, the binding energy of lithium polysulfides on ZnS, Co-N-C is calculated using equation (2) as:

$$E_{Li_2S_x+ZnS,Co-N-C} - E_{ZnS,Co-N-C} - E_{Li_2S_x} \quad (2)$$

where $E_{ZnS,Co-N-C}$ and $E_{Li_2S_x+ZnS,Co-N-C}$ are the energies of ZnS, Co-N-C surface and lithium polysulfides – ZnS, Co-N-C adsorption complex. The relative free energy of the discharge process from S_8 to Li_2S on the substrate was further calculated following the reaction sequence of:

$$S_8 + Li \overset{(3)}{\rightarrow} Li_2S_8 \overset{(4)}{\rightarrow} Li_2S_6 \overset{(5)}{\rightarrow} Li_2S_4 \overset{(6)}{\rightarrow} Li_2S_2 \overset{(7)}{\rightarrow} Li_2S$$

The corresponding reaction energies for the five steps were calculated from the equations (3-7), respectively:

$$E_{Li_2S_8+substrate} - E_{S_8+substrate} + 2E_{Li} \qquad (3)$$

$$E_{Li_2S_6+substrate} + \frac{1}{4}E_{S_8} - E_{Li_2S_8+substrate} \quad (4)$$

$$E_{Li_2S_4+substrate} + \frac{1}{4}E_{S_8} - E_{Li_2S_6+substrate} \quad (5)$$

$$E_{Li_2S_2+substrate} + \frac{1}{4}E_{S_8} - E_{Li_2S_4+substrate} \quad (6)$$

$$E_{Li_2S+substrate} + \frac{1}{8}E_{S_8} - E_{Li_2S_2+substrate} \qquad (7)$$

where E_{Li} is the energy of lithium metal per atom, and E_{S_8} is the gas-phase energy of S_8.

Figure 103a shows the optimized configurations of lithium polysulfides with polar ZnS, Co-N-C SAC, and ZnS, Co-N-C surfaces, in which Li^+ binds with sulfur atoms in the case of polar ZnS (a1-a3), and S_n^{2-} binds with cobalt and nitrogen in the case of the Co-N-C SAC surface (b1-b4), while Li^+ and S^{2-} bind with the sulfur and cobalt atoms on the ZnS, Co-N-C surface. The calculated results show that the binding energies of Li_2S_4, Li_2S_6, and Li_2S_8 on the ZnS, Co-N-C surface are -3.20 eV, -2.89 eV, and -2.96 eV, respectively, which are all higher (~ 1 eV higher) than the former SEB surface condition due to the synergistic effect of Co-N-C SAC and polar ZnS. Such enhanced binding strength toward lithium polysulfides can suppress their dissolution and migration from the cathode.

To confirm the team's DFT results, the cycling performance of 3D-OMSH / ZnS, Co-N-C/S cathode in the electrolytes without $LiNO_3$ additive was tested to further evaluate effectiveness of the team's DEB host in relieving the lithium polysulfide's shuttle effect. As shown in Figure 104, even in $LiNO_3$-free electrolyte, the 3D-OMSH / ZnS, Co-N-C/S cathode can still deliver a high initial specific capacity of 1230.92 mAh g^{-1} at 0.2 C and maintain specific capacity of 933.54 mAh g^{-1} after 100 cycles. Meanwhile, the CE of the 3D-OMSH / ZnS, Co-N-C cathode in $LiNO_3$-free electrolyte was only slightly lower than that in the normal 0.2 M $LiNO_3$ electrolyte, confirming effectiveness of 3D-OMSH / ZnS, Co-N-C host materials in suppressing the shuttle effect.

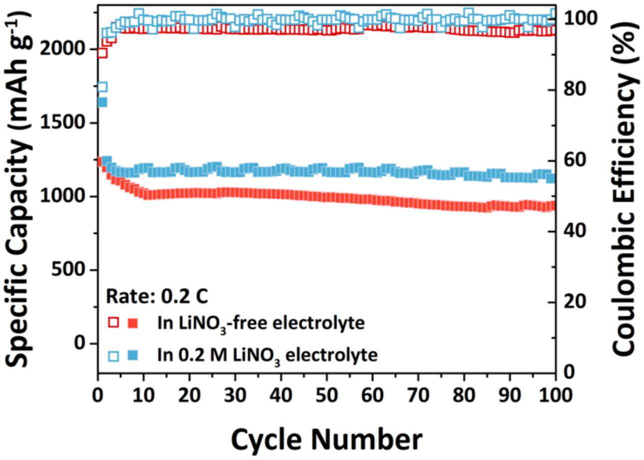

Figure 104. Cycling performance of 3D-OMSH / ZnS, Co-N-C/S cathode in the electrolytes with and without 0.2 M $LiNO_3$ additive at 0.2 C. Solid symbols indicate discharge specific capacity; hollow symbols indicate Coulombic efficiency.

To gain an in-depth understanding of the Co-N-C SAC surface in enhancing the electrochemical reaction kinetics, the whole reaction involving the formation of Li_2S from S_8 was considered. Figure 103b shows the relative free energy landscape for the discharge process from S_8 to Li_2S on the bare Gr and Co-N-C surfaces. The optimized structures of the intermediates on the Co-N-C SAC substrates are shown in the insets. The data clearly show that the discharge process is more thermodynamically favorable on the Co-N-C SAC surface compared to the Gr surface. Specifically, the reaction energy from solid S_8 to liquid Li_2S_8 on the Co-N-C SAC surface is more exothermic than that on the Gr surface. The last two steps—from Li_2S_4 to Li_2S_2 and from Li_2S_2 to Li_2S—exhibit larger energy barriers (~ 1.98 eV) compared to the other steps on both substrates, suggesting that the Li_2S_2/Li_2S precipitation process is the rate-limiting step during discharging. Nevertheless, on the Co-N-C SAC surface, the energy barrier of the endothermic precipitation process is effectively lowered (1.27 eV). This finding indicates that the Li_2S_2/Li_2S precipitation process is thermodynamically more favorable on the Co-N-C SAC surface because it demonstrates stronger binding strength toward lithium polysulfides, which can effectively adsorb the dissolved lithium polysulfides. Moreover, the Co-N-C SAC is electronically conductive, which can thus provide fast electron transfer between cobalt atoms of SAC and sulfur atoms of lithium polysulfides and further facilitate the weakening of the Li-S bonds of lithium polysulfides. Thus, SAC can significantly decrease the reduction barrier of lithium polysulfides, facilitate the Li_2S precipitation, and improve the reaction reversibility.

Patents/Publications/Presentations

The project has no patents, publications, or presentations to report this quarter.

Task 5.2 – Development of High-Energy Lithium-Sulfur Batteries (Dongping Lu and Jun Liu, Pacific Northwest National Laboratory)

Project Objective. The project objective is to develop high-energy, low-cost Li-S batteries with long lifespan. All proposed work will employ thick sulfur cathode (≥ 4 mg/cm^2 of sulfur) at a relevant scale for practical applications. The diffusion process of soluble polysulfide out of thick cathode will be revisited to investigate cell failure mechanism at different cycling. The fundamental reaction mechanism of polysulfide under the electrical field will be explored by applying advanced characterization techniques to accelerate development of Li-S battery technology.

Project Impact. The theoretical specific energy of Li-S batteries is ~ 2300 Wh/kg, which is almost three times higher than that of state-of-the-art Li-ion batteries. The proposed work will design novel approaches to enable Li-S battery technology and accelerate market acceptance of long-range EVs required by the EV Everywhere Grand Challenge.

Approach. The project proposes the following approach: (1) to identify and address key issues of applying high-energy sulfur cathodes including materials, binders, electrode architectures, and functional electrode additives, (2) to advance the mechanism study of sulfur cathode and electrolyte by using *in situ* / *ex situ* techniques and custom-designed hybrid cell setup, and (3) to verify effectiveness of the new approaches with coin/pouch cells by using high-loading electrodes (> 4 mg/cm^2), limited lithium (< 200% lithium excess), and lean electrolyte [electrolyte/sulfur (E/S) < 4 µL/mg].

Out-Year Goals. This project has the following out-year goals:

- Fabricate Li-S pouch cells with thick electrodes to understand sulfur chemistry/electrochemistry in environments similar to those witnessed in real application.
- Leverage the Li-metal protection project funded by the DOE and PNNL advanced characterization facilities to accelerate development of Li-S battery technology.
- Develop Li-S batteries with a specific energy of 400 Wh/kg at cell level, 1000 deep-discharge cycles, improved abuse tolerance, and less than 20% capacity fade over a 10-year period to accelerate commercialization of EVs.

Collaborations. This project engages in collaboration with the following: X-Q. Yang (BNL), J. Bao (PNNL), P. Khalifah (BNL), and J. Tao (PNNL).

Milestones

1. Optimize electrode architecture to realize sulfur utilization of > 1000 mAh/g in high loading sulfur electrode (> 4 mg S/cm^2) at very low porosity (< 40%). (Q1, FY 2021; Completed)
2. Build an electrode model to understand the effects of electrode porosity and tortuosity on the electrolyte transport and sulfur reaction kinetics. (Q2, FY 2021; Completed)
3. Enable a quasi-SE network by introducing PEs and/or SEs into the low porosity electrodes, and realize cell operation at an extremely low E/S. (Q3, FY 2021; Completed)
4. Identify compatible binder and solvent combinations to enable the scale-up preparation of the quasi-SE. (Q4, FY 2021; Completed)

Progress Report

To realize large-scale preparation of sulfur electrodes with both high mass loading and low porosity, a lubricant-assisted rolling method was developed by using PTFE as binder. As illustrated in Figure 105a, a uniformly mixed paste of S/KB, Super-P conductive additive, and PTFE binder was prepared with the assistance of lubricant (IPA). The paste was rolled into electrode film of different thickness and vacuum dried into free-standing electrodes (Figure 105c, denoted as the G2 electrode). This modified rolling processing prevents electrode cracking and cohesive failure issues as observed in conventional thick sulfur electrodes processed by slurry coating of S/C materials and binders (G1). The electrodes fabricated through the lubricant-assisted rolling method have controllable sulfur loading and thickness to fit the need of different cell designs.

The SEM characterization indicates that the surface of the G2 electrode is flat, uniform, and vey compact (Figure 105d). Long and thin fibers are observed across the electrode uniformly and are ascribed to the deformed PTFE binder (Figure 105e). Cross-sectional observation via plasma focused ion beam (PFIB) – SEM reveals the G2 electrode has a hierarchical structure composed of long slits (length > 10 µm), medium pores (1-10 µm), and small pores (< 1 µm); see Figure 105f-g. This is because the IPA functions as a lubricant and liquid template for forming a hierarchically porous architecture.

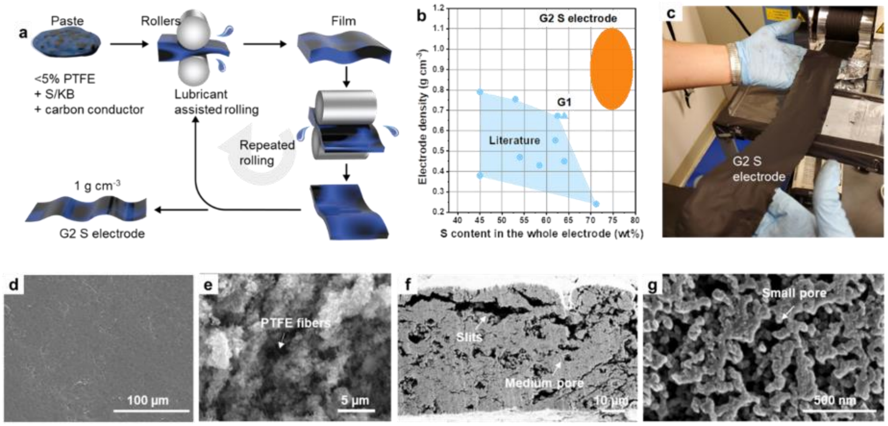

Figure 105. Preparation of the dense sulfur electrode. (a) Schematic illustration of the preparation process of the G2 electrode. (b) Comparison of electrode density and sulfur content in whole electrode between the G1, G2, and literature results. If electrode density was not directly reported, it was calculated by "S loading/(S content × electrode thickness)." (c) Photo of the free-standing G2 electrode. (d-g) Scanning electron microscope images of the G2 electrode: (d) surface, (e) cross- section (without milling), and (f-g) high-resolution images of the milled cross-section.

Compared to conventional slurry-casted electrodes (for example, G1), the G2 electrode has the significant advantage of high press density. For a pristine G2 with a sulfur loading of 4.3 mg cm^{-2}, the corresponding electrode thickness is only 55 µm, yielding a high electrode density of 1.1 g cm^{-3}. Compared with the reported literature results, a remarkable improvement in electrode density has been achieved by this process (Figure 105b). More importantly, with assistance of the IPA lubricant, the PTFE binder is deformed into long binder fibers and distributed evenly inside the electrode. Thus, the binder content in G2 can be reduced to an extremely low level of 1 wt% without sacrificing electrode quality, boosting sulfur content to > 80 wt% in the whole electrode. Using dense G2 electrodes with sulfur loadings > 7 mg cm^{-2}, high areal capacities of > 9 mAh cm^{-2} were achieved. This novel electrode processing method enables large-scale fabrication of dense, high-loading electrodes by using nanosized materials and a very lean amount of binder. Furthermore, additional polymer- or organic-based LICs can be uniformly integrated into the electrode architecture by using this method, improving sulfur utilization rate and reaction kinetics.

Patents/Publications/Presentations

The project has no patents, publications, or presentations to report this quarter.

Task 5.3 – Nanostructured Design of Sulfur Cathodes for High-Energy Lithium-Sulfur Batteries (Yi Cui, Stanford University)

Project Objective. The charge capacity limitations of conventional TM oxide cathodes are overcome by designing optimized nano-architectured sulfur cathodes. This study aims to enable sulfur cathodes with high capacity and long cycle life by developing sulfur cathodes from the perspective of nanostructured materials design, which will be used to combine with Li-metal anodes to generate high-energy Li-S batteries. Novel sulfur nanostructures as well as multi-functional coatings will be designed and fabricated to overcome issues related to volume expansion, polysulfide dissolution, and the insulating nature of sulfur.

Project Impact. The capacity and cycling stability of sulfur cathode will be dramatically increased. This project's success will make Li-S batteries to power EVs and decrease the high cost of batteries.

Approach. The approach involves three main efforts:

- Advanced nanostructured sulfur cathodes design and synthesis, including (1) engineer empty space into sulfur cathode to solve problem of electrode volume expansion, (2) develop novel sulfur nanostructures with multi-functional coatings for confinement of S/Li polysulfides to address issues of active materials loss and low conductivity, (3) develop/discover optimal nanostructured materials that can capture the polysulfide dissolved in the electrolyte, (4) develop space-efficiently-packed nanostructured sulfur cathode to increase volumetric energy density and rate capability, and (5) identify interaction mechanism between sulfur species and different types of oxides/sulfides, and find optimal material to improve capacity and cycling of sulfur cathode.
- Structure and property characterization, including *ex situ* SEM, XPS analysis, and *in operando* XRD and optical microscopy.
- Electrochemical testing including coin cells and pouch cells as well as a set of electrochemical techniques.

Out-Year Goals. The cycle life, capacity retention, and capacity loading of sulfur cathodes will be greatly improved (200 cycles with 80% capacity retention, > 0.3 mAh/cm^2 capacity loading) by optimizing material design, synthesis, and electrode assembly.

Collaborations. This project collaborates with the following: BMR PIs; SLAC: M. Toney *(in situ* X-ray); and Stanford: W. Nix (mechanics) and Z. Bao (materials).

Milestones

1. Understanding polysulfides dissolution behavior in polymer-based ASSLSBs. (Q1, FY 2021; Completed)
2. Demonstrating nanoscale encapsulation concept from liquid to ASSLSBs. (Q2, FY 2021; Completed)
3. Exploring mechanism of nanoscale encapsulation in improving ASSLSBs experimentally and theoretically. (Q3, FY 2021; Completed)
4. Enabling ASSLSBs with high energy density, long-term cycling stability, and high safety. (Q4, FY 2021; Completed)

Progress Report

Last quarter, the team studied the catalytic effect of TiS_2 coating in ASSLSBs. This quarter, the team further proved the catalytic efficacy and polysulfide capture of nanoscale encapsulation in ASSLSBs by testing the electrochemical performance of $Li_2S@TiS_2$ cathodes in SPE. As-assembled cells are constructed for galvanostatic cycling tests from 1.6 V to 2.8 V. A specific capacity as high as ~ 910 mAh g^{-1} Li_2S at 0.2 C is realized by $Li_2S@TiS_2$ cathodes, which is more than twice higher than that of the bare Li_2S one (~ 330 mAh g^{-1}) (Figure 106a). Additionally, the $Li_2S@TiS_2$ cathode with a high mass-loading of Li_2S is fabricated and tested in ASSLSBs, obtaining an areal capacity of 2.4 mAh cm^{-2} at 60°C (Figure 106b), which corresponds to a high cell-level energy density of 427 Wh kg^{-1}. The energy density is calculated from the average discharge voltage (2.1 V), cell capacity (2.4 mAh cm^{-2}), and total mass of the cathode (8.6 mg cm^{-2}, excluding current collector), the solid electrolyte (1.2 mg cm^{-2}), and the anode (2 mg cm^{-2}).

In addition, the rate performance of the as-prepared cathodes is investigated by cycling cells at different C-rates (Figure 106c). For the bare Li_2S cathode, significant capacity fading (from 330 mAh g^{-1} to 226 mAh g^{-1}) is observed during four cycles at 0.2 C, with the capacity severely decreasing to 38.5 mAh g^{-1} at a higher rate of 0.8 C. Comparatively, the $Li_2S@TiS_2$ cell, benefiting from the effective TiS_2 enhanced oxidation kinetics, shows a much better rate capability, achieving a discharge capacity of 660 mAh g^{-1}, 488 mAh g^{-1}, and 309 mAh g^{-1} based on Li_2S at 0.3 C, 0.4 C, and 0.8 C, respectively. Moreover, the $Li_2S@TiS_2$ cell exhibits stable cycling performance after charge/discharge cycling at 0.8 C at 80°C. After an initial discharge capacity of 490 mAh g^{-1} at 80°C, the $Li_2S@TiS_2$ cells retain 79%, 71%, and 68% of their initial capacity after 50, 100, and 150 cycles, respectively (Figure 106d). Average CE after 150 cycles is calculated to be 98.6%, which shows little shuttle effect owing to the efficient polysulfides trapping by TiS_2 encapsulation. These results show that TiS_2 encapsulation enables polysulfides entrapment and enhances the oxidation kinetics to achieve high performance in ASSLSBs.

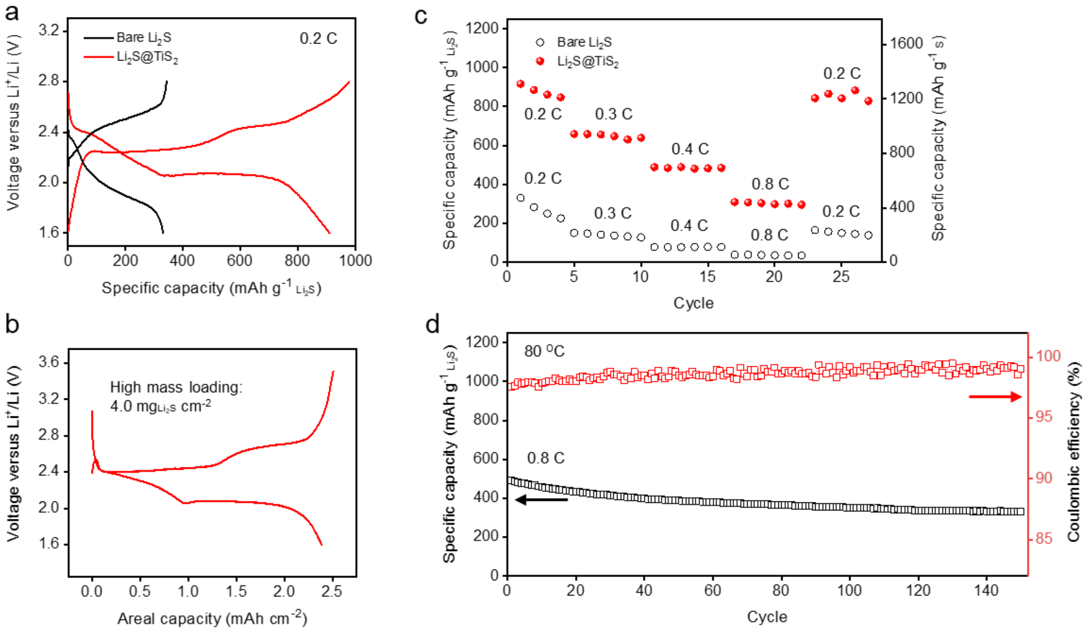

Figure 106. Electrochemical performance of $Li_2S@TiS_2$ cathodes and bare Li_2S cathodes in all-solid-state Li-S batteries. (a) Charge-discharge voltage profiles of $Li_2S@TiS_2$ and bare Li_2S cathodes at 0.2 C (1 C = 1,166mA g^{1} Li_2S) at 60°C. (b) Voltage profile and areal capacity of $Li_2S@TiS_2$ cathode with a high mass loading (4.0 mg cm^{-2}) at a current density of 0.04 mA cm^{-2} at 60°C. (c) Rate performance of $Li_2S@TiS_2$ and bare Li_2S cathodes at various charging rates, cycled at 60°C, within a potential window of 1.6-2.8 V versus Li^+/Li. (d) Cycling performance and Coulombic efficiency of $Li_2S@TiS_2$ cathode at 0.8 C for 150 cycles at 80°C.

Patents/Publications/Presentations

The project has no patents, publications, or presentations to report this quarter.

Task 5.4 –Investigation of Sulfur Reaction Mechanisms
(Enyuan Hu, Brookhaven National Laboratory; Deyang Qu, University of Wisconsin, Milwaukee)

Project Objective. The primary objectives are as follows:

- To continue conducting fundamental research on the mechanism of the sulfur redox reaction, especially those on the interplay of the dissolved polysulfides in electrolyte and those in the solid phase in cathode during charging.
- To continue developing the polymeric sulfur electrode, adequate anode, and corresponding electrolyte to achieve high-energy-density, long-cycle-life Li-S batteries. The team will focus on the overall dissolution of polysulfide in an electrolyte and the effectiveness of polymeric sulfur electrodes.
- To develop the alternative anode materials having low reactivity with dissolved polysulfide ions.
- To continue to develop and optimize creative electrode making processes to improve processability and aerial capacity (for example, dry process and thick electrodes).

Project Impact. Further understanding of the mechanisms of all reactions in a Li-S cell will lead to mitigation of the “shuttle effect.” The project results will thus guide development of sulfur cathode and Li-S designs with significant increase of energy density and of cycle life and with reduction of cost. This will greatly accelerate deployment of EVs and reduce carbon emission associated with fossil fuel consumption.

Approach. This collaborative project involves the following: (1) continue to synthesize cross-linked polymerized sulfur compounds, in which a sulfur is attached to the conductive backbone with covalent bonds; therefore, the polysulfides can be immobilized within the matrix, (2) investigate the sulfur redox reaction mechanism in the solid phase, (3) continue exploring the alternative anode materials that can cycle well and do not react with dissolved polysulfide and sulfur in the electrolyte to mitigate the “shuttle effect,” and (4) develop an engineering process for high sulfur loading electrodes.

One-Year Goals. In FY 2021, the interim goal is to develop a Li-S battery with sulfur-containing cathode of 600-800 mAh/g capacity with mitigation of the “shuttle effect.”

Collaborations. The PI works closely with beamline scientists at synchrotron facilities to develop novel Li-S characterization tools. The PI and co-PI collaborate closely with top scientists at ANL, LBNL, and PNNL, as well as U. S. industrial collaborators at GM, Duracell, Clarios, etc. The PI and co-PI also collaborate with scientists in China, Japan, and South Korea. These collaborations will be strengthened and expanded to give this project a vision on both today’s state-of-the-art technology and tomorrow’s technology in development, with feedback from the material designer and synthesizers upstream and from industrial end users downstream.

Milestones

1. Synthesize new polymeric sulfur compounds. Conduct preliminary electrochemical, optical, and synchrotron based testing of sulfur redox reaction in the solid phase (in cathode). (Q1, FY 2021; Completed)

2. Test alternative anode materials with both sulfur and polymeric sulfur electrodes and determine interaction with dissolved polysulfide ions and overall electrochemical performance. (Q2, FY 2021; Completed)

3. Investigate sulfur redox reaction in the solid phase in cathode. Test the newly synthesized polymeric sulfur materials. (Q3, FY 2021; Completed)

4. Test full cell in either coin-cell or pouch-cell format with polymeric sulfur cathode and alternative anode. (Q4, FY 2021; Completed)

5. Conduct preliminary investigations of sulfur redox reaction mechanism in the solid phase in cathode and the interplay between dissolved polysulfide ions in electrolyte and sulfide compounds in the solid. Complete and continue testing of polymeric sulfur cathode and alternative anode in full-cell format. (Annual Milestone; Completed)

Progress Report

In previous quarters, the sulfur organic polymers were thoroughly characterized, and their success, as well as complete inverse vulcanization, was validated. Although a small amount of elemental sulfur was remaining in the polymers, most of the sulfur was attached to the polymer backbones. The team concluded that a sulfur organic polymer cathode can cycle better if short-chain polysulfide ions are dominant in the electrolyte. This quarter, the team made sulfur in PAN coin cells to further verify their conclusions.

Figure 107 shows the initial 10 cycles of the S-polymers made with different S_8-to-PAN ratios. Two aspects can be observed in this study. First, the 1st discharge curves were always different to the subsequent cycles except in the case of the systems with very low sulfur content. It seems that electrochemical formation is necessary for the chemically synthesized compounds after high-temperature treatment. Second, up to 4:1 S_8:PAN ratio, there is little elemental sulfur in the synthesized compounds. Beyond the level of the saturation ratio, for example, 8:1 S_8:PAN ratio, a clear two-step discharge curve is evident in line with the existence of long-chain polysulfides or elemental sulfur.

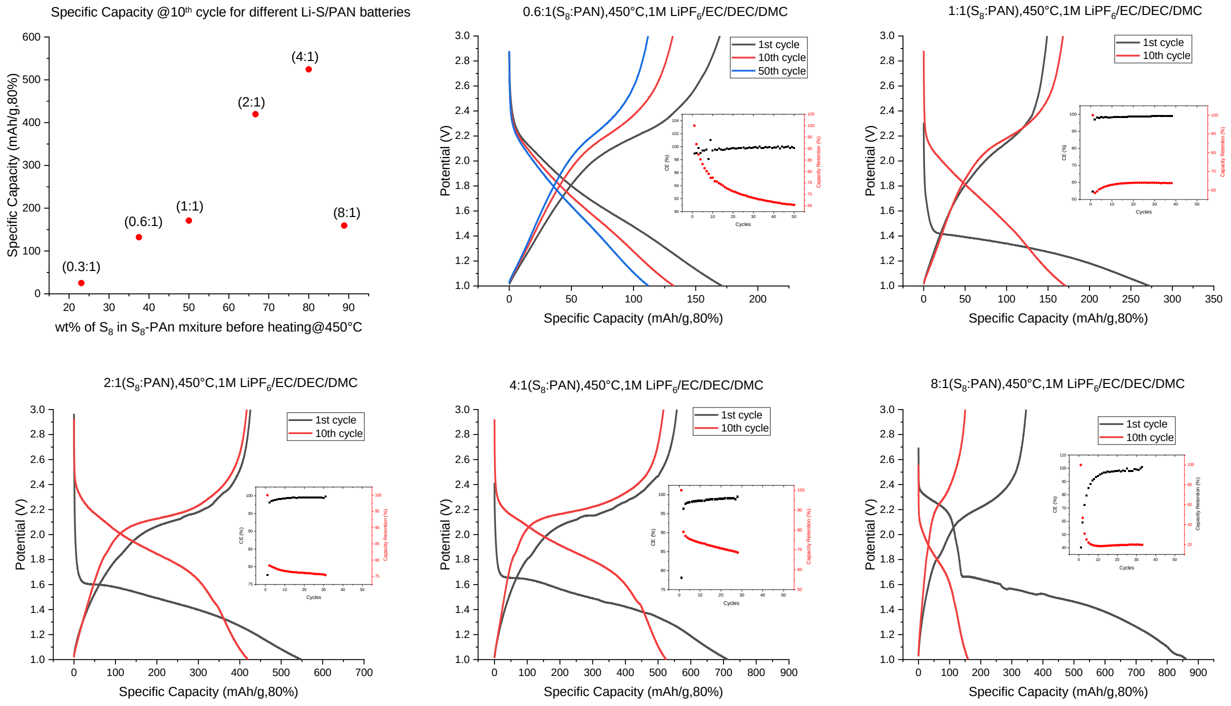

Figure 107. Comparison of multiple discharge and recharge curves of S-PAN cathode made with various sulfur-to-PAN ratios.

Figure 108 shows the impact of electrolyte on the cyclability of the S-polymer cathode. Interestingly, the S-polymer works in carbonate electrolyte, wherein the elemental sulfur cathode does not cycle. The team hypothesizes that sulfide free radicals can react with carbonate solvents. It appears sulfide free radicals may not be formed or become stabilized in the polymeric structure.

Figure 108 also shows that the sulfur PAN cathode does not cycle well in ether-based electrolyte, which is the traditional electrolyte system for elemental sulfur cathode. The evidence shows that after the 1st cycle, the high-voltage plateau starts to show up, which is the evidence for formation of soluble long-chain polysulfide ions.

The preliminary electrochemical evidence is consistent with what the team reported last quarter. The formation of long-chain polysulfide ions during the cycling is detrimental to the rechargeability of sulfur cathodes. They should be either restrained in the matrix of polymeric structure or completely avoided.

The team is investigating the mechanism of impact of solvents.

S-PAN @450°C, 1M $LiPF_6$/EC/DEC/DMC

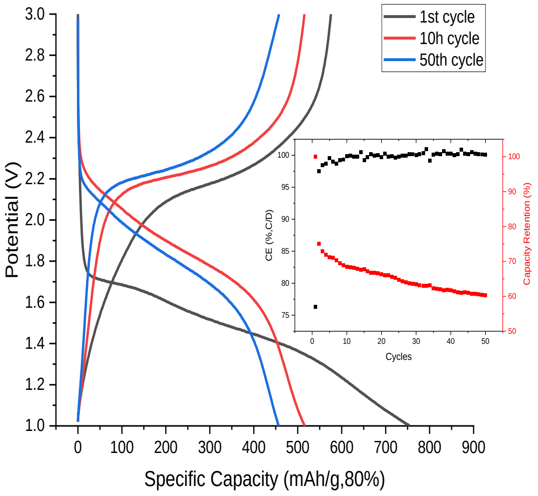

S-PAN @450°C, 1M LiTFSi/DME/DOL

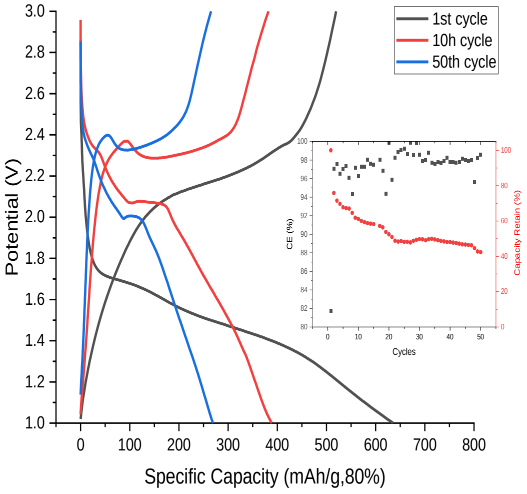

Figure 108. The comparison of S-PAN cathodes cycled in ether and carbonate-based electrolytes.

Patents/Publications/Presentations

The project has no patents, publications, or presentations to report this quarter.

Task 5.5 – New Electrolytes for Lithium-Sulfur Battery
(Gao Liu, Lawrence Berkeley National Laboratory)

Project Objective. The project objective is to develop new electrolytes, additives, and electrode compositions for Li-S battery with high ion-conductivity, stable toward polysulfide, and promoting the polysulfide affiliation with the electrode substrate to prevent polysulfide dissolution.

Project Impact. This work will address the high cost and low energy density of Li-ion rechargeable batteries. The emerging Li-S batteries could feature both high energy density and low cost. This project enables applications of the low-cost, abundant sulfur element as a major chemical component for electrical energy storage. This project will develop new approaches for electrolytes and electrode compositions of Li-S rechargeable batteries.

Approach. This project aims to develop new electrolytes and additives for Li-S battery. The properties of the ideal electrolyte for sulfur electrode would be high ion conductivity, stable toward polysulfide, and promoting the polysulfide affiliation with the electrode substrate to prevent polysulfide dissolution. The project is designed to first understand the electrode substrate interaction with the polysulfides in different electrolytes. This will lead to better understandings of the polysulfide nucleation and precipitation mechanisms in common electrolytes. The second stage of the project will focus on chemically modifying the structures of the solvent and salt electrolyte molecules to increase electrolyte stability and ionic conductivity, to prevent polysulfide dissolution, and to promote polysulfides precipitation.

Out-Year Goals. The team will also investigate the contribution of Li-metal electrodes to overall Li-S battery performance and will develop methods to stabilize Li-metal surface.

Collaborations. This project collaborates with J. Guo and W. Yang (ALS/LBNL), A. Minor (National Center for Electron Microscopy at LBNL/UCB), L-W. Wang (LBNL), and P. B. Balbuena, TAMU.

Milestones

1. Measure polysulfide dissolution in the new amphiphilic electrolytes. (Q1, FY 2021; Completed)
2. Map the Li-ion diffusion path in sulfur materials. (Q2, FY 2021; Completed)
3. Develop optimized sulfur electrodes according to the electrolyte properties and Li-ion transport in sulfur materials. (Q3, FY 2021; Completed)
4. Investigate the Li-metal electrode properties in the Li-S cell. (Q4, FY 2021; Completed)

Progress Report

A new approach is developed using the amphiphilic HFE electrolyte to further improve sulfur electrode cycling and to stabilize the lithium metal. Lithium anode corrosion and dendrite formation can be significantly reduced in the electrolyte with the presence of this fluoro-based amphiphilic electrolyte and with highly concentrated salt solution, leading to high CE. The team's HFE molecules are designed to have a bi-functional, amphiphilic structure consisting of a fluorocarbon moiety and an EO moiety on each end, respectively. The molecular structure in this study is 1,1,1,2,2,3,3,4,4-nonafluoro-6-(2-methoxyethoxy)hexane (F_4EO_2). The salt is 0.5 M LiTFSI. The base solvent is TTE, with F_4EO_2:TTE weight ratio of 1:5. The EO moiety is lithiophilic and incompatible with fluorinated solvents and thus is able to coordinate with Li^+. The fluorocarbon moiety is lithiophobic, but is also fluorophilic, which is associated with fluorinated TTE solvent. This structure feature results in the formation of micelle-like molecular complexes with lithium salts concentrated in the EO cores, which are dispersed by the TTE solvent. To improve the compatibility of the electrolyte with the sulfur electrode, a small amount of DOL is added to the micelle electrolytes. The DOL dissolves polysulfides, but at a controlled amount, the DOL acts to facilitate Li_2S_x formation to significantly improve the utilization of the sulfur materials. However, the polysulfides shuttle effect also increases with the addition of DOL. To curb the shuttle effect, additional LiTFSI is added to saturate the electrolyte to prevent the lithium polysulfides dissolution as well as to further stabilize the Li-metal electrode.

By balancing the DOL amount and LiTSFI salt concentration, a Li-S cell operated above 1200 mAh/g at over 99.5% CE is achieved.

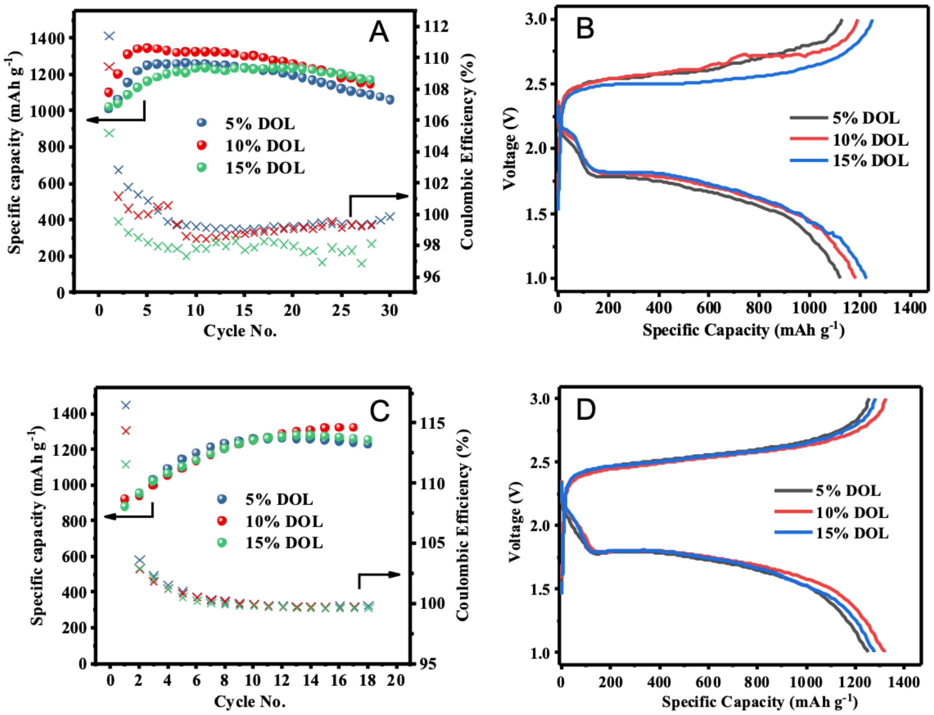

Figure 109. Li-S battery recycling with different amount of DOL added. (a) Capacity and Coulombic efficiency versus cycle numbers of the Li-S cell with the DOL additives at 5%, 10%, and 15% by weight. (b) Voltage and capacity profile of the Li-S cell at the 25th cycle [of panel (a)] with the DOL additive at 5%, 10%, and 15% by weight. (c) Capacity and Coulombic efficiency versus cycle numbers of the Li-S cell with the DOL additives at 5%, 10%, and 15% by weight, and saturated with LiTFSI salt. (d) Voltage and capacity profile of the Li-S cell at the 15th cycle [of panel (c)] with the DOL additive at 5%, 10%, and 15% by weight, and saturated with LiTFSI salt.

Patents/Publications/Presentations

Patent

- Novel Electrolyte Additives for Lithium-Sulfur Rechargeable Battery PCT patent filed by LBNL in November 2021.

TASK 6 – AIR ELECTRODES / ELECTROLYTES

Team Lead: Ji-Guang Zhang, Pacific Northwest National Laboratory

Summary and Highlights

The objective of this Task is to develop rechargeable Li-O_2 batteries with long-term cycling stability through in-depth research on more stable electrolytes and highly efficient catalysts for air electrodes, protection of Li-metal anodes, and deeper understanding on the oxygen reduction reaction (ORR) and oxygen evolution reaction (OER) mechanisms behind the electrochemical performance of Li-O_2 cells.

Highlights. The highlights for this quarter are as follows:

- The ANL team discovered a new metal-free catalytic platform of high efficacy for Li-O_2 cathodes. The charge potential can be consistently maintained below 3.50 V versus Li^+/Li, far outperforming systems that employ metal-based catalysts.
- The ANL / University of Illinois, Chicago (UIC) team developed a novel electrolyte for Li-O_2 batteries based on a $KMnO_4$ additive in dimethylsulfoxide (DMSO), which forms a protective coating on the lithium anode and enables long cycle life as well as high charge rates of Li-O_2 batteries. Computational studies help to explain how the additive contributes to improved performance.
- The PNNL team developed an air electrode with a 3D ordered macroporous structure that can effectively reduce the blocking of air electrode during cycling of lithium-oxygen batteries (LOBs). It also leads to uniform deposition/growth of discharge products during the discharging step, reducing the over voltage and cell impedance, therefore extending the cycle life of Li-O_2 batteries.

Task 6.1 – Rechargeable Lithium-Air Batteries
(Ji-Guang Zhang and Wu Xu, Pacific Northwest National Laboratory)

Project Objective. The objective of this project is to develop rechargeable Li-O_2 batteries with long-term cycling stability through in-depth research on more stable electrolytes and highly efficient catalysts for air electrodes, protection of Li-metal anodes, and deeper understanding on the ORR and OER mechanisms behind the electrochemical performance of Li-O_2 cells. In FY 2021, the team will further improve the cycle life and safety of Li-O_2 batteries using novel polymeric colloidal localized high concentration electrolytes (PC-LHCEs), binder-free catalysts with a robust artificial SEI layer, and synthesis of stable solvents. The fundamental mechanism behind the enhanced stability of Li-O_2 batteries using these new materials will also be investigated.

Project Impact. The project will develop rechargeable Li-O_2 batteries with long-term cycling stability through in-depth research on more stable electrolytes and highly efficient catalysts for air electrodes and protection of Li-metal anodes. This fiscal year, the team will further investigate stability of electrodes with different types of catalysts to keep the reversible reactions during the Li-O_2 battery operation and electrolytes to build more stable Li-O_2 batteries with long-term cycling capability.

Approach. Develop highly stable electrolytes, including novel PC-LHCEs with an optimization of Li-metal surface protection and effective catalysts to prevent the irreversible parasitic reactions at the electrodes (cathode and anode). The electrochemical test of Li||Li symmetric cell containing above stable electrolyte will be first measured comparatively with typical ether (TEGDME) based electrolytes to evaluate the stability of the electrolyte itself and the artificial SEI layer. Then, the stability of proposed electrolytes at the cathode side with reactive oxygen species during ORR/OER will be further characterized in the Li-O_2 cells. In addition, with new synthesis of solvents to stabilize the electrolyte system, the team will find the key parameters for suitable electrolyte in Li-O_2 batteries.

Out-Year-Goals. The long-term goal of the proposed work is to enable rechargeable Li-air batteries with a specific energy of 800 Wh/kg at cell level, 1000 deep-discharge cycles, improved abuse tolerance, and less than 20% capacity fade over a 10-year period to accelerate commercialization of long-range EVs.

Collaborations. This project collaborates with C. Wang of PNNL on characterization of cycled air electrodes by TEM/SEM, with P. Gao of PNNL on computational calculations and simulations, and with J. Read of ARL on oxygen solubility tests.

Milestones

1. Develop binder-free electrocatalysts on the surface of air electrode with polymer-supported SEI and redox mediators. (Q1, FY 2021; Completed)
2. Develop PC-LHCEs using osmosis effect. (Q2, FY 2021; Completed)
3. Understand the interphase properties of PC-LHCE/electrode. (Q3, FY 2021; Completed)
4. Develop new solvents that are stable against oxidation and singlet oxygen species for reversible Li-O_2 battery systems. (Q4, FY 2021; Completed)

Progress Report

This quarter, the team investigated the effect of 3-dimensionally ordered porous (3DOP) structure of air electrode with dual catalysis on the performance of LOBs. The interconnected 3DOP structure was successfully generated in single-walled carbon nanotubes (SWCNTs) based air electrodes by a template method and tested in LOBs. As a comparison, similar LOBs using the SWCNTs/carbon paper (SWCNTs/CP) as air electrode were also investigated. Figure 110 compares the SEM images of these two air electrodes. 3DOP air electrodes exhibit a clear open pore structure. In contrast, the SWCNTs/carbon air electrode has no macroporous structure (Figure 110a). Figure 110b shows that the LOB cell with a 3DOP air electrode has a smaller cell overpotential (1.018 V) as compared to the LOB cell with a SWCNTs/carbon air electrode (1.092 V). The LOB cell with the 3DOP air electrode also has much smaller charge transfer resistance after discharge, thus leading to better cycling stability (140 cycles) than the cell with a SWCNTs/CP air electrode (115 cycles) in the cut-off voltage range of 2.0 V to 4.5 V (Figure 110b). Dual catalysts (0.1 M 2,2,6,6-tetramethyl-1-piperidinyloxy, or TEMPO, added in electrolyte, and ruthenium added on the SWCNTs air electrode) were used in these batteries. The samples were cycled at a current density of 0.2 mA cm^{-2} under a capacity limited protocol of 1.0 mAh cm^{-2}.

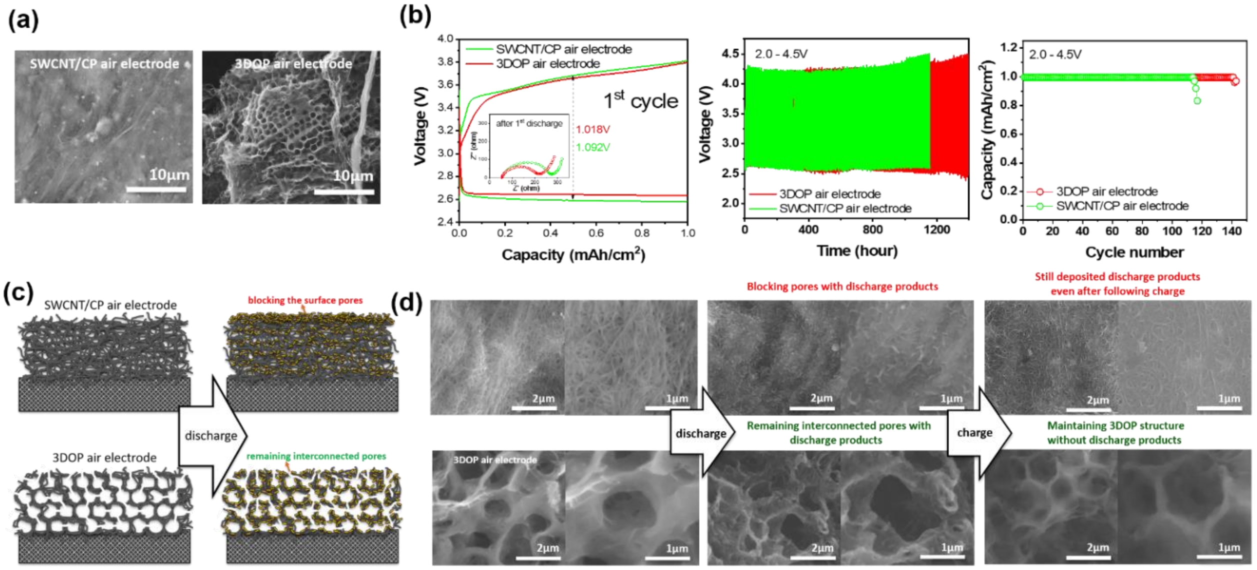

Figure 110. (a) Scanning electron microscopy (SEM) images of single-walled carbon nanotubes / carbon paper (SWCNTs/CP) [non-3DOP (left); 3DOP (right)] air electrodes. (b) 1st charge-discharge profiles of lithium-oxygen batteries (LOBs) with different air electrodes at a current density of 0.2 mA cm^{-2} under a capacity limited protocol of 1.0 mAh cm^{-2} (inset shows electrochemical impedance spectroscopy Nyquist plots of LOBs after 1st discharge to 2.0 V); charge-discharge profiles; and cycling stability of LOBs with different air electrodes. (c) Schematic illustration of effect of 3DOP structure on reversible formation and decomposition of discharge products. (d) SEM images of SWCNTs/CP and 3DOP air electrodes after 1st discharge and charge at a current density of 0.2 mA cm^{-2} under a capacity limited protocol of 1.0 mAh cm^{-2}. All samples were tested in the voltage range of 2.0-4.5 V at 25°C.

The schematic illustration in Figure 110c shows the structure of different air electrodes during the discharge process. The air electrode with 3DOP structure maintains the interconnected pore structure during cycling and facilitates electrolyte/O_2 transport in the air electrode, while the small pores of the non-3DOP electrode are quickly blocked by the discharge products during discharge. The electrode surfaces were examined by SEM after discharge and charge, as shown in Figure 110d. It is found that the air electrode with 3DOP structure can maintain its interconnected pores even after formation of discharge products, while the small pores in the non-3DOP air electrode were fully blocked with particles after discharge. After the subsequent charge process, the surface of 3DOP air electrode was almost fully recovered to its pristine state, while the non-3DOP air electrode still had a significant amount of discharge product (for example, Li_2CO_3) remaining. These results are consistent with the better cycling stability for LOB with 3DOP air electrode, as shown in Figure 110b. Therefore, maintaining appropriate pore structure of the air electrodes is critical for long-term cycling cyclability of LOBs.

Patents/Publications/Presentations

Publication

- Lim, H-S., W-J. Kwak, S. Chae, S. Wi, L. Li, J. Hu, J. Tao, C. Wang, W. Xu,* and J-G. Zhang.* "Stable Solid Electrolyte Interphase Layer Formed by Electrochemical Pretreatment of Gel Polymer Coating on Li Metal Anode for Lithium-Oxygen Batteries." *ACS Energy Letters* 6, No. 9 (2021): 3321–3331.

Task 6.2 – Lithium-Air Batteries
(Khalil Amine, Larry A. Curtiss, and Jun Lu; Argonne National Laboratory)

Project Objective. This project will develop new cathode materials and electrolytes for Li-air batteries for long cycle life, high capacity, and high efficiency. The goal is to obtain critical insight that will provide information on the charge and discharge processes in Li-air batteries to enable new advances to be made in their performance. This will be done using state-of-the-art characterization techniques combined with state-of-the-art computational methodologies to understand and design new materials and electrolytes for Li-air batteries.

Project Impact. The instability of current nonaqueous electrolytes and degradation of cathode materials limits performance of Li-air batteries. The project impact will be to develop new electrolytes and cathode materials that are stable and can increase energy density of electrical energy storage systems based on lithium.

Approach. The project is using a joint theoretical/experimental approach for design and discovery of new cathode and electrolyte materials that act synergistically to reduce charge overpotentials and increase cycle life. Synthesis methods, in combination with design principles developed from computations, are used to make new cathode architectures. Computational studies are used to help understand decomposition mechanisms of electrolytes and how to design electrolytes with improved stability. The new cathodes and electrolytes are tested in Li-O_2 cells. Characterization, along with theory, is used to understand the performance of materials used in the cell and to make improved materials.

Out-Year Goals. The out-year goals are to find catalysts that promote discharge product morphologies that reduce charge potentials and to find electrolytes for long cycle life through testing and design.

Collaborations. This project engages in collaboration with K. C. Lau (UC at Norridge), Y. Wu (OSU), D. Zhai (China), and R. Shahbazian-Yassar (UIC).

Milestones

1. Design functionalized cathodes to achieve high electrochemical performance of Li-O_2 batteries. (Q1, FY 2021; Completed)
2. Characterize cathode materials and investigate electrochemical behaviors. (Q2, FY 2021; Completed)
3. Understanding the processes of ORR and OER of these materials and reveal the possible parasitic reactions. (Q3, FY 2021)
4. By understanding the effects, engineer new catalysts with improved catalytic performance and suppressed side reactions. (Q4, FY 2021)

Progress Report

Lithium oxygen (Li-O_2) batteries have attracted extensive research interest due to their high energy density. Unfortunately, although the electrolyte stability and the nature of the deposited Li_2O_2, have been extensively studied, the large charge overpotential degrades the reaction kinetics with shortened cycle life. Metal-based catalysts have been explored extensively over the past year, but it is difficult to find success due to low efficacy and high degradation of electrolyte. Furthermore, the noble metals are typically the most effective, likely leading to future concerns in material cost.

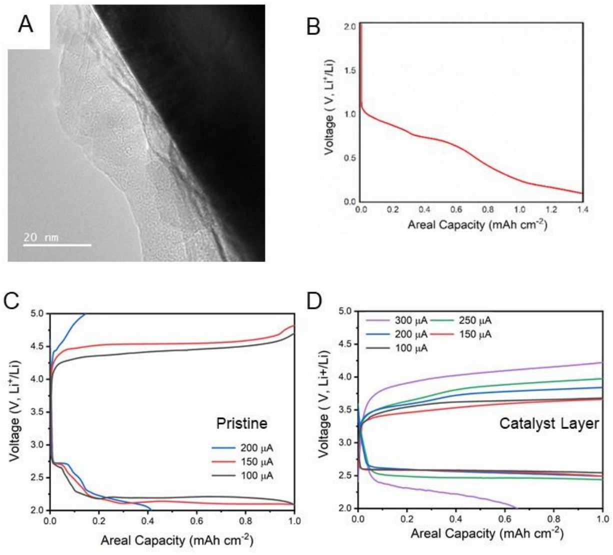

Figure 111. (a) Cryogenic transmission electron microscopy of catalytic layer formed in ether-based electrolyte over carbon nanotube. (b) Voltage profile of catalytic layer formation process. Rate performance of Li-O_2 assembled using (c) pristine carbon paper and (d) with catalytic layer formed over the carbon paper.

This quarter, the team successfully established a new metal-free catalyst platform for enabling low overpotential charge of Li-O_2 batteries. As seen in the cryogenic (cryo) – TEM results in Figure 111a, the catalytic layer can be found deposited neatly over the surface of carbon paper. This layer is derived from the lithiation of carbon paper in ether electrolyte (lithiation voltage profile shown in Figure 111b), akin to the SEI formation process. Directly applying the cathode with this catalytic layer yielded exceptionally low overpotential. Figure 111c-d compares the voltage profile at various cycles of cells using a pristine carbon paper with and without the catalytic layer, respectively. When the catalytic layer is present, the charge potential maintains well below 3.75 V versus Li^+/Li, while the pristine carbon paper experienced charge potentials well above 4.2 V versus Li^+/Li. Furthermore, the impact of the substrate selection was explored. Different types of carbon-based substrate (CNT, carbon black, graphite, and carbon paper) were used to form the catalytic layer, revealing varying degrees of impact on the final cell performance. The charge potential was observed to be the highest in the carbon paper system, followed by CNT, carbon black, and graphite. The team is studying the cause of this trend and the overall functioning mechanism offered by this novel metal-free catalytic layer.

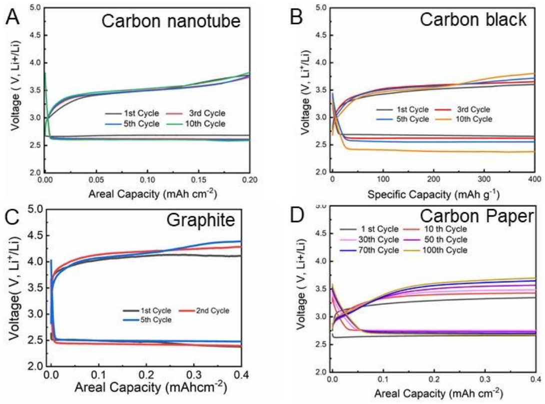

Figure 112. Voltage profile taken at various cycles of Li-O_2 using a catalytic layer formed over (a) carbon nanotube, (b) carbon black, (c) graphite, and (d) carbon paper. Tested at 50 μA cm^{-2}.

In conclusion, the team has discovered a new metal-free catalytic platform of high efficacy for Li-O_2 cathodes. The charge potential can be consistently maintained below 3.75 V versus Li^+/Li at 50 μA cm^{-2}, far outperforming systems that employ metal-based catalysts. Differences in the substrate of the catalytic layer were observed to affect performance of the cell, but it maintained a significant advantage over systems without any layer. Future efforts will include working to understand this trend and the underlying functioning mechanism of this catalytic layer.

Patents/Publications/Presentations

Patent

- Lu, J., K. Amine, Y. Guo, X. Zeng, and X. Bi. University of Chicago, Argonne, LLC (2021). "Cathode for Alkaline Earth Air Batteries." U. S. Patent Application 16/856,302.

Task 6.3 – Lithium Oxygen Battery Design and Predictions
(Larry A. Curtiss / Anh Ngo, Argonne National Laboratory; Amin Salehi-Khojin, University of Illinois, Chicago)

Project Objective. The objective of this work is to develop new materials for Li-O_2 batteries that give longer cycle life and improved efficiencies in an air environment. New electrolyte blends and additives will be investigated that can reduce clogging and at the same time promote the cathode functionality needed to reduce charge overpotentials. New cathode and anode materials will be investigated that can work in conjunction with the electrolytes to improve cycle life in the presence of air components.

Project Impact. Li-air batteries are considered as a potential alternative to Li-ion batteries for transportation applications due to their high theoretical specific energy. The major issues with the existing Li-O_2 systems include degradation of the anode electrode, reactions with air components, clogging of the cathode, and electrolyte instability. Thus, this project is using a comprehensive approach to improve cycle life and efficiency through developing new materials for electrodes, anodes, and electrolytes that work in synergy.

Approach. The experimental strategy is to use cathode materials based on 2D transition metal dichalcogenides (TMDs) that the team has found to be among the best ORR/OER catalysts. These cathode materials will be combined with new electrolyte blends and additives that work in synergy to reduce charge potentials and increase stability of the Li-air system. DFT and AIMD simulations are used to gain insight at the electronic structure level of theory of the electrolyte structure, and function both in bulk and at interfaces with the cathode, anode, and discharge product. CMD is used to obtain understanding at longer length and time scales of processes occurring in the electrolyte and growth mechanisms of discharge products. The team will also utilize a HT screening strategy based on experiment and theory to develop a large database of properties and outcomes of electrolyte combinations that can be analyzed using ML to predict electrolytes and additives with the best performance.

Out-Year Goals. The out-year goals are to find electrolytes that give high capacities and long cycle life in an air atmosphere using HT screening.

Collaborations. This project engages in collaboration with R. Assary, J. G. Wen, and S. Tepavcevic of ANL; B. Narayanan of University of Louisville; T. Li of Northern Illinois University; and F. Khalili-Araghi and R. Klie of UIC.

Milestones

1. Use a conductive metal-organic framework (MOF) for Li-O_2 battery to increase the number of active sites in cathode materials based on MOFs as well as localize them in pores. (Q1, FY 2021; Completed)
2. Utilize new TMD alloy catalyst for Li-O_2 batteries to increase charge/discharging rates. (Q2, FY 2021; Completed)
3. Investigate new concepts in electrolyte additives that work with the new TMD alloy catalyst to increase charge/discharge rates. (Q3, FY 2021; Completed)
4. Investigate new electrolyte additives that work with the TMD alloy catalyst to give anode protection. (Q4, FY 2021; Completed)

Progress Report

Li-O_2 batteries are considered as an advanced energy storage system that could provide a much higher specific energy than Li-ion batteries for electrical transportation. However, there are major issues with the existing Li-O_2 systems, including degradation of the anode electrode, poor volumetric energy density, poor charge/discharge rates, electrolyte instability, and high charge overpotential. This work is focused on finding a combination of electrolytes, additives, and cathode catalysts to enable a Li-O_2 battery that can operate in an air atmosphere with a low charge potential while maintaining a long cycle life. Previously, the team presented results for a new catalyst, a binary TMD alloy ($Nb_{0.5}Ta_{0.5}S_2$) that works in combination with a redox mediator resulting from a $KMnO_4$ additive to the electrolyte. This catalyst was found to facilitate both ORR and OER occurring during discharge and charge processes, respectively, while the redox mediator reduces the charge potential.

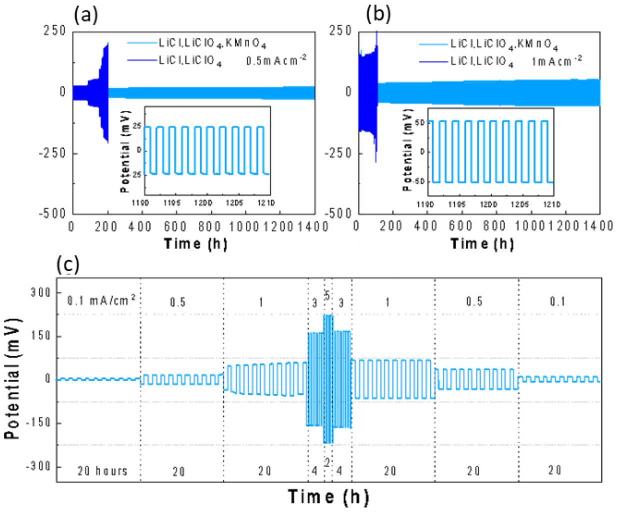

Figure 113. (a-b) Long-term cycling performance of symmetrical Li||Li cells with the $KMnO_4$ prepared electrolyte and the electrolyte prepared without $KmnO_4$ at 0.5 and 1 mA.cm^{-2} current densities, respectively. (c) Rate-capability of symmetrical Li||Li cell (with $KMnO_4$) at different current densities.

The chemical reaction of $KMnO_4$ with DMSO also results in a protective coating on the lithium anode that enables a long cycle life for the battery. This quarter, the team investigated properties of the $LiMnO_x$ coating formed on the lithium anode from the electrolyte. The long-term performance of the lithium anode was studied with a Li‖Li symmetrical cell using electrolytes with and without the colloidal MnO_2 electrolyte at two fixed capacities of 0.5 mAh cm^{-2} and 1 mAh cm^{-2} and current densities of 0.5 mA cm^{-2} and 1 mA cm^{-2}, respectively (Figure 113). Results indicate stable and long cycling performance (~ 1400 hours) with low overpotentials, 25 mV and 50 mV for 0.5 mA cm^{-2} and 1 mA cm^{-2}, respectively. The cells without the protective coating fail at a relatively early stage of < 200 hours with high overpotentials (150 mV and 200 mV) for 0.5 mA cm^{-2} and 1 mA.cm^{-2}, respectively. The conductivity of the SEI (accounting for two SEI layers in the symmetric Li|Li cells) was found to be $0.814 \pm 0.001 \times 10^{-3}$ S/cm, with activation energy of 0.65 ± 0.04 eV. The rate capability of symmetrical Li‖Li cells at different current densities of 0.1 mA cm^{-2} to 5 mA cm^{-2} was investigated. The overpotential for 3 mA cm^{-2} and 5 mA cm^{-2} is 161 mV and 220 mV, respectively.

The team also investigated the reaction of a lithium surface with MnO_2. To understand the chemistry and interactions between the MnO_2 and lithium, they have performed an AIMD simulation of an α-MnO_2/Li interface. This AIMD simulation reveals mixing between lithium and MnO_2, as shown in Figure 114. The RDF for the Li-Mn and Li-O bonds reveals formation of these bonds in the interface region. Similarly, the CNs of the lithium with respect to manganese and oxygen show about a factor of 2 between the number of Li-Mn and Li-O bonds near the interface (up to 3 Å of radius), suggesting that the composition of the interface is more likely to be composed of $LiMnO_2$ similar to experiment. Additionally, the number of atoms near the interface region (within 2 Å) gives a ~ 1:1:2 ratio for the Li:Mn:O. They have also studied the dynamics of this interface by calculating the MSD of each species as well as their corresponding

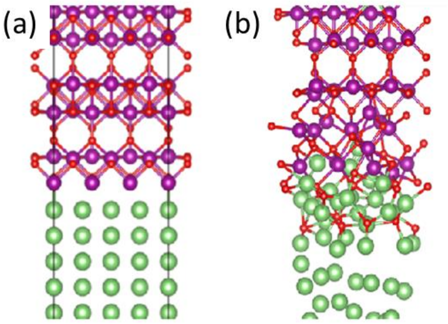

Figure 114. Density functional calculations of a lithium interface with MnO_2: (a) initial structure of α-MnO_2/Li interface, (b) final structure of the α-MnO_2/Li interface showing $LiMnO_x$ interlayer. The purple, red, and green spheres represent the manganese, oxygen, and lithium atoms, respectively.

diffusion coefficients (D). The simulation reveals that the D values of manganese and oxygen atoms are similar within this system, with values of 1.35×10^{-5} $cm^2\ s^{-1}$ and 1.27×10^{-5} $cm^2\ s^{-1}$, respectively, while lithium has a D value of 3.45×10^{-5} $cm^2\ s^{-1}$. This suggests that there will be favorable lithium transport within the MnO_2 layer consistent with the findings of the excellent rate-capability of the symmetrical Li‖Li cell.

Patents/Publications/Presentations

Publication

- Jaradat, A., C. Zhang, S. K. Singh, J. Ahmed, A. Ahmadiparidari, L. Majidi, S. Rastegar, Z. Hemmat, S. Wang, A. T. Ngo, L. A. Curtiss, M. Daly, A. Subramanian, and A. Salehi-Khojin. "High Performance Air Breathing Flexible Lithium–Air Battery." *Small* 17, No. 42 (2021): 2102072.

TASK 7 – SODIUM-ION BATTERIES

Team Lead: Xiao-Qing Yang, Brookhaven National Laboratory

Summary

The Na-ion battery will require investigations to identify optimal electrode materials, electrolytes, separators, and binders to reach full potential. The BMR program will therefore have a limited effort directed toward identifying Na-ion battery materials that have potential value for vehicle applications. Progress on these projects this quarter is described in this report.

Highlights. The highlights for this quarter are as follows:

- The ANL team (C. Johnson and K. Amine groups) working on iron content-variable layered sodium oxide cathodes reveal the electrochemical instability associated with higher levels of iron presence or higher charge cutoff voltages. High leakage current measurements on an O3 Ni-Mn-Co layered oxide cathode composition also demonstrate that surface instability exists above 4 V. Surface protection will be necessary for employing TM layered oxide cathodes for Na-ion batteries.
- The BNL team has applied advanced diagnostic techniques to the investigation and improvement of the new high-capacity and high-C rate multi-component sodium cathode materials P2-$Na_xMg_{0.2}[Fe_{0.2}Mn_{0.6}\square_{0.2}]O_2$ (MFM-2). The K-edge XANES of manganese and iron at various charge/discharge states suggests that the valence of manganese changes from the initial $Mn^{+3.8}$ to Mn^{+4}, while iron is oxidized from Fe^{+3} to $Fe^{+3.5}$ during charge.
- At LBNL, full cells containing lepidocrocite-structured sodium titanate (NTO) as the anode and $Na_3V_2(PO_4)_3$ (NVP) as the cathode were assembled. Good cycling results were obtained when the NTO electrode was pre-cycled in a half-cell configuration, to remove effects from SEI formation. Nearly the full theoretical capacity of the cathode was obtained reversibly during cycling in cells with N/P ratios of 1.0-1.04.
- The PNNL team developed a non-flammable, highly stable electrolyte that also exhibits excellent wettability with the PE or polypropylene (PP) separators commonly used in batteries, solving the problem of non-wettability of current Na-ion battery electrolytes. The HC||NaNMC cells with sodium bis(fluorosulfonyl)imide (NaFSI) / DMC:TFP electrolyte have demonstrated a high-capacity retention of 92.4% after 200 cycles with an excellent cycling CE of > 99.9.

Task 7.1 – Exploratory Studies of Novel Sodium-Ion Battery Systems
(Xiao-Qing Yang and Zulipiya Shadike, Brookhaven National Laboratory)

Project Objective. To meet the challenges of powering PHEVs and BEVs, new rechargeable battery systems with high energy and power density, low cost, good abuse tolerance, and long calendar and cycle life need to be developed. The primary objective of this project is to develop new advanced synchrotron-based material characterization techniques and apply these techniques to study the new rechargeable battery systems beyond the Li-ion batteries, namely the Na-ion battery systems for EVs.

Project Impact. The results of this project will be used for developing technologies that will significantly increase the energy density and cycle life and reduce the cost of beyond Li-ion battery systems. This will greatly accelerate deployment of EVs and reduce carbon emission associated with fossil fuel consumption and will help in the direction of building U. S.-based energy storage manufacture chains.

Approach. This project will use the synchrotron-based *in situ* X-ray diagnostic such as *in situ* XRD and *in situ* XAS tools, combined with TEM, STEM, and TXM imaging techniques developed at BNL to evaluate the new materials and redox couples to obtain in-depth understanding of the reaction mechanisms of these materials, aiming to improve existing materials and to provide guidance for new materials and new technology development for Na-ion battery systems.

Out-Year Goals. The out-year goal is to complete the synchrotron-based XRD, XAS, and XANES mapping studies of new cathode materials P2-$Na_{0.66}[Mn_{0.61}Ni_{0.28}Sb_{0.11}]O_2$ and P2-$Na_{0.7}Mg_{0.2}[Mn_{0.6}Fe_{0.2}\square_{0.2}]O_2$ (□ here representing TM vacancy) and a high-capacity, high-C rate, multi-component cathode material.

Collaborations. The BNL team has been closely working with top scientists on new material synthesis at ANL, LBNL, and PNNL, with U. S. industrial collaborators at GM and Johnson Controls, and with international collaborators.

Milestones

1. Complete XAS, including XANES and extended x-ray absorption fine structure (EXAFS) as well as 2D XANES mapping of the pristine P2-$Na_{0.66}[Mn_{0.61}Ni_{0.28}Sb_{0.11}]O_2$ cathode material at nickel and manganese K-edge. (Q1, FY 2021; Completed)
2. Complete nickel and manganese K-edge XAS (including XANES and EXAFS) of P2-$Na_{0.66}[Mn_{0.61}Ni_{0.28}Sb_{0.11}]O_2$ cathode material at different SOCs. (Q2, FY 2021; Completed)
3. Complete *ex situ* TEM, XRD study, and 2D XANES mapping of high-capacity high-C rate multi-component sodium cathode material with P2 type at different SOCs. (Q3, FY 2021; In progress)
4. Complete iron and manganese K-edge XAS of P2-$Na_{0.7}Mg_{0.2}[Mn_{0.6}Fe_{0.2}\square_{0.2}]O_2$ cathode material at different SOCs. (Q4, FY 2021; Completed)

Progress Report

This quarter, the fourth milestone was completed.

Development of New Diagnostic Techniques to Study and Improve Performance of High-Energy-Density Na-Ion Batteries. Na-ion batteries with gravimetric energy density potentially comparable to some Li-ion batteries and the raw materials are widely available. They have been pursued persistently for grid energy storage and low speed vehicles. Advanced diagnostic techniques developed by BNL have been successfully applied to investigation and improvement of new high-capacity, high-C rate multi-component sodium cathode materials P2-$Na_xMg_{0.2}[Fe_{0.2}Mn_{0.6}\square_{0.2}]O_2$ (MFM-2). Figure 115 shows the K-edge XANES of manganese (panels a-c) and iron (panels d-f) for MFM-2 at various charge/discharge states during the 1st cycle and 2nd charging. During the 1st charge process, manganese K-edge continuously shifts to higher energy range toward MnO_2 reference, suggesting that the valence of manganese changes from the initial +3.8 to +4. Meanwhile, iron K-edge also moves from the initial position to higher energy during the entire procedure, indicating iron is oxidized from +3 to +3.5. Based on the valence change of manganese and iron on charging, the specific capacity contributed by the oxidation of manganese and iron can be estimated to be 33.1 mAh g^{-1} ($Mn^{3.8+/4+}$) and 27.6 mAh g^{-1} ($Fe^{3+/3.5+}$), respectively. However, the total specific capacity in the initial charge up to 4.5 V is 124.1 mAh g^{-1}, which is much higher than the total contribution from $Mn^{3.8+/4+}$ and $Fe^{3+/3.5+}$. Previous studies have revealed that oxygen could contribute to the charge compensation in Mn-based layered cathode materials, where oxygen ions were partially oxidized during charge in the high voltage region. Therefore, it is very possible that the extra capacity for MFM-2 cathode during charge comes from oxygen redox.

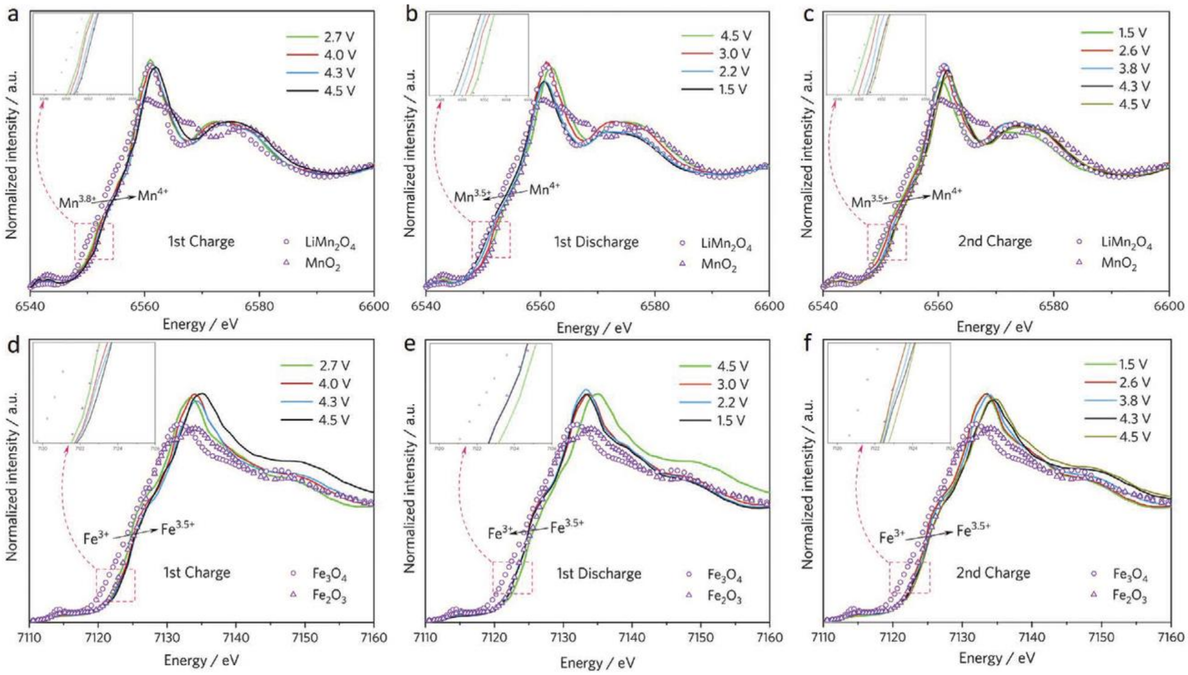

Figure 115. K-edge X-ray absorption near-edge spectrum of manganese (a-c) and iron (d-f) for P2-$Na_xMg_{0.2}[Fe_{0.2}Mn_{0.6}\square_{0.2}]O_2$ (MFM-2) at various charge/discharge states during the 1st cycle and 2nd charging.

Patents/Publications/Presentations

Publication

- Li, X-L., J. Bao, Z. Shadike, Q-C. Wang, X-Q. Yang, Y-N. Zhou,* D. Sun,* and F. Fang.* "Stabilizing Transition Metal Vacancy Induced Oxygen Redox by Co^{2+}/Co^{3+} Redox and Sodium-Site Doping for Layered Cathode Materials." *Angewandte Chemie International Edition* 60 (2021): 22026–22034. doi: 10.1002/anie.202108933.

Task 7.2 – Development of a High-Energy Sodium-Ion Battery with Long Life
(Chris Johnson and Khalil Amine, Argonne National Laboratory)

Project Objective. The project objective is to develop a high-energy Na-ion battery with long life. Moreover, the battery chemistry should utilize low-cost materials. The energy density target is 200 Wh/kg and/or 500 Wh/L, wherein the anode and cathode capacity targets are 600 mAhg^{-1} and 200 mAhg^{-1}, respectively.

Project Impact. A Na-ion battery on par with the energy density of a Li-ion battery can have a high impact in the transportation sector with the assumption that the cost is significantly below $85/kWh and that the battery pack provides a 300-mile range. The consumer is not concerned about the battery chemistry employed if these metrics can be met. Development of these battery chemistries will situate the United States in a strong position as relates to new low-cost energy storage systems beyond lithium ion.

Approach. In a team approach, the Na-ion battery group will create a versatile Na-ion battery chemistry with beneficial advantages such as low cost, safety, recycling, and sustainability of materials used. The team will work synergistically so that the final design is the culmination of advances in phosphorus carbon composites mated with optimized lead or other highly dense metalloids, such as tin and/or antimony and derivatives thereof, for the recyclable anode. Synthesis and optimization of such blended composite anodes will be conducted in parallel to diagnostic characterization of structures, phase formation, and cycling stability. Cathode work will begin at the end of the first year and will involve gradient cathodes consisting of Fe-Mn compositions, as well as intergrowths of layer stacking sequenced oxides. If resources allow, the team also will attempt to stabilize cathode surfaces using ALD methods, particularly for the benefit of staving off dissolution of manganese and iron / electrolyte reactivity. Electrolytes will be partly procured from H. Li at PNNL.

Out-Year Goals. The state-of-the-art Na-ion battery in the literature has now been surpassed by this team, but performance is still too low for commercialization. Thus, the goal is to move forward and continually invent the most superior Na-ion battery chemistry that can compete worldwide through work output from this project.

Collaborations. Researchers from PNNL who are developing electrolytes for Na-ion batteries will provide this project with formulations to test with the various electrode combinations investigated at ANL.

Milestones

1. Doped red phosphorus (RP) anode with high specific capacity and stable cycle life. (Q1, FY 2021; Completed)
2. *In situ* characterization of layered cathodes during synthesis; synthesize Ni-based, Fe-based, and Mn-based sodium layered cathodes. (Q2, FY 2021; Completed)
3. Advanced characterization on developed cathodes and anodes during charge/discharge. (Q3, FY 2021; Completed)
4. Performance optimization of synthesized layered cathodes and demonstration of full-cell development using optimal phosphorus anode and developed/commercial cathodes. (Q4, FY 2021; Completed)

Progress Report

Since the first report on reversible sodium cycling of $NaFe_{1/3}Mn_{1/3}Ni_{1/3}O_2$ in 2012,[1] the O3-type layered $Na(Fe,Mn,Ni)O_2$ cathodes have been of great interest because of their high theoretical capacity, decent cycle stability, and utilization of abundant, low-cost raw materials. Although the following comparative studies of the $NaFe_x(Mn_{0.5}Ni_{0.5})_{1-x}O_2$ system have suggested different optimum compositions depending on the research groups, there is a consensus that the iron content should not be higher than 50% for good cycle performance.[2-4] Building on these results, Z-F. Ma et al. have demonstrated prototype Na-ion battery full cells comprising the $NaFe_{1/3}Mn_{1/3}Ni_{1/3}O_2$ cathode and hard carbon anode couple and continuous effort to commercialize Na-ion batteries based on the $Na(Fe,Mn,Ni)O_2$ cathode.[5] Nevertheless, the developments of $Na(Fe,Mn,Ni)O_2$ cathodes have focused on optimizing performance within a moderate desodiation range, for example, below 4.0 V versus sodium. In such a moderate voltage range, decent cycle stability can be easily achieved, but with limited specific capacity, as $Fe^{3+/4+}$ redox is barely active. The cycle performance of the $NaFe_x(Mn_{0.5}Ni_{0.5})_{1-x}O_2$ cathodes rapidly deteriorates when the material is charged above 4.0 V versus sodium, and thus it has been presumed that the poor high-voltage performance is associated with the deteriorating effect of the active $Fe^{3+/4+}$ redox center. To better understand the mechanism by which the $Fe^{3+/4+}$ redox center affects the stability of the $Na(Fe,Mn,Ni)O_2$ cathode, the team has synthesized the morphology controlled $NaFe_x(Mn_{0.5}Ni_{0.5})_{1-x}O_2$ particles.

The $NaFe_x(Mn_{0.5}Ni_{0.5})_{1-x}O_2$ powder samples with various iron content (x = 0, 1/3, 1/2, 2/3, and 0.8) were synthesized by solid-state reaction of Na_2CO_3, Fe_3O_4, and $(Mn_{0.5}Ni_{0.5})(OH)_2$ precursors at 850°C in air. The $(Mn_{0.5}Ni_{0.5})(OH)_2$ was prepared by co-precipitation method using a continuous-stir-tank-reactor. The synthesized oxide particles have secondary particle morphology (average particle size ~ 10 µm) of spherically aggregated primary particle granules (Figure 116a). In Figure 116b, the XRD data show highly crystalline single-phase materials with the α-$NaFeO_2$ layered structure. The a- and c-axis lattice parameters of $NaMn_{0.5}Ni_{0.5}O_2$ are 2.965 Å and 15.90 Å, respectively. The lattice parameter linearly increases as the iron content increases in $NaFe_x(Mn_{0.5}Ni_{0.5})_{1-x}O_2$ and $NaFe_{0.8}Mn_{0.1}Ni_{0.1}O_2$ has a = 3.015 Å and c = 16.07 Å, respectively (Figure 116c). The larger lattice volume of the Fe-containing compounds is due to the larger ionic radius of high spin Fe^{3+} (64.5 pm) than the average ionic radius of $Ni^{2+}Mn^{4+}$ (61 pm). The linear relationship between the TM composition and lattice parameter is indicative of the solid-solution of TM cations.

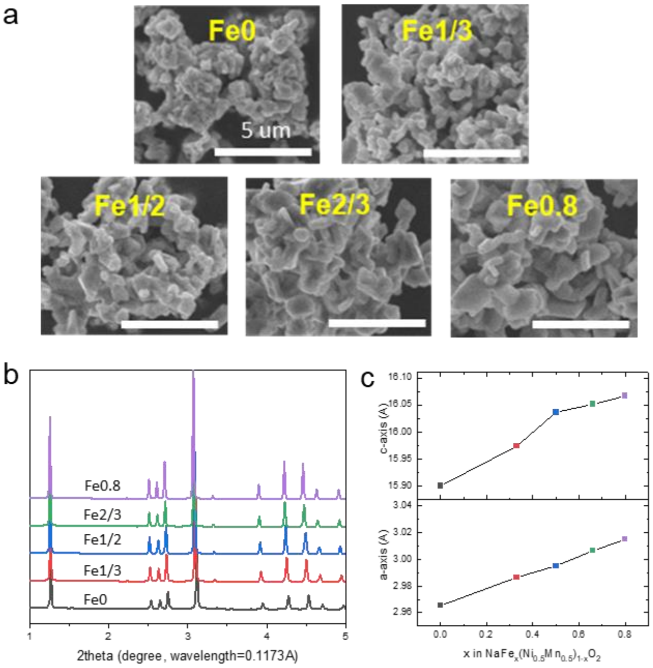

Figure 116. (a) Scanning electron microscopy particle morphology. (b) X-ray diffraction patterns. (c) Lattice parameters of the $NaFe_x(Ni_{1/2}Mn_{1/2})_{1-x}O_2$ (x = 0, 1/3, 1/2, 2/3, and 0.8) materials.

Figure 117a-e shows the initial charge and discharge profiles of the $NaFe_x(Mn_{0.5}Ni_{0.5})_{1-x}O_2$ cathodes. $NaMn_{0.5}Ni_{0.5}O_2$ (that is, Fe_0) exhibits several voltage steps corresponding to the phase transitions and Na-vacancy orderings. Iron substitution removes the voltage steps, making the voltage profile smoother indicating a solid-solution type voltage response. It is presumed that the substituted iron perturbs the charge ordering in the TM layers, suppressing coordinated layer gliding and Na-vacancy ordering during the electrochemical (de)sodiation process. Iron substitution also increases the initial polarization and average operation voltage. The electrochemical property of the high Fe-content samples, such as $Fe_{2/3}$ and $Fe_{0.8}$, resembles that of pure $NaFeO_2$. In Figure 117f, the $Fe_{1/2}$ sample shows good capacity retention when cycled between 3.8 V and 2.0 V versus sodium. The high-voltage charging of the cathode (that is, 4.3 V cut-off) significantly degrades cycle performance, as expected. However, after the rapid capacity drop during the first ~ 10 cycles, the cycle performance gradually improves, and the $Fe_{1/2}$ cathode exhibits better capacity retention than the Fe_0 electrode. It is not yet clear, though, whether the comparable (or even better) high-voltage cycle performance of the morphology-controlled $Fe_{1/2}$ cathode is simply due to the lower chemical stress (that is, lower specific capacity) or the optimized physicochemical properties of the project's sample. Overall, the preliminary structure and electrochemistry data collected on the morphology-controlled $NaFe_x(Mn_{0.5}Ni_{0.5})_{1-x}O_2$ materials corroborate the general performance trends that have been reported in the literature. In addition, the relatively decent cycle performance of the $Fe_{1/2}$ electrode requires revisiting the $NaFe_x(Mn_{0.5}Ni_{0.5})_{1-x}O_2$ cathode system. Studies are under way to elucidate the structural and electrochemical mechanisms behind the effect of iron substitution in the layered cathodes.

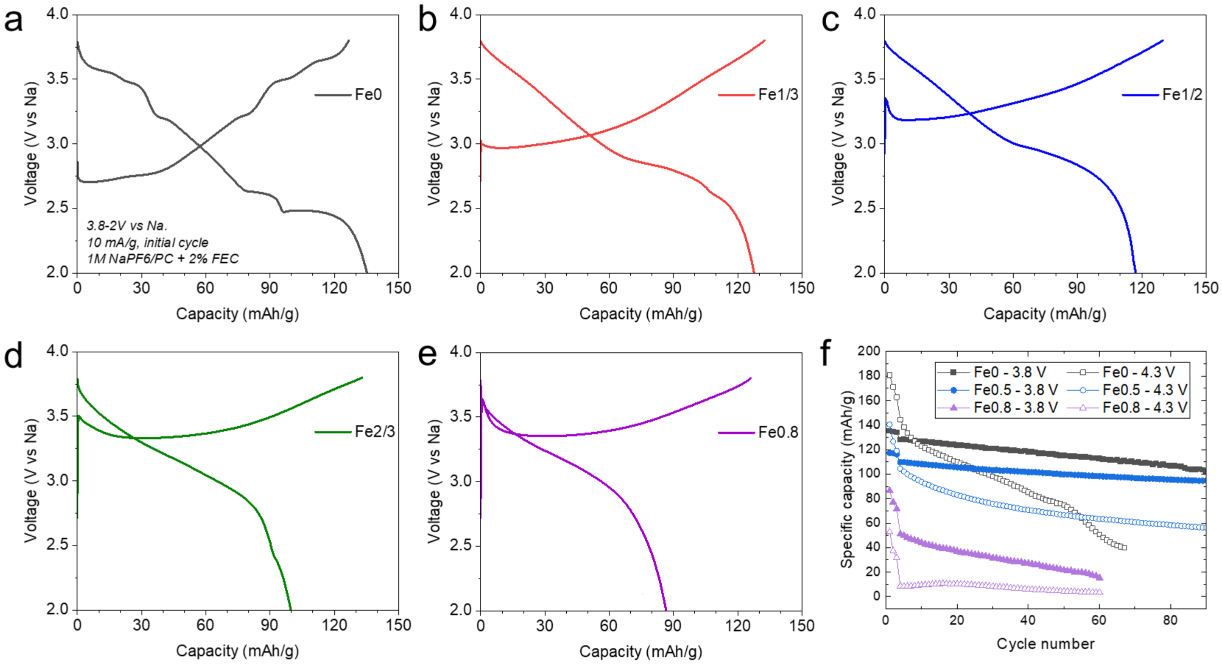

Figure 117. (a-e) Initial voltage profiles and (f) cycle performance of the $NaFe_x(Ni_{1/2}Mn_{1/2})_{1-x}O_2$ cathodes (x = 0, 1/3, 1/2, 2/3, and 0.8). Three formation cycles with 10 mA/g current density were followed by regular cycles with 30 mA/g.

To reveal the underlying degradation mechanism of sodium layered oxide cathode at high-voltage, the team has conducted *in situ* DEMS on their recently developed strained O3 $NaNi_{0.4}Mn_{0.4}Co_{0.2}O_2$ cathode. Figure 118a displays the *in situ* DEMS result during charge/discharge within 2.0-4.4 V. On charging beyond 3.8 V, a significant release of CO_2 can be clearly observed, although there is no evident oxygen outgassing. This might come from either decomposition of electrolytes or side reactions between oxygen radicals and electrolytes. Consistent with this observation, the high-precision leakage current measurement results (Figure 118b) showed that the parasitic current increased dramatically when the cut-off voltage was increased to over 4.0 V. These results confirmed that the side reactions between charged cathode and electrolytes during high-voltage charge might be the reason for the rapid capacity degradation of layered oxide cathodes. A rational control on the surface of layered oxide cathodes or electrolytes development is required.

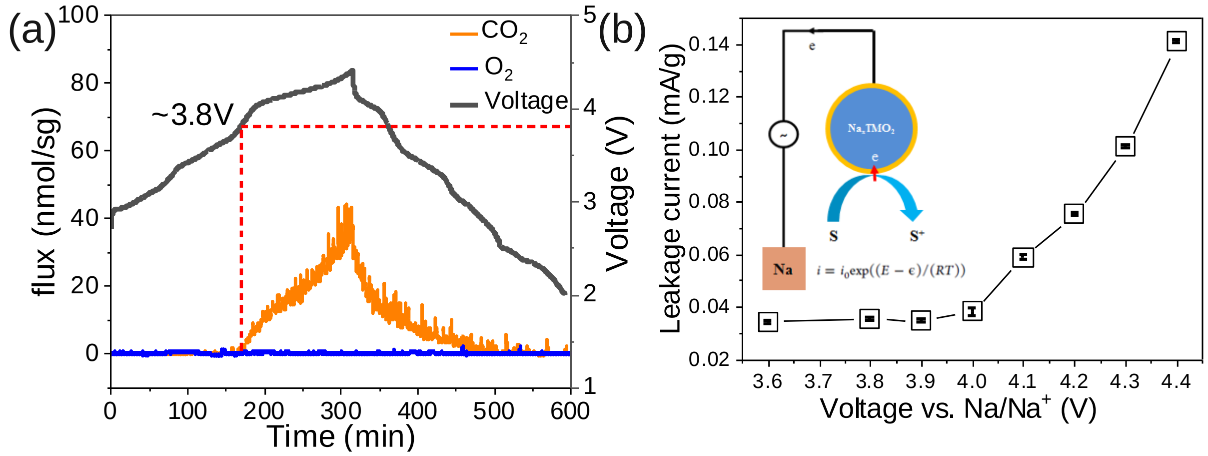

Figure 118. (a) *In situ* differential electrochemical mass spectrometry and (b) parasitic reaction study of O3 NaNi$_{0.4}$Mn$_{0.4}$Co$_{0.2}$O$_2$ cathode.

References

[1] Kim, D., E. Lee, C. Johnson, et al. *Electrochemistry Communications* 18 (2012): 66–69.

[2] Yabuuchi, N., M. Yano, H. Yoshida, S. Kuze, and S. Komaba, et al. *Journal of the Electrochemical Society* 160 (2013): A3131–A3137.

[3] Yuan, D., Y. X. Wang, H. X. Yang, et al. *ACS Applied Materials & Interfaces* 7 (2015): 8585–8591.

[4] Hwang, J-Y., S-T. Myung, Y-K. Sun, et al. *Journal of Power Sources* 324 (2016): 106–112.

[5] Wang, H., X-Z. Liao, Z-F. Ma, et al. *Journal of Alloys and Compounds* 724 (2017): 465–473.

Patents/Publications/Presentations

Publications

- Xiao, B., X. Liu, X. Chen, G. H. Lee, M. Song, X. Yang, F. Omenya, D. Reed, V. Sprenkle, Y. Ren, C. J. Sun, W. Yang, K. Amine, X. Li, G. L. Xu, and X. Li. "Uncommon Behavior of Li Doping Suppresses Oxygen Redox in P2-Type Manganese-Rich Sodium Cathodes." *Advanced Materials* (2021): 2107141.
- Xiao, B., X. Liu, M. Song, X. Yang, F. Omenya, S. Feng, V. Sprenkle, K. Amine, G-L. Xu, X. Li, and D. Reed. "A General Strategy for Batch Development of High-Performance and Cost-Effective Sodium Layered Cathodes." *Nano Energy* 89 (2021): 106371.

Presentation

- ECS Meeting, Virtual (October 10–14, 2021): "Electrolyte Engineering to Improve Cathode-Electrolyte Interface of Na$_{1-x}$FeO$_2$ Cathode for Sodium Ion Batteries"; J. Park.

Task 7.3 – High-Capacity, Low-Voltage Titanate Anodes for Sodium-Ion Batteries (Marca Doeff, Lawrence Berkeley National Laboratory)

Project Objective. The objectives are to understand differences in the sodium intercalation mechanism of various sodium titanate anodes through an array of synthetic, electrochemical, and structural characterization techniques, and to overcome practical impediments to their use, such as the high 1st-cycle Coulombic inefficiencies that are currently observed. The ultimate goal is to produce a 200-250 mAh/g anode that cycles reversibly.

Project Impact. Although several suitable cathode materials for Na-ion batteries exist, there are few suitable anode materials due to low potential instabilities. Therefore, sodium titanate variations will be synthesized through different routes to develop materials with various morphologies and dopants. Decreasing the 1st cycle inefficiencies and improving cycling performance will allow enabling technology for a practical high-energy Na-ion battery.

Approach. Candidate stepped layered titanates will be synthesized by appropriate routes (hydrothermal, solid-state, etc.). Materials will then be characterized electrochemically and physically. Structure-function relationships will be built to correlate the effect of changing structure (for example, step size) on electrochemical properties.

Out-Year Goals. A series of synchrotron characterization techniques will be used to further develop sodium titanate anode materials with stable cycling while delivering high capacities.

Collaborations. TXM is done in collaboration with Y. Liu (SSRL). Synchrotron hard, soft XAS, and X-ray Raman efforts are in collaboration with D. Nordlund and D. Sokaras (SSRL). Electrolyte design is done in collaboration with K. Xu (ARL).

Milestones

1. Characterize lepidocrocite titanates. (Q1, FY 2021; Completed)
2. Optimize electrode. (Q2, FY 2021; Completed)
3. Assemble, test, and study full cells. (Q3, FY 2021; Completed)
4. *Go/No-Go Decision*: On lepidocrocite titanate, stop if problems are not solved. (Q4, FY 2021; *Go Decision* since capacities are high)

Progress Report

This quarter, Na-ion full cells using the largest-capacity sodium titanate as anode [60°C – annealed $Na_{0.74}Ti_{1.815}O_4$ (NTO)] were assembled with $Na_3V_2(PO_4)_3$ (NVP) cathode and 1 M sodium hexafluorophosphate ($NaPF_6$) in EC:DEC ($v/v = 1/1$) electrolyte (Figure 119b). When cycled in a voltage window of 3.7 V ~ 0.8 V versus Na^+/Na at a current rate of C/10 (calculated based on NVP), the cell delivers an initial charge capacity of 125 mAh g^{-1} and a discharge capacity of 72 mAh g^{-1} (capacity normalized based on NVP). The irreversible loss is mainly due to the sodium consumption during the SEI formation at the sodium titanate anode side. After pre-cycling of the sodium titanate anode in a half-cell for one electrochemical cycle, the NVP/NTO full cell shows a significant reduction of 1st-cycle capacity loss and an improved discharge capacity of 94 mAh g^{-1} (Figure 119c), close to the value obtained in an NVP/Na half-cell (Figure 119a). Further improvements of the full-cell performance (for example, reversible capacity, capacity retention, etc.) can be anticipated from both the optimization of NVP cathode and balancing the ratio of cathode to anode.

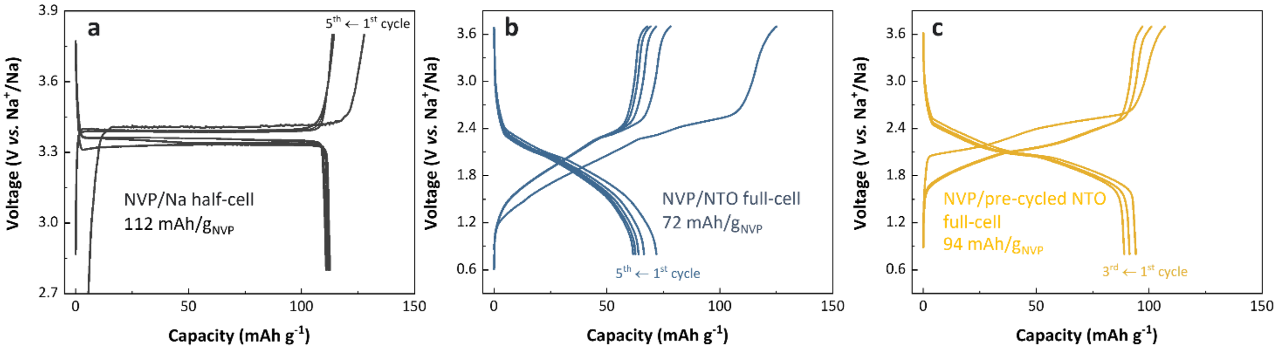

Figure 119. (a) The initial five cycles of $Na_3V_2(PO_4)3$(NVP)/Na half-cell cycled in 0.5 M $NaPhB_4$/DEGDME electrolyte. (b) The initial five cycles of NVP/60°C - annealed $Na_{0.74}Ti_{1.815}O_4$ (NTO) full-cell cycled in 1 M NaPF6-EC/DEC electrolyte. (c) The initial three cycles of NVP/60°C - annealed NTO full-cell cycled in 1 M $LiPF_6$-EC/DEC electrolyte; NTO electrode was pre-cycled in half-cell for one electrochemical cycle. All the cells were cycled at a current rate of C/10 calculated based on NVP. The capacity is normalized based on NVP. The N/P ratio is ~ 1.0-1.04.

Attempting to further increase the capacity of lepidocrocite-type titanate anode by increasing the number of available sites for sodium intercalation, the team completely replaced the interlayer sodium ions with half the number of magnesium ions to obtain a nominal composition of $Mg_{0.37}Ti_{1.815}O_4$ (MgTO). The MgTO material was prepared by stirring one gram of $Na_{0.74}Ti_{1.815}O_4$ material in 100 mL aqueous 4 M $MgCl_2•6H_2O$ solution at 80°C in a heated mineral oil bath for 7 days. The resulting powder was then vacuum filtered, washed, and dried at 100°C in an incubator. SEM – EDS analyses confirms the complete Na^+/Mg^{2+} ion-exchange. The preliminary electrochemical performance of MgTO phase was evaluated in a Na-ion half cell (Figure 120a). A discharge capacity of 217 mAh g^{-1} was obtained during the second cycle, slightly lower than what was obtained for the sodium titanate phase (227 mAh g^{-1}, Figure 120b). Mg^{2+} substitution for Na^+ has not proven successful so far, probably because immobile Mg^{2+} in the interlayer space interferes with Na^+ diffusion, causing a reduction of the practical capacity due to kinetics limitations. Further optimization of both the ion exchange process and dehydration step is under way; results will be reported next quarter.

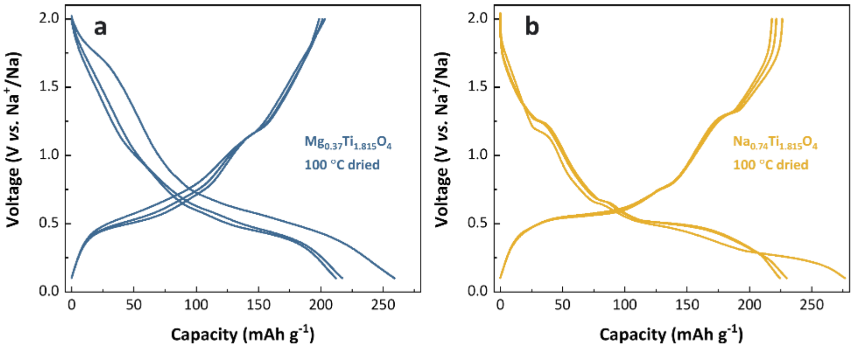

Figure 120. The initial three cycles of sodium half-cells containing electrodes of 100°C – annealed. (a) $Mg_{0.37}Ti_{1.815}O_4$. (b) $Na_{0.74}Ti_{1.815}O_4$. All cells were cycled in 0.5 M $NaPhB_4$ / DEGDME electrolyte at a current rate of 8 mA g^{-1}.

Patents/Publications/Presentations

The project has no patents, publications, or presentations to report this quarter.

Task 7.4 – Electrolytes and Interfaces for Stable High-Energy Sodium-Ion Batteries (Ji-Guang Zhang and Phung M. L. Le, Pacific Northwest National Laboratory)

Project Objective. The Na-ion battery is a potential alternative energy source for EVs and grid applications due to the low cost and the natural abundance of sodium. The performance of Na-ion batteries largely depends on development of electrode materials and electrolytes. In recent years, a series of potential electrode materials has been developed. However, a fundamental understanding of the electrochemistry of Na-ion batteries, especially the stability of the electrode-electrolyte interface in these batteries, is still not well established. This project will develop innovative electrolytes to enable fundamental understanding on the interface between electrode and electrolyte for stable operation of high-energy Na-ion batteries. A high-capacity anode will also be developed. The proposed research will enhance the achievable capacities of both anode and cathode for Na-ion battery and improve the stability of electrodes/electrolyte interface, establish correlation (electrolyte design rule) between electrochemical performances of Na-ion batteries and the electrolyte/interface properties, and enable long cycle life and safe operation of high-energy Na-ion batteries.

Project Impact. Success of this project will provide a solid understanding on the electrolyte/electrode interphase of Na-ion batteries and significantly improve their energy density, cycle life, and safety. It will also accelerate the practical application of Na-ion batteries in both EV and stationary energy storage.

Approach. This project will optimize the electrolyte components and concentrations to develop innovative electrolytes and additives with improved electrochemical and physical properties. Ether-based electrolytes with different salt will be optimized toward both anode (sodium metal and hard carbon) and cathode. Phosphate-based LHCE will be optimized to improve cycling performance of Na-ion batteries. SEI/CEI components of Na-ion battery in ether and phosphate electrolytes will be studied using XPS and SEM/TEM techniques to reveal the fundamental mechanism behind the improved stable performance of Na-ion batteries. Electrolyte additives in carbonate electrolyte will also be investigated to improve the electrochemical cathode performance. These approaches will unravel the origin of the SEI at the dynamic interface, providing guidance for the electrolyte and interface design and enabling high capacity and long life of Na-ion batteries.

Out-Year Goals. This project will select the electrolyte compounds and identify the formation of interfacial SEI layer on hard carbon and CEI layer-on-layer oxide cathode and its effect on the electrode materials. It will also provide guidance on electrolyte optimization and to improve CE of sodium deposition/stripping to be more than 99%.

Collaborations. This project will collaborate with ANL, LBNL, and other leading scientists in the field of cathode and anode materials for Na-ion batteries. It will also collaborate with C. Wang and M. Engelhard of PNNL for TEM and XPS characterization.

Milestones

1. Develop high-capacity carbon anodes in Na-ion batteries with optimized electrolytes. (Q1, FY 2021; Completed)
2. Develop high-voltage electrolytes (≥ 4.2 V) to increase energy density of Na-ion batteries. (Q2, FY 2021; Completed)
3. Characterize CEI/SEI interphase properties in optimized electrolyte to probe the mechanism of high-voltage cycling stability of Na-ion batteries. (Q3, FY 2021; Completed)
4. Develop electrolytes that are compatible with conventional polymer separators. (Q4, FY 2021; Completed)

Progress Report

Wettability is a significant concern in developing the Na-based electrolytes that usually exhibit a higher polarity compared to those of Li-ion analogs. The typical separators (PE or PP) commonly used in Li-ion batteries have a poor wettability with most of Na-ion electrolytes using carbonate solvents (such as 1 M $NaPF_6$ in PC) reported in literature. As a result, glass fiber has had to be used in most previous studies on Na-ion batteries except when ether- or ester-based electrolytes were used. On the other hand, most electrolytes used for Na-ion batteries are flammable. To address these problems, a new electrolyte based on tris(2,2,2-trifluoroethyl) phosphate (TFP) solvent has been developed. This electrolyte is not only compatible with PE separator, but is also non-flammable and stable in a high voltage Na-ion batteries. Therefore, it has a great potential for large-scale applications.

To investigate the compatibility of TFP-based sodium electrolyte with PE separator, the performances of high-voltage (4.2 V) NaNMC||HC full cells using TFP-based electrolytes were systematically studied. As a comparison, similar cells with the carbonate-based electrolyte [1 M $NaPF_6$/EC:EMC (3:7 in vol)] were also studied as a baseline with PE separator. All cells have been cycled three cycles at a low rate of 0.05 C (1 C = 200 mAh g^{-1}) to stabilize SEI layers prior to long-term cycling at 0.2 C. Figure 121 compares the electrochemical performance of these cells during long-term cycling. In carbonate-based electrolyte, the full cell exhibits fast capacity decay with only 33.5% capacity retention (169 mAh g^{-1} for 4th cycle, 56.6 mAh g^{-1} for 200th cycle) after 200 cycles (Figure 121a). The average CE of this cell during long cycling is quite low (< 99.2%), indicating continuous side reactions due to unstable electrode/electrolyte interphases, poor compatibility between electrolyte and electrodes, and limited high-voltage stability, which is consistent with the poor oxidation stability of the electrolyte (Figure 121b). In contrast, the full cell with 1 M NaFSI/TFP electrolyte shows much better cycling performance with 80.4% capacity retention (164.8 mAh g^{-1} for 4th cycle, 132.5 mAh g^{-1} for 200th cycle) after 200 cycles at 0.2 C. Moreover, NaFSI/TFP was further modified to improve its ionic conductivity and reduce its viscosity by adding an optimized amount of DMC in the electrolyte to form the advanced electrolyte named NaFSI/DMC:TFP). The cell with NaFSI/DMC:TFP electrolyte has demonstrated the best performance among three HC||NaNMC cells investigated in this work, as shown in Figure 121. A high-capacity retention of 92.4% (162 mAh g^{-1} for 4th cycle; 149.7 mAh g^{-1} for 200th cycle) after 200 cycles with an excellent cycling CE of > 99.9% (Figure 121b) has been achieved.

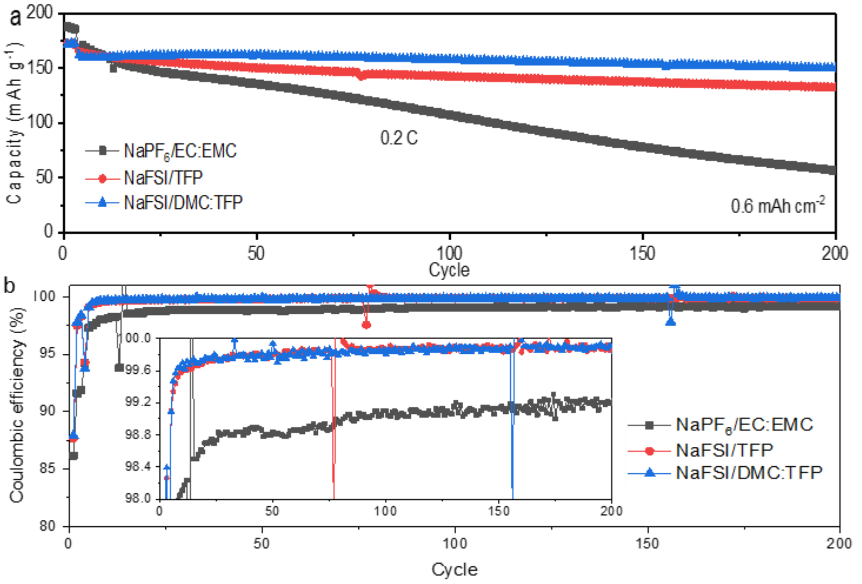

Figure 121. Electrochemical performance of HC||NaNMC full cells: Discharge capacity (a) and CE (b) of HC||NaNMC full cells using different electrolytes cycled at 0.2 C in a voltage range 1.2 – 4.2 V after three formation cycles at 0.05 C. The cathode loading is 0.6 mAh cm^{-2}.

Patents/Publications/Presentations

The project has no patents, publications, or presentations to report this quarter.

Innovation Center for Battery500
(Jun Liu, Pacific Northwest National Laboratory; Yi Cui, Stanford University)

Project Objective. The project aims to develop commercially viable lithium battery technologies with a cell-level specific energy of 500 Wh/kg through innovative electrode and cell designs that enable the extraction of the maximum capacity from advanced electrode materials. In addition to achieving high specific energy, the project aims to be able to achieve 1,000 cycles for the developed technologies.

Project Impact. The Battery500 Consortium will develop next-generation lithium battery technologies that will significantly increase energy density, improve cycle life, and reduce cost. This will greatly accelerate deployment of EVs and reduce carbon emission associated with fossil fuel consumption. The consortium will utilize first-class expertise and capabilities in battery research in the United States and develop an integrated and multi-disciplinary approach to accelerate development and deployment of advanced electrode materials in commercially viable high-energy batteries. The advances made in this consortium will also benefit the improvement of current Li-ion battery technologies.

Approach. This project will utilize an assortment of national resources located at the national laboratory level and university level. The lithium anode combined with a compatible electrolyte system and two cathodes—one high-Ni $LiNi_xMn_yCo_zO_2$ and another sulfur—will be studied and developed to reach high energy density. The project focus is to design novel electrode and cell architectures to meet the 500 Wh/kg goal. The consortium will work closely with R&D companies, battery/materials manufacturers, and end users / original equipment manufacturers to ensure that the developed technologies are aligned with industry needs and can be transitioned to production.

Out-Year Goals. This project aims for the following out-year goals. First, fabricate and test a pouch cell capable of 350 Wh/kg and 350 cycles. Second, fabricate and test a pouch cell capable of 400 Wh/kg and 100 cycles.

Collaborations. Collaboration among consortium team members will be well coordinated by the leadership team, which includes the keystone project leads and co-leads along with PIs at all member institutions. Collaboration with the community outside of this consortium and with industry will be facilitated by the executive committee, the advisory board, and the industry committee.

Milestones

1. Benchmark Li-anode architecture with 50-µm lithium anode using protocols for 350 Wh/kg cells, and achieve over 200 cycles in coins. (Q1, FY 2021; Completed)
2. Optimize pressure effect for Li-S from coin cells. (Q2, FY 2021; Completed)
3. Provide new electrolyte formulation for Li-S (PNNL). (Q3, FY 2021; Completed)
4. Demonstrate 350 Wh/kg pouch cell with > 450 cycles; 400 Wh/kg > 100 cycles; and > 450 Wh/kg. Demonstrate good cycling of Li-S pouch cell at 300 Wh/kg. (Q4, FY 2021; In progress)

Progress Report

Keystone Project 1: Materials and Interfaces

The goal of Keystone 1 is to provide the materials and chemistry support for Keystone projects 2 and 3. The Binghamton team evaluated the high-voltage and high-temperature thermal stability of novel electrolytes, including LHCE. The UT Austin group benchmarked and evaluated the failure mechanisms of undoped, high-capacity $LiNiO_2$ (LNO) in LHCE compared with carbonate electrolytes. The PNNL team developed a two-layer lithium coating for improving the morphology, CE, and cycle life of Li-metal anodes. The Stanford group explored longer-chain equivalents of their FDMB solvent and found an improved electrolyte formula for anode-free pouch cells. The UCSD team explored the effects of binder composition on the performance of high-loading and low-porosity sulfurized polyacrylonitrile (SPAN) electrodes.

The Binghamton team worked with PNNL and Stanford to determine the electrochemical and thermal stabilities of their novel electrolytes. Besides the previously reported LiFSI/FDMB and M47 LHCE electrolytes, two additional electrolytes, T3 and ED2 from PNNL, were studied under the same conditions. The isothermal calorimetry experiments were performed at 30°C, 45°C, and 60°C with charging to 4.8 V at C/10 rate (1C = 200 mAh g^{-1}). The results of the four ether-based electrolytes are compared to the baseline carbonate electrolyte in Figure 122. All electrolytes are stable up to ~ 4.4 V and even up to 60°C. However, differences between the electrolytes can be clearly observed when charged above 4.4 V. T3 was as stable as the baseline carbonate electrolyte at each temperature without any obvious side reaction. The 1 M LiFSI/FDMB showed similar stability as T3 and the carbonate electrolyte at 30°C and 45°C, but began to show side reactions above 4.6 V at 60°C, associated with a large heat release. Meanwhile, the stabilities of M47 LHCE and ED2 were lower than the other electrolytes, where apparent side reactions were observed at all three temperatures above 4.5 V. Comparatively, the M47 LHCE had much more heat release than ED2, indicating the worst thermal stability among these five electrolytes. Interestingly, the heat flux of the ED2 electrolyte decreased with increasing temperature, which is contrary to other electrolytes. Overall, the ether-based electrolytes were less stable than the carbonates under the extreme conditions of these tests, but all are stable at 30°C for charging voltages up to 4.4 V where long-term tests are under way. In the end, a compromise must be reached between electrolyte stability under extreme conditions and ability to plate lithium with near 100% efficiency.

The UT Austin team benchmarked an undoped, pure-nickel LNO cathode with carbonate and LHCE electrolytes to highlight the remarkable performance enabled by advanced electrolytes. Figure 123a shows the cycling performance of LNO cathodes in Li-metal pouch cells with a typical carbonate electrolyte (LP57, 1 M $LiPF_6$ in 3:7 EC:EMC with 2% VC) as well as with the baseline LHCE (LiFSI-1.2DME-3TTE). After 200 cycles, the cell with LHCE showed a more than 5-fold improvement in capacity retention. When the cathodes from these cells were harvested and assembled into new cells, most of this capacity difference remained, indicating that the capacity loss during cycling was mostly associated with the cathode itself (Figure 123b). The improved capacity retention of LNO in the LHCE electrolyte can be attributed to several factors, including formation of a more robust CEI. Figure 123c shows the XPS data for the cathodes cycled in each electrolyte. The cathode cycled in LHCE shows the presence of sulfur and nitrogen species, which can be attributed to decomposition of the lithium salt, lithium bis(fluorosulfonyl)imide. Similarly, an increase in fluorine concentration and the presence of lithium fluoride can be attributed to salt decomposition as well as to decomposition of the fluorinated solvent. Lithium fluoride is known to be an effective CEI component, contributing to improved stability of LNO in LHCE. In addition to improved surface stability, LNO in LHCE is also subject to reduced microcracking relative to the same cathode in carbonate electrolyte. Figure 123d shows the cross-sectional SEM images of the LNO cathodes after 200 cycles. The cathode particles, which were cycled in LHCE, show a small number of cracks, typical also of pristine cathode material. Meanwhile, the particles cycled in LP57 show many microcracks. While 200 cycles are not enough for complete particle pulverization, that is, destruction of the secondary particle structure, microcracks can disrupt the ion or electron conduction pathway and allow for electrolyte penetration and increased surface reactivity. The findings demonstrate that the viability of high-nickel cathodes and their degradation mechanisms should be re-evaluated in light of using advanced electrolytes, such as LHCE.

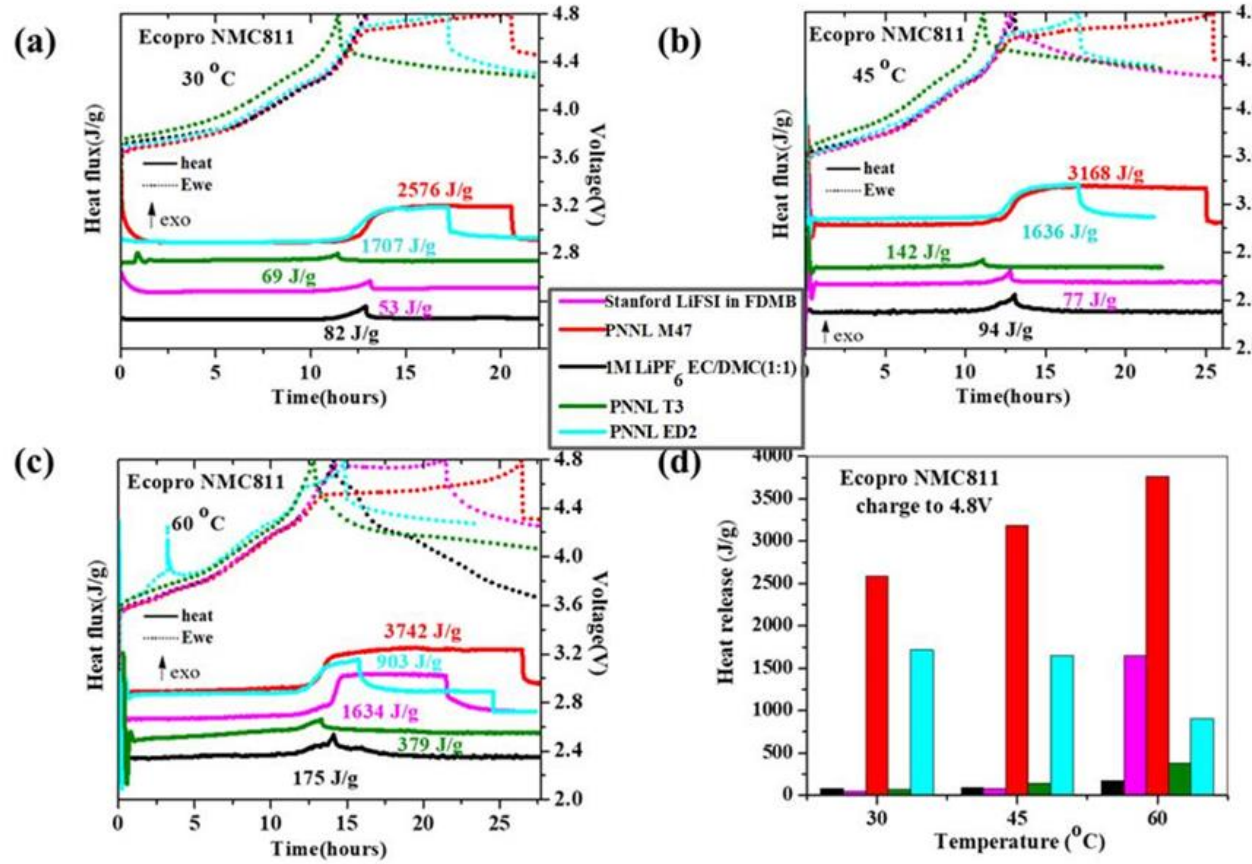

Figure 122. *Operando* differential scanning calorimetry measurements (dotted curves for electrochemical test and solid curves for measured heat flux) of novel ether-based M47, ED2, T3, 1 M LiFSI/FDMB electrolytes and traditional carbonate electrolyte [1 M $LiPF_6$ in EC/DMC (1:1)] for NMC-811 charged to 4.8 V while held at (a) 30°C, (b) 45°C, and (c) 60°C isothermally. (d) Summary of total heat release.

The PNNL team developed an ionic conductive double-layer coating for Li-metal anode protection to improve battery performance. The protective double layer consists of a top layer (TL) based on a cross-linkable polymer and a bottom layer (BL) of PEO-based PE. PEO is well known to be stable with lithium metal and to have a high donor number for lithium ion as well as high chain flexibility, which are important for promoting ion transport in the protection layer. However, it needs to be covered by durable materials to preserve its integrity because PEO can swell and even dissolve in LEs. For this reason, the cross-linkable polymer is selected as the TL to maintain the integrity of the PEO-based layer that directly covers the Li-metal surface. The cycle life of Li||Li symmetric cells composed of a thin lithium anode (50 µm) and 75 µL of DME-LHCE (LiFSI-1.2DME-3TTE) electrolyte was investigated at a current density of 1 mA cm^{-2} and a capacity of 1 mAh cm^{-2}, as shown in Figure 124a. Bare lithium shows a short circuit failure at ~ 960 hours. The top-layer-coated lithium (TL@Li) and double-layer-coated lithium with pure PEO in the bottom layer (DL-0@Li) have longer cyclability, but lead to a higher polarization than bare lithium. To reduce polarization during cycling, an additive was added to the double layer. The double layer with the additive-coated lithium (DL-3@Li) exhibits a long cycling lifespan for 1,000 hours without significant increase in polarization. Based on this result, DL-3@Li was selected as the optimum protection layer for the Li-metal electrode. The coating layer morphology was checked by SEM using a DL-3 coated copper foil, which was prepared by the same process as DL-3@Li. As shown in Figure 124b, total thickness of the coating layer is ~ 630 nm, including ~ 180 nm of top layer and ~ 450 nm of bottom layer.

The thickness of DL-3 coated on lithium is similar to that coated on copper foil. In addition, DL-3@Li delivers a stable deposition/stripping behavior with a slightly improved average CE value compared to the bare lithium (Figure 124c). Furthermore, in Li||NMC-622 coin cells consisting of a NMC-622 cathode (4.2 mAh cm^{-2}), a thin lithium foil (50 µm), and 75 µL DME-LHCE, the Li||NMC-622 cell using DL-3@Li exhibits a higher capacity retention of 92.4% after 220 cycles at a current density of 2.1 mA cm^{-2} (that is, C/2 rate) compared to those using bare lithium (74.6%, Figure 124d). To understand the mechanism behind the improved electrochemical performance, SEM images of Li-metal electrodes extracted from the cycled coin cells are compared in Figure 124e. The cycled DL-3@Li exhibits a flat, smooth surface without lithium dendrites, while the bare lithium anode shows a rough and porous surface with massive dendritic lithium. This result demonstrates that uniform lithium deposition and controlled side reactions can be achieved on lithium metal at a high current density after DL-3 coating.

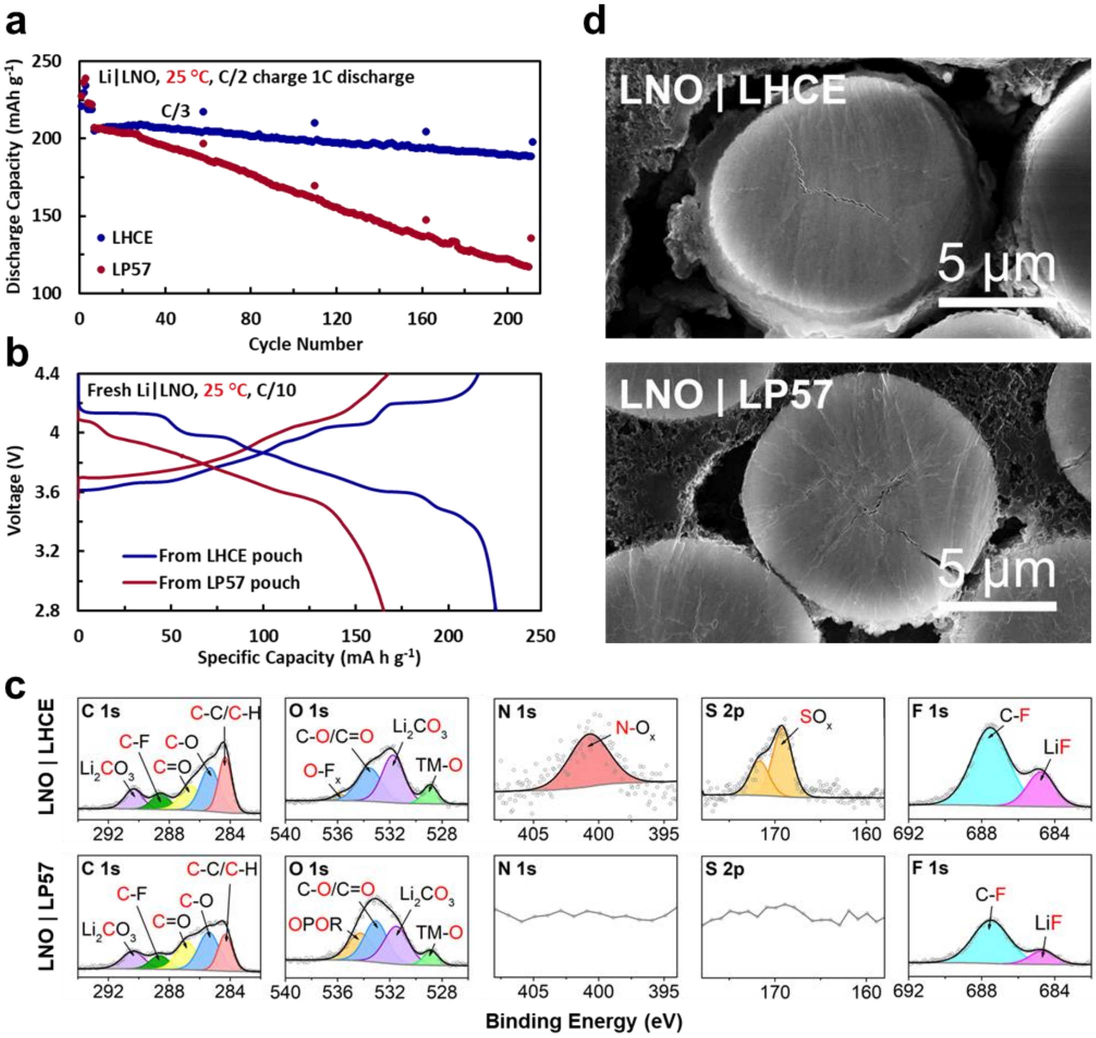

Figure 123. (a) Cycling performances of Li-metal pouch cells with LNO cathodes at C/2 charge and 1C discharge rate, with C/3 rate every 50 cycles. (b) Charge-discharge curves of fresh coin cells assembled using the cathodes recovered from the cycled pouch cells. (c) Cross-sectional scanning electron microscopy images of LNO cathodes recovered from cycled pouch cells after 200 cycles in LHCE (top) and carbonate electrolyte (bottom). (d) X-ray photoelectron spectroscopy data of LNO cathodes recovered from cycled pouch cells after 200 cycles in LHCE (top) and carbonate electrolyte (bottom). Spectra were normalized across samples for each element.

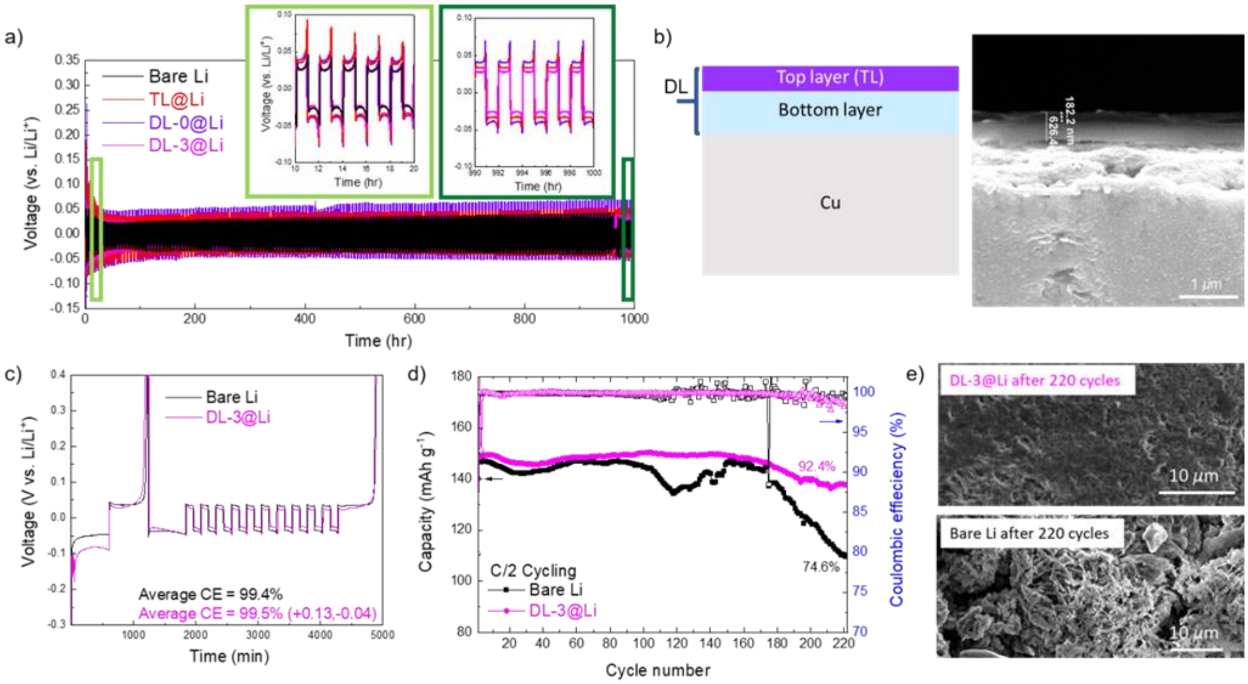

Figure 124. (a) Voltage profiles of Li-metal deposition/stripping in Li||Li symmetric cells (1 mAh cm^{-2}) at current density of 1 mA cm^{-2}. (b) Schematic illustration and cross-sectional scanning electron microscopy (SEM) image of DL-3@Cu. (c) Average Coulombic efficiencies of Li||Cu cells using bare lithium and DL-3@Li. (d) Cycling performances of Li||NMC-622 cells (4.2 mAh cm^{-2}) at high rate (C/2, 1C = 4.2 mA cm^{-2}) in voltage range of 2.8-4.4 V at 25°C. (e) Surface SEM images of bare lithium and DL-3@Li after 220 cycles.

The Stanford team has developed a family of rationally designed electrolyte solvent ether molecules: FDMB, fluorinated 1,5-dimethoxypentane (FDMP), fluorinated 1,6-dimethoxyhexane (FDMH), and fluorinated 1,8-dimethoxyoctane (FDMO), all of which are very stable relative to lithium metal and to high-voltage cathodes, such as high-Ni NMC. However, there is a balance between electrode stability and reasonable ionic conduction. The molecular structures, design logic, and battery performance are shown in Figure 125. Generally, longer fluorinated chains result in higher stability, yet lower ionic conductivity; therefore, a balance needs to be achieved (Figure 125a-b). After screening different electrolyte recipes, the team has identified 1 M LiFSI/1DME/6FDMH (by volume) as the best electrolyte even compared to previously reported 1 M LiFSI/FDMB [see: *Nature Energy* 5 (2020): 526–533]. The 1 M LiFSI/1DME/6FDMH electrolyte showed a replicable 99.4% Li-metal CE and high oxidative stability, enabling 120 cycles in an anode-free Cu||NMC-811 pouch cell (Figure 125c-e).

The UCSD team studied ether-based LHCEs for high CE and dendrite-free lithium anode. Previous studies from P. Liu's group at UCSD have demonstrated that the ether-based LHCE enables long cycle life for Li||SPAN cells. The 1st generation LHCE is 1.8 M LiFSI in diethyl ether (DEE) / BTFE (LDEE), which shows a high lithium CE of 99.5% at 0.5 mA cm^{-2}. The Li||SPAN cell exhibits stable cycling without any capacity fade for > 1,200 cycles in LDEE, when the electrode loading is 2 mg cm^{-2}. However, the boiling point of DEE is 35°C. As a result, the LHCE was volatile, even with a high salt concentration. To reduce the volatility of LHCE, the DEE was replaced by diisopropyl ether (DiPE), dibutyl ether (DBE), and DME, which have boiling points of 69°C, 141°C, and 85°C, respectively. The Li-metal CE in these LHCEs was investigated using PNNL's modified method. At 0.5 mA cm^{-2} and 1 mAh cm^{-2}, the LDEE, LDBE, LDiPE, and LDME show CEs of 99.50%, 98.93%, 99.17%, and 99.11%, respectively (Figure 126a). Besides the CE, the morphologies of deposited lithium films in these electrolytes were examined by SEM. The lithium films were plated on copper substrates in Li||Cu cells, at 1.2 mA cm^{-2} for 6 mAh cm^{-2}. All the lithium films plated in ether-based LHCEs present similar large lithium particles with sizes of ~ 10 μm (Figure 126b-e). The high Li-metal CEs and dendrite-free lithium morphologies in these ether-based LHCEs indicated that they are promising electrolyte candidates for long-cycle-life Li||SPAN batteries. The cycling tests of Li||SPAN cells using these electrolytes are under way.

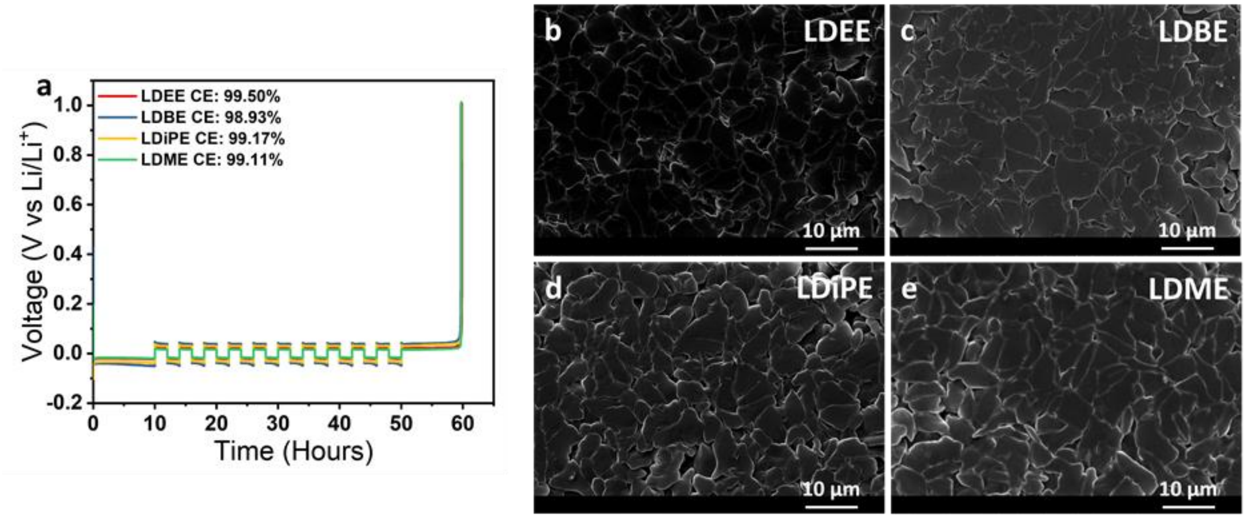

Figure 125. The comparison of localized high concentration electrolytes (LHCE) based on different ethers. (a) The plating/stripping voltage profiles of Li||Cu cell cycled in different LHCEs. Prior to the test, a condition cycle was carried out on all the cells. In this step, a lithium film was first deposited onto the copper foil at 0.5 mA cm^{-2} for 10 hours, and then fully stripped to 1 V. Another lithium film (5 mAh cm^{-2}) was deposited again; only 1 mAh cm^{-2} capacity of lithium film was stripped and plated for 10 cycles. Finally, the lithium film was fully stripped to 1 V. The current density during this test was 0.5 mA cm^{-2}. The morphologies of the deposited lithium film in different LHCEs, at 1.2 mA cm^{-2} for 6 mAh cm^{-2}. (b) LDEE (1.8 M LiFSI in diethyl ether). (c) LDBE (1.8 M LiFSI in dibutyl ether). (d) LDiPE (1.8 M LiFSI in diisopropyl ether). (e) LDME (1.8 M LiFSI in 1,2-dimethoxyethane).

S. Meng's group at UCSD studied the reaction mechanisms of SPAN. This quarter, the bonding environment of sulfur in the SPAN was analyzed by FTIR to probe the pristine molecular structure of SPAN. Figure 127a shows the FTIR spectrum of SPAN synthesized at 300°C, 450°C, and 550°C, with wavenumber ranging from 890 cm^{-1} to 970 cm^{-1}, which corresponds to the ring breathing in the pyridine ring when a C−S bond is included. In previous studies, the S-C bond has been exclusively assigned to the C at position 4 on the pyridine ring. However, as shown in Figure 127a, there are in fact three different types of C−S bonds in the pristine SPAN molecule, and the peak area ratios of different C−S bonds will change as the synthesis temperature varies. According to the elemental analysis of the pristine SPAN synthesized at the three temperatures (Figure 127c), there is a significant amount of hydrogen present in the molecule. On average, every two repeating units of SPAN molecule will host one hydrogen atom. The presence of hydrogen in the pristine SPAN has been largely ignored in previous studies, and the impact of the hydrogen to the reaction mechanism of SPAN remains unclear. With the presence of hydrogen in the SPAN molecule, it is possible that a portion of sulfur has added to the positions other than position 4. The red peak in the FTIR spectrum might represent the sp^3 S-C(N) bond in the SPAN molecule, which will break the conjugated electron structure of the pyridine ring and lead to the formation of H-C or H-N bonds. The blue peaks in the FTIR spectrum might correspond to the S-C(N) sites that have been linked to bridging S_x, which is a temperature-sensitive bond whose presence decreases as the synthesis temperature increases. The observation from the FTIR is in agreement with the elemental analysis, as the sulfur content decreases when the synthesis temperature increases. The decrease in the sulfur content in the SPAN synthesized at higher temperature might largely come from the loss of the bridging S_x. Lastly, the green peak in the FTIR spectrum corresponds to the S-C bonds at position 4. Figure 127b illustrates the locations of different S-C(N) bonds and the presence of hydrogen in the pristine SPAN molecule. More characterization and analysis, such as Raman, NMR, and XPS, are in progress to further decipher the exact molecular structure of SPAN and the reaction mechanism between lithium and SPAN.

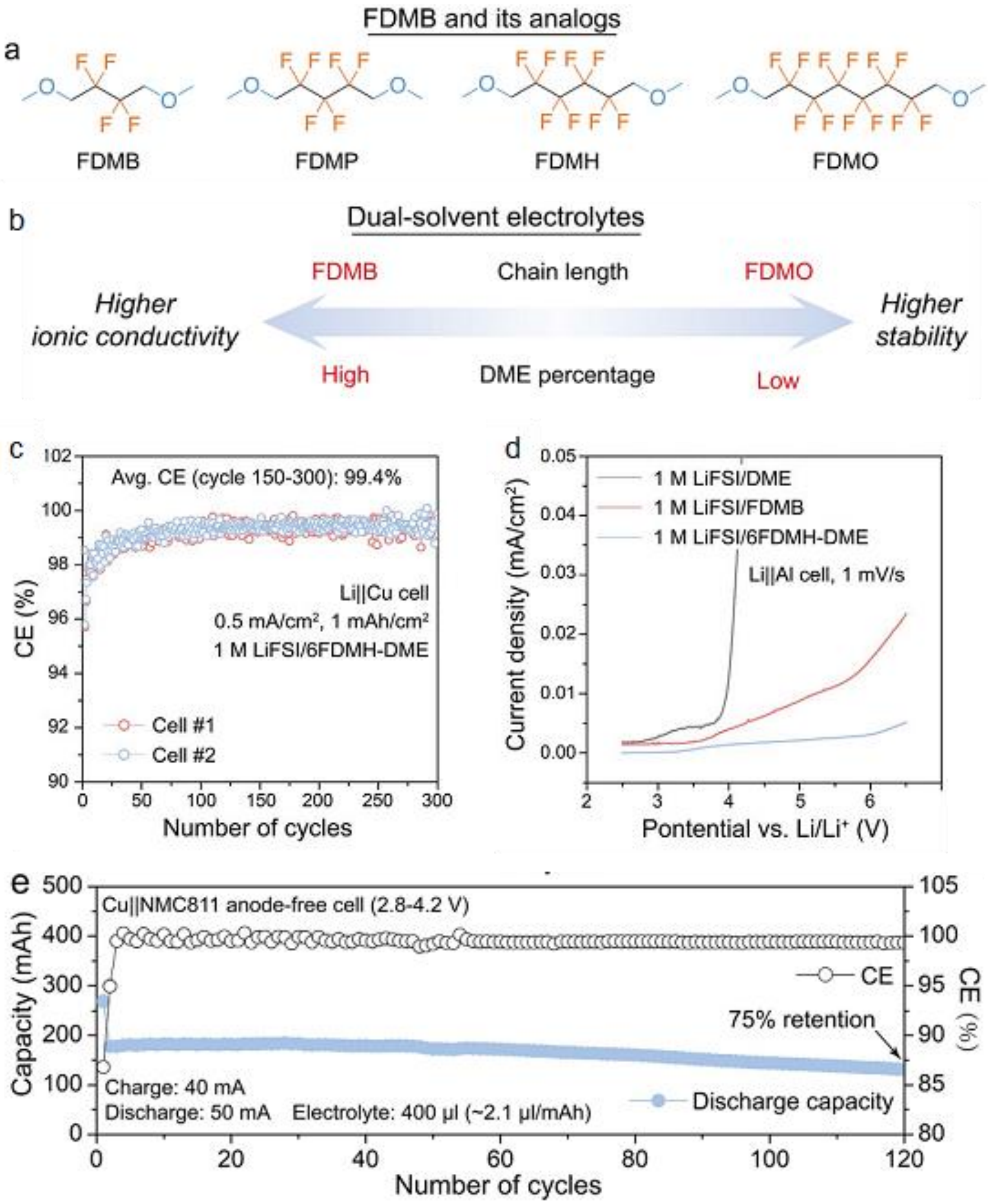

Figure 126. (a-b) Molecular structures and design logic of FDMB and its analogs. (c) Long cycling Coulombic efficiency of Li||Cu half cells. (d) Linear sweep voltammetry showing the high-voltage stability of developed electrolytes. (e) Anode-free pouch cell performance using the best electrolyte, 1 M LiFSI/1DME/6FDMH.

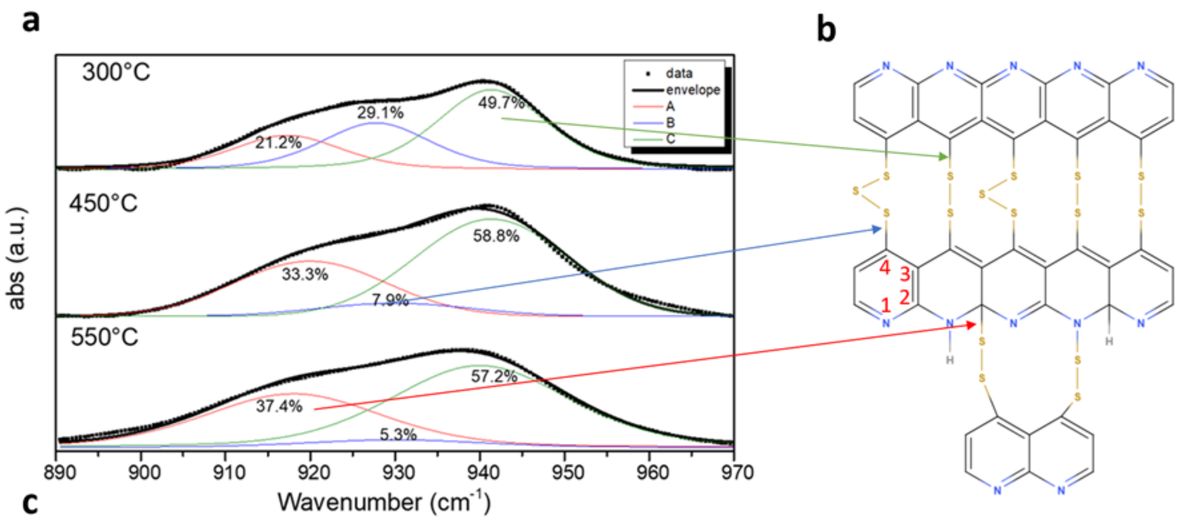

c

Material	C wt%	N wt%	H wt%	S wt%	Molecular Formular
300SPAN	34.33	12.32	0.30	46.48	$C_{2.86}N_{0.88}H_{0.3}S_{1.45}$
450SPAN	38.18	14.49	0.51	40.22	$C_{3.18}N_{1.04}H_{0.51}S_{1.26}$
550SPAN	39.03	15.64	0.51	29.43	$C_{3.25}N_{1.12}H_{0.51}S_{0.92}$

Figure 127. (a) Fourier transform infrared spectrum of SPAN synthesized at 300°C, 450°C, and 550°C. (b) The proposed sulfur bonding environment in the pristine SPAN molecule. (c) Elemental analysis of SPAN synthesized at 300°C, 450°C, and 550°C.

Highlights of Keystone Project 1

The highlights for this quarter are as follows:

- The high-voltage and high-temperature stabilities of baseline LHCE as well as other novel electrolytes were explored through *operando* DSC. (Binghamton University)
- The stability of undoped $LiNiO_2$ cathode with advanced electrolytes was demonstrated by a comparison between LHCE and a typical carbonate electrolyte (92% capacity retention after 200 cycles with LHCE versus 56% for carbonate). (UT Austin)
- A thin two-layer protective coating for lithium metal was developed to improve the morphology of lithium plating and enhance the cycle life of Li-metal cells. (PNNL)
- Long-chain fluorinated ether molecules were synthesized and tested in dual-solvent mixtures to optimize between stability and conductivity, leading to improved anode-free pouch cell performance (75% retention after 120 cycles). (Stanford University)
- Ether-based LHCEs with high CE and dendrite-free lithium anode, as well as the reaction mechanism of SPAN, were studied and reported. (UCSD)

Keystone Project 2: Electrode Architecture

The UCSD team has systematically investigated the effect of binders on the cycling performance of high areal capacity SPAN cathodes (> 6 mAh cm^{-2}) with different porosities. The cycling stability of the SPAN electrode with a porosity of 50% using a PVDF binder was tested first. To mitigate the effect of lithium degradation on the cell cycling performance, a 1.8 M LiFSI in DEE/BTFE electrolyte (LDEE) was used for the test. The Li||SPAN cell shows a rapid capacity fading from 650 mAh g^{-1} to 400 mAh g^{-1} within 60 cycles when the electrode loading was 10 mg cm^{-2}. The corresponding voltage profiles indicate a fast polarization increase (Figure 128a/d). Their previous studies revealed that the mechanical failures of cracking, delamination, and volume change are likely the root cause of the rapid capacity fading of the 10 mg cm^{-2} SPAN electrode. Optimizing the polymer binder is a practical approach to improve the electrode mechanical integrity. As a comparison, the 6 mAh cm^{-2} SPAN cathode using a CMC binder exhibited stable cycling. It maintained 94.5% of its capacity (based on the 3rd cycle) at the 60th cycle, while the PVDF electrode at the 60th cycle only delivered capacity retention of 66.7% (Figure 128a). Another critical step toward high energy density Li||SPAN battery is to reduce the cathode porosity, as lower porosity electrode requires less electrolyte, resulting in higher cell-level energy density. The binder plays a key role at low porosity because the SPAN electrode will expand outwardly due to the limited spaces inside, which will apply significant stress on the binder skeleton. SPAN cathodes with 40% and 30% porosity were tested, and the results are shown in Figure 128b-c. The capacity of PVDF-based electrodes quickly decays from 600 to < 150 mAh g^{-1} within 10 cycles. In contrast, the 30% and 40% porosity SPAN electrodes using CMC binder were able to maintain high capacity retention of 95.1% and 94.4%, respectively (Figure 128e-f), clearly demonstrating the benefits of using CMC for high areal loading, low porosity SPAN cathodes. This work proves the importance of binder on low porosity thick SPAN cathodes and paves the road for high energy density Li||SPAN cell.

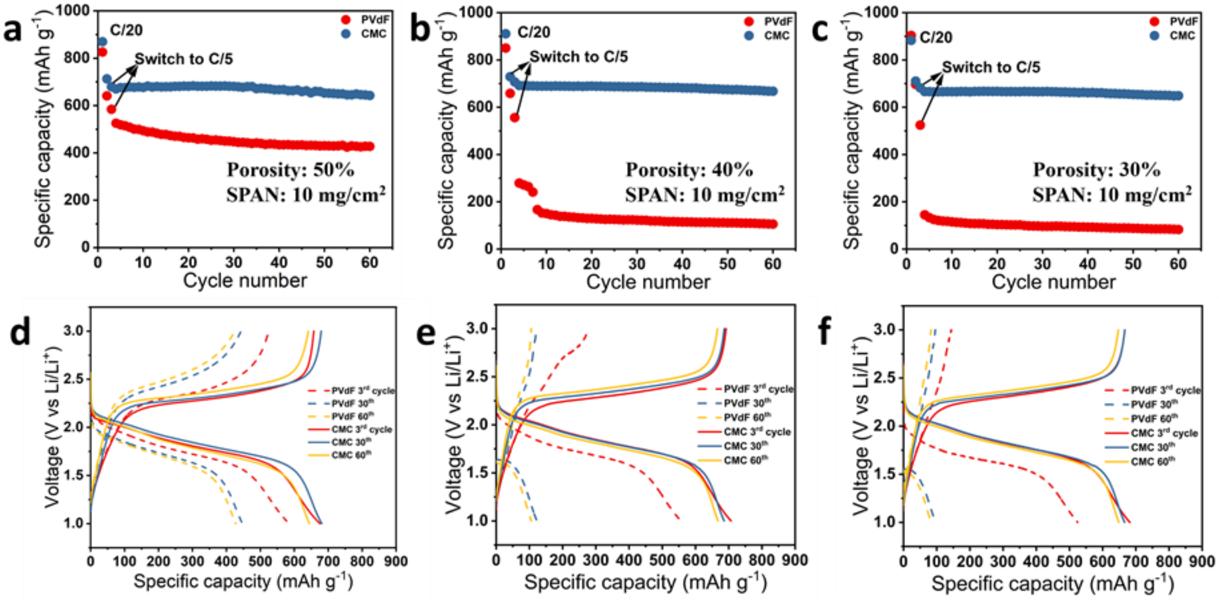

Figure 128. Comparison of the cycling performance of high areal capacity SPAN electrodes. (a) 50% cathode porosity, (b) 40% cathode porosity, and (c) 30% cathode porosity. Voltage profiles of Li||SPAN cells with (d) 50% cathode porosity, different binder, (e) 40% cathode porosity, different binder, and (f) 40% cathode porosity, different binder. The mass loading of the SPAN cathode is 10 mg cm^{-2}. The cell was cycled under C/20 rate for two formation cycles and then cycled under C/5 rate.

This quarter, the BNL and UCSD teams studied how the sulfur-based species evolve in the SPAN electrodes using a combination of XRF and sulfur K-edge XAS, which not only provides global elemental distribution over the electrode at the millimeter-length scale, but also probes the spatially resolved chemical information of sulfur-based species using the micro-sized beam. Figure 129a shows an XRF image of a pristine SPAN cathode (2 × 4 mm^2 area) measured at an incident X-ray beam energy of 2480 eV. An inhomogeneous distribution of sulfur-based species was observed, as depicted with circles for high-S and low-S concentration areas in Figure 129a. The corresponding XAS spectra of the selected areas are shown in Figure 129b. The absorption intensity, so-called the “edge-jump,” indicates the total absorption of sulfur species at the spot where the micro-sized beam [16 μm (horizontal) × 5 μm (vertical)] was probed. For a more detailed investigation of the chemical state, the XAS plot is normalized, as shown in Figure 129c. A spectral distortion is observed at the XANES, which should be mainly caused by self-absorption due to the high sulfur concentration for the spectrum collected from the high sulfur area. Except for the spectral distortion, the chemical status (valence state of sulfur) of the pristine SPAN cathode is uniform and only has a slight thickness variation that might have been induced by the slurry casting process used for electrode fabrication. Both spectra represent the same three major peaks as indicated: 1 (2468.5 eV), 2 (2470.8 eV), and 3 (2472.5 eV) (Figure 129c). These peaks can be attributed to the transition from sulfur 1s to S-C π*, S−S σ*, and S−C σ* states in the SPAN structure, respectively. The corresponding bonding structure is displayed with a colored circle over the SPAN structure in Figure 129d. The proposed structure in Figure 129d is adopted from the paper published by Fanous et al. in the literature. This model is only one of several structures that have been proposed, which might be due to the variance of the synthesis route and the resulting complexity of the polymeric structure of SPAN. Although the proposed structures differ in detail, all of them incorporate covalent bonding between sulfur and carbon in the SPAN, rather than the physical absorption of elemental sulfur in carbon.

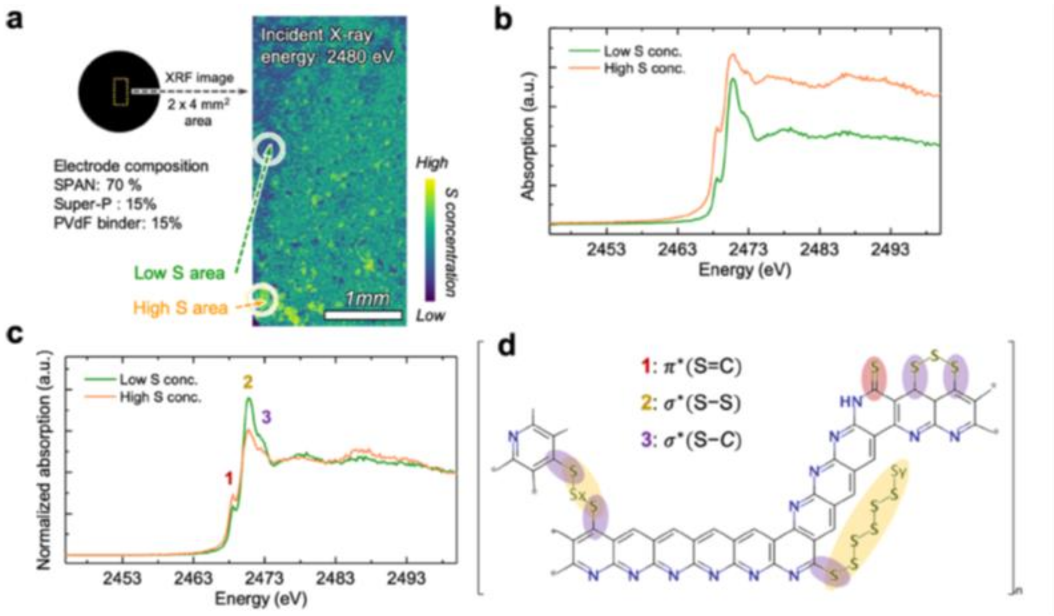

Figure 129. (a) X-ray fluorescence (XRF) image of pristine SPAN cathode measured at incident X-ray beam energy of 2480 eV with indications of inhomogeneous distribution of sulfur-containing chemical species. (b) Measured sulfur K-edge μXANES spectra at the selected area for low-sulfur and high-sulfur concentration indicated in the XRF image.(c) Normalized sulfur K-edge μXANES spectra. (d) Model structure of SPAN redrawn based on the previous report by Fanous et al. The red, yellow, and purple regions indicate that S=C, S−S, and S−C bonds exist in the SPAN in this study.

The INL team has applied a unique electrochemical analytic technique to determine the effectiveness in the use of cathode active materials, such as NMC-811, in different electrode formulations and fabrication processes, by characterizing the utilization efficiency during the charge and discharge regimes in the formation cycle. Borrowing the concept of CE, several different CEs are defined below and used as an indicator to denote different retentions. The same formulation is used to describe the lithium inventory retention. Like the CE for the capacity retention (CE_Q) as:

$$CE_Q = (Q_{dis} / Q_{ch}) \times 100\% \qquad (1)$$

The CE for the lithium inventory retention (LIR) is quantified as:

$\mathrm{CE_{LIR}} = (Q_{\mathrm{Li\_dis}} / Q_{\mathrm{Li\_ch}}) \times 100\%$ (2)

where the theoretical specific capacity associated with lithium inventory change (Q_{Li}) for each charge or discharge regime was calculated with the associated SOC change in the pseudo-OCV versus SOC curve after the data transformation and the theoretical NMC-811 specific capacity per % SOC. Furthermore, the LIR in the respective charge and discharge regime can be accessed separately as

$\mathrm{CE_{ch}} = (Q_{\mathrm{Li\_ch}} / \mathrm{Q_{ch}}) \times 100\%$ (3)

$\mathrm{CE_{dis}} = (Q_{\mathrm{Li\_dis}} / \mathrm{Q_{dis}}) \times 100\%$ (4)

and yield a "round-trip CE" ($\mathrm{CE_{RT}}$) for the charge-discharge cycle as:

$\mathrm{CE_{RT}} = \mathrm{CE_{ch}} \times \mathrm{CE_{dis}}$ (5)

Applying the above electrochemical analytic method and the CE formations, two NMC-811 formulations and cell configurations were examined to investigate their performance. One formulation uses ECOPRO NMC-811 in a coin-cell assembly with flooded electrolyte (E cell) and another TARGRAY NMC-811 of the same slurry composition, mass loading, and calendering condition in a double-layer pouch cell configuration and 8 g/Ah Gotion LP30 electrolyte (T cell). Both E coin cells and T pouch cells went through the same formation cycle protocol with C/10 charge and discharge rate and 4.4 V cutoff with 15-min rest between charge and discharge regimes (with rest). Some of the E coin cells were subjected to no rest at the end of charge and discharge (without rest).

Figure 130 summarizes the comparisons of (a) $\mathrm{CE_Q}$ and $\mathrm{CE_{LIR}}$ and (b) $\mathrm{CE_{ch}}$, $\mathrm{CE_{dis}}$, and $\mathrm{CE_{RT}}$ among E coin cells (with and without rest) and T pouch cells for the formation cycle. Based on capacity, all E and T cells' $\mathrm{CE_Q}$ are roughly the same as a function of cutoff voltage in the range of 85% to 90%. Considering $\mathrm{CE_{LIR}}$, T cells follow the same trend and in the same range with $\mathrm{CE_Q}$, whereas E cells exhibit a much lower range of values. In contrast, if $\mathrm{CE_{ch}}$, $\mathrm{CE_{dis}}$, and $\mathrm{CE_{RT}}$ are evaluated, the kinetic effect associated with the cathode formulation (primarily the grain size disparity) and configuration (primarily the electrode dimensions and electrolyte amounts, cell compression) in the cells are clearly distinguished. The utilization efficiency as reflected by $\mathrm{CE_{ch}}$ for E and T cells with rest are almost identical. Without rest, $\mathrm{CE_{ch}}$ for E cells are lower, indicating the test protocol does affect the performance in the evaluation protocol. The lower $\mathrm{CE_{LIR}}$ in E cells is due to the worse utilization efficiency in the discharge regime, as shown by the $\mathrm{CE_{dis}}$.

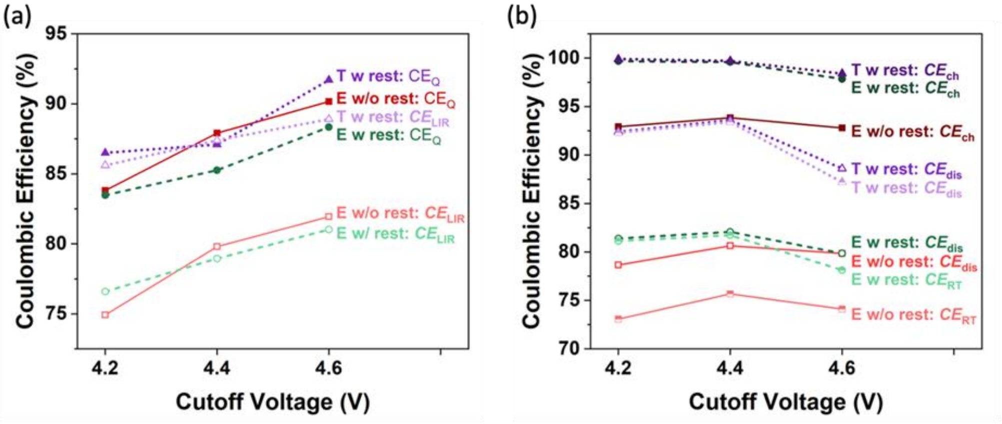

Figure 130. Comparison of Coulombic efficiencies (a) $\mathrm{CE_Q}$ and $\mathrm{CE_{LIR}}$ and (b) $\mathrm{CE_{ch}}$, $\mathrm{CE_{dis}}$, and $\mathrm{CE_{RT}}$ among ECOPRO (E) coin cells and TARGRAY (T) pouch cells, all made of the same slurry formulation, mass loading, and calendering density and gone through the same formation cycle protocol at C/10 charge and discharge rate and between 2.8 V and 4.4 V with 15-minute rest (with rest) at the end of charge and discharge. Some of the E cells were subjected to no rest (without rest) before the next step in the test.

Highlights of Keystone Project 2

The highlights for this quarter are as follows:

- UCSD showed that binder choice and porosity are essential for the cycling stability of high-loading SPAN cathode, concluding that the more elastic CMC binder is a good choice for low porosity cathode.
- BNL/UCSD showed that the distribution of sulfur-based species is inhomogeneous on the pristine SPAN cathode, but the chemical status (valence state of sulfur) is uniform.

Keystone Project 3: Cell Fabrication, Testing, and Diagnosis

Keystone 3 continues to focus on the integration of advancements from Keystone 1 and 2, optimization of cell design and the advancement of methods to better understand cell aging and failure through advanced testing and diagnostics. This quarter, the team advanced cell designs capable of extended cycle life (600+ cycles), advanced understanding of the mechanical response of Li-S cells, refined thermodynamic models for Li-S cells, and enhanced understanding of cell design and Li-metal thickness on cell failure.

The INL team used *in situ* monitoring of pressure evolution of Li-S pouch cells to enhance understanding of cell failure mechanisms. During cell operation in a fixed gap fixturing configuration, pressure evolves over the course of cycling. During early cycling, as expected, a decrease in pressure during discharge is observed (Figure 131a). The change in thickness is dominated by reduction in the thickness of the Li-metal anode, while at the cathode side of the cell, elemental sulfur (S_8) converts to Li_2S through multiple polysulfide intermediate steps. This conversion increases the volume of the sulfur active materials and thus increases the thickness of the cathode. However, the cathode-related increase is less than the reduction observed on the anode, hence the overall reduction in cell thickness during discharge. However, the pressure behavior was found to evolve during cycling (Figure 131b), with an initial drop of normalized pressure corresponding to a reduced anode thickness. Here, the reduced thickness is due to Li-metal loss caused by the generation/accumulation of polysulfides in the electrolytes. Afterward, the normalized pressure stabilizes when higher external pressure is applied (39.4 kPa and 98.5 kPa), suggesting more uniform anode thickness and anode structure with increased cycles. However, under lower applied pressure (7.8 kPa), a stable normalized pressure only lasted a short time followed by a gradual increase in normalized pressure, suggesting the increased anode thickness and unstable anode structure associated with the build-up of SEI and electrochemically isolated lithium (dead lithium). By analyzing the electrochemical and mechanical response from the cell (Figure 131c), that is, by comparing differential capacity (dQ/dV) with differential pressure (dP/dV) curves during discharge, information for understanding electrode evolution could be obtained. Uniform stripping of lithium (during discharge) or plating (during charge) should produce a peak intensity for dP/dV that closely tracks the dQ/dV trend, as seen in the CSE-based pouch cell under 98.5 kPa pressure. However, it was found that the peak intensity of dP/dV did not follow the dQ/dV trend when low-pressure was applied (for example, 7.8 kPa), suggesting a porous Li-metal anode structure is more easily generated under lower stack pressure. Post-test evidence agrees well with the inferences based on analysis from normalized pressure and dP/dV (Figure 131d) where a smoother surface, denser and thinner cross-section, and lower sulfur content were observed at higher applied pressure. In addition to stabilizing anodes, high pressure was found to enhance the cathode connectivity and avoid cathode cracking over cycling (Figure 131e). These results provide valuable information for developing a high-energy density Li-S battery with high-sulfur mass loading in cathodes.

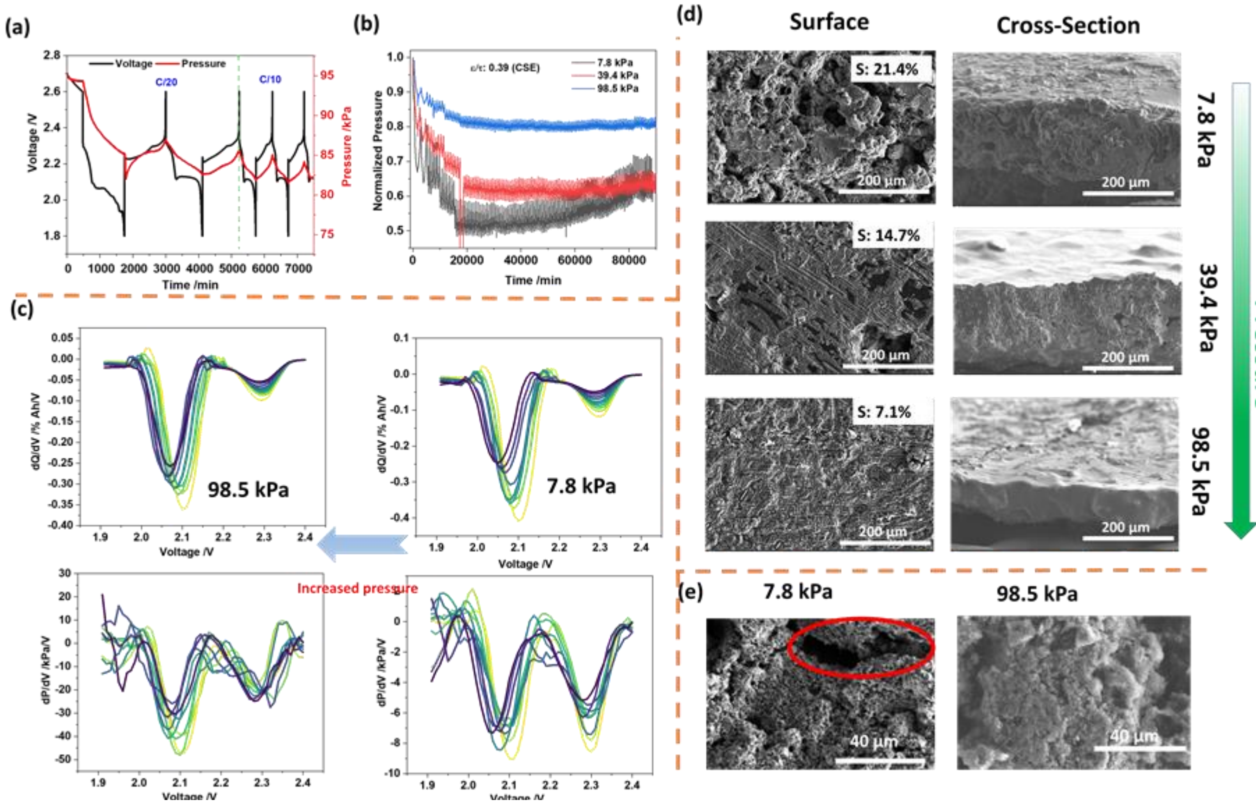

Figure 131. (a) The voltage and pressure variation during charge and discharge processes of calendered sulfur electrode-based Li-S pouch cell under 98.5 kPa pressure. (b) Normalized pressure change trend for calendered sulfur electrode-based pouch cells under different pressures. (c) dQ/dV and dP/dV curves over cycling during discharge process for calendered sulfur electrode-based cell under the pressure of 98.5 kPa and 7.8 kPa. (d) Scanning electron microscopy (SEM) images of surface and cross-sectional morphologies of Li-metal anodes in Li-S pouch cells at the end of charge after 120 cycles as a function of stack pressures. The upper right corner of surface morphology images shows the mass fraction of sulfur near the surfaces. (e) SEM images of surface morphologies of sulfur electrodes in calendered sulfur electrode-based pouch cells under the different pressures after 120 cycles at the end of charge.

UT-Austin and UW team developed hierarchical modeling of the Li-S system. A 0D thermodynamic model was developed with the capability to solve for voltage and concentrations of the Li-S system at equilibrium for various SOCs. Having the true thermodynamic state of a cell without the complications of other physical processes such as kinetics and transport is important to understand the fundamental behavior of the cell. The thermodynamics of the cell are modeled with the assumption that there are three regions of depths-of-discharge (DODs) corresponding to: (1) presence of S_8(s), (2) no solids, and (3) presence of Li_2S(s). Depending on the region, sets of equations related to the Nernst equations for each electrochemical reaction, sulfur mole conservation, charge balance, electroneutrality, and solubility product constraint exist. The 0D model was compared to a full one-dimensional (1D) model with kinetic and transport dynamics for a simulated GITT experiment where the cell was discharged to a specific DOD (solid lines) and allowed to relax (dotted lines), as shown in Figure 132. The final relaxed voltage for each relaxation simulation for a DOD is plotted as a gray cross in Figure 133. The results from the thermodynamic model in each of the three regions are also plotted and shown to match the full physics model. A C/20 discharge using the full model is also plotted as a reference.

The team also developed a 0D thermodynamic-kinetic model and compared all three models, as shown in Figure 134. Figure 134a-b shows zoomed in plots of the relaxation behavior at DOD = 96%. Figure 134a is of a standard parameter set found in the literature, where Figure 134b is for a set of diffusion-limited parameters (all diffusion coefficients are divided by 5, and cathode thickness is multiplied by 1.5). In the diffusion-limited set of parameters, it is shown that there is ~ 60 mV of overpotential, and the individual contributions of activation and concentration overpotential are distinct. The overpotential in the standard set is completely dominated by kinetics, which is a surprising result for low C-rates of C/20. Developing models to study the relaxation behavior with analog to GITT theory can be useful to identify the dominating behavior and aid experimentalists in analyzing cell design.

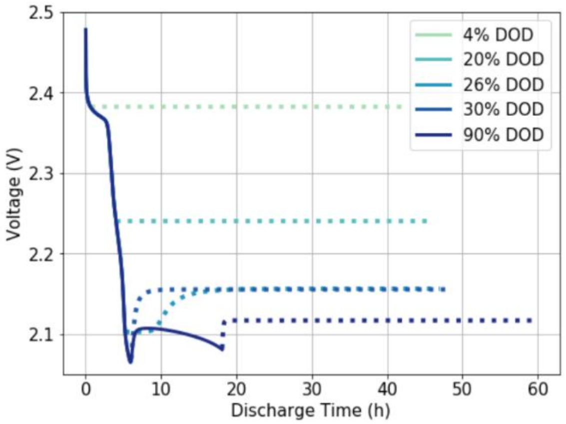

Figure 132. Relaxation simulations at various depths of discharge using full physics 1D model

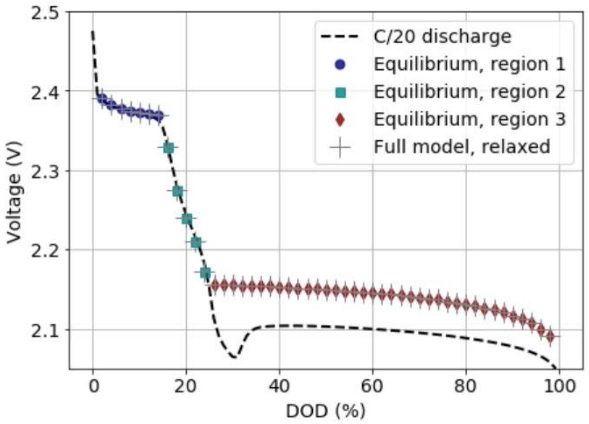

Figure 133. Relaxed voltages simulated using the thermodynamic equilibrium model and the full model.

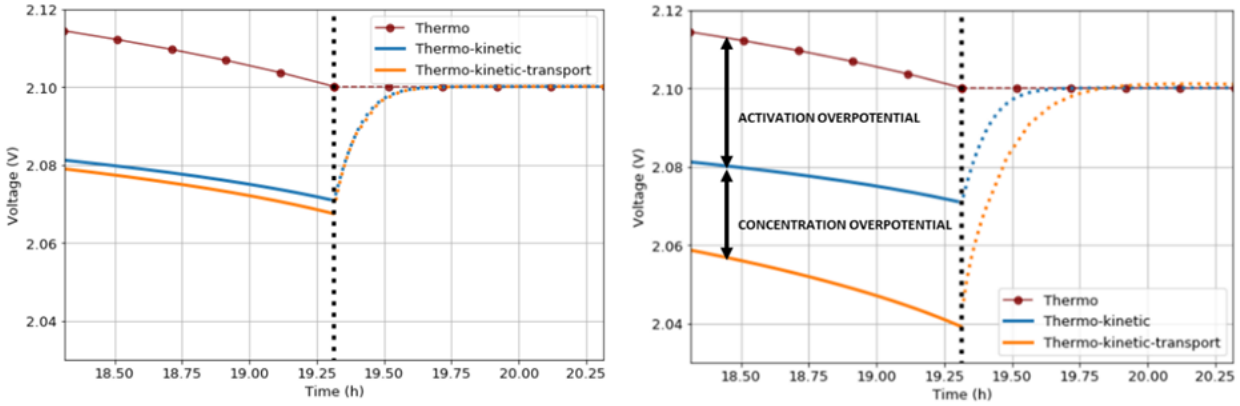

Figure 134. (left) Comparison of thermodynamic, thermodynamic-kinetic, and full model at depth of discharge (DOD) = 96% for standard parameters. (right) Comparison of thermodynamic, thermodynamic-kinetic, and full model at DOD = 96% for diffusion-limited parameters.

The team transformed the governing equations into the frequency domain to solve for impedance. Having a hierarchy of models allows mechanisms to be elucidated more readily and enables impedance analysis. For example, Figure 135a shows Nyquist plots simulated using the full physics model where the team explored phenomena at high frequencies. In Figure 135b, simulated using the 0D model with only thermodynamics and kinetics, the effects of ohmic resistance (starts at origin) are no longer observed and the 45° straight line that is representative of porous electrode behavior is not visible. Eliminating these can help elucidate other mechanisms more easily as there are actually 2-3 charge transfer semicircles (not shown) at lower frequencies.

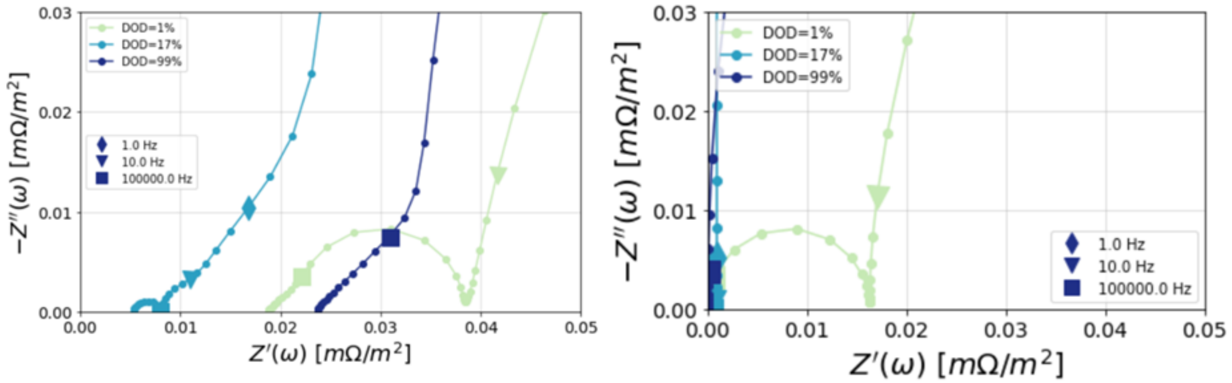

Figure 135. (left) Nyquist plot of full physics model. (right) Nyquist plot of 0D model with no spatial variation.

The PNNL team enhanced the understanding of pouch-cell failure based on high energy designs. By altering the thickness of the Li-metal anode, several trajectories of cell failure were observed (Figure 136). Opposite to the widely accepted concept that thick Li-metal anode is helpful in extending the cycling life, this team showed that a more rapid cell failure could occur due to kinetic limitations, which could limit cycle life. Therefore, reducing the thickness could prolong the cycle life and also leads to a more gradual failure near the end of life. The difference between the designs arises due to the uniformity and thickness of the SEI that forms during cycling. For the thinner lithium anode, a more uniform SEI was formed, minimizing the kinetic decay and the formation of electrochemically isolated lithium (dead lithium). The results of this work were published in 2021 in *Nature Energy* (see Publications section).

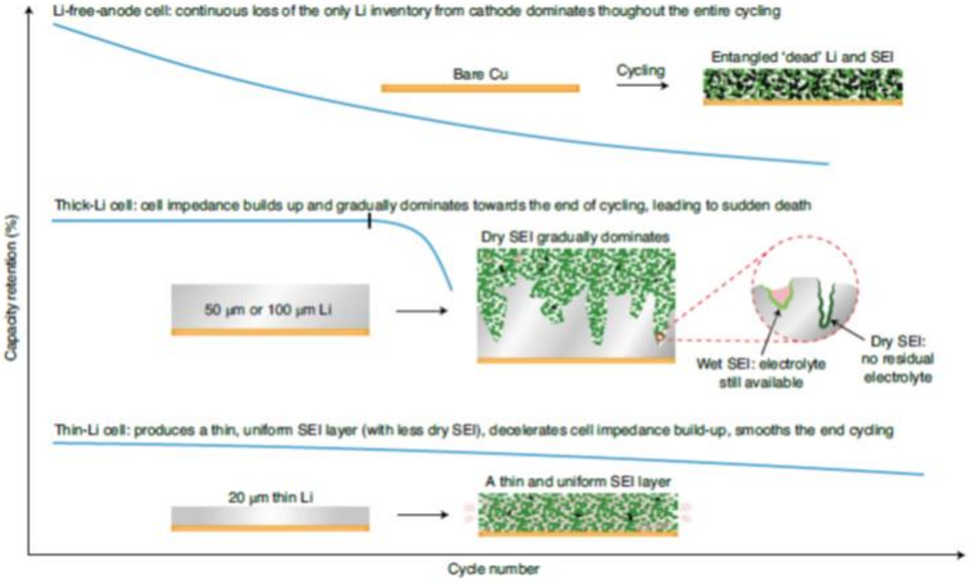

Figure 136. Cell failure trajectories as a function of cell design and initial lithium metal thickness.

Meng's group at UCSD studied the pressure tailored lithium metal deposition. It was found that the pressure has a significant impact on both the CE as well as the plating morphology of the Li-metal anode in previous studies of this group. At ~ 350 kPa stack pressure, the lithium was deposited in a perfectly packed columnar structure. However, it is worth noting that the bottom part of lithium deposits turns from relatively porous at 70 kPa to completely dense at 350 kPa, though the top part of lithium deposits at four different pressures are all dense, indicating the pressure effect plays an important role at the initial stage of lithium nucleation. This quarter, with this assumption, the pressure effects on lithium nucleation and initial growth stage with reduced lithium deposition loading at 2 mA/cm^2 for 0.33 mAh/cm^2 under 70 kPa, 140 kPa, 210 kPa, and 350 kPa were examined respectively. As shown in Figure 137a-b, the as-formed lithium nuclei showed completely different morphology at different applied stack pressure.

Cryo-FIB 3D reconstruction was used to quantify the porosity and volume of lithum deposits formed under 70 kPa and 350 kPa. Ideally, the total deposited lithium (0.333 mAh/cm^2) should exhibit a theoretical thickness of 1.620 µm with zero porosity. Plating at 70 kPa and 350 kPa, the lithium layer thickness is measured to be 3.677 µm and 1.697 µm, respectively (Figure 137e); the porosity is calculated to be 43.57% and 0.51%, respectively (Figure 137f). Based on these numbers, the pure deposited lithium volumes at 70 kPa and 350 kPa are normalized as 1.107 and 1.036, respectively, above the theoretical value of 1 (Figure 137g). The increased volume is ascribed to the porous electrode structure, where more lithium deposits are exposed to LE and form SEI with large surface areas. It is essential to eliminate the porosity of lithium deposition to minimize the surface exposure to LE that causes extra parasitic reactions consuming both electrolyte and active lithium during the plating process. With these new results, it is safe to conclude that without enough uniaxial stack pressure, lithium deposit grows freely at the vertical direction perpendicular to the current collectors (Figure 137a). The free-growing lithium whiskers have been extensively observed in previous *in situ*/*operando* study of the lithium plating process using optical microscope and environmental TEM, where no stack pressure was present in their experimental set-up. Under the stack pressure, the nucleation and initial growth of the lithium deposits will turn to lateral growth along the surface of the current collector (Figure 137d). At the critical pressure when the resistance at the interface exceeds the surface energy of growing laterally, the lithium deposition first grows laterally to fill the intergranular voids, followed by growing at the interface vertically due to the limitation of space laterally and forming a columnar structure. These results indicate that stack pressure can be used to precisely control lithium deposition morphology.

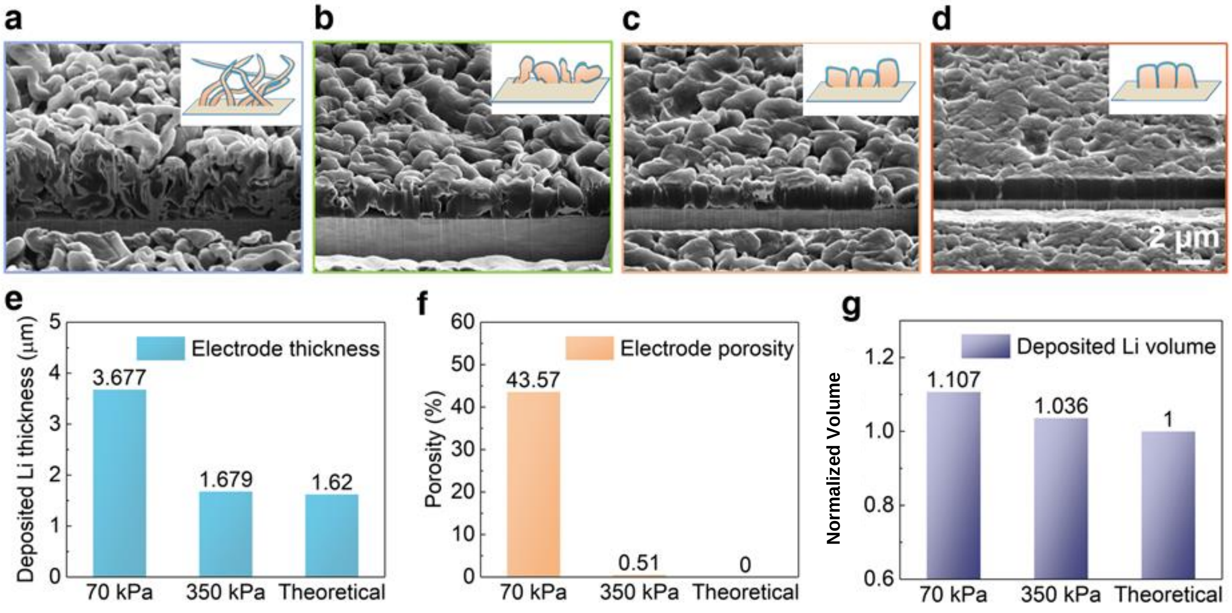

Figure 137. Quantifying pressure effects on initial growth of lithium metal. Cross-section scanning electron microscopy images of lithium deposits under pressure of (a) 70 kPa, (b) 140 kPa, (c) 210 kPa, and (d) 350 kPa at 2 mA/cm^2 for 10 minutes. (e) Electrode thickness, (f) electrode porosity, and (g) normalized volume of pure deposited lithium calculated from 3D reconstruction results.

Highlights of Keystone Project 3

The highlights for this quarter are as follows:

- The *in situ* monitoring study of pressure evolution of Li-S pouch cells to enhance understanding of cell failure mechanisms was carried out. (INL)

- Development of thermodynamic and kinetic-based Li-S cell models. (UT-Austin/UW)
- Identification of role of lithium thickness on failure pathway. (PNNL)
- A finding that at critical pressure, the lithium deposition first grows laterally to fill the intergranular voids, followed by growing at the interface and forming the columnar structure, which indicates that stack pressure can be used to precisely control the lithium deposition morphology. (UCSD)

Patents/Publications/Presentations

Patent

- Ren, X., W. Xu, and J-G. Zhang. "High Efficiency Electrolytes for High Voltage Battery Systems." U. S. Patent No. 11,094,966, August 17, 2021.

Publications

- Niu, C., D. Liu, J. A. Lochala, C. S. Anderson, X. Cao, M. E. Gross, W. Xu, J-G. Zhang, M. S. Whittingham, J. Xiao, and J. Liu. "Balancing Interfacial Reactions to Achieve Long Cycle Life in High Energy Lithium Metal Batteries." *Nature Energy* 6 (2021): 723–732. doi: 10.1038/s41560-021-00852-3. Note: This paper was published last quarter, but not listed in the respective report.
- Xie, Q., Z. Cui, and A. Manthiram. "Unveiling the Stabilities of Nickel-Based Layered Oxide Cathodes at an Identical Degree of Delithiation in Lithium-Based Batteries." *Advanced Materials* 33 (2021): 2100804. doi: 10.1002/adma.202100804.
- Kim, S. C., X. Kong, R. A. Vilá, W. Huang, Y. Chen, D. T. Boyle, Z. Yu, H. Wang, Z. Bao, J. Qin, and Y. Cui.* "Potentiometric Measurement to Probe Solvation Energy and its Correlation to Lithium Battery Cyclability." *Journal of the American Chemical Society* 143, No. 27 (2021): 10301–10308. doi:10.1021/jacs.1c03868.
- Y. Tsao, H. Gong, S. Chen, G. Chen, Y. Liu, T. Z. Gao, Y. Cui, and Z. Bao. "A Nickel-Decorated Carbon Flower/Sulfur Cathode for Lean-Electrolyte Lithium–Sulfur Batteries." *Advanced Energy Materials*, 11 (2021): 2101449.
- Z. Wu, S-M. Bak,* Z. Shadike, S. Yu, E. Hu, X. Xing, Y. Du, X-Q. Yang, H. Liu,* and P. Liu. "Understanding the Roles of the Electrode/Electrolyte Interface for Enabling Stable Li||Sulfurized Polyacrylonitrile Batteries." *ACS Applied Materials & Interfaces* 13 (2021): 31733–31740.
- Mishra, L., A. Subramaniam, T. Jang, K. Shah, M. Uppaluri, S. A. Roberts, and V. R. Subramanian. "Perspective – Mass Conservation in Models for Electrodeposition/Stripping in Lithium Metal Batteries." *Journal of the Electrochemical Society* 168 (2021): 092502. doi: 10.1149/1945-7111/ac2091.

Presentations (Invited)

- BMW Supervisors (July 14, 2021): "The Creation of a Rechargeable World"; M. S. Whittingham.
- Denver X-Ray Conference (August 5, 2021): "The Lithium Battery: The Origins to Domination - The Role of Structure and Disorder"; M. S. Whittingham.
- Nottingham, Roosevelt Memorial, United Kingdom (2021): "Energy Storage to Ameliorate Global Warming: The Lithium Battery and Its Journey to Domination"; M. S. Whittingham.
- LBNL ALS (August 11, 2021): "The Lithium Intercalation Battery: Its Origin, Future Challenges, and the Role that Characterization Plays"; M. S. Whittingham.

- UL (August 11, 2021): “Lithium Batteries: Future Trends and the Energy/Safety Tradeoff”; M. S. Whittingham.
- MRS Serbia, Yucomat (August 30, 2021): “The Lithium Battery, From a Dream to Readiness to Take on Climate Change – Materials Opportunities and Challenges”; M. S. Whittingham.
- Alfred University Seminar (September 2, 2021): “The Lithium Battery, From a Dream to Readiness to Take on Climate Change – Materials Opportunities and Challenges”; M. S. Whittingham.
- Italian Chemical Society Opening Plenary (September 14, 2021): “The Lithium Battery, From a Dream to Readiness to Take on Climate Change – Opportunities and Challenges for Chemists”; M. S. Whittingham.
- CIIF-WLA – Build Low Carbon Cities, Shenzhen, China (September 14, 2021): “The Critical Role that Energy Storage Plays in Reducing the Carbon Footprint of Cities”; M. S. Whittingham.
- Cambridge University, United Kingdom (September 30, 2021): “The Lithium Battery, From a Dream to Readiness to Take on Climate Change – Materials Opportunities and Challenges”; M. S. Whittingham.
- Award Talk, Faraday Medal of Royal Chemical Society, United Kingdom, Virtual (September 6, 2021); Y. S. Meng,
- Keynote Address, XRD Workshop Hosted by Benha University, Egypt, Virtual Conference (August 23, 2021); Y. S. Meng.
- Keynote, Singapore Section, ECS Chapter Talk (July 7, 2021); Y. S. Meng.
- John Deere (August 2021): “Development of Next Generation Batteries: Performance and Safety”; P. Liu. Invited.
- Automotive & Battery Safety Conference (September 27, 2021); P. Liu. Invited.
- *TUBA* World Conference on Energy Science and Technology (TUBA WCEST-2021), (August 8–12, 2021): “Sustainable Battery Chemistries for E-Mobility and Renewable Energy Storage”; A. Manthiram.
- Battery Safety Science Symposium: Advancing Safer Energy Storage through Science (August 11, 2021): “Sustainable Next-Generation Battery Chemistries”; .A. Manthiram.
- MateriAIZ Seminar Series, Arizona State University and University of Arizona, Phoenix, Arizona (August 27, 2021): “Sustainable Battery Chemistries for Electrical Energy Storage”; A. Manthiram.
- 50 Global Leaders of Energy Storage and E-Mobility Convention, ETN, Virtual, India (September 15, 2021): “Sustainable Battery Chemistries for Energy Storage”; A. Manthiram.
- Indian Oil R&D Golden Jubilee Webinar Series, Virtual, Indian Oil, India (September 17, 2021): “Sustainable Battery Chemistries for Energy Storage”; A. Manthiram.
- Shell (July 6, 2021): “Electrochemical Energy Storage: From Materials Science to Prototype Batteries and Cell Manufacturing”; J. Xiao.
- Molecular Foundry 2021 Annual User Meeting, LBNL (August 20, 2021): “From Materials Science to Prototype Batteries and Cell Manufacturing”; J. Xiao.
- Oregon Center for Electrochemistry Conference, University of Oregon (September 24, 2021): “Electrochemistry in Energy Storage Research”; J. Xiao.

APPENDIX – ACRONYM GUIDE

Acronym	Full Description
1D	one-dimensional
2D	two-dimensional
3D	three-dimensional
3DOP	three-dimensionally ordered microporous
AC	alternating current
ACS	American Chemical Society
AFM	atomic force microscopy
AIMD	*ab initio* molecular dynamic
ALD	atomic layer deposition
ALS	Advanced Light Source
ANL	Argonne National Laboratory
APS	Advanced Photon Source
ARL	U. S. Army Research Laboratory
ASR	area specific resistance
ASSB	all-solid-state battery
ASSLB	all-solid-state lithium battery
ASSLMB	all-solid-state lithium-metal battery
ASSLSB	all-solid-state lithium-sulfur battery
ATR	attenuated total reflectance
BBP	benzyl butyl phthalate
BE	baseline electrolyte
BEV	battery electric vehicles
BL	bottom layer
BMIM	1-butyl-3-methylimidazolium
BMR	Advanced Battery Materials Research Program
BNL	Brookhaven National Laboratory
CCCV	constant current / constant voltage
CCD	critical current density
CE	Coulombic efficiency
CEI	cathode electrolyte interface
CMC	carboxymethyl cellulose
CMD	classical molecular dynamics
CNC	carbon nano-cages
CNT	carbon nanotube
COP	critical overpotential
CPE	composite polymer electrolytes
cryo	cryogenic
cryo-FIB	cryogenic – focused ion beam
cryo-STEM	cryogenic – scanning transmission electron spectroscopy
CSE	cluster-based solid electrolytes
CV	cyclic voltammetry
DBE	dibutyl ether
DB-ML-FF	density-based machine-learning force field

Acronym	Full Description
DCA	dicyanamide
DEB	double-end binding
DEC	diethyl carbonate
DEE	diethyl ether
DEGDME	diethylene glycol dimethyl ether
DEMS	differential electrochemical mass spectrometry
DFT	density functional theory
DiPE	diisopropyl ether
DIW	direct ink writing
DL	double layer
DLR	Deutsches Zentrum für Luft- und Raumfaurt
DME	1,2-dimethoxyethane
DMSO	dimethylsulfoxide
DOD	depth-of-discharge
DOE	U. S. Department of Energy
DOL	1,3-dioxolane
DOS	density of states
dP/dV	differential pressure
dQ/dV	differential capacity
DRT	distribution of relaxation times
DSC	differential scanning calorimetry
EC	ethylene carbonate
ECS	Electrochemical Society
EDS	energy dispersive X-ray spectroscopy (also known as EDX)
EELS	electron energy loss spectroscopy
eGF	exfoliated graphene fluoride
EIS	electrochemical impedance spectroscopy
eLi	engineered lithium
EMC	ethyl methyl carbonate
EMIM	1-ethyl-3-methylimidazolium
eNMR	electrophoretic nuclear magnetic resonance
EO	ethylene oxide
E/S	electrolyte/sulfur
EV	electric vehicle
EXAFS	extended X-ray absorption fine structure
FDMB	fluorinated 1,4-dimethoxylbutane
FDMH	fluorinated 1,6-dimethoxyhexane
FDMO	fluorinated 1,8-dimethoxyoctane
FDMP	fluorinated 1,5-dimethoxypentane
FF	force field
FIB	focused ion beam
FSI	bis(fluorosulfonyl)imide
FTIR	Fourier transform infrared
FZJ	Forschungszentrum Jülich
GB	grain boundary
gc	glass/ceramic

Acronym	Full Description
GCPL	galvanostatic cycling with potential limitation
GITT	galvanostatic intermittent titration technique
GM	General Motors
Gr	graphene
GSE	glassy solid electrolyte
HAADF	high-angle annular dark-field
HCE	high-concentrated electrolyte
HEV	hybrid electric vehicles
HFE	hydrofluoroether
HPC	high-performance computing
HRTEM	high-resolution transmission electron microscopy
HT	high throughput
IL	ionic liquid
INL	Idaho National Laboratory
IPA	isopropanol
IR	Infrared
KB	Ketjenblack
KMC	kinetic Monte Carlo
LBNL	Lawrence Berkeley National Laboratory
LBO	Li_3BO_3
LCO	$LiCoO_2$
LCRC	Laboratory Computing Resource Center
LDBE	1.8 M LiFSI in dibutyl ether
LDEE	1.8 M LiFSI in diethyl ether / BTFE
LDiPE	1.8 M LiFSI in diisopropyl ether
LDME	1.8 M LiFSI in 1,2-dimethoxyethane
LE	liquid electrolyte
LFP	$LiFePO_4$
LGPS	$Li_{10}GeP_2S_{12}$
LHCE	localized high concentration electrolytes
LIC	lithium-ion conductor
LiTFSI	lithium bis(trifluoromethanesulfonylimide)
LLNL	Lawrence Livermore National Laboratory
LLZ	lithium – lanthanum – zirconium
LLZO	$Li_7La_3Zr_2O_{12}$
LLZTO	Li-La-Zr-Ta-O
LPS	Li_3PS_4
LPSCl	Li_6PS_5Cl
LSiPCl	$Li_{9.54}Si_{1.74}P_{1.44}S_{11.7}Cl_{0.3}$
LYC or LYCl	Li_3YCl_6
MC	Monte Carlo
MD	molecular dynamics
MGF	mixed glass former
MIC	molecular ionic composites
ML	machine learning
MLMD	molecular dynamics simulation with machine-learning potential

Acronym	Full Description
MOF	metal-organic framework
MOS	mixed oxy-sulfide
MOSN	mixed oxy-sulfide nitride
MPI	message-passing interface
MRS	Materials Research Society
MSD	mean square displacement
MWCNT	multi-walled carbon nanotube
MYEGA	Mauro–Yue–Ellison–Gupta–Allan model
NaFSI	sodium bis(fluorosulfonyl)imide
NaNMC	$NaNi_{0.68}Mn_{0.22}Co_{0.10}O_2$
nano-FTIR	Fourier transform infrared nano-spectroscopy
NASICON	sodium super ionic conductor
NBO	nonbridging oxygen
NBS	nonbridging sulfur
NCM	nickel – cobalt – manganese
ND	neutron diffraction
NEB	nudged elastic band
NMC	nickel – manganese - cobalt
NMC-622	$Ni_{0.6}Mn_{0.2}Co_{0.2}$
NMC-811	$Ni_{0.8}Mn_{0.1}Co_{0.1}$
NMP	N-methyl-pyrrolidone
NMR	nuclear magnetic resonance
NN	neural network
N/P ratio	capacity ratio between anode (negative electrode) and cathode (positive electrode)
NPCE	nonflammable polymer composite electrolytes
n-PDF	neutron diffraction and pair distribution function
NPT	constant number of atoms (N), pressure (P), and temperature (T)
NSLS	National Synchrotron Light Source
NTO	sodium titanate
OCV	open circuit voltage
OER	oxygen evolution reaction
OMSH	ordered microporous sulfur host
ORNL	Oak Ridge National Laboratory
ORR	oxygen reduction reaction
OSU	Ohio State University
PAH	polycyclic aromatic hydrocarbon
PAN	polyacrylonitrile
PAQS	poly (anthraquinonyl sulfide)
PBDT	poly(2,2’-disulfonyl-4,4’-benzidine terephthalamide)
PC	propylene carbonate
PC-LCHE	polymeric colloidal localized high concentration electrolyte
PDMS	polydimethylsiloxane
PE	polyelectrolyte, or polymer electrolyte
PEEK	polyether ether ketone
PEGDGE	poly (ethylene glycol) diglycidyl ether

Acronym	Full Description
PEO	poly(ethylene oxide)
PES	photon emission spectroscopy
PFIB	plasma focused ion beam
PGE	polymer gel electrolyte
PHEV	plug-in hybrid electric vehicle
PI	principal investigator
PNNL	Pacific Northwest National Laboratory
POSS	polyhedral oligomeric silsesquioxane
PP	polypropylene
PST	partially sintered tapes
PSTFSI	poly(4-styrenesulfonyl(trifluoromethanesulfonyl) imide)
PSU	Pennsylvania State University
PTFE	polytetrafluoroethylene
pTFSI	triflimide-based polyion
PVB	polyvinyl butyral
PVDF	polyvinylidene (di)fluoride
Py	pyrrolidinium
$Pyr_{13}FSI$	*N*-propyl-*N*-methylpyrrolidinium bis(fluorosulfonyl)imide
$Pyr_{14}TFSI$	*N*-butyl-*N*-methylpyrrolidinium bis(trifluoromethanesulfonyl)imide
RDF	radial distribution function
rGO	reduced graphene oxide
RMSE	root mean square error
RP	red phosphorus
SAXS	small angle X-ray scattering
SC	single crystalline
SE	solid electrolyte
SEB	single-end binding
SEI	solid electrolyte interphase
SEM	scanning electron microscopy
SEO	polystyrene-*b*-poly(ethylene oxide) block copolymer
SIC	single ion conductor
SIMS	secondary ion mass spectrometry
SLAC	Stanford Linear Accelerator Center
SOC	state of charge
SPAN	sulfurized polyacrylonitrile
SPE	solid polymer electrolyte
SPM	scanning probe microscopy
SRO	short-range order
SS	stainless steel
SSB	solid-state battery
SSE	solid-state electrolyte
SSI	solid-state ion
SSLB	solid-state lithium batteries
SSLMB	solid-state Li-metal batteries
SSRL	Stanford Synchrotron Radiation Lightsource
STEM	scanning transmission electron microscopy

Acronym	Full Description
SWCNT	single walled carbon nanotube
TAMU	Texas A&M University
TEGDME	tetraethylene glycol dimethyl ether
TEM	transmission electron microscopy
TEMPO	2,2,6,6-tetramethyl-1-piperidinyloxy
TFC	thin-film composite
TFP	tris(2,2,2-trifluoroethyl) phosphate
TFSI	trifluoromethanesulfonimide
TGA	thermal gravimetric analysis
TL	top layer
TM	transition metal
TMD	transition metal dichalcogenide
TOF-SIMS	time-of-flight secondary ion mass spectrometry
TRL	technology readiness level
TTE	1,1,2,2-tetrafluoroethyl-2,2,3,3-tetrafluoropropyl ether
TXM	transmission X-ray microscopy
UCB	University of California, Berkeley
UCSD	University of California, San Diego
UH	University of Houston
UIC	University of Illinois, Chicago
UM	University of Michigan
UMD	University of Maryland
UT	University of Texas
UW	University of Washington
VASP	Vienna *ab initio* simulation package
VTO	Vehicle Technologies Office
XAFS	X-ray absorption fine structure
XANES	X-ray absorption near edge structure
XAS	X-ray absorption spectroscopy
x-PDF	synchrotron X-ray diffraction and pair distribution function
xPEO	cross-linked PEO
XPS	X-ray photoelectron spectroscopy
XRD	X-ray diffraction
XRF	X-ray fluorescence
XRT	X-ray tomography